Title
Causes and consequences of unsteady crustal magma transport

Author
Karlstrom, Leif

Publication Date
2011

Peer reviewed|Thesis/dissertation

Causes and consequences of unsteady crustal magma transport

by

Leif Karlstrom

A dissertation submitted in partial satisfaction of the
requirements for the degree of
Doctor of Philosophy

in

Earth and Planetary Science

in the

Graduate Division

of the

University of California, Berkeley

Committee in charge:

Professor Michael Manga, Chair
Professor Mark A Richards
Professor Philip S Marcus

Fall 2011

Causes and consequences of unsteady crustal magma transport

Abstract

Causes and consequences of unsteady crustal magma transport

by

Leif Karlstrom

Doctor of Philosophy in Earth and Planetary Science

University of California, Berkeley

Professor Michael Manga, Chair

Magma transport pathways through Earth's crust span 12–15 orders of magnitude in time and space, with unsteadiness at all scales. However emergent organization of this system is widespread, recorded by spatial loci of volcanism at the surface and large–scale, rapid outpourings of magma throughout the geologic record. This thesis explores several mechanisms for the organization and time evolution of magma transport, from the deep crust to the surface. A primary focus (Chapters 2–5) is the filling, stability and drainage of magma chambers, structures which function both as reservoirs feeding individual volcanic eruptions and as stalling points in the crust where magma accumulates and differentiation occurs. We show that magma chambers may dictate the spatio–temporal organization of magma rising through crust (Chapters 2–3), control the surface eruptive progression of extreme mantle melting events (Chapter 4), and actively set the size of calderas that form during shallow, crystal rich eruptions (Chapter 5). Each of these chapters explores variations on a hypothesis: interactions between magma chamber stresses and the rheology of surrounding crustal materials evolve during magma transport and this unsteady process helps determine the magnitude, location, and timing of surface eruptions. The last part of this thesis (Chapters 6–7) focuses on surface transport processes, the meandering of melt channels on the surface of glaciers and lava flows. We show that the meandering instability is a generic feature of flow over an erodable substrate, despite significantly different fluid characteristics and erosion mechanics.

To Jana for real inspiration,
To Michael for taking a chance,
To Mousumi for a good suggestion,
and
To my parents, Karl and Anne, for getting me outside.

Contents

List of Figures

List of Tables

Acknowledgments

Thanks are due to collaborators on this work: Michael Manga, Mark A. Richards, Josef Dufek, Maxwell L. Rudolph and Parmesh Gajjar.

Chapter 1

Introduction

Volcanism is the surface manifestation of gradual and continuous upwelling and melting of Earth's convecting mantle. Beginning in the earliest stages of planetary evolution, volcanism will continue until heat generated through accretion, differentiation and radioactive decay is dissipated for billions of years. Remarkably, although melt production may be steady over geologically significant time intervals (∼10–100 million years), eruptions are episodic and spatially variable over time scales as small as decades. Where and when volcanism occurs depends on a complex interplay between the processes of melt transport, and external forces related to tectonics, climate perturbations, tides, and seismicity. Although challenging, deducing these key controls is a critical issue in Earth Science. Over time scales of human lives, understanding the recurrence and longevity of eruptions is crucial for assessing hazards and for characterizing the significant effects of volcanic forcing on climate. Over geologic time, the distribution and rate of volcanism largely govern atmospheric composition and the growth of continents. Volcanic events are implicated in the largest mass extinctions of life on Earth, but also provided a locus of heat and nutrients for the first life. Continual volcanic cycling thus provides a fundamental and direct coupling between the solid Earth, atmosphere, hydrosphere and biosphere.

Melting of mantle rocks drives surface volcanism through two primary endogenic mechanisms,1) the lowering of melting temperatures due to volatile addition, and 2) decompression [Turcotte and Schubert, 2002]. These mechanisms provide a basic framework for understanding where volcanic activity occurs on Earth. Subduction of oceanic crust introduces volatiles to mantle rocks, and volcanoes occur above subducted plates. Upwelling of hot and/or chemically distinct mantle induces anomalously rapid decompression and thus melting. Seismically imaged structures underlying oceanic volcanic centers such as Hawaii and Galapagos [e.g., Villagomez et al., 2007], as well as intra–continental "hotspots" such as Yellowstone [Smith et al., 2009] provide strong evidence that upwelling is ongoing under these regions. The thermochemical mantle convection responsible for transporting heat from within the Earth to the surface is thus our basic paradigm for understanding magma generation on geologic time scales. However, melting of mantle rocks is only the first step leading to surface volcanism.

Melting occurs first at grain boundaries [e.g. Cooper and Kohlstedt, 1984, Holtzman

et al., 2003], and buoyant magma must segregate from the mantle matrix before it can ascend. Primary melt ascent rate is thus limited by its ability to segregate and accumulate. Initial porosity is low but grows as melting progresses, and two phase buoyancy instabilities may enhance or suppress melting as porous flow is superimposed on larger scale upwellings [Hernlund et al., 2008]. This is the first of many occasions where unsteady processes may modulate a more steady base transport state. Once segregated, reactive and thermal erosion may channelize rising melts, creating porosity waves that enhance ascent rates and discretize previously homogeneous porous flow [e.g., McKenzie, 1984, Spiegelman, 1993].

Magmas must ascend through the Mohorovičić discontinuity, a sharp chemical transition that defines the base of the crust. The density decrease associated with this interface may cause magmas to stall, mix, and mingle with surrounding rocks [Hildreth and Moorbath, 1988]. Accumulations of melt reach large volumes at these depths [Cox, 1993], and discrete batches of melt generated lower in the transport network may accrue enough overpressure to actively fracture surrounding rocks, creating dikes that propagate on elastic timescales and drain a broad source region. Dike propagation occurs while driving pressures remain high (another source of unsteadiness in transport) [Rubin, 1995b], perpendicular to the least principle stress in the crust. They are guided upward by a decreasing lithostatic load, remote stresses due to tectonics and other local overpressurized sources. Dikes become the most efficient transport mechanism through an increasingly inhospitable thermal and mechanical environment in the upper crust, and frozen dikes are pervasive in exposed mid to lower crustal terrains (Figure 1.1, [Dumond et al., 2007]).

Crustal rocks transition from ductile to brittle on geologic timescales as the cool surface environment is approached and hydrothermal circulation modulates the geothermal temperature gradient. Depending on the rheological structure of the crust [Bürgmann and Dresen, 2008], background stresses associated with tectonics take over from those associated with magma transport as the principle stress guide for dikes. Stalled magmas will chemically evolve more rapidly in the shallow crust, be affected by surface loads, and reach depths at which water, the primary volatile dissolved in magmas, begins to exsolve. Ascent through upper portions of the crust depends critically on supply, as the input of enthalpy necessary to traverse this cool thermal environment increases. Magmatism at this stage integrates deeper unsteady transport with forcing on scales relevant to surface processes: loading and unloading from glaciers [e.g. Jellinek et al., 2004] and landscape evolution [Woods et al., 2002], triggering by earthquakes (static as well as perhaps dynamic stress changes) [Manga and Brodsky, 2006], and hydrothermal interactions [Reid, 2011]. These processes impose fluctuations in the thermomechanical background of the crust, and thus affect pathways and speed of magma ascent.

Background forcing also affects the properties of the magma itself. Stalled magma may partially crystallize or lose volatiles, dramatically increasing its viscosity and allowing for magma mixing during transit as fluid batches with different ascent speeds interact. A tremendous variety of magma transport processes are possible, as documented by frozen and uplifted crustal sections (Figure 1.2) [e.g, Miller and Paterson, 2001], surface eruption structures [e.g., Hildreth, 2007], and indirect observation (geodetic and seismic measurements

[e.g. Anderson et al., 2010]) of active eruptions. At the surface, monogenetic cones represent transient batches of magma with little interaction or modification by the crust, while evolved volcanic centers such as stratovolcanoes require variable and evolving reservoirs that capture some batches of rising magma but not others [Hildreth, 2007]. Caldera–forming eruptions are sourced from long–lived, high crystallinity shallow magma storage zones that are constructed over 100s of thousands to millions of years [Bacon and Lanphere, 2006], well mixed and thermally buffered to high crystal volume fractions [Huber et al., 2009] in a locked state before rapid mobilization and catastrophic evacuation during eruption.

Modern eruptions provide the clearest window into magma transport processes, even though all but the surface emplacement is hidden. Remote measurements provide constraints on active subsurface transport, while a record of ascent (rate as well as pressure, temperature, and composition) on eruptive scales is recorded by textural features of erupted magmas [e.g., Houghton et al., 2004], crystallization in the conduit [e.g., Blundy and Cashman, 2005], and bubbles locked in frozen melt [e.g., Manga et al., 1998]. Historical eruptions provide analogs to all but the largest volume ("super–eruptions") and hottest (kimberlitic) frozen eruptions. These modern examples demonstrate that eruption style reflects magma ascent rate and viscosity [Gonnermann and Manga, 2007]. Transitions from Plinian eruptions to lava dome formation, and from explosive to effusive basaltic eruptions, can be largely predicted on the basis of these two parameters (Figure 1.3 and [Gonnermann and Manga, 2011]). Such seemingly simple control parameters disguise a much more complex story: both ascent rate and magma viscosity reflect the integration of deeper magma transport processes. Considering that unsteadiness in volcanic eruptions may occur on minute timescales, the full range of processes reflected in a given eruption spans up to 12–15 orders of magnitude in time (eruption unsteadiness to mantle melting over millions of years) and space (microscale grain boundary melting to dike transport over thousands of kilometers). This range is estimated for all relevant magma transport processes in Table 1.1.

A mechanistic synthesis of magma transport processes covering the range of important spatiotemporal scales is not yet possible. The regime diagram for eruption dynamics (Figure 1.3) is an important part of this synthesis, and further refinements will bring transitions in eruption style into clearer focus, but prediction of deeper controls on crustal magma transport is still an unrealized goal in volcanology. Such controls allow exploration of magma transport dynamics as a function of the eruptive control parameters, magma ascent rate (e.g., what triggers eruptions and determines maximum basal pressures for conduit flow?) and viscosity (e.g., what deep processes are responsible for the observed multimodal distribution of arc magma compositions?). It may also be possible to invert active eruption processes for transport history, or back out transport dynamics from the eruptive record.

This thesis provides several steps towards understanding magma transport (Table 1.1). Focusing primarily on magma storage processes, the first three chapters identify generic controls on the filling and stability of magma chambers and with application to spacing of arc volcanoes and the duration of Large Igneous Province "main phase" eruptions. These applications are not intended to be exhaustive, but rather represent the potential for synthesizing models for unsteady magma transport with geologic data. Chapter four studies the drainage

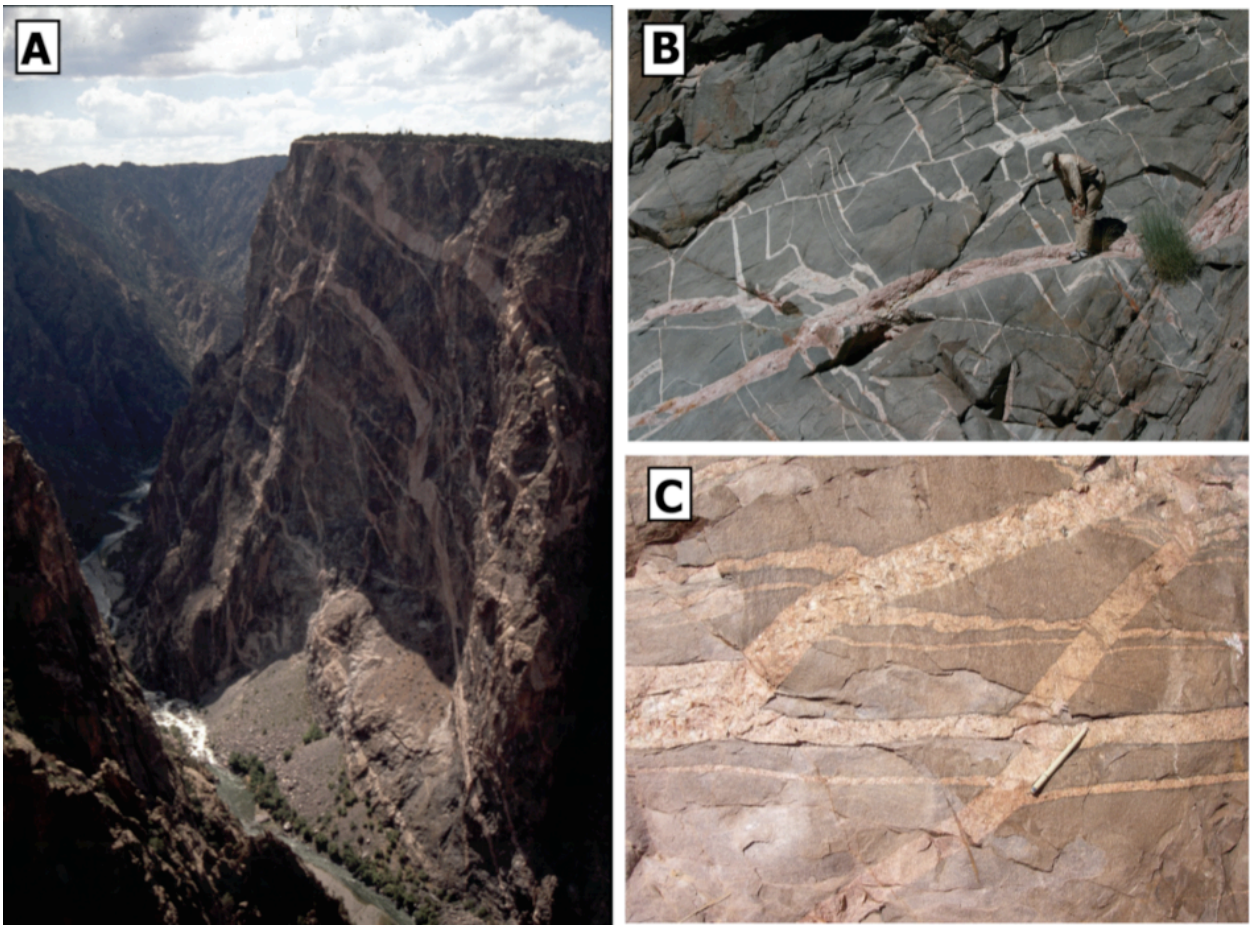

Figure 1.1: Examples of dike networks at a variety of scales in exposed mid to lower crustal terrains [Dufek et al., 2011]. a) Pegmatite dikes cross cutting gneisses on the 670-m-high Painted Wall, Black Canyon of the Gunnison CO. b) Orthogonal dike network of granite and pegmatite cross cutting grandiorite in Upper Granite Gorge, Grand Canyon AZ. c) Four generations of granite dikes in Lower Granite Gorge, Grand Canyon AZ.

of shallow magma chambers during caldera forming eruptions, coupling multiphase conduit flow with magma chamber deformation with application to the geologic record of caldera forming eruptions. Chapters five and six focus on surface transport processes, unsteady channelization instabilities (meander formation) in supraglacial streams and lava channels. The modeling in these chapters identifies common fluid/solid instabilities as the origin for meandering channels in very different environments. This work demonstrates that, while the mechanics of mass transfer may differ significantly across geologic settings, instabilities that determine larger scale structures may be largely insensitive to mechanism in some cases. Identifying such features in subsurface magma transport is a promising direction for future work.

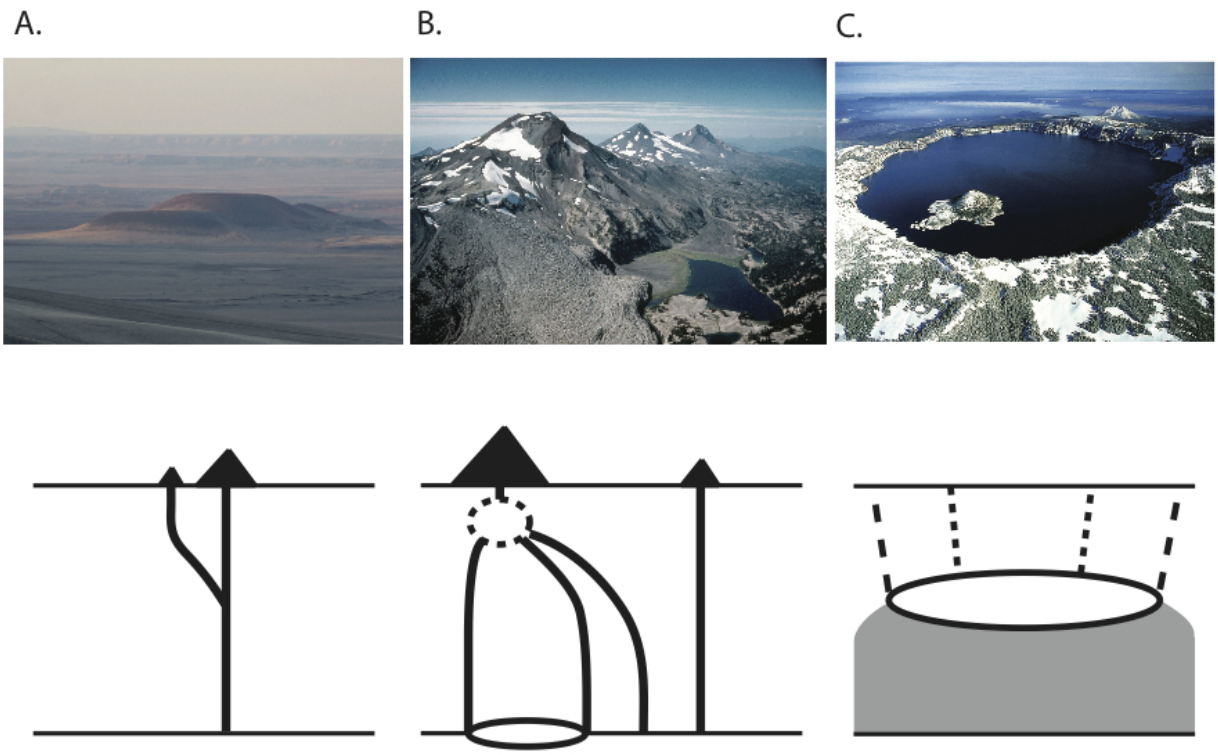

Figure 1.2: Examples of magmatic plumbing and their associated volcanic surface expressions. a) Monogenetic cone from the San Francisco volcanic field, AZ and cartoon of simple dike feeder. b) Evolved stratovolcoanes in the Cascade arc (Three Sisters, OR), with implied storage at one or more locations within the crust. c) The caldera at Crater Lake National Park, OR, an example of eruption from a shallow and extensive magma chamber requiring prolonged assembly.

Unsteady process	**Time scales**	**Spatial scales**	**References**
Melting of mantle matrix	$10^{10} - 10^{13}$ s	$10^{-3} - 10^{-6}$ m	[1]
Melt extraction from mantle matrix	$10^{10} - 10^{13}$ s	$10^{4} - 10^{5}$ m	[2,3]
Melt channelization	$10^{7} - 10^{9}$ s	$10^{-1} - 10^{2}$ m	[4,5]
Dike formation	?	$10^{0} - 10^{2}$ m	[6]
*Dike propagation/interaction	$10^{4} - 10^{8}$ s	$10^{0} - 10^{4}$ m	[7]
*Magma chamber formation	? -10^{13} s	$10^{2} - 10^{5}$ m	[8,9]
*Magma chamber drainage	$10^{3} - 10^{8}$ s	$10^{2} - 10^{5}$ m	[10,11]
*Conduit flow	$10^{0} - 10^{4}$ s	$10^{-2} - 10^{4}$ m	[12]
*Surface eruption/transport	$10^{0} - 10^{4}$ s	$10^{0} - 10^{4}$ m	[13,14]
Background forcing:			
Tectonics	$10^{12} - 10^{13}$ s	$10^{4} - 10^{5}$ m	[15]
*Edifice construction	$10^{7} - 10^{12}$ s	$10^{3} - 10^{4}$ m	[16]
Climate	$10^{7} - 10^{12}$ s	$10^{4} - 10^{5}$ m	[17]
Geomorphic unloading	$10^{3} - 10^{10}$ s	$10^{2} - 10^{4}$ m	[18]
Basal loading (from mantle)	$10^{11} - 10^{13}$ s	$10^{4} - 10^{5}$ m	[19]

Table 1.1: Processes occurring during magma transport from source region to surface, with the range of temporal and spatial scales over which these processes are unsteady. Stars indicate topics addressed in this work. References are [1] Holtzman et al. [2003], [2] Hernlund et al. [2008], [3] citeMarsh:1974aa, [4] McKenzie [1984], [5] Spiegelman [1993], [6] Rubin [1995b], [7] Ito and Martel [2002], [8] Pinel and Jaupart [2003], [9] Karlstrom et al. [2009], [10] Jellinek and DePaolo [2003], [11] Karlstrom et al. [2010a], [12] Gonnermann and Manga [2007], [13] Griffiths [2000], [14] Gurioli et al. [2003], [15] Gottsmann et al. [2009], [16] Muller et al. [2001], [17][Huybers and Langmuir, 2009], [18] Jellinek et al. [2004], [19] Farnetani and Richards [1994]

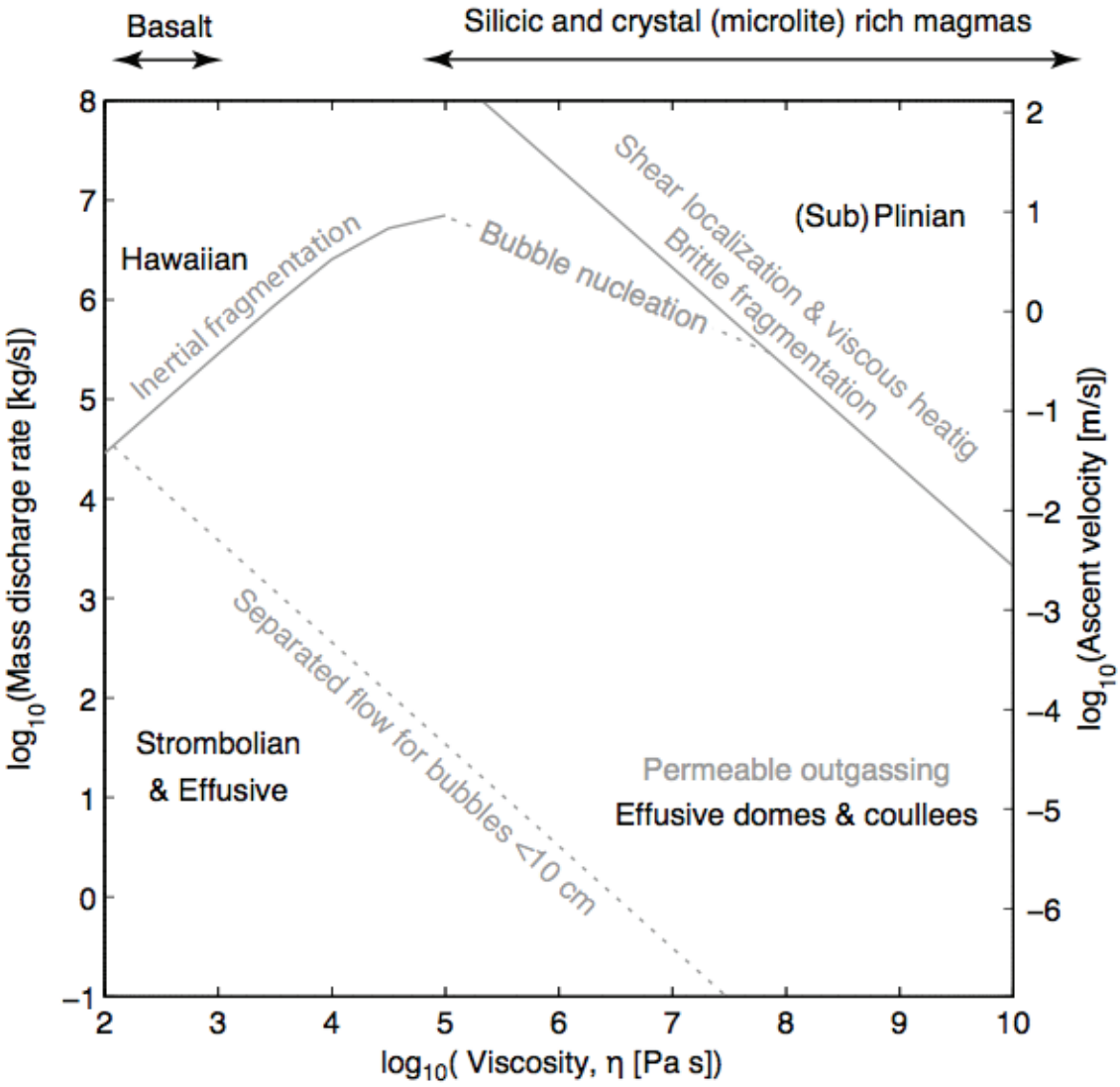

Figure 1.3: Regimes of eruption styles and associated conduit processes, as a function of magma viscosity and ascent rate [Gonnermann and Manga, 2011].

Chapter 2

Organization of volcanic plumbing through magmatic lensing by magma chambers and volcanic loads

2.1 Introduction

The presence of volcanic edifices requires a focusing of magma ascending from the mantle and lower levels of the crust. The spatial extent and processes of magma transport beneath volcanoes that govern the discrete morphology and spacing of volcanic centers are, however, difficult to constrain because the transport network is buried beneath the surface, and it evolves on timescales that range from hours (volcanic eruptions [e.g., Stasuik et al., 1993, Petcovic and Dufek, 2005]) to $\sim 10^6$ years (crustal melt flux [e.g., Dimalanta et al., 2002, Dufek and Bergantz, 2005]).

Melt ascending from the upper mantle must negotiate structural controls imposed by material and rheological boundaries within the crust, as well as an increasingly cool thermal environment, that act to slow and sometimes stall magma ascent. In addition, tectonic stresses and near-surface faults may often play a significant and location-specific role in the organization of volcanism [e.g., Nakamura et al., 1977, Vigneresse et al., 1999]. These background features determine the environment through which magma migrates, and may influence the locations of deep-seated magma chambers [e.g., Kavanagh et al., 2006] as well as the pathways available to volcanism [e.g., Galland et al., 2007]. Within the confines of these initial conditions, the processes of magma transport organize the volcanic plumbing system into discrete centers that then are expressed as volcanoes on the surface. These centers in turn affect the background state of the crust, and represent thermomechanical anomalies that will exert increasingly long-range influence over their active lifetimes.

Two general approaches are typically followed to explain the formation and evolution of volcanic centers. These take either a “bottom up” or “top down” perspective, whereby processes occurring at the melt source region or at the surface dominate the organization

and focusing of rising magma. Implicit in both approaches is the assumption that boundary conditions at the top or bottom interface of the transport region dominate internal dynamics. The "top down" models account for the effect of volcano building on the stress state in the underlying crust [e.g., Pinel and Jaupart, 2000, Muller et al., 2001], and the role of lithospheric flexure in the formation and subsequent organization of volcanoes [ten Brink, 1991, Hieronymus and Bercovici, 1999]. Volcano loading and subsequent flexural stresses can have a significant effect on subsurface processes, though it is of note that all "top down" studies to date require the presence of an initial volcano to focus magma. "Bottom up" models [e.g., Marsh and Carmichael, 1974, Olson and Singer, 1985, Ihinger, 1995], on the other hand, establish discrete volcanic centers much earlier in the transport network. Here, fluid dynamic instabilities (Rayleigh-Taylor type) generate zones of enhanced melting in the mantle source region; subsequent ascent and eruption of these melts generates edifice spacing corresponding to the spacing of the melting zones.

There is, however, an additional possibility for the organization of a magma plumbing system, in which localization occurs intermediate to the "top" and "bottom" regions, prior to the first eruption. It has been recognized that individual components of the magmatic transport system (dikes, chambers) can significantly alter the mechanical and thermal properties of their surroundings [e.g., Ito and Martel, 2002, Jellinek and DePaolo, 2003, de Silva and Gosnold, 2007]. Here we show that localization via surface or source boundary conditions are end-member cases for the formation of volcanic centers, and that magmatic plumbing systems may be actively self-organized in the subsurface through interactions between magma chambers and dikes in addition to volcanic edifices. These focusing processes are not mutually exclusive, nor are they necessarily part of a mechanistic hierarchy. Rather, interfacial, structural, and internal dynamic controls on magmatic localization form the basis of a general physical framework for understanding volcanic centers.

We propose a new addition to this framework, and develop a simple static model of dike focusing due to an overpressured and buoyant magma chamber beneath a free surface. This chamber growth mechanism (hereafter referred to as "magmatic lensing") is an effective way to localize rising magma, and we show that it may dominate the static effects of surface loading in many cases. Temporal evolution of the mechanical system, including thermally induced rheological modulation of crustal stresses and chamber rupture are not considered here, but are the subject of a companion paper [Karlstrom et al., 2009] that considers the stability of magma chambers that grow via dike focusing. Magmatic lensing is a process that has implications for the formation of magmatic plumbing, and extends previously proposed ideas for the formation of discrete volcanic centers.

As a qualitative application of our model, we then show how the spacing of magma chambers controlled by magmatic lensing might be used to interpret arc volcano spacing, and to constrain chamber sizes and depths. We compile a database of spacing between discrete Holocene stratovolcanoes around the Pacific Rim, and show that the observed average spacing between centers may be produced in our model by dike-lensing magma chambers. We are unable to uniquely constrain chamber depth or size, but show that chambers at mid to lower crustal depths with a range of volumes fit the observational data equally well. We find

that circum-Pacific volcano spacing is not correlated with plate convergence rate or crustal thickness (for crust thicker than 20 km), consistent with the idea that long-term magma storage modulates spacing. Based on our calculations and observations of Pacific Rim arc volcanoes, we hypothesize that volcanic plumbing is a self-organizing system that evolves to a given surface morphologic expression constrained – but not solely determined – by the surface and source-region boundary conditions.

2.2 Methods

We model a magma chamber in two spatial dimensions as a pressurized and buoyant cylindrical cavity in an elastic half space [e.g., Odé, 1957, Gudmundsson, 2006], as depicted in Figure 2.1. This model is static, in that we do not directly address dike propagation or time-dependent stresses such as might arise from viscoelastic or yielding rheology, and we neglect any buoyant rise of the magma chamber. However, even in the lower crust dike propagation timescales should be shorter than both the viscoelastic relaxation timescale of the country rock and the Stokes rise time of the chamber [Karlstrom et al., 2009], and evidence of pervasive diking in mid to lower crustal terrains (10-25 km depth) [e.g., Dumond et al., 2007] provides observational support for the assumption of some elastic behavior at depth. As our present purpose is to compare the mechanical properties of magmatic lensing to other melt focusing proposals at a range of depths, such a simple analysis is justified. In this level of analysis, we also neglect depth-dependent density [Grosfils, 2007], and the more complicated chamber geometries inferred for real volcanic systems [e.g., Newman et al., 2006].

Solutions are obtained to the equations of linear elasticity by the method of stress functions [Fung, 1965]. Boundary conditions at the chamber wall are:

$$\sigma^n = \Delta P + \Delta\rho g R \cos\phi \tag{2.1}$$

$$\sigma^t = 0 \tag{2.2}$$

and at the free surface $y = 0$

$$\sigma^n = 0 \tag{2.3}$$

$$\sigma^t = 0 \tag{2.4}$$

where σ^n is the normal stress and σ^t is the tangential stress, ΔP is the chamber pressure over lithostatic, $\Delta\rho$ is the density difference between magma and the country rock, R is the radius of the chamber, g is gravity and $r\cos\phi = y$ defines the polar coordinate system used to write down boundary condition equation 2.1 (Figure 2.1). Using the bipolar coordinate system [e.g., Jeffery, 1921], we obtain approximate stress functions (detailed in the Appendix) from which displacements and deviatoric stresses may be determined. We use the convention that positive stresses are compressive.

To evaluate the influence of a volcanic edifice for which an analytic solution is not possible, we calculate stresses due to a chamber and a triangular surface load with the Direct Boundary

Integral code BEMECH [Gao and Davies, 2002]. We discretize the free surface with 150 quadratic boundary elements extending 5000 times the volcano width to approximate an infinite boundary, and use exponential node spacing near the corners of the volcanic edifice to more accurately resolve the load; the edifice is exponentially discretized with 23 elements. The surface satisfies the boundary conditions

$$\sigma^n = \begin{cases} \rho_b g h \frac{(w-|x|)}{w} & \text{if } -w \leq x \leq w \\ 0 & \text{otherwise} \end{cases} \tag{2.5}$$

$$\sigma^t = 0 \tag{2.6}$$

with h the height of the volcano, w its half-width, and $\rho_b = 3000$ kg/m^3 an upper bound for density (Figure 1). The circumference of the magma chamber is described by 176 uniformly spaced quadratic boundary elements. We assume a lithostatic background stress field for the simulations here, but do address the qualitative effects of regional deviatoric tectonic stress, a possible scenario in many realistic circumstances [e.g., Muller et al., 2001]. Mesh refinement does not change our results significantly, and comparison with available analytical solutions for the case of no edifice (equations 2.19-2.21) confirms the accuracy of the method.

2.3 Magmatic Lensing

The magma chamber is supplied by melt contained in rising dikes, and represents a location where migrating magma stalls or accumulates. We assume that dikes propagate in a direction perpendicular to the least compressive principal stress at the dike tip [e.g., Anderson, 1951]. Dikes are often modeled as two-dimensional fluid filled mode-I fractures driven by overpressure and buoyancy [Rubin, 1995a]. Dikes propagate, in the most general sense, when the potential energy released through propagation is sufficient to fracture rock at the crack tip [Griffith, 1920]. This is a threshold energy criterion for propagation, and is a feature of all "critical" dike propagation models, though so-called "sub-critical" dike propagation [Atkinson and Meredith, 1987] may also be an important magma transport mechanism over short distances [Chen and Jin, 2006].

We use the less general but more convenient Stress Intensity Factor formulation of Linear Elastic Fracture Mechanics [e.g., Rubin, 1995b], from which the simplest model of a dike is derived: a uniformly pressurized elliptical crack that propagates when the stress intensity factor K exceeds the critical value $K \geq K_{crit} = \Delta P_{dike}\sqrt{L}$. Here K_{crit} is the critical Stress Intensity Factor or facture toughness of the host rock, ΔP_{dike} is the dike overpressure, and L is the length of the dike. We take $K_{crit} = 10^6$ Pa m$^{1/2}$ [Rubin, 1995b], with the understanding that this value is not well constrained for crustal materials, and may vary dike to dike as well as with depth [e.g. Atkinson and Meredith, 1987]. Therefore, the threshold stress for dike propagation in our model is 10^6 Pa (but see below), and far-field deviatoric principal stresses in excess of this value may re-orient the trajectory of a rising dike.

It should be emphasized that our threshold approach is a simplification because the evolving stress field generated by the dike itself must be accounted for to determine the true

propagation direction. Indeed, a detailed numerical calculation of dike propagation from volcanic centers [Meriaux and Lister, 2002] reveals that calculation of dike trajectories solely from the ambient stress field may be inaccurate. Nevertheless, Meriaux and Lister [2002] show that the qualitative aspects of dike re-orientation remain unchanged, and that magmatic lensing effects may even be amplified when the more detailed mechanics are included. The re-orientation of dikes has been found to be significant even when more geometrically detailed propagation is accounted for [Muller et al., 2001], and more realistic ellipsoidal chamber geometries [e.g., Gudmundsson, 2006] do not affect the first order stresses. Some treatments of dike propagation neglect the strength of crustal rocks [e.g., Pinel and Jaupart, 2000], on the grounds that its contribution to the overall force balance is negligible. We note, however, that processes occurring at the dike tip still control the propagation direction, and that any other "critical" dike model will also contain a threshold driving stress criteria for propagation.

Our approach is a class of parameterization that captures the physics of interest. We expect our results to be most accurate in the limiting case when chamber stresses are much larger than dike stresses, a situation that may be typical (see Discussion) even though dike overpressures (determined by dike length and buoyancy) may vary. We also expect that our choice of 1 MPa as a threshold stress for dike re-orientation is an upper bound, as the fully coupled problem reveals that dikes may be much more easily affected by background deviatoric stresses [Meriaux and Lister, 2002]. Our criteria for dike reorientation should thus provide a conservative estimation of magmatic lensing.

For chambers that are significantly overpressured or buoyant with respect to regional stresses there exists a region below the chamber inside which stresses are larger than the critical stress of 1 MPa, and trajectories of rising dikes are focused toward the magma chamber (Figure 2.1). We quantify this region through the notion of a "capture radius" at a given depth below the magma chamber, measured from the center of the chamber parallel to the free surface (Figure 2.1, 2.2.a), and defined by the distance for which chamber stresses are large enough to affect rising dikes. Because chamber stresses fall off rapidly in magnitude away from the chamber, this capture radius depends on the depth at which it is evaluated (Figure 2.2.b), and we arbitrarily choose 10 km below the chamber as the depth at which we evaluate dike capture.

2.4 Magma Chamber Overpressure

The importance of magmatic lensing depends critically on the magnitude of stresses exerted by the magma chamber, but bounds for chamber stresses are poorly constrained. Chamber overpressure develops through a variety of processes that include volatile exsolution, magmatic differentiation, melting or solidification of wall rocks, and injection of new magma into the chamber [e.g., Tait et al., 1989, Folch and Marti, 1998, Annen and Sparks, 2002]. Of these, the largest elastic pressures ΔP are generated through injection of largely incompress-

ible magma through dikes or melting of wall rocks, and follow

$$\Delta P = \frac{1}{\beta}\frac{\Delta V}{V}, \tag{2.7}$$

where ΔV is the change in chamber volume V, and $\beta \sim 10^{-11}$ Pa^{-1} is the magma compressibility [Tait et al., 1989]. Because the initial generation of melt (with $\Delta V = (1.1 - 1.15)V$ upon melting [e.g., Rapp and Watson, 1995]) may induce enormous pressures through equation 2.7 (modulated heavily by anelastic processes such as compaction, and porosity shock waves dues to permeability contrasts in the magma source region [e.g., Spiegelman, 1993]), dikes that remain at high melt fraction during propagation should very often have higher pressure than magma chambers. An upper bound on magma chamber overpressure in this case is given by the stress at which chamber rupture occurs, resulting in a draining of magma from the chamber, and a decrease of chamber overpressure (also following equation 2.7).

However, the mechanisms by which chamber rupture occurs are not well understood. A number of studies [e.g., Sartoris et al., 1990] use the criterion that chamber rupture occurs when tensile stresses at the wall of the chamber exceed the tensile strength of rocks. This leads to maximum overpressures on the order of 1-10 MPa, for laboratory-determined values of rock failure [Atkinson and Meredith, 1987, Gudmundsson, 1988]. This is likely an underestimate of maximum chamber overpressure at depth, which may also be a function of tectonic regime, as rock failure depends on confining stresses and background deviatoric stresses. The rheology of magma chamber wall rocks will be strongly affected by prolonged heating, and thus "critical" brittle fracture may not be the dominant mode of initial chamber rupture. Anelastic processes, such as the viscous blunting of dike tips, and viscoelastic relaxation of deviatoric stresses around the chamber have been shown to strongly affect the initiation and propagation of cracks [e.g., Dragoni and Magnanensi, 1989, Jellinek and DePaolo, 2003, Chen and Jin, 2006]. However, these processes are not straightforward to quantify, so other criteria are currently more reliable for estimating maximum chamber overpressures.

Thermal considerations of long-distance dike propagation by Rubin [1995a] have been used to place bounds on pressures needed to drive a dike from magma chamber to surface [Jellinek and DePaolo, 2003]. By balancing the elastic propagation of a dike and the gradual solidification of dike walls, critical driving magma chamber pressures are 10-100 MPa for a range of material properties. This critical overpressure depends on the composition and tectonic setting of the chamber [Jellinek and DePaolo, 2003], and provides an upper bound on the driving pressures needed for propagating dikes to overcome the geothermal gradient (avoid freezing) between chamber and surface.

Another approach to estimating chamber overpressure comes from volcano geodesy, where ground deformation in volcanic areas due to inflating magma chambers can be measured. Geodetic measurements of this kind are now standard at many active volcanoes worldwide [e.g., Massonnet et al., 1995, Pritchard and Simons, 2004, Yun et al., 2006], and provide estimates for the theoretical chamber overpressure necessary to produce observed ground deformation. While strongly model dependent, there are some examples which may be used

with reasonable confidence to be representative of true chamber overpressures. In particular, Newman et al. [2001, 2006] estimate magmatic overpressure in the Long Valley Caldera over a several year period using a viscoelastic magma chamber model, and find that geodetic data are well fit for overpressures in the range of 10-70 MPa, depending on the chamber model geometry. These pressures are not an upper bound on chamber overpressure, as the Long Valley Caldera did not erupt during the period of observation. It is of note that a purely elastic model also fit the data but required overpressures of up to 500 MPa, several times lithostatic pressure [Newman et al., 2001], a result that is common in studies that use solely elastic models. Such high overpressures are unrealistic for long term deformation, but may be possible as transient overpressure before rupture. Houlie et al. [2009] combine seismicity and geodesy to infer a time series of magma chamber pressure at La Piton de la Fournaise volcano that exceeds 100 MPa (and lithostatic pressure) on several occasions over a 20 year period [Houlie et al., 2009].

We can assume, based on these observations, that magma chamber overpressure can grow quite large, during the inflation period prior to eruption. We use 100 MPa as a large but not unreasonable upper bound for magma chamber overpressure, and acknowledge that there is significant uncertainty in this quantity. We also quantify the magmatic lensing mechanism for lower magma chamber overpressure (Figure 2.7). However, as chamber inflation is to first approximation due to influx of magma, magmatic lensing constitutes a positive feedback (larger overpressures generated by magma influx result in a larger capture radius) that provides a means for magma chambers to attain the largest possible overpressure. We also note that once chamber rupture occurs and magma leaves the chamber, overpressure will rapidly decrease according to equation 2.7.

2.5 Results

For a magmatic plumbing system containing a chamber but no surface volcanic edifice, the capture radius at any depth may be calculated implicitly by setting the maximum deviatoric principal stress equal to the critical stress of 1 MPa. Figures 2.3 and 2.4 show details of the analytic solution. We observe that for overpressure in the range of 10-100 MPa and chamber depths from 5-30 km below the surface, the capture radius is much larger than the chamber radius (set for the purposes of illustration to 3.5 km in Figure 2.3). The capture radius may exceed 10 times the chamber radius for overpressures under our estimation of maximum possible overpressure (100 MPa). This suggests that magmatic lensing may be a first-order transport process whenever an overpressured inclusion dominates the local stress field. We also observe that the presence of a free surface has a profound effect on the magnitude of principal stresses for shallow chambers. Whereas the stresses around a two dimensional chamber in an infinite medium fall off as $\Delta P/r^2 + \Delta\rho g/r \approx \Delta P/r^2$ (because overpressures are likely several orders of magnitude larger than buoyancy effects), the stress-free boundary acts to concentrate deviatoric principal stresses near the surface on the sides of the chamber, and reflect these stresses below the chamber.

Surface stress reflection has important consequences for the initiation of dikes from a magma chamber [Pinel and Jaupart, 2003], and for shallow chambers it results in a dramatic increase in capture radius at depth (Figures 2.3 and 2.4). The seemingly discontinuous capture radius at 5 km depth in Figure 2.3 is due to the particular choice of 1 MPa for the threshold "critical stress" of dike capture, as well as the size of the chamber, and occurs much more dramatically for less conservative estimates of dike capture. An expanded parameter space is represented in Figure 2.4, where two choices of critical stress are plotted as isosurfaces, varying chamber depth and chamber radius. This figure contains the information in Figures 2.3 and 2.2 as a subset of a higher-dimensional depiction of the parameter space. It also summarizes important features of the analytical solution, Equations 2.19-2.21, relevant to magmatic lensing. Capture radius at 10 km depth below the chamber (Figure 2.2.a) may be directly read off of this figure by fixing chamber radius and depth, then traversing along the distance axis from 0 km until the critical stress surface of interest is reached. This distance is the capture radius for these parameters. For example, from Figure 2.4, a 2.5 km radius chamber at 5 km depth has a capture radius of $\sim 10 - 15$ km if the critical stress is 1 MPa (as used in this paper, and represented by the blue isosurface), whereas it would have a capture radius of ~ 50 km for a critical stress of 0.2 MPa (upper orange isosurface). In this way, the particular choice of threshold chamber stress strongly affects the capture radius (compare blue 1 MPa isosurface to orange 0.2 MPa isosurface in Figure 2.4). For shallow chambers, deviatoric principal stresses are concentrated in lobes on either side of the chamber (Figure 2.4): the imposition of a stress threshold produces a seemingly discontinuous increase in capture radius as chamber depth decreases and overpressure increases (e.g., Figure 2.3 and Figure 2.2.b). At first glance it might appear that because of the stress reflection, shallow chambers exert a stronger influence on rising dikes than deeper chambers (Figure 2.4a., orange surface). However, as capture radius is a function of overpressure and a choice of critical stress, different choices of these parameters can result in the opposite dependence (Figure 2.4, lower blue surface and Figure 2.3).

The effect of an edifice is quantified using a triangular normal load with a density of 3000 kg/m^3. We chose 2 representative triangular volcano shapes to demonstrate the effect of edifice loading on magmatic lensing: one that is 2 km across and 1 km high, and one that is 4 km across and 1 km high. These are not meant to fit all real volcanoes, but illustrate concentrated versus more broadly dispersed surface loading. They are comparable to lower density Cascade Volcanic Arc, USA, volcanoes, which are of course not triangles and not two dimensional [Hildreth, 2007]. Figure 2.5.a shows the greatest principal deviatoric stress field due to the edifice loading alone, along with eigenvectors depicting approximate dike trajectories. As shown by Muller et al. [2001], a volcanic edifice alone may capture rising dikes, because load-induced stresses decay with depth approximately as $1/r$ (the limiting case of a surface line load - "Flamants solution" [Fung, 1965]).

However, the presence of a pressurized and buoyant magma chamber below an edifice changes the overall stress landscape significantly. In this case, principal deviatoric stresses at the top boundary of the chamber are opposite in sign to the edifice stresses and there is a resulting cancellation: this is a fully coupled problem, and the resulting far-field stresses are

hence different than those predicted by either limiting case. Figure 2.5 graphically illustrates details of these mechanical interactions. Figure 2.5.c shows the greatest principal deviatoric stress field due to a chamber and a compressive edifice load (least principal deviatoric stress magnitudes are exactly equal but opposite in sign), a model for the stresses due to a relatively small volcano (2 km wide by 1 km high) with a 2 km radius magma chamber beneath it. By comparing this to the case of no edifice load (Figure 2.5.b) it is clear that, particularly in the region between the chamber and the surface, a direct cancellation of stresses has occurred (however, normal stresses for the case in 2.5.c do not exhibit this cancellation). In contrast, Figure 2.5.d depicts the stresses due to the combined effects of a chamber and a tensile edifice load. While this particular geometry does not have a direct geological interpretation, it is meant to illustrate the force balance: deviatoric stress gradients due to the load and chamber are in the same direction between the load and the chamber, so the magnitude of the combined stresses in this region are larger than those of a chamber alone. It is also interesting to note that the stress trajectories for the volcano-chamber system focus towards the edifice and a central conduit system. This implies that surface eruptions most likely occur from within the volcano, consistent with observations and the theoretical results of others [Pinel and Jaupart, 2003], although the vent locations may move towards the base of the edifice if a central conduit is not well established [Kervyn et al., 2009].

By varying chamber radius and depth with constant edifice load, overpressure and buoyancy, we evaluate the capture radius of the combined chamber-edifice system for two example volcano sizes (Figures 2.6 and 2.7). Overpressure ΔP is set to 100 MPa (except for Figure 2.7), and $\Delta\rho$ to 300 kg/m^3. Principal deviatoric stresses are evaluated 10 km below the chamber (Figure 2.2) to determine the capture radius. This allows us to evaluate the relative importance of the surface and the edifice at different depths. For small volcanoes, edifice loading has only a first-order lensing effect for shallow systems (< 10 km) with small magma chambers. At a depth of 5 kilometers (Figure 2.6.a), the effect of increasing chamber size is to reduce the capture radius, until it disappears altogether for chambers of 1 km radius (for the smaller volcanic load). At greater depths, an edifice load acts in a similar way, though with fading influence as chamber depth is increased. The stress cancellation of the combined chamber-edifice system results in a decreased capture radius at depth, although chamber lensing is often the dominant mechanism. In fact, a comparison of the edifice plus chamber system to the chamber alone (Figure 2.6.b-.d) shows that the effect of an edifice on the capture radius 10 km below a chamber becomes negligible at a chamber radius that scales with depth. For these chambers, the edifice is at most a 10% effect. Finally, Figure 6.d shows that the free surface ceases to influence chambers deeper than roughly 20 km, and the capture radius approaches that of a chamber in an infinite medium.

The relative size of the volcanic load determines the efficacy of the magma chamber to focus dikes, even if the load alone has no direct influence. This follows from the longer range $1/r$ scaling of stress magnitude with distance from the load. The transition from edifice-dominant to chamber-dominant capture occurs at greater depths, with edifice influence reaching all the way to 20 km depth for small chambers (Figure 2.6.b-.c). Mechanical interaction between chamber and edifice results in an increase in capture radius over the half

space solution at 10 and 20 km depths for large chambers (> 4 km radius), while it decreases the capture radius for smaller chambers.

The effect of magma chamber overpressure is quantified in Figure 2.7. We choose a particular chamber depth (10 km), and vary chamber overpressure at a fixed radius to find the capture radius 10 km below the chamber (20 km below the free surface). At this depth, only the larger (4 km width) volcano exerts stresses over the 1 MPa threshold. These calculations demonstrate the strongly coupled nature of the combined chamber-edifice loading, and the importance of even small magmatic overpessure. Large chambers (> 2 km radius) strongly affect the capture radius, and increasing chamber overpressure results in a transition from edifice-dominated to chamber-dominated lensing. Also plotted are chambers with a smaller (2 km width) volcano, for which only the (albeit rather unrealistic) 4 km radius chamber has a capture radius at this depth (Figure 2.6.b), demonstrating the influence of edifice loading on lensing even when the edifice alone cannot reorient rising melt.

Although we do not treat background stresses explicitly in the present study, regional deviatoric stresses are common in volcanic settings. Muller et al. [2001] show that the effect on edifice lensing of a regional deviatoric stress that increases with depth is to decrease the capture radius. We expect a similar effect for chamber lensing. Regional tensile stresses, such as found in extensional tectonic environments such as the Basin and Range, USA, may be qualitatively evaluated as similar to the tensile load imposed in Figure 2.5.d. Regional extension will concentrate deviatoric stresses vertically, and hence decrease the capture radius.

We treat cylindrical magma chambers in this study, but pressurized magma chambers of more complicated geometries will exhibit stress concentration in regions of high curvature. Seismic observations [e.g., Barker and Malone, 1991, White et al., 2008] and geodetic inversions from active volcanic areas [e.g., Newman et al., 2006] suggest ellipsoidal magma chambers at a few kilometers depth, and we expect enhanced lensing (for a given overpressure) in the near field for ellipsoidal chambers of high aspect ratio.

2.6 Discussion

A magmatic plumbing system is a transport network composed of channels, dikes and magma chambers that, in the case of volcanic centers, drains an area of melt to a discrete point on the surface where it is expressed as a volcano. Except in very special cases (e.g., Hawaii [Okubo et al., 1997]) the subsurface topology and temporal evolution of magmatic plumbing are difficult to observe and are poorly known. There remains considerable debate about the general extent to which intrusive and extrusive igneous processes are connected [e.g., Bachmann et al., 2007], and whether plutonic scale magma chambers exist at all [e.g., Glazner et al., 2008]. However, even if such large chambers may not necessarily exist at high melt fraction for extended periods of time, the existence of calderas indicates that shallow high melt fraction, extensive, and continuous bodies of magma exist at least transiently. Moreover, long-lived magma storage is often invoked to explain mineral crystallization ages in arc

[e.g., Cooper and Reid, 2003] and continental [e.g., Simon and Reid, 2005] settings, and lower crustal melt accumulation and transport has been documented in a number of arc sections (e.g, Talkeetna [Hacker et al., 2008] and Kohistan [Jagoutz et al., 2007], where concentrically zoned mafic and ultramafic intrusive rocks are suggestive of a large deep chamber). Pressurization, and hence magmatic lensing, should occur whenever an inclusion of ascending melt stalls or accumulates.

We have shown that dike focusing by components of the plumbing system can be first-order processes and that, while not unique or necessarily mutually exclusive, these effects should be considered viable mechanisms for volcanic center localization. "Bottom up" models, based on fluid [e.g., Marsh and Carmichael, 1974] or elastic [Vogt, 1974] instability originating from the melting source region are difficult to test, in part because fundamental aspects of the "bottom" of the magmatic plumbing system are still poorly understood. A "top down" perspective is more straightforward to relate to real volcanic systems because the shape and size of volcanic loads are known, and faults can be mapped at the Earth's surface. Previous work has demonstrated that edifice building may affect the volume and compositional evolution of erupted lavas [e.g., Pinel and Jaupart, 2000, Ban and Yamamoto, 2002], and may affect the trajectories of rising dikes [Muller et al., 2001]. Elastic plate flexure due to edifice loading [e.g., ten Brink, 1991, Hieronymus and Bercovici, 1999] provides a mechanism for volcano spacing as well as dike focusing, although as noted by Muller et al. [2001], it is most effective when the volcano half-width is greater than 1/4 times the elastic plate thickness.

However, a solely top-down view of magmatic transport process and organization must still reconcile localization with the need for an initial load. And the presence of calderas whose size dwarfs the pre-existing volcanoes [e.g., Lipman, 1984] suggests that edifice loading or shallow structural control alone cannot serve to concentrate these prodigious melt bodies. Fluid instability-driven models [e.g., Marsh and Carmichael, 1974, Olson and Singer, 1985] take the perspective that localization occurs near the magma source region, however this class of models must reconcile a timescale problem relating diapir ascent directly to volcanism, which occurs over a different range of timescales and rheologies [e.g., Canon-Tapia and Walker, 2004]. Still, the presence of diapiric melt instabilities cannot be ruled out, and recent tomographic images of the mantle wedge do reveal interesting large-scale upper mantle low seismic velocity structures beneath arc volcanoes in the Japan Trench [Tamura et al., 2002]. Seismic imaging is a promising means of defining active magmatic structures in the crust, and has been successful particularly at shallow (generally < 10 km) depths where it can be corroborated with independent petrologic evidence [e.g. Auger et al., 2001, Scaillet et al., 2008]. Yet deeper magmatic systems remain difficult to observe and interpret [Lees, 2007].

We suggest that discrete volcanic centers may also be organized between the source and the surface, through the internal dynamics of magma transport. Several authors have recently begun to explore this possibility, and shown that particular components of a magmatic system (dikes, magma chambers) can co-evolve to simultaneously structure and mechanically stabilize the system [e.g., Ito and Martel, 2002, Jellinek and DePaolo, 2003]. This perspective is in some ways a compromise between the "top down" and "bottom up" models, in

that features of both fit into the present framework as end member cases, but it provides a way for maturing magma plumbing to actively modulate the crustal environment over the lifetime of melt supply.

2.7 Spacing of volcanic centers around the Pacific Rim

The magmatic lensing mechanism provides a natural lengthscale for the spacing of volcanic centers: the capture radius of the chamber (Figure 2.1). However, as demonstrated in Figure 2.3, the depth at which the capture radius is evaluated (or equivalently, the distance below the chamber from which dikes may be focused) and the depth of the magma chamber beneath the free surface both affect this lengthscale. As rheological and material interfaces provide a natural location for the formation of large magma chambers [e.g., Kavanagh et al., 2006], we hypothesize that for volcanic systems that develop large magma reservoirs, the spacing of volcanoes may be controlled by the capture radius of a magma chamber at a mid to lower crustal structural discontinuity, such as the Mohorovičić discontinuity (Moho) or the brittle-ductile transition. We compile and analyze a database of volcanoes to test this hypothesis below, noting that there are other plausible alternative hypotheses for chamber depth under arc volcanoes that could be treated in a similar way [e.g., Pinel and Jaupart, 2000]. At this stage, we are merely interested in testing whether a simple geometry for arc plumbing systems results in an internally consistent model prediction in the magmatic lensing framework, fully realizing that other localization processes operate in reality.

The spacing of volcanoes on the Earth's surface has been used for decades to compare with models for magmatic plumbing [Marsh and Carmichael, 1974, Vogt, 1974, Mohr and Wood, 1976, ten Brink, 1991, de Bremond d'Ars et al., 1995, Muller et al., 2001], but the scatter in spacing is large and it is difficult in many cases to define a single volcanic center from which to base spacing measurements. Indeed, based on this scatter, there exists the opinion that simple measures of volcanic spacing do not support idealized transport theories [e.g., de Bremond d'Ars et al., 1995, Hildreth, 2007]. Some studies of volcano spacing try to circumvent the natural variability in volcano spacing by focusing on particular localities, so that regional differences in style and geometry of tectonics might be avoided. However, the continued development of several relevant worldwide geophysical databases provides the opportunity to compare volcanic systems on a global scale, such that it is possible to look for generic features of volcanic processes at increasing levels of detail [e.g., Hughes and Mahood, 2008].

We use the volcano database of the Smithsonian Institute's Global Volcanism Program [Siebert, 2002], and select stratovolcanoes around the circum-Pacific volcanic belt that clearly correspond to a single center as a proxy for volcanic systems that likely reflect magmatic storage over their lifetimes [e.g., Cooper and Reid, 2003]. Because we hypothesize that volcanic plumbing is self-organized in the subsurface, we use only Holocene volcanoes as an

estimation of recently active volcanic centers. Stratovolcanoes alone are used in an attempt to include volcanic centers that experience roughly the same dynamic evolution and that may have reasonably long-lived magma chambers. Extinct centers and the extinct volcanoes above them are not considered, but should not contribute significantly to the organization of subsequent systems, provided magma chambers develop beneath the Holocene volcanoes. By hypothesizing the presence of deep storage beneath arc volcanoes, we are assuming that shallow reservoirs do not contribute significantly to volcano spacing; these assumptions define an upper bound on lensing-induced spacing.

We employ stringent criteria for choosing data points within the catalogued volcanoes in the Smithsonian database. We follow the general selection method of de Bremond d'Ars et al. [1995], who performed a similar analysis on an earlier version of this database. Details of the selection process may be found in de Bremond d'Ars et al. [1995] and we provide only a brief summary of our approach. By examining each potential volcanic center, we exclude those that either 1) correspond to the same geographic "center" as another volcano (i.e., are part of the same edifice or edifice complex, which may form after the initial edifice load is established [Kervyn et al., 2009]) or 2) are sufficiently close to other convergent margins that complicated tectonic stresses are likely (i.e., multiple trenches within a few tens of kilometers, or volcanoes that are significant outliers from the trench axis). We do not consider any volcanoes in the South Pacific because of criteria (2), and 27 listed Holocene stratovolcanoes in other locations are excluded by criteria (1) and (2). We included some arc volcanoes not classified as stratovolcanoes (submarine volcanoes in the Mariana Arc [Fryer, 1996]). These volcanoes were included to populate our database in areas with thin crust, and each included point was checked to ensure that it is a discrete, recently active volcanic center. This leaves 341 volcanoes in the American Cordillera, Kamchatka and Japan. Details of all volcanoes, included and excluded, are provided in the supplementary data. We calculate volcano spacing by finding the spherical arclength between all points in our database with the Haversine Formula. We then run a minimization algorithm to find the nearest neighbor to each volcano. This is an approximation to the more rigorous spacing analysis of de Bremond d'Ars et al. [1995], who calculate spacing via a coordinate system local to each arc. We find similar results, and hence do not consider their approach necessary here.

With this spacing data, we use the CRUST 2.0 global crustal model (http://mahi.ucsd.edu/Gabi/rem.html) to find the crustal thickness (including sediment) beneath each volcano. The resolution of this model is fairly low at 2x2 degrees, but it is useful nonetheless as it picks out broad-scale regional variability in crustal thickness. The largest model crustal thickness used in this study is 70 km in the Chilean Arc, and the smallest is 6.57 km in the Mariana Arc, encompassing the range of crustal thicknesses found on Earth.

To facilitate visualization of the resulting plot of crustal thickness versus spacing, we bin data points according to crustal thickness, in 10 km bins. Different choices of bin size maintain similar average spacing. The resulting average spacing for each bin along with its standard deviation are shown in Figure 2.8, along with a histogram of the datapoints in each bin. We find that average volcano spacing is 31- 43 km in crust thicker than $\sim$ 20 km and

is wider, 56.6 ± 31.7 km, for crustal thicknesses less than ~ 20 km. It appears, despite the large variance, that there is no significant correlation between crustal thickness and volcano spacing for crust thicker than 20 km, and that for thinner crust there are hints of an anti correlation (Figure 2.8). Our finding is in contrast to a similar study of volcanoes in the East African Rift Zone [Mohr and Wood, 1976], that found a positive correlation between spacing and lithospheric (rather than crustal) thickness. However we note that Mohr and Wood [1976] include data from all Tertiary volcanoes, as well as calderas and other classes of volcanic edifice, which we excluded from our analysis.

These observations, while exhibiting large variability, are generally consistent with our model. Hypothesizing in this case that the primary magma reservoir for arc volcanoes lies at the Moho [e.g. Kavanagh et al., 2006], the parameters that vary most between arcs are the convergence rate, which likely controls melt production rate [e.g., DeMets et al., 1990, Davies and Bickle, 1991], and crustal thickness. However, based on other studies [e.g., de Bremond d'Ars et al., 1995] and our own calculations, there is no obvious correlation between plate velocities and arc volcano spacing. Such an observation is consistent with the presence of long-term magma storage in arcs, and that magma transport is heavily modulated subsequent to melt generation. Muller et al. [2001] find a rough linear trend between volcano size and spacing in the Cascadia arc, and suggest that this supports "top down" focusing. We do not discount the possibility that edifice loading affects spacing, but note that edifice size is influenced by eruption volumes and frequency, which may also be related to magma chamber size and magmatic lensing. Additionally, Muller et al. [2001] use volcanoes of all types in their analysis, while we restrict ourselves to volcanoes active in the Holocene.

As to the relationship between crustal thickness and volcano spacing, Figure 2.6 implies that below ~ 20 km depth, the presence of a free surface (or an edifice load) has a negligible effect on capture radius. This is what we observe in Figure 2.8, where spacing is largely insensitive to increasing crustal thickness for bins greater than ~ 20 km. At shallow depths, it is possible that the increase in apparent volcano spacing is a result of discontinuous stress "reflection" from the free surface (Figure 2.4), and similar arguments would imply a general anti correlation between the depth of magmatic lensing and crustal thickness in arcs. However, a number of complicating factors make this direct comparison more tenuous. As noted by Fryer [1996], the distribution of volcanism in the Mariana arc appears to be controlled by faults relating to the processes and geometry of subduction. In such shallow systems, we expect that such features exert dominant control on the organization of the plumbing system. Tectonically-induced structural control on shallow features of magmatic systems is likely important in other arcs as well, such as Cascadia [Hildreth, 2007]. However, discrete centers are still observed along strike of these faults, and it is possible that focusing due to magma chambers and volcanic loads operates in conjunction with tectonics to produce the local variability in volcano spacing we observe.

With the understanding, then, that our or any idealized model cannot hope to capture the variability in Figure 2.8, we are nonetheless interested in calculating the spacing implied by the magma lensing model (with no edifice load). Model predictions that fit the observational data are non-unique, as there is a trade-off between chamber size and overpressure for a given

result. To produce a capture radius of $\sim 15 - 20$ km at depths greater than ~ 20 km, a 1.5 km radius magma chamber at the Moho would need to have 100 MPa of overpressure, while a 4 km radius chamber needs 20 MPa. Our observations and calculations are thus self-consistent, resulting in a reasonable range of values for both chamber radius and overpressure to produce the observed mean volcano spacing.

2.8 Conclusion

As has been recognized in both field-based and statistical studies of volcano spacing in arcs, there is little support for the idealized view of arc volcanoes as single or double chains of evenly-spaced edifices. However, the existence and distribution of volcanoes as primary surface expressions of terrestrial magmatism requires explaination. Our calculations suggest a mechanism by which magma chambers can organize and modulate transport processes within the crust. This magmatic lensing should be considered an extension of the proposed focusing of rising dikes by volcanic edifices, and it is an independently operating mechanism within the initial confines of local structures and tectonics; we have shown that magma chamber lensing of dikes is more effective than edifice lensing in many cases. While the maximum capture radius of an edifice alone (in an isotropic background stress field) is on the order of 10-20 times the edifice size [Muller et al., 2001], the capture radius of a magma chamber alone is greater or equal in magnitude for realistic chamber overpressures. Shallow magma chambers and long-lived, high volume reservoirs should dominate mechanical organization of the system. Further, we have shown that the combined stresses of a chamber and an edifice are strongly coupled, and that in fact the presence of an edifice acts to reduce the capture radius of the system when the dimensions of the chamber and edifice are the same order of magnitude.

It has been suggested [e.g., Pinel and Jaupart, 2000] that these coupled systems form due to edifice loading, which creates a density trap at shallow depths below the edifice. Such chambers do not resolve the question of initial volcanic center discretization, but may provide a stabilizing feedback to the spacing of the system once it is established. Discrete magmatic centers may form before a volcanic edifice is built, however, if a deeper chamber forms prior to the first surface eruption. It seems plausible that in fact multiple chambers exist within a given plumbing system, set by the various rheological boundaries and structures that exist between the source region and the surface, stabilized by the internal lensing dynamics. The apparent dichotomy between small closely spaced centers and larger widely spaced edifices that has been observed in some arcs (e.g., Cascadia [Hildreth, 2007] and the Central Andes [Savant and de Silva, 2005]) may in this light reflect the interaction of tectonics and magmatic lensing at different levels within the crust.

Systems that operate via magmatic lensing, particularly if multi-level magma storage occurs, should sample magmas of potentially diverse composition. These chambers could then function as places of magma homogenization similar to the proposed MASH zones of the lower crust [e.g. Hildreth and Moorbath, 1988]. Erupted lavas in these systems would

then represent the integrated hybridized upwelling magmatic signal from a broad region of the crust.

Magma chambers need not be present under all volcanoes, especially sites (often associated with oceanic islands) that more directly sample primitive magmas, and in these environments it may be that surface loading controls the focusing of rising magma into discrete centers [Hieronymus and Bercovici, 1999]. But a broad array of volcanological settings do require magma storage prior to eruption, and in these cases we suggest that magma chambers play an organizational role in the formation of volcanic centers. The subsequent longevity and stability of the center may also be governed by magma chamber dynamics [Jellinek and DePaolo, 2003] resulting from the combined interaction of thermally induced rheological evolution of the country rock, melt supply, and chamber depth [Karlstrom et al., 2009], which in turn depend on tectonic environment.

Finally, we note that pressurized dikes exhibit a focusing behavior similar to the magma chambers presented here [Ito and Martel, 2002, O'Neill et al., 2007], and so may be expected to play a role in developing plumbing systems. However, despite a range of interesting dike interactions [Ito and Martel, 2002], in the presence of a larger background stress (such as a large magma chamber or volcano), these effects will be heavily damped. Dike interactions, and the smaller scale stress-induced re-orientation of channelized melt, may be most important where far-field loads are not present, and may be responsible for the creation of sizeable magma chambers.

Lensing of rising melt by the components of a magmatic plumbing system such as dikes, chambers and volcanic edifices is a concise theoretical framework for understanding active localization of volcanic activity on Earth's surface. The structure of the plumbing system, and which of the above dominates lensing, should depend on tectonic environment, structural controls and magma supply rate, and hence vary from place to place. It is likely that edifice morphology, lava composition, and erupted volumes are also a strong function of the subsurface topology; a better characterization of these plumbing systems is certainly warranted to further explore this possibility. However, we suggest that magmatic lensing plays an important role in the set of processes that govern volcanic plumbing, and provides a mechanism that, once established, may evolve to modulate structural anisotropy and inhomogeneity in the crust. In this way, it provides a means of affecting regional tectonics and sustaining long-lived, multi-level magmatic systems.

2.9 Appendix

Solutions to the equations of linear elasticity in two dimensions may be found by the method of stress functions [Fung, 1965] whereby the equilibrium equations are satisfied by a scalar function χ satisfying the biharmonic equation:

$$\nabla^4 \chi = 0 \tag{2.8}$$

and the appropriate boundary conditions. With this function stresses, in a two dimensional orthogonal coordinate system in which the coefficients of the metric are equal, are given by

$$\sigma_{11} = h\frac{\partial}{\partial q_2}\left(h\frac{\partial \chi}{\partial q_2}\right) - h\frac{\partial h}{\partial q_1}\frac{\partial \chi}{\partial q_1} \tag{2.9}$$

$$\sigma_{22} = h\frac{\partial}{\partial q_1}\left(h\frac{\partial \chi}{\partial q_1}\right) - h\frac{\partial h}{\partial q_2}\frac{\partial \chi}{\partial q_2} \tag{2.10}$$

$$\sigma_{12} = -h\frac{\partial^2 (h\chi)}{\partial q_1 \partial q_2} + h\chi\frac{\partial^2 h}{\partial q_1 \partial q_2}, \tag{2.11}$$

where q_1 and q_2 are spatial coordinates, and h is the coefficient of the metric [Love, 1944].

We use the bipolar coordinate system, given in terms of cartesian coordinates by the complex mapping [e.g. Jeffery, 1921, Pinel and Jaupart, 2000]

$$x + iy = \frac{k(\sinh\alpha + i\sin\beta)}{\cosh\alpha - \cos\beta}. \tag{2.12}$$

Here α and β are spatial coordinates; curves of constant α and β trace orthogonally intersecting circles, $i = \sqrt{-1}$, and k is a dimensional constant equal to one half the distance between the two foci of the coordinate system, curves of constant α [Jeffery, 1921]. In this coordinate system, the problem of a circular cavity in a half space is naturally posed: the cavity and the free surface are given by $\alpha = \alpha_0$ and $\alpha = 0$. The radius of the cavity is then

$$R = k\ \mathrm{csch}(\alpha_0), \tag{2.13}$$

and the straight-line distance from the free surface to the center of the cavity is

$$d = k\tanh(\alpha_0/2). \tag{2.14}$$

Boundary conditions (equations 2.1-2.4) are now given by

$$\sigma_{\alpha\alpha}|_{\alpha=\alpha_0} = \Delta P + \Delta\rho g y = \Delta P + \Delta\rho g k\left(1 + 2\sum_{n=1}^{\infty} e^{-n\alpha_0}\cos(n\beta)\right), \tag{2.15}$$

$$\sigma_{\alpha\beta}|_{\alpha=\alpha_0} = \sigma_{\alpha\alpha}|_{\alpha=0} = \sigma_{\alpha\beta}|_{\alpha=0} = 0. \tag{2.16}$$

Stress functions that satisfy equation 2.8 and these boundary conditions take the general form

$$\chi = \sum_{n=0}^{\infty} f_n(\alpha)\cos(n\beta). \tag{2.17}$$

We find that a three term expansion of this sum captures the details; the contribution of higher order terms is small. Therefore, we use the following approximate stress function:

$$\begin{aligned}\chi &= A_1\alpha k + \frac{1}{h}\left(B_1\left(\cosh\left(2\alpha\right)-1\right)+C_1\sinh\left(2\alpha\right)\right)\cos\left(\beta\right)+ \\ &\quad \frac{1}{h}(A_2\left(\cosh\left(3\alpha\right)-\cosh\left(\alpha\right)\right)+B_2(\sinh\left(3\alpha\right)-3\sinh\left(\alpha\right)))\cos\left(2\beta\right)),\end{aligned} \tag{2.18}$$

where $h = k^{-1}(\cosh\alpha - \cos\beta)$ and the A_n and B_n are constants evaluated to satisfy the boundary conditions. After doing so, the final stress components are:

$$\begin{aligned}\sigma_{\alpha\alpha}(\alpha,\beta) &= e^{-3\alpha_0}\left(\tfrac{\sinh\left(\alpha\right)}{\sinh\left(\alpha_0\right)}\right)^2(e^{3\alpha_0}(\Delta P + k\Delta\rho g)+\operatorname{csch}(\alpha_0)(-k\Delta\rho g\cos\left(3\beta\right) \\ &\quad (\cosh\left(\alpha\right)-\cosh\left(\alpha-2\alpha_0\right)+\sinh\left(\alpha\right)+7\sinh\left(\alpha-2\alpha_0\right))+ \\ &\quad k\Delta\rho g\cos\left(2\beta\right)(2+3\cosh\left(2\alpha\right)-3\cosh\left(2(\alpha-\alpha_0)\right)-2\cosh\left(2\alpha_0\right)+ \\ &\quad 15\sinh\left(2\alpha_0\right)+21\sinh\left(2(\alpha-\alpha_0)\right)-14\sinh\left(2\alpha_0\right))-e^{\alpha_0}\cos\left(\beta\right) \\ &\quad ((\Delta P+10k\Delta\rho g)\cosh\left(\alpha-3\alpha_0\right)+k\Delta\rho g(\cosh\left(\alpha-\alpha_0\right)- \\ &\quad 11\cosh\left(\alpha+\alpha_0\right)+30\cosh\left(\alpha_0\right)\sinh\left(\alpha\right)+8(\sinh\left(\alpha-3\alpha_0\right)- \\ &\quad 2\cosh\left(\alpha\right)\sinh\left(\alpha_0\right)))-\Delta P(\cosh\left(\alpha-3\alpha_0\right)+\sinh\left(\alpha-3\alpha_0\right)+ \\ &\quad \sinh\left(\alpha+\alpha_0\right))))),\end{aligned} \tag{2.19}$$

$$\begin{aligned}\sigma_{\beta\beta}(\alpha,\beta) &= \tfrac{1}{4}e^{-3\alpha_0}\operatorname{csch}^2(\alpha_0)(-2e^{3\alpha_0}(\Delta P+k\Delta\rho g)(1+\cosh\left(2\alpha\right))+ \\ &\quad 2e^{-2(\alpha+\alpha_0)}(-9e^{2\alpha_0}k\Delta\rho g-11e^{4\alpha_0}k\Delta\rho g+e^{6\alpha_0}(\Delta P+k\Delta\rho g)+ \\ &\quad e^{2\alpha}(-1+e^{2\alpha_0})(k\Delta\rho g(3+4e^{2\alpha_0}+e^{4\alpha_0})+\Delta Pe^{4\alpha_0})+ \\ &\quad e^{4\alpha}(k\Delta\rho g(9+12e^{(2\alpha_0)}-2e^{4\alpha_0})+\Delta Pe^{4\alpha_0}))\cos\left(\beta\right)\left(\tfrac{\cosh\left(\alpha\right)}{\sinh\left(\alpha_0\right)}\right)- \\ &\quad e^{-2(2\alpha+\alpha_0)}\cos\left(2\beta\right)\operatorname{csch}(\alpha_0)(e^{2\alpha_0}(-6-18e^{2\alpha}-e^{4\alpha}+24e^{6\alpha}+ \\ &\quad 9e^{8\alpha})k\Delta\rho g+2e^{2\alpha+6\alpha_0}(\Delta P+2k\Delta\rho g)-2e^{4\alpha_0}(k\Delta\rho g(6+11e^{2\alpha}- \\ &\quad 2e^{4\alpha}+2e^{6\alpha})+e^{6\alpha}\Delta P)+6e^{6\alpha}k\Delta\rho g(3+\cosh\left(2\alpha\right)+2\sinh\left(2\alpha\right)))- \\ &\quad k\Delta\rho g\cos\left(3\beta\right)\operatorname{csch}(\alpha_0)(\cosh\left(\alpha+2\alpha_0\right)+15\sinh\left(\alpha\right)-25\sinh\left(3\alpha\right)+ \\ &\quad 7(2\sinh\left(\alpha-2\alpha_0\right)-5\sinh\left(3\alpha-2\alpha_0\right)+\sinh\left(\alpha+2\alpha_0\right)))),\end{aligned} \tag{2.20}$$

$$\begin{aligned}\sigma_{\alpha\beta}(\alpha,\beta) &= -\tfrac{1}{2}e^{-7\alpha_0}(1+e^{4\alpha_0})(\cos\left(\beta\right)-\cosh\left(\alpha\right))\operatorname{csch}^3(\alpha_0)\operatorname{sech}(2\alpha_0)\sin\left(\beta\right) \\ &\quad \sinh\left(\alpha\right)(e^{-\alpha+6\alpha_0}(\Delta P+k\Delta\rho g)-6(1+3e^{2\alpha})k\Delta\rho g\cos\left(\beta\right)-e^{4\alpha_0} \\ &\quad (k\Delta\rho g(-32\cos\left(\beta\right)\cosh^2\left(\alpha\right)+\sinh\left(\alpha\right)(3-16\cos\left(\beta\right)\sinh\left(\alpha\right))+ \\ &\quad \sinh\left(\alpha\right)\Delta P)+\cosh\left(\alpha\right)(\Delta P+k\Delta\rho g(1+48\cos\left(\beta\right)\sinh\left(\alpha\right))))- \\ &\quad 2e^{2\alpha_0}k\Delta\rho g(\cos\left(\beta\right)-3\sinh\left(\alpha\right)+3\cos\left(\beta\right)(\cosh\left(2\alpha\right)+5\sinh\left(2\alpha\right)))).\end{aligned} \tag{2.21}$$

Deviatoric stresses, from which the conclusions in the text are based, follow from the tensor equation

$$\sigma^{dev} = \sigma - \operatorname{tr}(\sigma), \tag{2.22}$$

and principal stresses are eigenvalues of the corresponding component matrix.

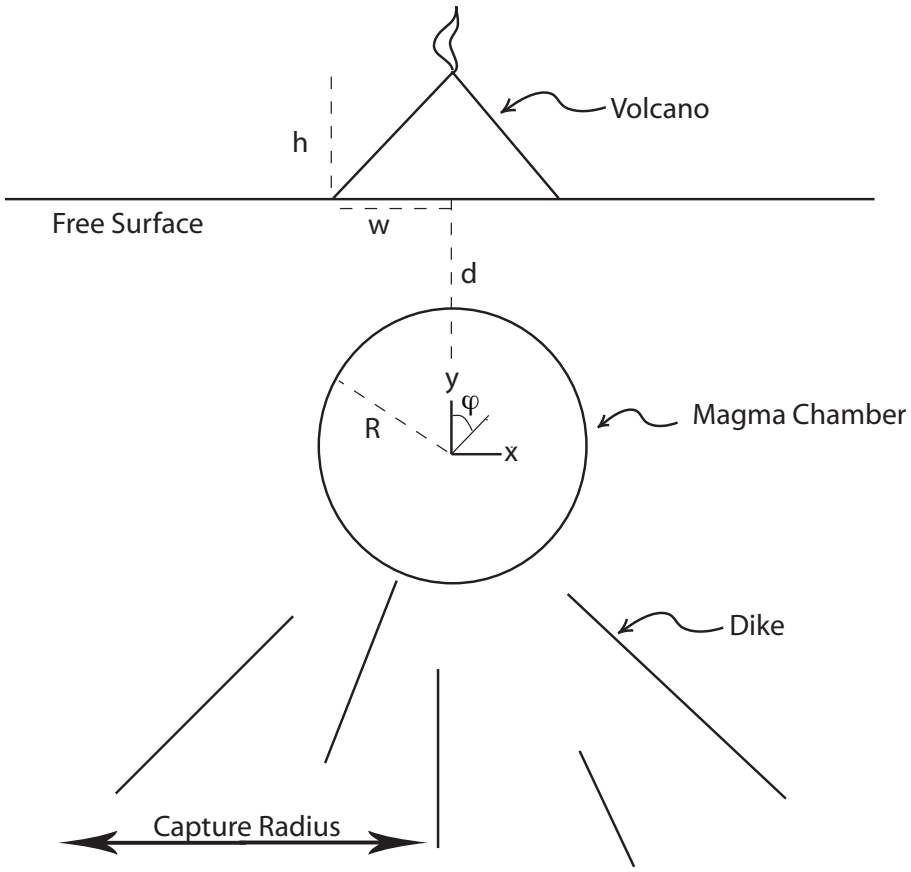

Figure 2.1: Geometry of the model problem. A circular magma chamber, overpressured and buoyant with respect to its surroundings, lies beneath a volcano sitting on an otherwise free surface. Chamber stresses focus rising dikes from a region defined by the magnitude of principal deviatoric stresses around the chamber. The "capture radius" of the chamber is the horizontal extent of this region, defined at a given depth below the chamber.

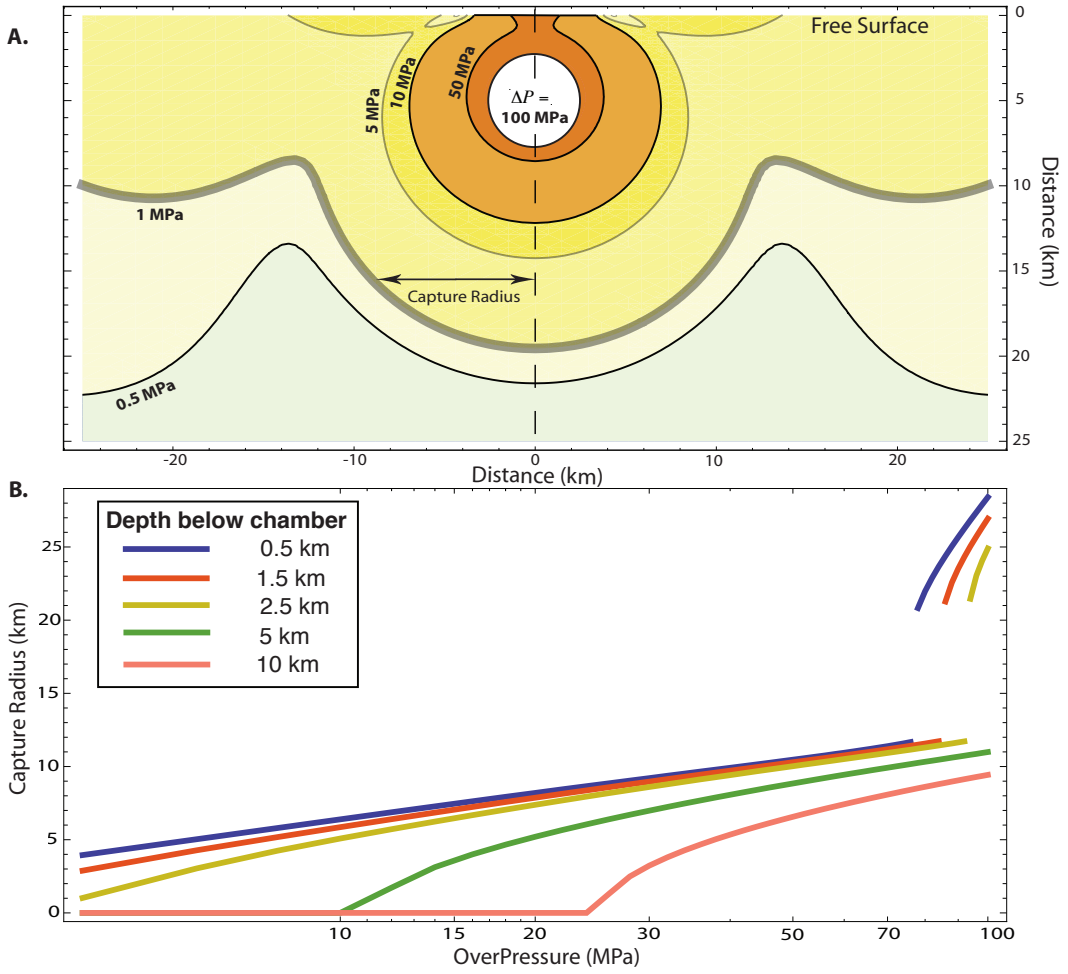

Figure 2.2: (a) Contours of least compressive deviatoric principal stress around a 2.5 km radius chamber at 5 km depth below the surface. $\Delta P = 100$ MPa, and $\Delta\rho = 300$ kg/m^3. The region in which dikes may be affected by chamber stresses is shown with a thick grey contour. This region defines the "capture radius," which is shown at 10 km below the chamber. (b) Capture radius as a function of chamber overpressure, for the geometry depicted in (a). Note that capture radius depends on depth below the chamber, and that (for this example) depths of < 2.5 km below the chamber experience a discontinuous increase in capture radius (see text). A smaller threshold stress (here set to 1 MPa) will result in a significantly larger capture radius.

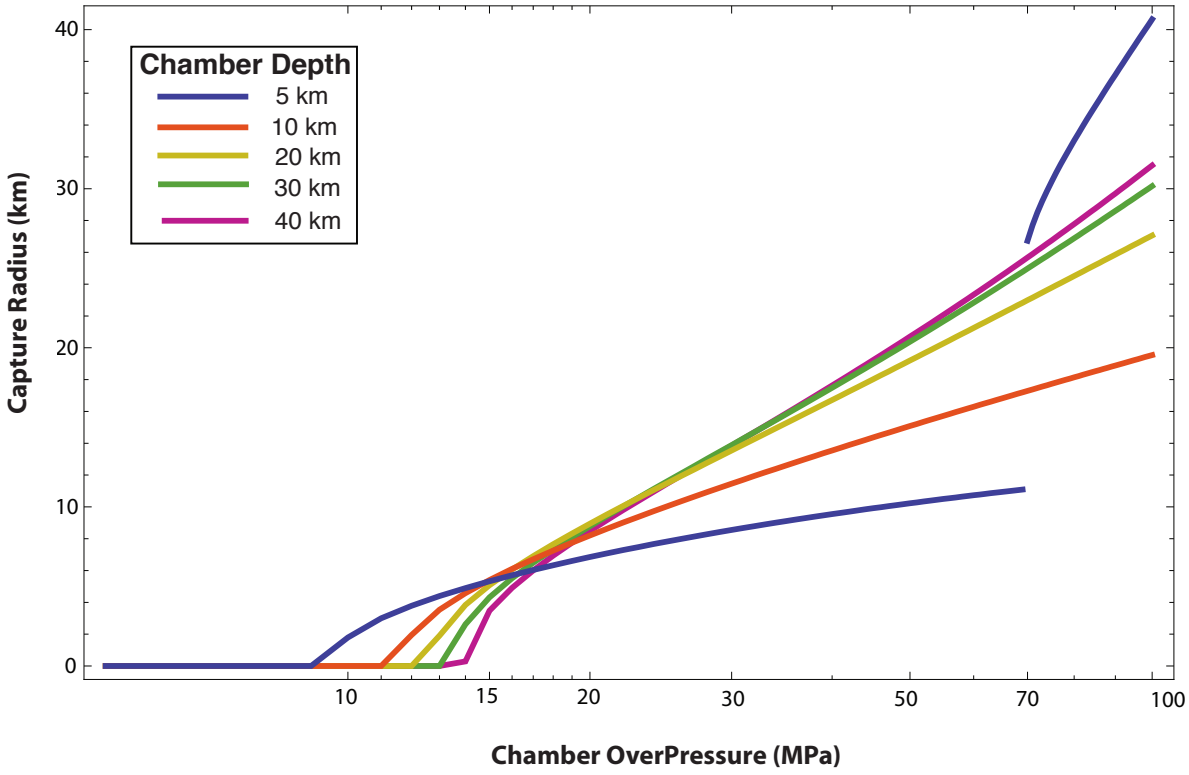

Figure 2.3: Capture radius as a function of overpressure for a chamber with no edifice load. Chamber radius is set to 3.5 km, and buoyancy to $\Delta\rho = 300$ kg/m^3. The capture radius is evaluated 10 km below the center of the chamber (see Figure 2.2), for five example depths. The discontinuity present for the 5 km depth chamber is a result of this particular choice of chamber radius, and is not present for chamber radii < 3 km. See Figure 2.4 for details of a larger parameter space, and the text for discussion of this surface reflection of deviatoric stresses.

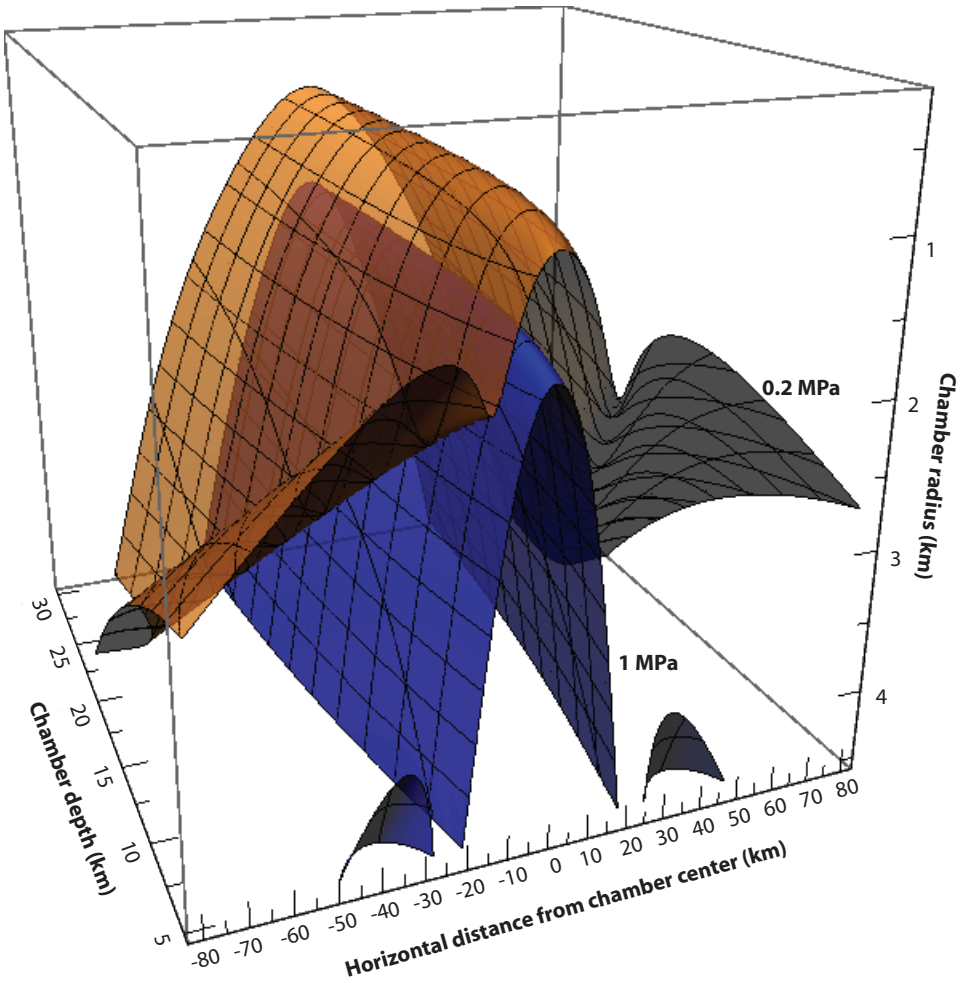

Figure 2.4: Isosurfaces of greatest principal deviatoric stress from equations 2.19-2.21, to illustrate how varying chamber size and depth affects the capture radius 10 km below the chamber. The upper orange surface corresponds to 0.2 MPa, and the lower blue surface to 1 MPa, representing different theoretical choices of threshold deviatoric stress needed to focus rising dikes. Axes are chamber depth, chamber radius, and horizontal (x-coordinate in Figure 2.1) distance from the chamber center. Holding chamber depth and radius constant, the chamber's capture radius may be found by traversing from 0 to one of the isosurfaces and reading off the horizontal distance at which this occurs. Note the increase in capture radius for large shallow chambers ('lobes' on the blue and orange surfaces), and the effect of smaller threshold stresses for dike capture.

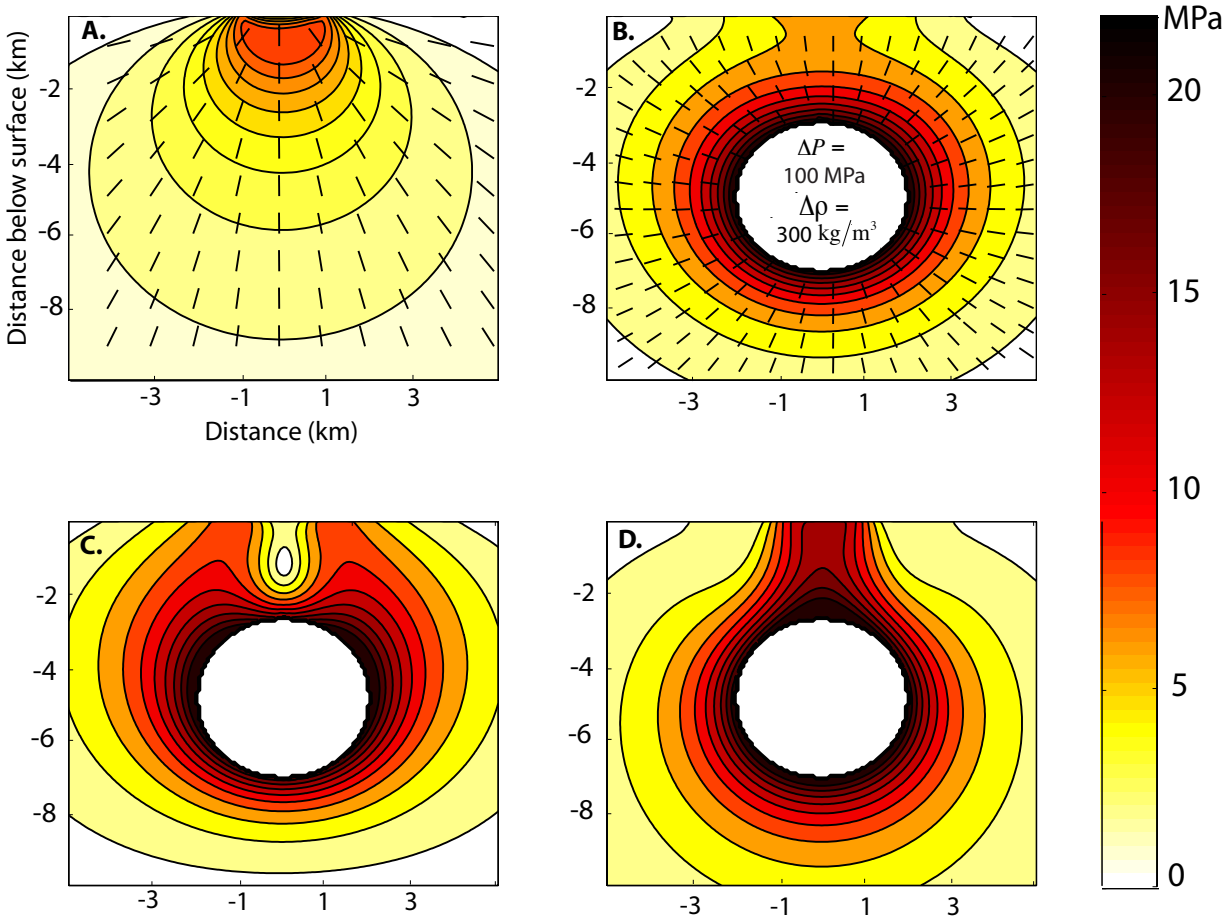

Figure 2.5: Numerical calculations of tensile deviatoric principal stresses in a 10 km x 10 km area just below the surface. (a) A triangular edifice load with a width of 2 km and height of 1 km on a free surface. Contoured are tensile deviatoric principal stresses (eigenvalues), and selected stress trajectories (eigenvectors) of deviatoric compressional principal stress. (b) A pressurized and buoyant chamber (shaded white for visualization) under a free surface, with no edifice load. Chamber radius is 2 km, depth is 5 km, $\Delta P = 100$ MPa and $\Delta\rho = 300$ kg/m^3. Contours and stress trajectories are the same as in part (a). (c) Chamber with the edifice of part (a). There is a cancelation of deviatoric stresses above the chamber in this case. (d) Chamber with tensile 'edifice' load. Here the stress gradients are in the same direction, resulting in amplified stresses and longer range focusing.

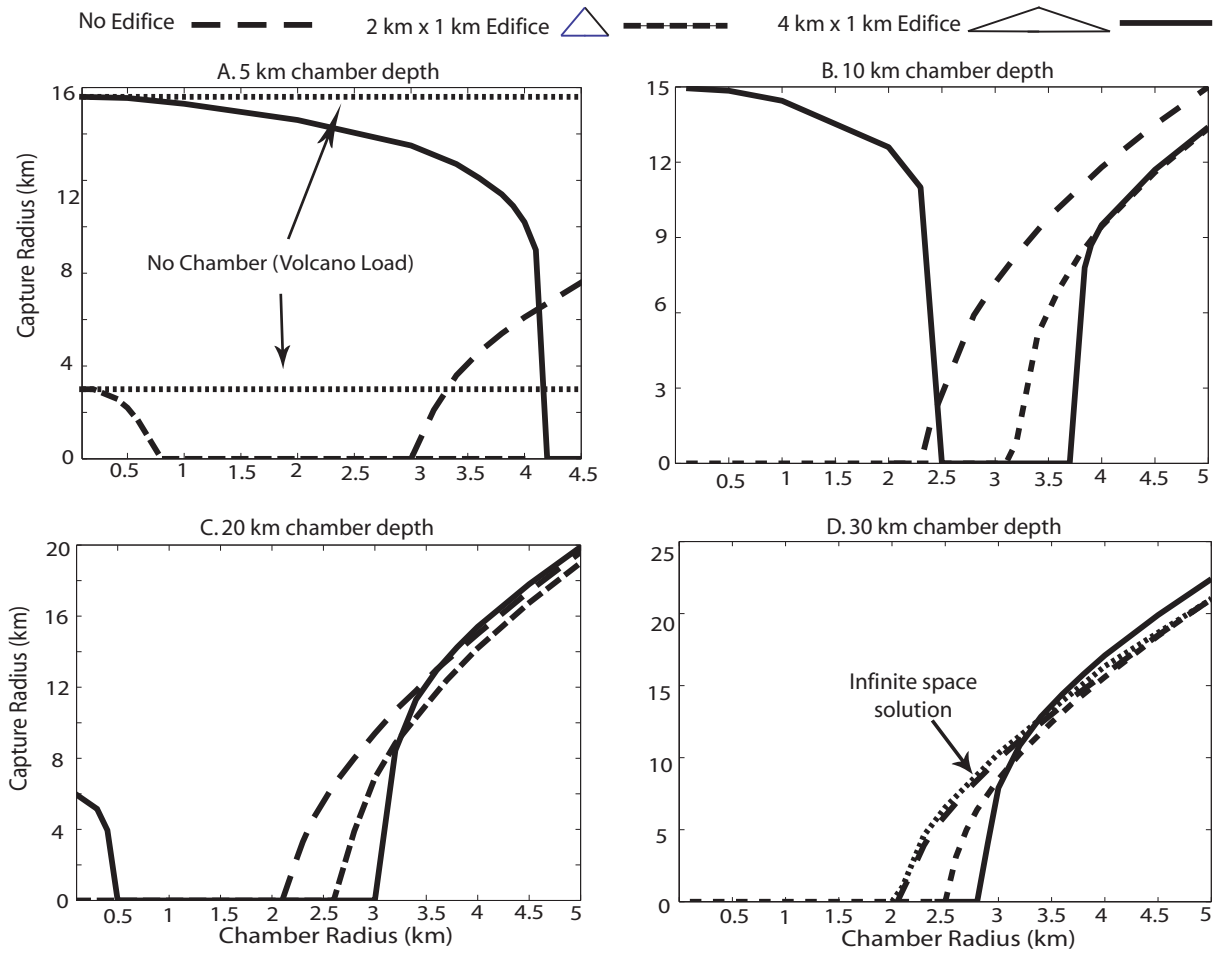

Figure 2.6: Capture radius of the combined chamber and edifice system, evaluated 10 km below the chamber, at four depths. Chamber overpressure is set to 100 MPa, and buoyancy to 300 kg/m^3. Plotted are examples of two volcano sizes (2 km x 1 km and 4 km x 1 km), the half-space solution without an edifice load, and capture radius curves at 15 km depth for edifice loads only, to compare with chamber capture. (a) 5 km chamber depth (b) 10 km chamber depth (c) 20 km chamber depth (d) 30 km chamber depth

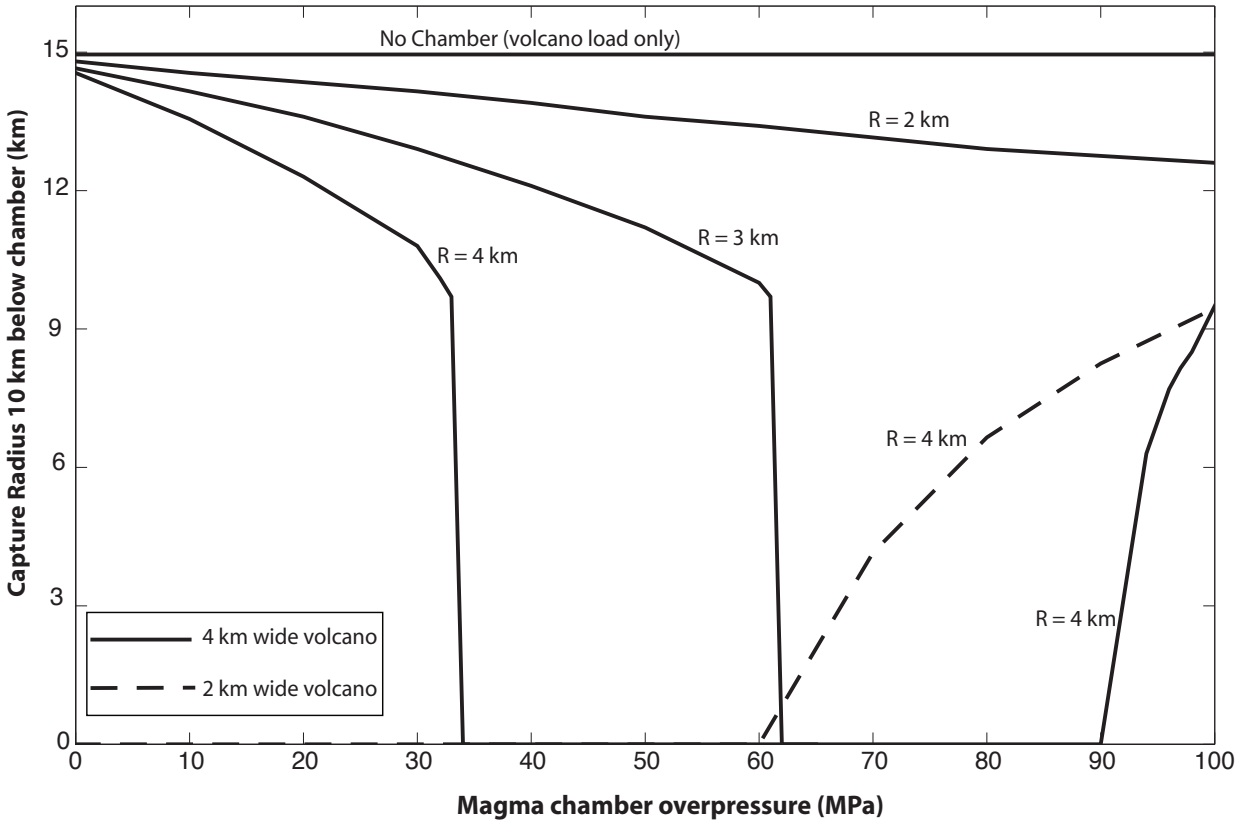

Figure 2.7: Capture radius of the combined chamber and edifice system 10 km below the chamber, varying magma chamber overpressure. Chamber depth is set to 10 km, and $\Delta\rho =$ 300 kg/m^3. Curves represent chambers of different radii, with two examples of surface volcano loading: a 4 km wide volcano (solid curves), and a 2 km wide volcano (dashed curve). Note from Figure 2.6.b that only 4 km radius chambers have a capture radius at this depth. Plotted for reference is the capture radius of the larger volcano load alone at this depth (25 km below the surface). The smaller load alone does not affect dikes at this depth. The strongly coupled nature of this system is observed for a range of magma chamber overpressure, as is the transition from edifice-dominated to chamber-dominated lensing. Deeper chambers will dominate lensing to a greater degree.

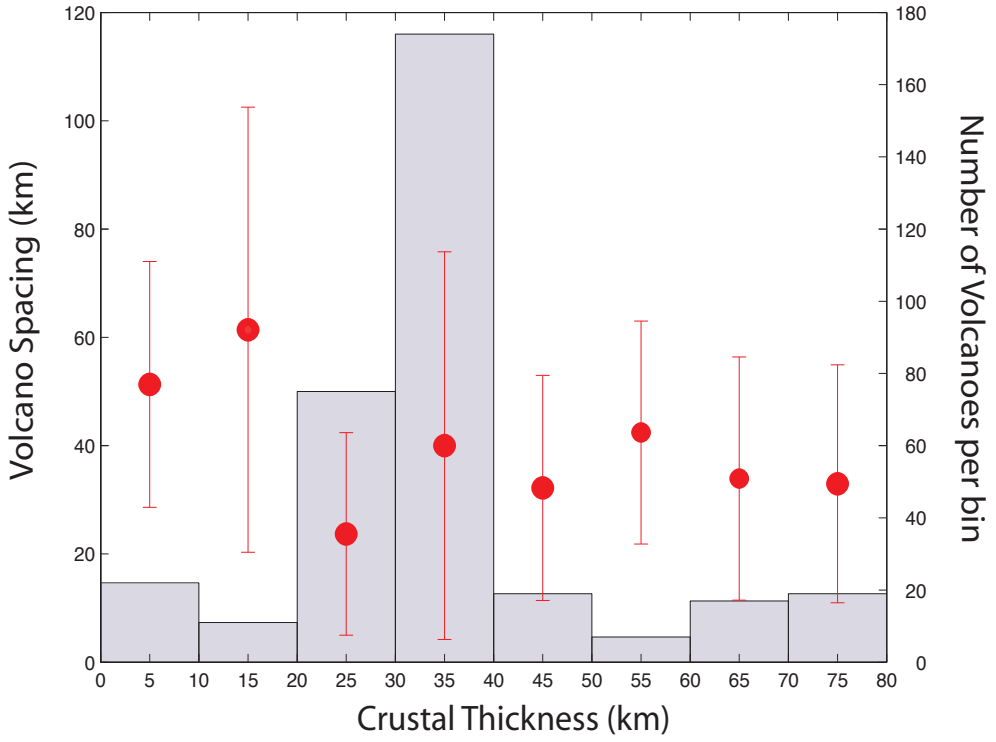

Figure 2.8: Volcano spacing plotted versus crustal thickness for the circum-Pacific Rim volcano database described in the text. Total number of entries is 341. Individual volcano pairs are binned according to crustal thickness (shown in the histogram), then averaged to produce the spacing data points shown. Error bars show one Standard Deviation. Right hand scale goes with the histogram, and left hand scale with the average spacing data. The minimum number of entries in a bin is 9 (50-60 km).

Chapter 3

Magma chamber stability in arc and continental crust

3.1 Introduction

Magma transport within the crust is a fundamental and poorly constrained component of volcanism. It provides the only physical link between melting processes in the mantle and volcanic eruptions, and is responsible in large part for the assemblage of its own substrate - both oceanic and continental crust - through the emplacement and solidification of magma chambers, dikes, and sills. Crustal magma chambers are of particular importance in this transport system, as they form the largest-scale reservoirs that store rising melt, and modulate both the composition and dynamics of higher-level transport including volcanic eruptions. These structures reside at multiple levels of the crust and on large spatial scales: exposed calderas (e.g., Bachmann et al. [2007]), plutons (e.g., Paterson et al. [1995]), layered mafic intrusions (e.g., Ernst and Buchan [1997]), as well as deeper structures inferred to be magmatic intrusions from remote imaging methods, such as lower crustal cumulate bodies (e.g., Cox [1993]). Yet it remains poorly understood where and how melt reservoirs are emplaced, what distinguishes one class of intrusion from another, and to what extent such intrusive igneous processes are linked to volcanism (Canon-Tapia and Walker [2004]). Many aspects of magma chamber growth and evolution subsequent to emplacement also remain controversial, especially in regards to the formation of large (10-100 km scale) intrusive structures.

Ultimately, what must dictate the longevity of a magma transport system is melt supply. However a variety of other factors may influence whether rising magma erupts to the surface, solidifies within the crust, or forms an active storage system as chambers. Rheological and material interfaces (such as the Moho or the brittle-ductile transition) provide a natural initial density trap for rising magmas (e.g., Kavanagh et al. [2006]), and structural heterogeneities in the near surface may re-orient and capture dikes (e.g., Valentine and Krogh [2006]). Large background deviatoric stresses will do the same - for example, extensional

tectonic stresses can promote vertical dike transport without storage (Gudmundsson [2006]), while the presence of volcanic edifice loads or pressurized magma chambers tend to focus dikes subvertically, and may trap magmas (Pinel and Jaupart [2003]). Thermal viability is also important. Magma chambers and dikes in a long-lived transport system must survive the geothermal gradient, and thus transport enough enthalpy to remain liquid over long distances (Barboza and Bergantz [2000], Rubin [1995b]).

It is also likely that many of the transport processes operating in the crust are strongly coupled to each other (Meriaux and Lister [2002], Melnik and Sparks [2005]) and to the rheological evolution of the crust as whole (e.g., Dufek and Bergantz [2005]). In a previous paper (Karlstrom et al. [2009]), we addressed some mechanical aspects of this coupling by modeling the focusing or "lensing" of dikes by a combined magma chamber and volcanic edifice system (Figure 3.1). Here we extend this analysis to determine the thermal stability of such a system, focusing on the growth of initially small ($\sim$ 1 km) chambers. We model the time evolution of a magma chamber fed by a spatially and temporally stochastic distribution of rising dikes, and by doing so address

1. Rheological and stress evolution associated with long-lived high melt fraction systems in a geothermal temperature gradient.

2. Average compositional evolution of the magma chamber and assimilation of country rock.

3. Stability of the system: will the magma chamber rupture, freeze, or exist in dynamic equilibrium within the crust for the lifetime of constant melt supply?

4. The possibility for large-scale growth of a high melt fraction reservoir.

This procedure aims to identify the key dynamical regimes to expect from dike-fed magma chambers in a viscoelastic crust.We map out a 3 parameter (initial volume, lower crustal melt flux, depth) magma chamber "stability field" for two end member emplacement scenarios - an arc setting where the country rock is amphibolite, and the intruding basalt is hydrous (2 weight % H_2O), and continental crust composed of tonalite with intruding magmas of anhydrous basalt.

We find that the evolution of chamber volume and composition are strong functions of depth and composition, and generally that steady-state ("stable") chamber volumes are more likely to exist for realistic lower crustal melt flux in hydrous environments. We also find a range of physical parameters for which chamber growth is roughly exponential in time and mechanically stable (i.e., no eruption occurs) that we refer to as "runaway", suggesting that rapid large-scale growth of magma chambers is possible under some circumstances, provided melt is continually supplied. While the details vary, stable or runaway chambers result from lower crustal melt flux values that range from $\sim 10^{-4}$ to $\sim 10^{-1}$ $m^3/m^2/yr$ for

mid to lower crustal depths and both compositions in this study, with deeper and/or drier compositions produced a slightly broader range of runaway unstable chambers. The stability field results are then compared in a qualitative way to three classes of magmatic intrusions: caldera-forming shallow magma chambers, mid-crustal plutons, and layered mafic intrusions.

3.2 How to grow a large crustal magma chamber: magmatic lensing

A magma chamber is commonly and loosely defined as a reservoir of high melt-fraction magma in the crust or upper mantle (possibly only transiently), that acts as a capacitor for magma ascent and as a place of chemical evolution through a combination of fractionation and melting (e.g., DePaolo [1981], Marsh [1989], Bachmann and Bergantz [2003]). The mixture inside the chamber may become buoyant and/or over-pressured in time due to a variety of processes, including fractional crystallization, volatile exsolution and magma recharge, leading to deviatoric stresses in the country rock that may be tens of MPa in magnitude (e.g., Tait et al. [1989], Jellinek and DePaolo [2003], Fowler and Spera [2008]). This stress field is geometry-dependent, and for all but the most symmetric chamber shapes (spheres), stresses at the chamber margin are concentrated in areas of high curvature (e.g., Sartoris et al. [1990], Gudmundsson [2006], Grosfils [2007]). If the chamber overpressure is high enough, dikes will emanate from these locations of high deviatoric stress and transport magma from the chamber, thereby lowering the overpressure. This has been studied in a number of cases, for simple geometries (e.g., Meriaux and Lister [2002], Pinel and Jaupart [2005]).

It is not well established how magma chambers are recharged, or whether melt in the lithospheric mantle and lower crust travels through diapirs (e.g., Miller and Paterson [1999], Gerya et al. [2004]), dikes (e.g., Clemens and Mawer [1992]), or in a network of channels (e.g., Spiegelman and Kenyon [1992]). Feeder dikes have been inferred to supply large mafic intrusions (e.g., Ernst and Buchan [1997]), lower crustal terrains (e.g., Williams et al. [2009]), and must exist for thermally viable long distance transport (Bruce and Huppert [1989]). We assume here that dike transport is important, and that the propagation direction of rising melt should be broadly governed by the principle stresses in the surrounding medium, involving contributions from the rising magma itself and any background stresses (e.g., Muller et al. [2001]). Dikes will propagate in a direction orthogonal to the least compressive principle stress in the medium at the dike tip. Therefore, magma chambers that are buoyant, over-pressured, or both may generate stresses that affect the trajectories of rising dikes by focusing, or "lensing," dikes from a distance greater than the footprint of the chamber at depth - potentially many times the radius of the chamber for realistic overpressures (Karlstrom et al. [2009]). Magmatic lensing is a mechanism in which magma chambers can attain the largest possible overpressures through recharge, although our model is consistent with any mechanism of unsteady magma supply.

3.3 A thermomechanical model

We develop a two-dimensional coupled thermal and mechanical model of dike focusing due to an over-pressured and buoyant cylindrical chamber with a viscoelastic shell (Figure 3.1) in an otherwise infinite elastic medium to study the time evolution of a crustal magma plumbing system at different levels in the continental geotherm. The model contains a thermodynamic description of the chamber and its surroundings, a temperature- and time-dependent country rock rheology, and a mechanical model for chamber stresses based on the mechanism of magmatic lensing. Interactions between magma chamber and host rock are primarily responsible for determining the stability of the system. Emphasis is on simplicity in the model components; we do not strive for details of transport mechanics, focusing only on a few generally dominant processes. This approach seems a necessary first cut at a fully coupled crustal magma transport model.

Further simplification follows from a consideration of the important timescales involved in this process, summarized and quantified in Table 3.1. These are the magma supply timescale τ_d (the time for a dike to ascend from the source to the chamber), the Maxwell viscoelastic relaxation timescale τ_{ve}, the elastic pressurization timescale τ_e, and the timescale for thermal diffusion through the thickness of the viscoelastic shell τ_t (for typical shell thicknesses of $10^2 - 10^3$ m). We assume that dike ascent speed V_{dike} is limited by the viscosity of the basaltic magma η_d, and subsequently find that dike ascent times are several orders of magnitude smaller than the others for timescales of interest (Table 1).

In evaluating the timescales above we assume two dimensional elliptical dikes of aspect ratio $H/L = 10^{-3}$ (Figure 3.1) that propagate with a constant overpressure ΔP_d (see model description below for details). We take the viscosity of primitive basaltic melt $\eta_d = 10^2 - 10^4$ Pa s, dike transit length scales of $D = 10^4 - 10^5$ m, thermal diffusivity of $\kappa = 10^{-6}$ m^2/s, the viscosity of wall rocks $\eta_{wr} = 10^{18} - 10^{25}$ Pa s, and Young's modulus E of wall rocks 10^{10} Pa. Chamber volume V_c and average melt flux Q_{avg} are taken in the range discussed in the Implementation section, R_c is the maximum capture radius of the magma chamber, and other geometric parameters are defined in Figure 3.1.

Given these rough relations, we model the temporal evolution of the transport system in an iterative sequence of three one- and two-way coupled steps: 1) Dike propagation leading to mechanical chamber expansion, 2) Thermal evolution of the chamber and country rock 3) Viscous relaxation and rheological evolution around the chamber. The second and third steps of this process are two-way coupled. Though simplified, this model allows a rich variety of interactions (Figure 3.2) that lead in time to chamber rupture, freezing or stable growth. In fact, consideration of Figure 3.2 with respect to the timescales in Table 1 leads to a spectrum of model chamber dynamics (Results section).

The magma chamber

A magma chamber in the crust is modeled as an over-pressured and buoyant cylindrical inclusion surrounded by a viscoelastic shell and imbedded in an infinite elastic medium

Name	Scaling	Range of times
Dike transit timescale	$\tau_d \sim \frac{D\eta_d L}{\Delta P_d H^2}$	$10^4 - 10^8$ sec
Elastic timescale	$\tau_e \sim \frac{\Delta P_{crit} V_c}{E Q_{avg} R_c}$	$10^4 - 10^{12}$ sec
Viscoelastic timescale	$\tau_{ve} \sim \frac{\eta_{wr}}{E}$	$10^8 - 10^{15}$ sec
Thermal diffusion timescale	$\tau_t \sim \frac{(R_2 - R_1)^2}{\kappa}$	$10^{10} - 10^{12}$ sec

Table 3.1: Important timescales for magma chamber - host rock interactions. Dike transit timescale measures ascent from source region to chamber, Elastic timescale measures pressurization due to magmatic lensing of dikes through capture radius R_c, Viscoelastic timescale is the Maxwell relaxation time of the heated chamber wall rocks, and the Thermal diffusion timescale is measured over the typical thickness of the viscoelastic shell ($10^2 - 10^3$ m). Variables are defined in the text.

(Bonafede et al. [1986], Dragoni and Magnanensi [1989]). Our modeling takes place on a two dimensional slice of this system, making all volume estimates in this paper a function of the cylinder radius. The chamber grows through the addition of magma from dikes, and in some cases because of wall rock melting. Overpressure relative to lithostatic pressure in the chamber generates deviatoric stresses outside the chamber that decay with distance r as $\sim \Delta P/r^2 + \Delta\rho g/r$, where ΔP is the chamber overpressure, $\Delta\rho g$ is the magma buoyancy. Deviatoric stresses re-orient rising dikes that travel within a region where these deviatoric stresses are large enough to affect dike propagation. We pick a simple model for dike propagation (discussed below) that results in dike focusing around the chamber where deviatoric stresses are ≥ 1 MPa (Karlstrom et al. [2009]).

This region may be quantified at any depth below the chamber through the notion of a "capture radius," measured from the center of the chamber at a given depth to the point where the magnitude of greatest deviatoric principle stress falls below 1 MPa (defined in Figure 3.1). The capture radius will be zero at sufficient depth below the chamber, but may be several times the chamber radius at depths of 5-10 km below the chamber (Karlstrom et al. [2009]). Rising magma will pass through the largest capture radius of the chamber on its way to the surface. Although this capture radius is geometry dependent, and is affected strongly by the presence of a free surface (e.g., Pollard [1973], McTigue [1987]), capture by small or deep-seated magma chambers is well approximated by an infinite space solution (see Results section), and the far-field stresses calculated from a spherical chamber are similar to

more complex geometrical formulations (e.g., Sartoris et al. [1990], Yun et al. [2006]).

Geometric effects and material interfaces represent corrections to simple elastic cavity solutions in the appropriate limits, and are most pronounced in the near-field (where, incidentally, much of the interesting physics occurs). Our treatment of chamber stresses is not meant to capture all quantitative aspects of chamber rupture, and we retain an analytical approach to study a few clearly defined aspects of this problem, namely, the dynamic regimes that arise from a particular parameterization of chamber stresses and mechanical constitutive relations as well as free surface effects. A fully numerical treatment coupling advection, multicomponent magma thermodynamics and elasticity would be an interesting extension of this model, but is not attempted here.

In calculating the stresses in an infinite space, we apply the equilibrium equations of linear elasticity (equation 3.11), with boundary conditions

$$\sigma_{rr,in}|_{r=R_1} = \Delta P + \Delta\rho g R_1 \cos\phi \tag{3.1}$$

$$\sigma_{r\phi,in}|_{r=R_1} = 0 \tag{3.2}$$

$$\sigma_{rr,in}|_{r=R_2} = \sigma_{rr,out}|_{r=R_2} \tag{3.3}$$

$$U_{r,in}|_{r=R_2} = U_{r,out}|_{r=R_2} \tag{3.4}$$

where σ_{in} and σ_{out} refer to stresses inside and outside the shell, U_{in} and U_{out} are displacements inside and outside the shell, ΔP is the chamber overpressure, $\Delta\rho g$ is the buoyancy of the magma chamber, R_1, R_2, and ϕ are defined in Figure 3.1. Boundary conditions for the free surface case are slightly different, outlined in Appendix A. Our parameterization of gravitational body forces (equation 3.1) provides a means of coupling thermally-induced buoyancy evolution in the chamber to stresses, and absorbs a reference buoyancy of the magma into the overpressure ΔP. Buoyancy is small compared to other sources of deviatoric stress in our model. We neglect the depth-dependent density of the crust, noting that density differences alone do not significantly affect the location of reservoir failure (Grosfils [2007]).

Viscoelastic solutions are then found via the correspondence principle (Fung [1965]), from which time-dependent stresses are found (Appendix A). These solutions have the property that deviatoric stresses in the viscoelastic shell decay in time at a rate determined by the shell viscosity (Figure 3.3), although there are some differences between pressurized and buoyant chambers in this regard, as well as free surface effects (Appendix A). Viscous relaxation of chambers stresses may prevent chamber rupture, and is a possible mechanism for the growth of large over-pressured chambers (e.g., Jellinek and DePaolo [2003]). Viscoelastic relaxation of stresses affects rising dikes as well, because the bulk crust is assumed elastic on dike-rise timescales, and dikes propagating in the country rocks ($r > R_2$) will still experience deviatoric chamber stresses (Figure 3.3). Viscous creep effectively increases the chamber size by propagating elastic normal stress boundary conditions on the inner radius of the shell ($r = R_1$) to the outer radius ($r = R_2$) on the Maxwell timescale τ_{ve} (Appendix A).

The extent of the viscoelastic shell is determined through thermal considerations with a one-parameter melt fraction curve to relate crystal content of the magma to temperature (discussed below), and the viscosity is taken to be time and temperature dependent, but constant throughout the shell. This couples thermal evolution to mechanical effects. Thermal expansion of the magma and shell is neglected in the calculations leading to equations 3.12-3.17, as the expansivity of magma is roughly 6 orders of magnitude smaller than the compressibility.

Not all chambers will exhibit a viscoelastic shell as formulated above, and indeed this is an important component of our model. Chambers that receive a sufficiently high melt flux through dikes will mechanically expand more rapidly than the thermal diffusion timescale, erupting before a shell forms. This condition requires that the Peclet number for chamber recharge (taken to be the ratio of chamber expansion from recharge and heat diffusion timescales in our model) must be larger than one:

$$\mathrm{Pe} = \frac{Q_{avg} R_c}{R_1^2} \frac{R_1^2}{\kappa} = \frac{Q_{avg} R_c}{\kappa} > 1. \tag{3.5}$$

Under these conditions a magma chamber may quickly rupture to drain mass and overpressure. Because we are primarily interested in those magma chambers that drive surface eruptions, we assume that chamber draining occurs only when dikes propagate to the surface. While certainly not strictly true in reality, as is evidenced by relic dikes and sills that terminated in the crust (e.g., Rubin [1995a]) and long-distance lateral transport through dikes (Ernst et al. [1995]), this assumption simplifies the analysis as an end-member scenario.

We use a thermal criterion to determine the "critical" overpressure needed to drive dike propagation to the surface. By balancing the freezing and elastic opening of a crack, Rubin [1995b] and Jellinek and DePaolo [2003] derive the pressure required to propagate a dike from the source region to the surface. This pressure necessarily exceeds the tensile strength of rock, leading to chamber overpressures in our model that exceed the threshold dike propagation stress. We find values of this critical overpressure in the range of 20-100 MPa, consistent with magma chamber overpressures inferred from ground deformation measurements in volcanic areas (e.g., Newman et al. [2001], Yun et al. [2006]), noting that inferences of magma chamber overpressure in shallow systems are sensitive to depth, and thus cannot be directly applied to rupturing of deep chambers.

Purely elastic formulations of reservoir failure that include tensile failure and gravitational loading in a self-consistent way (e.g., Grosfils [2007]) require rupture-inducing overpressures that exceed lithostatic in some cases. Conversely, chamber rupture based on laboratory tensile-failure experiments (e.g., Gudmundsson [1988]) implies dike overpressures that are too low to overcome the geotherm (Rubin [1995a]), and that reservoir failure may happen frequently. In place of a more complete failure model, we choose a constant "critical" overpressure of 75 MPa to rupture the magma chamber. This choice reflects uncertainty in the specific mechanisms of reservoir failure, which may involve different physics than we model here (e.g., Chen and Jin [2006], Lengline et al. [2008]). We expect that this value is an approximate upper bound on the chamber overpressure necessary to trigger an eruption, and

models a (silicic) magma viscosity of 10^7 Pas, surface heat gradient of 68 mW/m^2 (Rudnick et al. [1998]), static Young's modulus E of 70 Gpa, Latent heat L of 400 kJ/kg, heat capacity of 1100 J/Kg K, and thermal diffusivity κ of 1 mm^2/s.While different choices of these parameters will change the minimum critical overpressure needed for eruption, our main results are not sensitive to a particular choice.

Dike transport

Many quantitative dike models in the geologic literature are based on the assumptions of Linear Elastic Fracture Mechanics, and that dikes resemble fluid-filled pressurized and/or buoyantly driven opening-mode cracks (Rubin [1995a]). Cracks propagate when the potential energy released through propagation is sufficient to fracture rock at the crack tip (Griffith [1920]). This is a threshold energy criterion for propagation, and is a feature of all "critical" dike propagation models, though so-called "sub-critical" dike propagation (e.g., Atkinson and Meredith [1987]) is a viable magma transport mechanism over short distances (Chen and Jin [2006]). It is also possible that, in regions of partial melt, transport is dominated by porous flow and channelization (e.g., Spiegelman and Kenyon [1992], Holtzman et al. [2003]), though thermally viable long-distance transport is achieved through melt coalescence into a dike.

We model a dike as a uniformly pressurized ellipse of constant aspect ratio (Jaeger and Cook [1969]) in an infinite medium. In a polar coordinate system centered around the dike tip, taking ξ to be the radial coordinate and θ the angle from long axis of the dike, principle stress eigenvalues and (un-normalized) eigenvectors take the form

$$\sigma_{dike\pm} = \frac{K}{(2\xi)^{1/2}} \left[\cos(\theta/2) \pm 2\sin(\theta)\right] \mathbf{v}_{\pm} \tag{3.6}$$

$$\mathbf{v}_{\pm} = \mathbf{e}_{\xi} + \left[\cos(3\theta/2) \pm \tan(3\theta/2)\right] \mathbf{e}_{\theta} \tag{3.7}$$

.

Here $\sigma_{dike\pm}$ are the magnitudes of principle stresses oriented along $\mathbf{v}_{\pm}$, $\mathbf{e}_{\xi}$ and $\mathbf{e}_{\theta}$ are unit vectors centered on the dike tip, and K is the Stress Intensity Factor of a modified Griffith theory (e.g., Rubin [1995a], Roper and Lister [2005]). Dikes propagate in this scheme if $K = \Delta P_d \sqrt{l} \geq K_c$, where K_c is the "critical" Stress Intensity Factor (Rubin [1995a]) and ΔP_d is the dike overpressure. We assume that dikes propagate with this minimum condition $K = K_c = 10^6$ Pa m$^{1/2}$ at all times as a lower bound for continuous propagation (Karlstrom et al. [2009]). Far-field deviatoric principle stresses in excess of dike stresses around the crack tip then re-orient the trajectory of the rising dike. This dike model captures the physics of interest in the present application - (1) a dike will not propagate unless it is sufficiently driven (a threshold model), and (2) a dike exerts a stress field that helps to determine its own trajectory. We note that our approach to dike propagation in an external field is an approximation to the dynamics of truly coupled dike-chamber interactions, and may actually underestimate the efficacy of magmatic lensing (Meriaux and Lister [2002]).

However, qualitative aspects of dike focusing are unchanged in more detailed studies. We exclude stress interactions between dikes, although such interactions can lead to interesting organization of magma transport (Ito and Martel [2002], Kühn and Dahm [2008]). In the presence of large background stresses (such as the magma chamber considered here), dike interactions should be of lower order importance, although they may be important for the initial formation of magma reservoirs (Kühn and Dahm [2008]). We also note that while dikes are emplaced elastically, this does not mean that their surroundings (particularly the magma chamber and wall rocks) are strictly elastic. Hence, dike interactions and chamber evolution may occur over different timescales (Table 3.1).

While magma supply to the lower crust is not certain, a variety of studies have generally found lower bounds on the order of 10^{-3} $m^3/m^2/yr$ to $10^{-4} m^3/m^2/yr$ in arc settings (see Dufek and Bergantz [2005] for a compilation of this data). We use the stochastic framework of Dufek and Bergantz [2005] to model continued melt supply through dikes. Dikes are intruded randomly in space and in time at the base of our simulated domain, constrained only to conform to a long-term average volume flux. We use a Monte Carlo algorithm (Manno [1999]) to produce a spatially random distribution of dikes with a Gaussian distribution of melt volume (and therefore size). These dikes propagate vertically unless far-field deviatoric stresses exceed stresses near the dike tip, at which point dike trajectories are re-oriented to follow the least compressive principle stress.

Thermochemical model

Much effort has been devoted to understanding the thermal evolution of magma chambers. While complex multi-component convective processes may occur throughout the lifetime of the chamber (e.g., Turner and Campbell [1986], Ruprecht et al. [2008]), the enormous crustal thermal resistor ensures that conduction will be the primary mode of heat transfer near the wall of a magma chamber, driven both by the sensible and latent heat content of the magma chamber. The rate-limiting factor in both cooling/crystallization and possible heating/melting events is therefore conductive heat transfer between the chamber interior and the host rock (Carrigan [1988], Marsh [1989]).

While simple analytic conductive cooling models have been used widely to investigate the thermal evolution of magma bodies (e.g., Younker and Vogel [1976], Spera [1980], Hort [1997], de Silva and Gosnold [2007]), models that take into account laboratory melt crystallization experimental results (e.g., Annen and Sparks [2002], Dufek and Bergantz [2005]) and multi-component heat transfer (e.g., Spera and Bohrson [2001], Gerya et al. [2004]) allow for more detailed petrologic predictions. We use a nonlinear melt fraction-temperature curve as a proxy for composition in two end-member cases: country rock of amphibolite (Dufek and Bergantz [2005]) or tonalite (Petcovic and Dufek [2005]) bulk composition, and intruding basalt that is either anhydrous or contains 2 weight % H_2O (Appendix B). Evolution of melt fraction can then be used as a proxy for compositional evolution of a magma chamber, including chamber buoyancy and the mixing of melt from country rock and dikes.

We use an Alternating Directions Implicit (ADI) finite difference numerical scheme to

solve the time-dependent heat conduction problem based on the treatment of Dufek and Bergantz [2005], but modified to include a more general local enthalpy to couple a mechanical model to the thermal model. Conservation of energy for the system dictates:

$$\frac{\partial H(\mathbf{x},t)}{\partial t} = \frac{\partial}{\partial \mathbf{x}} k_{mix} \left(\frac{\partial}{\partial \mathbf{x}} T(\mathbf{x},t) \right) \tag{3.8}$$

where $H(\mathbf{x},t)$ is the local enthalpy at point $(\mathbf{x},t)$, given by

$$H(\mathbf{x},t) = \rho_{mix} \int_{T_{ref}}^{T(\mathbf{x},t)} c_{mix} dT + \rho_{mix} f(\mathbf{x},t) L + P\delta V(\mathbf{x},t). \tag{3.9}$$

We use enthalpy to parameterize local energy, because it remains a continuous function through phase changes. $\mathbf{x}$ is the position vector of the local energy balance, t is time, $L = 400$ J/Kg is the latent heat of fusion, and $T(\mathbf{x},t)$ is temperature. The variables k_{mix}, c_{mix} and ρ_{mix} refer to mixture quantities, defined in appendix B, that allow us to treat mixing and melting of the country rock in the magma chamber. The work term $P\delta V(\mathbf{x},t)$ is a local quantity that reflects the addition of new magma to the chamber due to dike lensing, and $f(\mathbf{x},t) \in [0,1]$ is the local melt fraction. We impose a steady state geothermal gradient upon the country rock with a surface heat flux of 68 mW/m^2 and a surface temperature of 10 degrees C, using reflecting temperature boundary conditions on the sides of the 2D numerical domain. More details about the specifics of this thermal model can be found in Dufek and Bergantz [2005], although we assume here that dike transit does not significantly affect the background geotherm, because of the difference in timescales (Table 3.1).

The crystal content of a magma has a profound impact on its rheology (e.g., Marsh [1981]), and we use melt fraction as a proxy for purely viscous, visco-elastic or elastic behavior in the mechanical model. Regions that contain 0.6 or higher melt fraction (equations 3.58 - 3.62) are considered purely viscous (radius $r < R_1$ in Figure 3.1), and regions with 0.05 melt fraction or lower are considered purely elastic ($r > R_2$). Melt fractions between 0.05 and 0.6 ($R_1 < r < R_2$) are modeled with a Maxwell viscoelastic rheology, with an exponential temperature dependent viscosity (Appendix B). Viscosities calculated in this way are a crude approximation to more detailed parameterizations of magma viscosity based on dissolved water content, crystallinity and silica content (e.g., Scaillet et al. [1998], Hui and Zhang [2007]).

Important model approximations

Studies that have focused on magma chamber convection have shown that mixing processes, e.g. driven by the injection of basaltic melt into a more evolved silicic chamber, may have important consequences for the rejuvenation and eruptibility of large silicic systems (Bachmann and Bergantz [2003]), as well as cooling and crystallization rates (e.g., Hort [1998]). External eruptive triggering (e.g., Roche and Druitt [2001]) or volatile exsolution in shallow chambers may have similar first order effects (e.g., Tait et al. [1989], Huppert and Woods

[2002]). However, these processes are not within the scope of this work. Here we exclude explicit dynamics within and around the magma chamber, and assume that the interior is well mixed at all times.

By excluding advection in our simulations, we also assume that lower crustal rheology is elastic on the timescales of magma chamber evolution, with the diapiric rise of a large buoyant magma chamber within the crust being negligible on the timescale of magmatic lensing. This assumption is readily justified both observationally and theoretically. The Stokes rise-velocity for a magma chamber scales as $\rho g R_1^2/\mu \sim 10^{-10} - 10^{-12}$ m/s, much slower than typical dike speeds, and abundant field evidence for diking in lower crustal terrains (e.g., Dumond et al. [2007]) demonstrates that the mid to lower crust is elastic on sufficiently short timescales.

We use an analytic solution to determine viscoelastic stresses and a numerical solution for thermal evolution, so there are a number of approximations necessary to make the thermal and mechanical calculations consistent. While the analytical solution limits the extent to which the chamber can respond to an anisotropic thermo-mechanical environment, this approximation significantly simplifies the calculations and reduces the parameter space that must be explored. It allows us to focus on the dynamic behavior that results from interaction between heat diffusion, viscoelastic relaxation and elastic pressurization in a relatively simple system. The evolution of damage due to repeated diking is neglected, although it is almost certainly an important component of magma transport (especially in the shallow crust), as propagating dikes will be influenced by structural heterogeneities (Gaffney et al. [2007]). To maintain a circular magma chamber that thermally evolves in a vertical temperature gradient, we impose circular symmetry on the magma chamber by organizing the entire melted region after each timestep into 7 circular rings of constant melt fraction. The innermost ring is completely liquid ($f(\mathbf{x}, t) = 1.0$), the next has $f(\mathbf{x}, t) = 0.8$, and so on. For rings that are below the critical melt fracion of 0.6 (viscoelastic rheology), we use the highest ring temperature to determine the viscosity of the entire shell. This choice does optimize the viscoelastic relaxation effects, and thus represents a lower bound for the shell viscosity. Particular choices of melt fraction curve (Appendix B) result in shell viscosities of $\sim 10^{19} - 10^{22}$ Pas for both tonalite and amphibolite. The re-organization of melt in this way is a crude approximation for mixing processes inside the chamber, and is consistent with the dynamical assumption that the chamber interior is well mixed at all times.

Differences in the petrology of amphibolite and tonalite require that we treat the melting of these country rocks in different ways. Amphibolite is a mafic end-member proxy for lower crustal compostion in arc settings, and its major element composition is similar to basalt (e.g., Helz [1982], Wolf and Wyllie [1994]). We therefore treat the melting and solidication of basalt and amphibolite country rocks interchangeably, by assimilating melted country rock into the chamber melt at each time step. This is consistent with the assumption of a mixed chamber, and ensures a stable solution. The more evolved nature of amphibolitic partial melts is not accounted for, as it should constitute a negligible perturbation to the bulk chamber composition.

Tonalite, however, is chemically dissimilar to basalt, being essentially in the second stage

of its petrological evolution (Wolf and Wyllie [1994]). As such, we treat the melting of tonalite country rocks with two separate binning procedures for basaltic and tonalitic melt, with tonalitic melt always placed outside the intruded basalt. Because tonalite has a lower melting temperature than the anhydous basaltic input, this can result in a "jelly sandwich" configuration, where partially solidified basaltic material is sandwiched between high melt fraction tonalite and basalt. We choose the inner melt rings (basaltic composition) to determine the extent of the viscoelastic shell. This procedure does not treat the mixing processes that must occur between these two magmas, but our conclusions should depend more on a consistent treatment of melting than on detailed advective dynamics.

Finally, while we use the mechanism of magmatic lensing to model chamber recharge, subsequent thermal evolution is consistent with other means of unsteady magma supply through dikes. While details will vary, the main dynamic regimes that we find depend primarily on the average supply of enthalpy to the chamber, not the specifics of the magma deliver system.

3.4 Implementation

We implement the magmatic system model in three steps, capturing an averaged thermo-mechanical coupling between components of the plumbing system.

Step 1. Magmatic lensing

We use a dynamic model of dike propagation in which a stochastic distribution of dikes, with (2D) volumes that satisfy the mean lower crustal melt flux at the base of a discretized rectangular domain, rise toward a magma chamber. Dikes propagate incrementally; if the chamber stress field at a grid point is greater than the dike-tip stress field, we re-orient the dike along the greatest principle stress eigenvector. Otherwise, the dike moves vertically. We use the infinite space solutions (equations 3.12 - 3.17) to calculate the stresses for simulations at 20 and 40 km depth, assessing the free surface effects separately.

If a dike intersects the magma chamber, the chamber volume increases according to $V_{new} = V_{old} + V_{dike}$, and chamber overpressure according to the thermodynamic condition $P_{new} = P_{old} + \beta^{-1}(V_{new} - V_{old})V_{old}^{-1} + \delta P_{pc}$. This assumes that pressure changes propagate throughout the chamber very rapidly, so that local phase changes contribute to the entire chamber pressure. Magma compressibility β is calculated assuming a basaltic composition (Dobran [2001]), and thermal expansivity is neglected. Pressures induced by phase change δP_{pc} (determined by the thermal calculation) are included. We assume that, as an upper bound, there is a 15% volume change due to melting or solidification of magma (Dobran [2001]). Although this volume change varies with mineral phase (Ghiorso and Carmichael [1987]), most important phases (with the exception of plagioclase) exhibit a negative volume change upon solidification, and we assume that holds for the bulk magma here. The liquid interior of the chamber is assumed to have a basaltic dike composition initially, but we track chamber bulk compositional evolution through the mixture quantities (equations 3.64 - 3.66). Dike propagation continues until all dikes either reach the chamber or the top of the

numerical domain. If a dike intersects another dike, dike volumes are additive.

Step 2. Thermal evolution

Using the updated chamber volume (and heat content) from the dike, we discretize melt into rings of constant melt fraction (7 total for amphibolite/hydrous basalt, and 14 total for tonalite/anhydous basalt). We next implement the ADI scheme to determine the new temperature field solving equation (3.8), using local differences in melt fraction to update the latent heat. The work term added to equation (3.9) is assumed constant over the volume of the chamber at each timestep. We iterate until convergence is achieved, then update melt fraction according to equations (3.58) - (3.62), and calculate inner and outer chamber radii. If the outer radius reaches the boundary of the domain, the simulation is stopped. These cases are then run with a larger domain, however, there are parameters under which chamber growth exceeds all domain sizes tested (see Results).

Step 3. Viscoelastic relaxtion

With the inner and outer radii determined by the thermal calculation, we first check for either 1) possible chamber eruption due to excess of deviatoric stress at anywhere within the viscoelastic shell, i.e. $\sigma_{rr,in} - \sigma_{\phi\phi,in} > \Delta P_{crit}$ (Jellinek and DePaolo [2003]), or 2) chamber freeze-out $R_1 \leq 2$ grid cells (where $R_1 \leq 60 - 150$ m, depending on the chamber size). If either occur, the simulation is stopped. If not, we calculate new stresses throughout the domain according to equations (3.12) - (3.17), with timestep $t = 500$ years (a step size consistent with long-term averaged melt supply). In these calculations, the constant shell viscosity is updated to match the highest temperature in the shell, and we check that other choices (for example the average shell temperature) do not significantly affect the results.

This sequence is repeated for 2000 time steps (1 million years), or until eruption/freezing occurs. The model as formulated contains five variable parameters: Lower-crustal melt flux, initial chamber radius ($R_1 = R_2$), initial chamber overpressure (ΔP), bulk composition of the dike and country rock (equations (3.58) - (3.62)), and depth below the surface. However, because of the coupling between thermally and mechanically determined overpressure, choice of the initial ΔP is somewhat arbitrary, as both pressure and buoyancy are determined at each time step to ensure consistency between thermal and mechanical models. ΔP is set to an intial value of 10^6 Pa in all runs.

We run simulations with 8 choices of averaged lower crustal melt-flux ($Q_{avg} = 10^{-5}\mathrm{m}^3/\mathrm{m}^2/\mathrm{yr} - 10^0\mathrm{m}^3/\mathrm{m}^2/\mathrm{yr}$). This range encompasses observed estimates of lower crustal melt flux in arcs (Dimalanta et al. [2002]), as well as the higher values estimated from decompression melting mantle plume models (Olson [1994], Farnetani and Richards [1995]). We use 4 values of initial radii (100, 500, 1000 and 2500 m), and 2 chamber depths (20 and 40 km) to test the effect of mid to lower crustal temperature profiles on chamber stability. A more thorough test of chamber depth using a halfspace viscoelastic solution (equations 3.41-3.46) is also performed for a few cases to ensure that neglect of the free surface does not affect results, and to test the depth dependence of dynamic chamber stability. However, shallow chambers are not the main focus of this study. We also test 2 end member compositional scenarios. Amphibolite composition country rocks are used as a proxy for arc environments, and are also similar to expected lower crust compositions (e.g., Christensen and Mooney [1995]).

We do 32 runs at 20 km and 40 km depth for amphibolite. Tonalite composition country rocks are to be expected in more compositionally evolved settings. Because rocks of this composition partially melt at lower crustal depths, we do 32 runs at 20 km depth only. The total number of simulations is thus 96. Repeat simulations were undertaken in all cases where the stochastic distribution of dikes seemed to affect results, however, in most cases the results are robust to multiple runs. Resolution tests are performed in both space and time to determine the consistency and stability of solutions, and we ensure that energy is conserved to within 1 % through each timestep (Appendix B).

3.5 Results

We find four dynamic regimes of magma chamber evolution. Chambers of any size tested are unstable in many cases, either "freezing" or "erupting" (pressure exceeds the critical overpressure), due to an insufficient or excess melt flux rising from the base of the crust, respectively. However, there are parameters for which chambers rapidly reach a stable size (steady state) as long as melt supply is constant. There is also a "runaway growth" regime, in which viscous relaxation prevents chamber deviatoric stresses from growing while melt influx is still high enough for chamber growth. This regime is rendered finite in most cases, because wall-rock viscosities are bounded from below by the solid-liquid transition, which limits the stress relaxation timescale.

Typical snapshots of the simulations are shown in Figure 3.4. Figure 3.5 shows example time evolution of volume. Model results for all parameter choices are compiled in dimensionless "stability field" representations for amphibolite and tonalite average crustal compositions in Figures 3.6 - 3.7. To make compilations, each run is averaged temporally in these parameters (change in melt fraction, overpressure, shell viscosity, melt flux received by the chamber), and the dynamic results of the run are expressed in terms of averages. Each point on Figures 3.6 - 3.7 corresponds to an averaged set of model runs, and is colored according to the end result.

Figure 3.6 shows the stability field in terms of initial chamber size and melt flux through the crust. Figure 3.7 plots the same data, but cast in terms of physical timescales. The abscissa is the total number of timesteps in a given run. Small values indicate that the final result occurred very quickly, and represents a thermally or mechanically unstable system. Values approaching 10^6 years represent a thermally stable system. The ordinate is a ratio of average elastic and average viscoelastic timescales (Table 3.1). Large values (generally > 1) represent systems that are viscously dominated, with a low shell viscosity. Systems with small values of this ratio (generally < 1) are elastically dominated, growing and pressurizing in response to melt influx. Because of the nonlinear melt fraction curves used (Appendix B), there are compositional differences between the lines dividing elastically- or viscously-dominated dynamics, such that $\tau_e/\tau_{ve} = 1$ does not strictly define regimes in Figure 3.7. This representation does separate the model results, however, and is useful for deciphering which set of processes determines the outcome in a given run.

Dynamic regimes of chamber evolution

Frozen chambers

In the case of chambers that freeze, melt volume supplied by dikes in each time step (500 years) is a small fraction of the chamber volume, and does not supply enough enthalpy to prevent progressive solidification. Such a situation is aided by a net negative volume change of solidifying magma, which causes under-pressurization of the chamber and negative work, although it incurs a positive latent heat contribution to the enthalpy balance (equation 3.8). Mechanically, the decrease in pressure decreases the capture radius of the magma chamber (Figure 3.1), and hence the chamber focuses less melt from dikes. Progressive cooling of wall rocks (and hence progressive increase in wall rock viscosity) in a slowly solidifying chamber also feeds this process; because of the assumption of an Arhennius-type viscosity, this effect is exponential in time. Freezing thereby constitutes a negative feedback loop. In our model, chambers that receive less than $\sim 10^{-4}$ m^3/m^2/yr melt flux freeze irrespective of size or depth in the geotherm, although smaller and shallower chambers are slightly more susceptible to freezing. As is exemplified in Figure 3.5, deeper chambers generally freeze-out more slowly than shallow chambers, although the stochastic nature of melt supply causes some exceptions to this rule.

Erupted chambers

Chamber eruption is caused by exactly the opposite feedback processes. In this case, enthalpy supplied by dikes balances heat lost by conduction, and high melt influx results in rapid chamber expansion. If expansion and pressurization is larger than the rate of thermal diffusion, no viscoelastic shell forms and the chamber erupts on the elastic pressurization timescale. Likewise, eruption occurs if a shell exists but chamber pressurization occurs more quickly than the viscoelastic timescale. Net melting results in positive volume change, and hence positive work, with positive chamber overpressurization and negative latent heat. Magmatic lensing is amplified, resulting in a larger influx of magma. Such feedbacks lead to very high overpressures, and chamber rupture can occur on short timescales (Figure 3.7). Chamber eruption occurs in most model runs if the flux is sufficiently high (greater than $\sim 10^{-1}$ m^3/m^2/yr), and are represented by red symbols in Figures 3.6 - 3.7. However, eruption is a strong function of depth and size: larger, deeper chambers are the most stable (Figure 3.6).

Red-blue symbols in Figures 3.6 - 3.7 denote a "transitively eruptive" regime in which chambers progressively freeze, but sometimes erupt before the inner radius shrinks to zero. This occurs because freezing is accompanied by an (exponential) increase in shell viscosity. Chambers that receive sufficient melt influx to pressurize significantly despite progressive solidification may then erupt as the shell viscosity increases. These results are run-dependent.

Stable chambers

Dynamic equilibrium is achieved for model runs that balance the competing dynamics, with Pe ~ 1 and $\tau_e/\tau_{ve} \sim 1$ (equation 3.5 and Table 3.1). There are both a temporally stable and a transient or unstable regime in which this occurs. Stable equilibrium results when chamber growth decreases asymptotically in time until subsequent volume changes are less than 0.5 % of the chamber volume, and deviatoric stresses relax in the viscoelastic shell. These results are represented by green symbols in Figures 3.6 - 3.7. Such chambers necessarily have an average elastic timescale larger than the Maxwell time (Figure 3.7), and grow thick viscoelastic shells (Figure 3.5) - although this thickness is composition dependent. Amphibolite melts past the critical melt fraction more readily than tonalite, so shell thicknesses are smaller in these settings. Total melt volume of both country rock plus basaltic magma (i.e., the chamber volume) remains approximately constant in time (Figure 3.8), but melt fraction of country rock increases. In fact, large assimilation of country rock occurs primarily in stable chambers. Progressive heating of the domain does ultimately make this stable period finite, as does the slow build-up of stresses in some cases.

Runaway chambers

Transient dynamic equilibrium, or "runaway growth" occurs when the elastic pressurization timescale is smaller than the thermal diffusion time (Table 3.1), such that chamber growth occurs in each timestep but the ratio of pressurization time to Maxwell time is near unity (Figure 3.7). This results in deviatoric stress relaxation, however, continued melt influx causes the slow but continuous build-up of these stresses. Enthalpy is supplied to the system through dikes in large enough quantity that growth exceeds solidification. Such dynamic equilibrium is a "runaway growth" regime, and can result in rapid growth of chambers. However, the build-up of deviatoric stresses over long times (up to ~ 100 ka for amphibolite, slightly longer for tonalite) due to the continued influx of largely incompressible fluid into the chamber results in eventual chamber rupture.

This runaway growth regime is a direct result of the nonlinearity built into our model system by the imposition of a critical melt fraction, which places a lower bound on the magnitude of the wall rock viscosity, and hence an upper bound to the relaxation of stresses in the viscoelastic shell. Model runs in which runaway growth was accompanied by increasing shell stresses are represented by purple-red colored symbols in Figures 3.6 - 3.7; runs in which growth was not accompanied by significant build-up of shell stresses are colored purple or purple-green (depending on whether the results were run-dependent). Some stable cases may still eventually erupt, however, because finite numerical domain width precludes assessment of a possible final chamber size for some of these fastest growing transient equilibrium model runs. Maximum average growth rates are $\sim 0.004 \pm 0.0005$ km^2/yr, implying that a chamber may grow from 1 km radius to 10 km in ~ 100 ka. This is roughly of the same order as the timescale for deviatoric stresses to become large, thus 100-fold increases in magma chamber volume are realistic in this system, provided that lower crustal melt flux is constant over this

period.

The effects of magma and country rock composition

We find that, all other parameters the same, magma chambers operating in each end member compositional scenario differ substantially in final behavior. The tonalitic proxy composition, (defined by equation 3.60), contains less modal hydrous minerals, and has a correspondingly higher solidus and liquidus (Appendix B). Seismic velocities of the lower crust are more consistent with an amphibolite-like composition grading to granulite facies in arc settings, while tonalite grading to granulite is expected in continental environments (Christensen and Mooney [1995]). In our simulations, chambers in tonalitic country rock are less stable than their 'wet' counterparts, having little to no equilibrium regime, both freezing and erupting more quickly. In addition, these chambers melt more crustal material, leading to thicker viscoelastic shells. Crustal melting in the "runaway growth" regime is responsible for inhibiting "equilibrium" chambers (Figure 3.6), and it is this large degree of crustal anatexis that is the most significant difference between the compositions.

Assimilated percentages are measured with respect to the magma that reaches the chamber and do not necessarily represent the total fraction of assimilation in crustal melt, as dikes that are not captured by a magma chamber leave the system in our model. Total crustal melt does not exceed $\sim 40\%$ by volume of intruded magma, consistent with other studies that invoke other mechanical processes (e.g. crustal extension Hanson and Glazner [1995]) to localize and maintain the mafic enthalpy to assimilate large volumes of crust. Stable chambers in a bulk amphibolitic country rock can assimilate up to $\sim 50\%$ by volume of their surroundings as melt, whereas the same chamber in a tonalitic environment may assimilate more, up to $\sim 60 - 70\%$.

This difference may be attributed to the sharp step in the melt fraction curve (equation (3.60)) associated with the melting of plagioclase feldspar (Appendix B). Prolonged heating of tonalite will therefore produce a higher melt fraction shell than similar heating of amphibolite, over the range of 850-950 degrees C. A significant volume of tonalite country rock melts completely in the "runaway growth" regime chamber, and thus can initiate a switch from a predominantly mafic magma chamber to a mostly felsic - but still high melt fraction - chamber as the anhydrous basalt with its higher solidus and liquidus slowly cools. Chambers that assimilate large fractions of crust by necessity need a large supply of enthalpy. Because there are dynamically stable chambers within a range of lower crustal melt flux (Figure 3.6), the average percentage by volume of total crustal melt in a stable chamber is $\sim 20\%$ for our "wet" compositions, and $\sim 40\%$ for "dry" compositions.

Examples of the difference between anatexis "wet" and "dry" settings are illustrated in Figure 3.8. While by no means an exhaustive paramater space search, these curves are nonetheless representative of the controls exerted on chamber melting by a combination of depth, melt flux, composition and initial size. It is evident that composition plays a leading role in assimilation of country rock, although melt flux is still the most important parameter, as it sets the space of stable and runaway chambers in which significant melting can occur.

The water content of the intruded magma also plays an important role in long-term chamber evolution. While we choose a relatively narrow range of basaltic compositions with 0 and 2 weight % H_20 as dike material (compared to the upper observed limits of up to $\sim 6-8$ weight % water in arc settings (Wallace [2005])), the melt fraction curves of these choices are nonwithstanding quite different (Appendix B). We emphasize that the one-paramater melting curves in our model are proxies for real rock melting behavior, which will have different modes and hence a more complicated melting process.

Because we consider "end member" compositional scenarios in which "wet" basalt is paired with "wet" country rock and "dry" basalt is paired with "dry" country rock, it is natural to expect that our results represent end member dynamical regimes. The fact that we do find significantly different long-term behavior of chambers in these scenarios, however, is an indication that composition does have a significant effect on magma chamber evolution, and that chambers in more anhydrous environments will tend to be less stable and less long-lived (at least at high melt fraction). It is possible that large magma bodies may exist for long time periods at low melt fraction (e.g., Bachmann and Bergantz [2003], Huber et al. [2009]). Because we end our simulations when the liquid-like portion (meltfraction > 0.6) of the magma chamber freezes, this is a scenario we cannot address. In both compositional cases, time evolution results in a bulk density that decreases in time, in accord with the differentiation and mixing processes that are taking place (equations (3.64) - (3.66)). Short-lived chambers do not experience significant density evolution in our scheme.

Chamber pressurization and stress evolution

We use a numerical domain that is ~ 10 times the chamber diameter, so that melt flux reaching the chamber at the start of each run is much less than the total. However, continued pressurization and growth of the magma chamber increases its capture radius, thereby focusing more melt from a larger region. Underpressurization or net freezing of the chamber decreases the capture radius and the amount of melt focused. In other words, feedbacks in the magmatic lensing process (Figure 3.2) strongly affect the evolution of melt supply to the chamber, particularly the coupling of thermal to mechanical evolution. Because of the assumed 15 % volume change that accompanies melting or solidification (Dobran [2001]), large pressures are induced by melting and freezing of magma, and this acts in concert with rheological effects to amplify or damp elastic pressurization stresses (Figure 3.10). Without consideration of these effects (including the threshold rupture criteria), chamber overpressures reach unrealistically high values that approach lithostatic, as illustrated for a chamber with an evolving shell of 100-300 meters in Figure 3.10. Chamber pressurization also affects the energy balance, and hence thermal evolution, through the work term in equation (3.8) that accounts for work due to melting or solidification at each timestep. However, evaluation of this effect shows that it contributes little to the total energy budget, on the order of a few percent at each timestep.

As is discussed in Jellinek and DePaolo [2003], the most import aspect of viscoelastic rheology around magma chambers is to relax stresses that might otherwise rupture the

chamber and generate volcanic eruptions. This is the process responsible for the "stable equilibrium" regime of chamber growth, but strong coupling to the thermal evolution of the shell means that the dynamics are time dependent. It is possible for viscoelastic effects to "shut off" as well as "turn on" chamber rupture. The blue-red symbols in Figures 3.6 - 3.7 denote this behavior. However, temperature affects deviatoric stresses in a doubly exponential manner, through the relaxation timescale τ_{ve} (e.g., Dragoni and Magnanensi [1989]) and the temperature-dependent viscosity law (equation 3.63):

$$\sigma_{dev}(\mathbf{x},t) \sim \sigma_{dev}(\mathbf{x})e^{-t/\tau_{VE}} \sim \sigma_{dev}(\mathbf{x})e^{-t(EA^{-1}e^{nRT(\mathbf{x},t)/Q})} \tag{3.10}$$

where $\sigma_{dev}(\mathbf{x},t)$ is the deviatoric stress at position vector $\mathbf{x}$ and time t, E is the Young's modulus of chamber wall rocks, $T(\mathbf{x},t)$ is temperature, and all other constants are defined in Appendix B. The viscosity used to define the viscoelastic timescale τ_{ve} in equation (3.10) is strictly a function of both stress and temperature, however, the doubly exponential effect of temperature will dominate, such that deviatoric stresses relax in a narrow temperature range. This feature of the stress evolution may have implications for the possible timescales of eruptibility, as dike propagation (in our formulation) will not occur to drain the chamber. To erupt such a chamber, other processes (such as volatile exsolution, roof collapse or external triggers) not considered here must operate.

The effects of depth

For magma chamber stability, the proximity of a stress free surface has two major effects. The first is to concentrate deviatoric stresses on the sides of the chamber (e.g., Pinel and Jaupart [2003], Grosfils [2007]), which acts to destabilize the chamber and promote ring fracture formation. The second is to modulate the capture radius of the chamber, which upon shallowing exhibits a decrease, and then a sharp increase in the immediate vicinity of the free surface (Karlstrom et al. [2009]). For chambers surrounded by viscoelastic country rocks, both of these effects are time dependent.

This is illustrated in Figure 3.9, for choices of chamber size (R_1 = 1 km, R_2 = 2 km), depth (5 km), shell viscosity ($\nu = 10^{19}$ Pas) and overpressure (ΔP = 100 MPa) that emphasize the differences between this case and the symmetric overpressure solutions in an infinite medium. The free surface generally begins to affect normal stress concentration at the wall of an elastic chamber when the ratio of depth d to radius R satisfies $d/R < 3$ (Grosfils [2007]). However the time evolution of viscoelastic stresses (plotted in Figure 3.9.a as the first stress invariant) makes the surfaces effects more pronounced because the effective normal stress boundary conditions expand in time (Appendix B). The capture radius begins to be significantly affected at depths more shallow than 20 km for the small chambers we consider here (Figure 3.9.b).

Because of the added complexity of near-surface effects, and the complexity of the analytical half-space solution (equations 3.41-3.46), we leave a more complete parameter search of shallow chambers for future work. For the 20 and 40 km depth chambers, additional

stress concentrations due to free surface effects are less than 15 %, and would not change the results significantly. However, we have run a number of test cases at shallow depths to explore the general trends. Picking the same initial size and melt flux as in Figure 3.5, we find that the effect of decreasing depth is generally to inhibit the stable regimes of chamber growth. For example, a "wet" composition run using 1 km initial radius, 10^{-3} $m^3/m^2/yr$ melt flux (which is stable 20 and 40 km depths in Figure 3.6) enters an eruptive regime at 10 km depths. This is due to the stress concentration effects (easier to rupture a chamber) and the cool country rocks (higher shell viscosity, more solidification).

We anticipate that a more thorough study of these effects may have applications to the conditions for caldera-forming chambers, and to active shallow volcanic areas, where ground deformation measurements (e.g., Newman et al. [2001]) provide insight in to short-term chamber dynamics. Within the framework of our model, geodetic measurements may be inverted not only for chamber geometry and pressure, but for lower-crustal melt flux and dynamic regime (which bounds the active lifetime).

3.6 Discussion

Summary of model results

It will be useful in the following discussion to summarize model results in terms of the four dynamical processes of interest laid out in the introduction.

1. Rheological and stress evolution associated with long-lived high melt fraction systems in a geothermal temperature gradient.

   The development of a viscoelastic shell around magma chambers has a profound effect on their long-term dynamics. The ratio of elastic to viscoelastic timescales governs the relaxation of deviatoric stresses that prevents chamber rupture. By coupling this process to the thermal evolution of a magma chamber, and to particular parameterizations of rock composition, we find that such temperature-induced rheological changes are strong functions of the local geotherm and composition. Deeper chambers and chambers surrounded by more felsic country rocks generally have the greatest rheological impact on their surroundings.

2. Average compositional evolution of the magma chamber and assimilation of country rock.

   In our simplified treatment of magma chamber processes, we are unable to address the details of compositional evolution within the chamber (e.g. Gerya et al. [2004]). However, we do address crustal assimilation, and find that melting of country rocks

by magma chambers is a strong function of their composition and water contents. We find assimilated tonalitic country rock of up to $\sim$ 70% the total chamber volume in "runaway growth" chambers (Figure 3.8). Amphibolitic end member chambers, on the other hand, assimilate up to 50 % by volume country rock only in the "stable" regime. We note that these are the extreme values of crustal melting that are achieved over long periods of continued enthalpy supply without eruption. "Freezing" or "eruptive" chambers rarely assimilate more than a few percent by volume of country rock (Figure 3.8), which may be considered to be more average.

3. Stability of the system: will the magma chamber rupture, freeze, or exist in dynamic equilibrium within the crust for the lifetime of constant melt supply?

   The stability of magma chambers is governed primarily by lower crustal melt supply (3.6). Melt flux smaller than $\sim 10^{-4}$m^3/m^2/yr does not transport enough enthalpy to thermally sustain magma chambers, and these chambers freeze in all cases. The range of stable chambers is a function of depth and composition, but encompasses melt fluxes consistent with the upper estimates of melt flux in arc settings ($\sim 10^{-3}$ m^3/m^2/yr, which is also comparable to the average melt flux per kilometer of mid-ocean ridge, e.g., Chen [1996]). We emphasize that a more three dimensional treatment of this problem will almost certainly decrease this stable range of melt flux, because chambers will both lose more heat via conduction and focus rising melt more efficiently in three dimensions. Chamber eruption is found for melt flux exceeding 10^{-1} m^3/m^2/yr in most cases, however, deep chambers with an initially large size are less sensitive to large melt influx, and may be in the "runaway growth" regime for melt fluxes of this magnitude. Mantle plume-scale melt flux may therefore, in principle, sustain rapid but stable growth of deep-seated magma chambers, and magmatic lensing provides one mechanism by which large radiating dike swarms associated with these features (Ernst et al. [1995]) might be emplaced.

4. The possibility for large-scale growth of a high melt fraction reservoir.

   The "runaway growth" regime of magma chambers depends critically on both a sufficiently high melt flux, and a shell viscosity that remains low enough to relax the large stresses generated by this melt influx. Runaway growth, therefore, depends greatly on depth and composition. Magma chambers in tonalitic country rocks are more prone to this behavior, but large scale growth occurs for some range of parameters in all of the depths and compositions tested in this study. This growth may occur very rapidly, with 100-fold volumetric increases in 100 ka, but will likely be shut off by shell viscosities that can no longer relax chamber stresses.

Application to Terrestrial magmatic systems

The construction of large igneous intrusions in the Earth's crust has been argued to result from either diapir-dominated or dike-dominated transport processes (Petford [1996], Miller and Paterson [1999]). We assume here that the latter is more realistic, although the two may share significant similarities, and base our arguments on 1) the short dike rise timescale compared to the Stokes velocity of a melt diapir in the crust, and 2) the mechanism of magmatic lensing, whereby a stalled pressurizing inclusion of melt may focus rising melt to attain a large volume. There is considerable field evidence to support dike transport of melt in middle to lower crustal terrains (e.g., Jagoutz et al. [2006], Dumond et al. [2007]), but kilometer scale viscous advective processes have also been inferred (e.g., Zak and Paterson [2005]). While we cannot hope to address specific field observations and analytical studies directly with the simplified modeling framework presented here, general features of magmatic transport processes and timescales may be constrained.

Predictions of our model include chamber growth rates, bulk assimilation of crustal rocks, and constraints on lower crustal melt flux needed to produce stable and/or large chambers. The broad dynamical regimes of chamber evolution that result are physically general, and should translate to real intrusions. In this framework, it is interesting to ask whether various classes of intrusion (e.g., calderas, plutons, layered mafic intrusions) might be differentiated by dynamic regime alone. In addition, we would like to point out some specific measurements of transport processes that our modeling addresses.

Caldera-forming chambers

Calderas are the best geologic evidence for large (up to ~ 100 km scale) high melt fraction crustal magma chambers, and are the center of much controversy regarding spatiotemporal pluton-volcano connections (e.g., Lipman [2007], Glazner et al. [2008]). While there are many complementary ways to approach this problem, remote sensing of deformation in calderas provides important constraints on processes that are difficult to obtain from the rock record. For example, Newman et al. [2001] model surface deformation at Long Valley caldera assuming inflation is due to an inflating shallow magma chamber with a viscoelastic shell. They infer a shell viscosity ($\sim 10^{16}$ Pa s) that is much lower (and perhaps more realistic) than our estimated bound on wall-rock viscosity ($\sim 10^{19}$ Pa s, Appendix B), especially for shallow chambers in a normal geotherm. Our modeling indicates that the size of viscoelastic shell is composition- and depth-dependent, with $1 \leq R_2/R_1 \leq 2$ for tonalitic country rocks, and $1 \leq R_2/R_1 \leq 1.5$ for amphibolite in deeper chambers, and generally very small for 5-10 km deep chambers. In fact, because shallow stable or runaway chambers are very difficult to achieve in a "normal" geotherm, we suspect that the crust must be pre-warmed to form large, high melt fraction bodies in the shallow crust.

Because constant magma addition increases chamber overpressure to values that approach lithostatic in a purely elastic model, rupture will occur unless chamber stresses are relaxed. Indeed, as demonstrated in Figure 3.10, the use of purely elastic pressurization as a proxy

for magma chamber dynamics both results in unrealistically large overpressure and misses important time-dependent dynamics (Results section). We note that the "runaway growth' regime of magmatic lensing accommodates chamber growth in $10^5 - 10^6$ year, which is similar to the range of timescales postulated in other studies of caldera-forming eruptions (e.g., Hanson and Glazner [1995], Bachmann and Bergantz [2003], Simon et al. [2008]). Caldera roof collapse depends on the concentration of deviatoric stresses and the development of ring fractures (e.g., Gudmundsson [1988]). If the wall rocks are viscoelastic (equations 3.41-3.46, Figure 3.12) the concentration of these stresses occurs only after ~ 1 Maxwell time, suggesting a lag between melt pressurization and collapse in caldera-forming eruptions.

Hughes and Mahood [2008] compile a database of calderas around the Pacific Rim, finding that calderas are typically found in regions of local compressive tectonic stresses. This may be explained through consideration of the mechanical aspects of magmatic lensing (Karlstrom et al. [2009]), whereby the capture radius of the chamber (and therefore the incoming melt flux) is increased with background compressive stresses. As pointed out by Jellinek and DePaolo [2003], extensional stresses promote storage of an already-existing magma chamber by providing strain to accommodate melt influx and decrease chamber overpressures. However, for small chambers, extension also serves to shut off the magmatic lensing mechanism by creating more horizontally oriented least compressive stresses and decreasing the capture radius of the chamber. This will inhibit the interaction of rising dikes with already-existing magma chambers. Hence it is possible that local tectonic extension may both inhibit the growth of small magma chambers and promote the stability of larger ones.

Plutons and Layered Mafic Intrusions

Recent detailed geochronology indicates that some (and perhaps most) intrusive suites have crystallization histories of several million years (e.g., the Tuolomne Intrusive Suite and Mt. Stuart Batholith, Miller et al. [2007]), and individual plutons may have been constructed over 1 Ma (Coleman et al. [2004]). In the Sierra Nevada Batholith, plutons were emplaced at depths ranging from 5 km in the East (e.g. the Bridgeport "Low P" zone) to > 25 km in the South and Southwest (Ague and Brimhall [1988], Pickett and Saleeby [1993]). If we use directly modern estimates for arc melt flux as a proxy for melt flux at the time of emplacement of the Sierra Nevada Batholith, and assume intrusion depths of 20 km we find that it is indeed possible to achieve chambers in the stable equilibrium or freezing regimes (Figure 3.6). Based on this evidence, it does appear possible that 1-10 km scale chambers could in principle exist at high melt fraction for extended periods (≥ 1 Ma). If the crust were prewarmed by previous episodes of intrusion, stable chambers (perhaps caldera-forming de Silva and Gosnold [2007]) would be more likely in the shallow crust.

Particular examples of well-exposed pluton-country rock contacts in the Sierra Nevada offer other field evidence for the dynamic regimes of chamber growth. For example, the Jackass Pass pluton (McNulty et al. [1996]) displays structural evidence for dike-assembled magma chambers and for ductile creep that would imply a rheological gradient at the chamber margin. Distinct absence of ductile flow markers and a sharp pluton-wall rock contact in

the Piute Meadow (Albertz [2005]) pendant could be the result of a rapidly freezing intrusion, or chambers in a "runaway growth" or "eruptive" regime that expand without forming a viscoelastic shell. On the other hand, observations of increasing strain intensities toward the pluton in the Saddlebag Lake pendant (Albertz [2005]) are consistent with the development of rheological gradients. It seems clear that pluton assemblage is a complex and variable process, and that relic batholithic structures represent time-integrated portraits of multiple chambers in different dynamical regimes, associated with different and discrete volcanic centers, as high precision dating of plutons (Matzel et al. [2006]) and possible analog volcanic systems (de Silva and Gosnold [2007]) are beginning to suggest.

Layered Mafic Intrusions found in predominantly cratonic settings form another class of intrusions with which to compare our model. Based on estimates of total volume and emplacement time, Cawthorn and Walraven [1998] estimate that the Bushveld complex (total volume $\sim 10^6$ km^3) filled at an average rate of $9 - 15$ km^3/yr, and suggest that eruptive removal of magma is required in order to fit the estimated cooling rates. By extrapolation to 2D using a spatial dimension of 100 km for the Bushveld, this volumetric influx rate is comparable to the highest melt fluxes that we model (10^0 m^3/m^2/yr), which are an estimate of mantle plume melt rates (Farnetani and Richards [1995]). This is a possible source for Bushveld melt (Hatton [1995]). Geobarometry on pelitic gneiss suggests that the depth of crystallization for at least part of the Bushveld Complex was $\sim$ 20 km (Stevens et al. [1997], Johnson et al. [2003]), though others have argued, based on geochemical evidence, for a deeper-seated "staging chamber" (e.g. Harris et al. [2005]). Extensive isotopic analyses (e.g., Harris et al. [2005], Majer et al. [2000], Kruger [2005]) also suggest significant crustal assimilation, which may have reached upwards of 40 % of the total melt volume (Harris et al. [2005]).

Based on these observations, we speculate that the Bushveld magma chamber may have been in the "runaway growth" regime of our model. Leucosomes and migmatitic textures Johnson et al. [2003] extend orthogonally into the country rocks $400 - 700$ m from the intrusion, suggesting a lower bound to the viscoelastic shell around the chamber. If these estimates of shell thickness are correct and representative (even within an order of magnitude), this implies a very thin thermally altered region (less than 1 % of the Bushvelds North-South extent), and hence very rapid emplacement. Detailed thermal modeling of phase equilibria for the aureole beneath the Bushveld Complex (Johnson et al. [2003]) result in a melt fraction-temperature parameterization that most qualitatively matches our tonalite curve for the range of melt fractions modeled in that study (≤ 0.3 volume fraction melt). Crustal assimilation similar to the 40 % inferred for the Bushveld is quite possible in our model (Figure 3.8), though we again stress that this is a qualitative comparison, as in particular our chamber geometry is highly idealized. If the Bushveld Complex represents a "runaway growth" regime magma chamber, the rapid emplacement of such a high volume chamber in the mid crust is quite possible in $\sim$ 75 ka (Cawthorn and Walraven [1998]), and chamber rupture is an inferred consequence of this mode of emplacement.

Conclusion

Within the conceptual model developed here, we have shown that (1) there are four distinct dynamical regimes for chamber gowth: long-lived ($\geq$ 1 Ma) and thermally viable magma chambers are possible at a range of depths, as are thermally viable chambers that can rapidly grow, (2) viscoelastic properties of the coupled chamber/country rock system can "shut off" as well as "turn on" chamber rupture, and (3) magma chambers may assimilate a range of crustal rocks, depending on the dynamical regime. While most chambers in eruptive or freezing regimes will not assimilate more than a few percent by volume of crust, a narrow range of dynamically stable chambers may assimilate $> 60\%$ by volume of the surrounding crust if the crust is relatively evolved and dry, and up to $\sim 40\%$ by volume for "wet" magma within amphibolitic country rock. These percentages are relative to the amount of melt reaching the chamber, and should not be necessarily considered to represent the bulk assimilated fraction of crustal melt, nor necessarily a firm characteristic of all long-lived chambers.

Comparison of our models to realistic systems are largely speculative at this stage, however we believe that highly disparate intrusive structures may be reasonably cast into a framework of dike-fed magma chamber growth. Our approach suggests that differences in magmatic intrusions worldwide are due to differences in local physical parameters and not physical processes. Lower crustal melt flux is the most important of these parameters, and this likely determines the overall stability and size of a given intrusion. However, crustal composition, background stresses and depth of emplacement are also important and may strongly modulate chamber behavior. In particular, the influence of tectonics will strongly affect the rise of magma through the crust, and indeed forms much of the framework for our understanding of volcanism generally (e.g., Canon-Tapia and Walker [2004]). Likewise, interactions between magma chambers, dikes and multiphase fluid processes are ultimately responsible for surface volcanism, and a better characterization of topological evolution of the system will further our ability to link the rock record and other time-integrated evidence to magma transport physics.

3.7 Appendix

Viscoelastic chamber stresses

We solve the equilibrium equations of Linear Elasticity (e.g., Fung [1965]),

$$\nabla^2 \mathbf{u} + \frac{1}{1 - 2\nu_{1,2}} \nabla(\nabla \cdot \mathbf{u}) = 0 \tag{3.11}$$

where $\mathbf{u}$ are the vector elastic displacements, and $\nu_{1,2}$ is Poisson's ratio for the shell ($\nu_1 = 0.4$, to account for the presence of partial melt) and the country rocks ($\nu_2 = 0.25$). We assume that the Young's moduli inside and outside the shell are equal, $E = 70$ GPa. Subject to

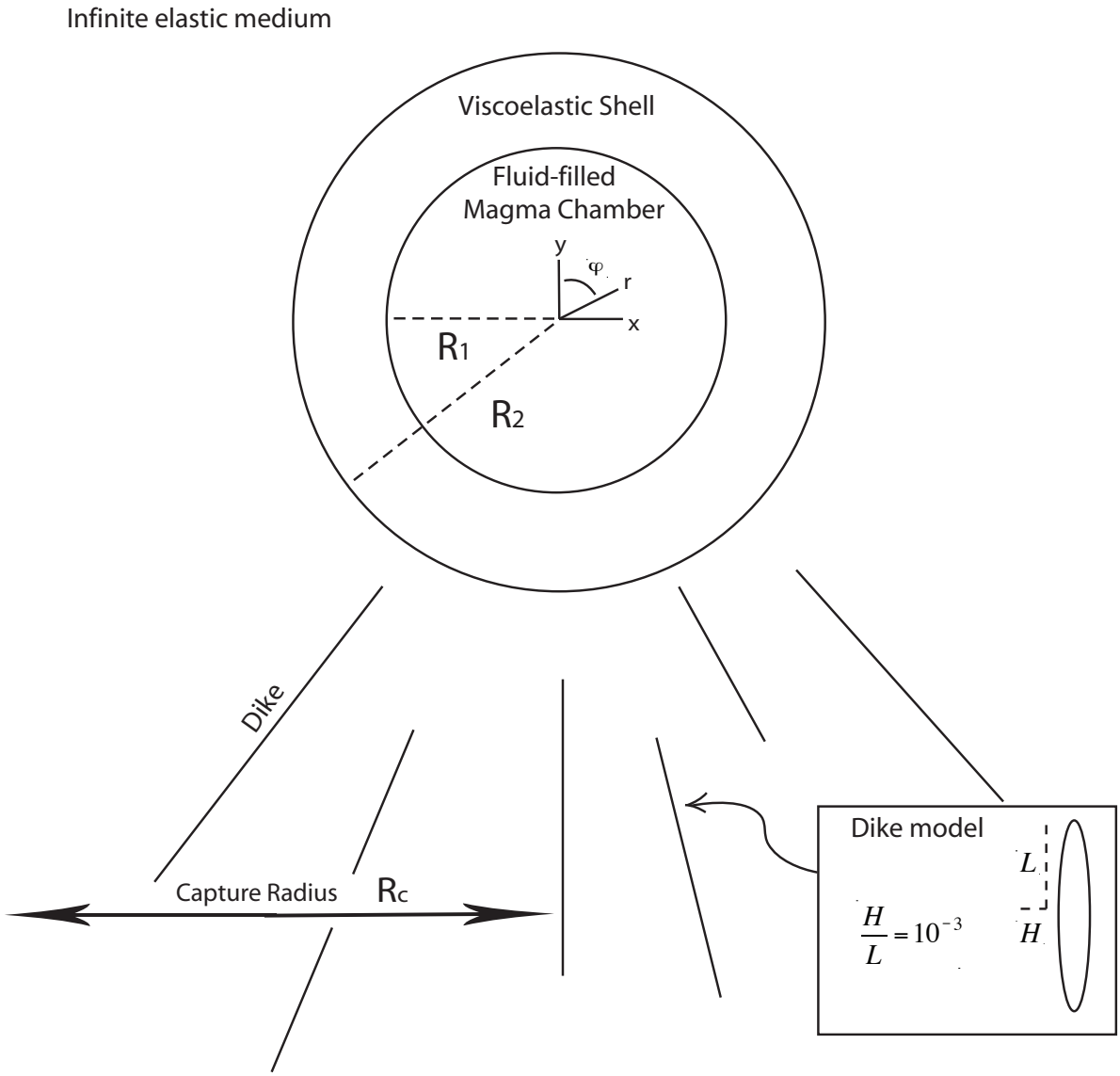

Figure 3.1: The model problem, with a radial coordinate system centered on the cylindrical chamber. The magma chamber consists of a high melt fraction interior ($r \leq R_1$), and a viscoelastic shell ($R_1 \leq r \leq R_2$) that is overpressured and buoyant with respect to the surrounding elastic country rock. Dikes, modeled as uniformly pressurized ellipses with aspect ratio $h/l = 10^{-3}$, are focused toward the chamber from a region defined by the deviatoric stresses exerted by the chamber. This "capture radius" defines the magmatic lensing mechanism (Karlstrom et al. [2009]).

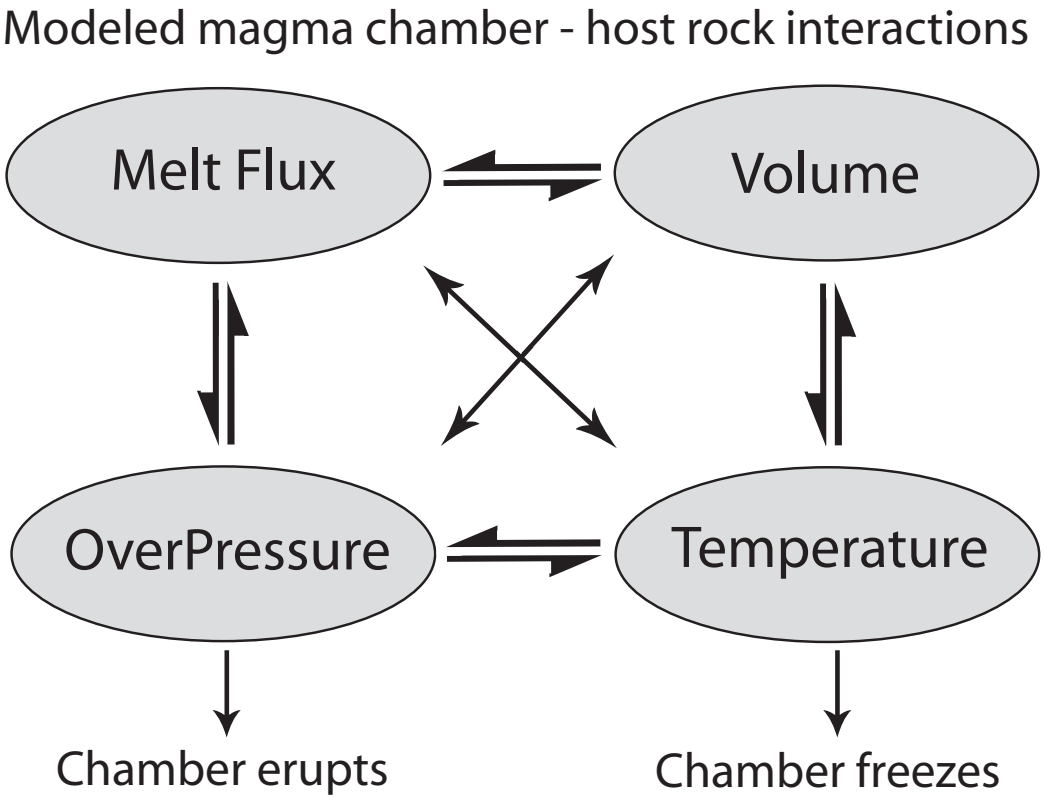

Figure 3.2: Possible interactions in the coupled thermal and mechanical model. Feedbacks between melt influx, pressurization and phase change are responsible for the end member dynamical regimes: freezing and erupting chambers. Balance of these competing effects results in stable chambers.

boundary conditions in equations (3.1) - (3.4), we use the method of stress functions for which a general solution to the equilibrium equations in polar coordinates (r, ϕ) exists (Fung [1965]). Taking care to avoid multiple-valued displacements, stresses inside the viscoelastic shell are

$$\sigma_{rr,in}(r,\phi) = \bar{A}_1 - \frac{\bar{B}_1}{r^2} + \left(\frac{\bar{C}_1(2\nu_1 - 3)}{r} - \frac{\bar{D}_1}{r^3} + 8\bar{E}_1 r\right)\cos(\phi) \tag{3.12}$$

$$\sigma_{\phi\phi,in}(r,\phi) = \bar{A}_1 + \frac{\bar{B}_1}{r^2} + \left(\frac{\bar{C}_1(1 - 2\nu_1)}{r} + \frac{\bar{D}_1}{r^3} + 24E_1 r\right)\cos(\phi) \tag{3.13}$$

$$\sigma_{r\phi,in}(r,\phi) = \left(\frac{\bar{C}_1(1 - 2\nu_1)}{r} - \frac{\bar{D}_1}{r^3} + 8\bar{E}_1 r\right)\sin(\phi) \tag{3.14}$$

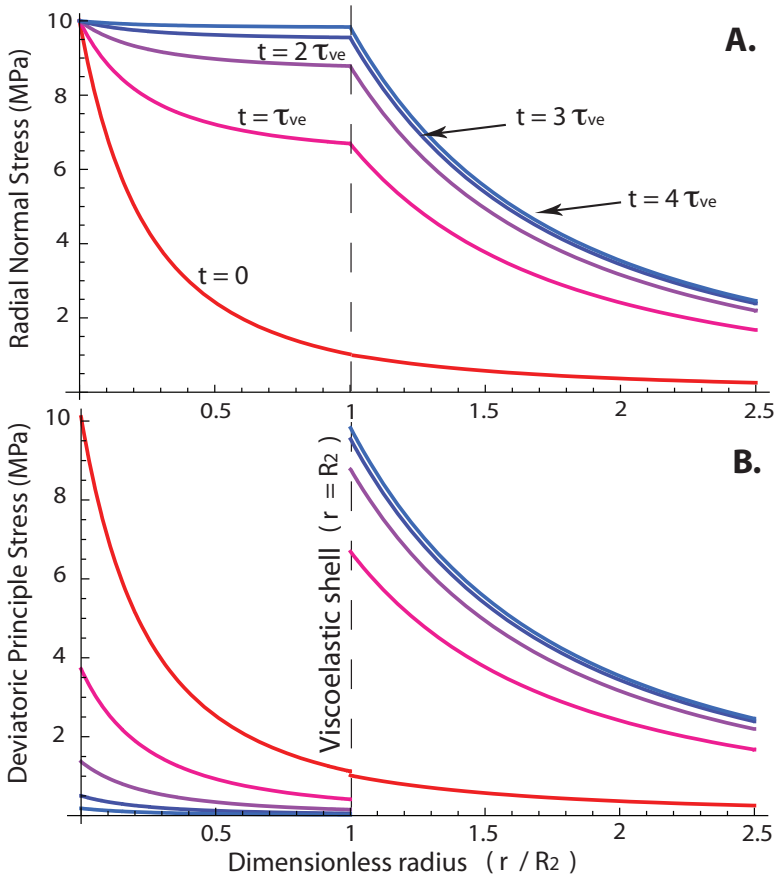

Figure 3.3: (a) Time evolution of the infinite space radial normal stress σ_{rr} (Appendix A) outside the magma chamber. The viscoelastic shell acts to propagate inner boundary conditions toward the edge of the shell in time. Curves are multiples of the maxwell time of a chamber with shell viscosity of 10^{19} Pas. (b) Time evolution of greatest principle deviatoric stress outside the magma chamber. Deviatoric stresses inside the viscoelastic shell relax in time (but see Appendix A for differences between overpressure, buoyancy, and half-space solutions in this regard), while deviatoric stresses in the surrounding elastic medium increase.

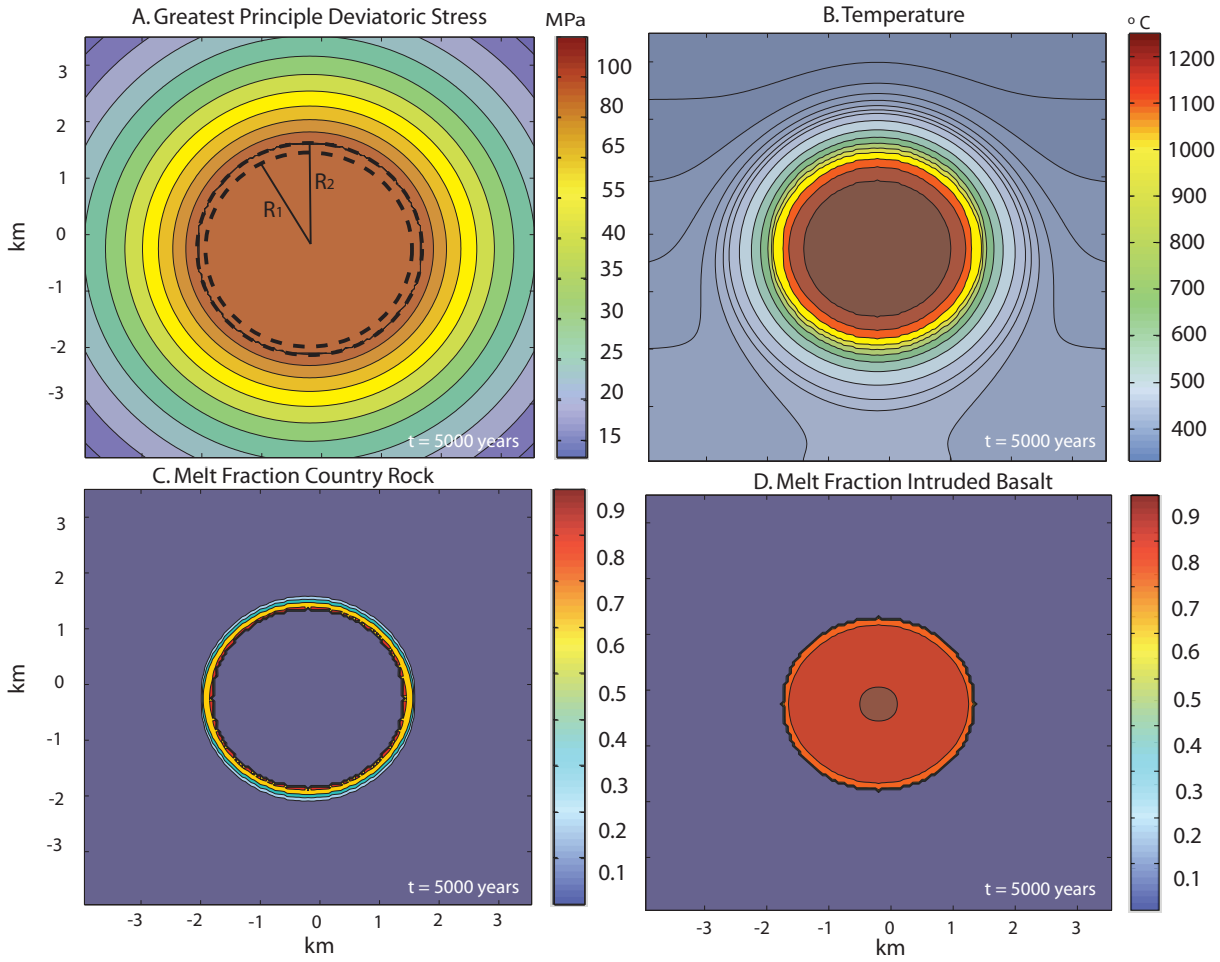

Figure 3.4: 5000 years into the evolution of a 1 km initial radius chamber at 40 km depth. The intruding basalt is hydrous, the country rock is amphibolite, and the chamber is in a "stable" dynamic regime. Distance scale is the same in all panels and represent half the total numerical domain of the calculation. (a) Maximum principle deviatoric stresses around the chamber. Focused dikes propagate orthogonal to plotted contours. The threshold stress of 1 MPa occurs outside the panel window. (b) Temperature field. An initially static geotherm is perturbed by the presence of a hot chamber, resulting in 'reverse' temperature gradients near the bottom of the chamber. (c) Fraction of country rock melt around magma chamber, showing circular binning of melt around chamber. (d) Fraction of intruded basaltic melt.

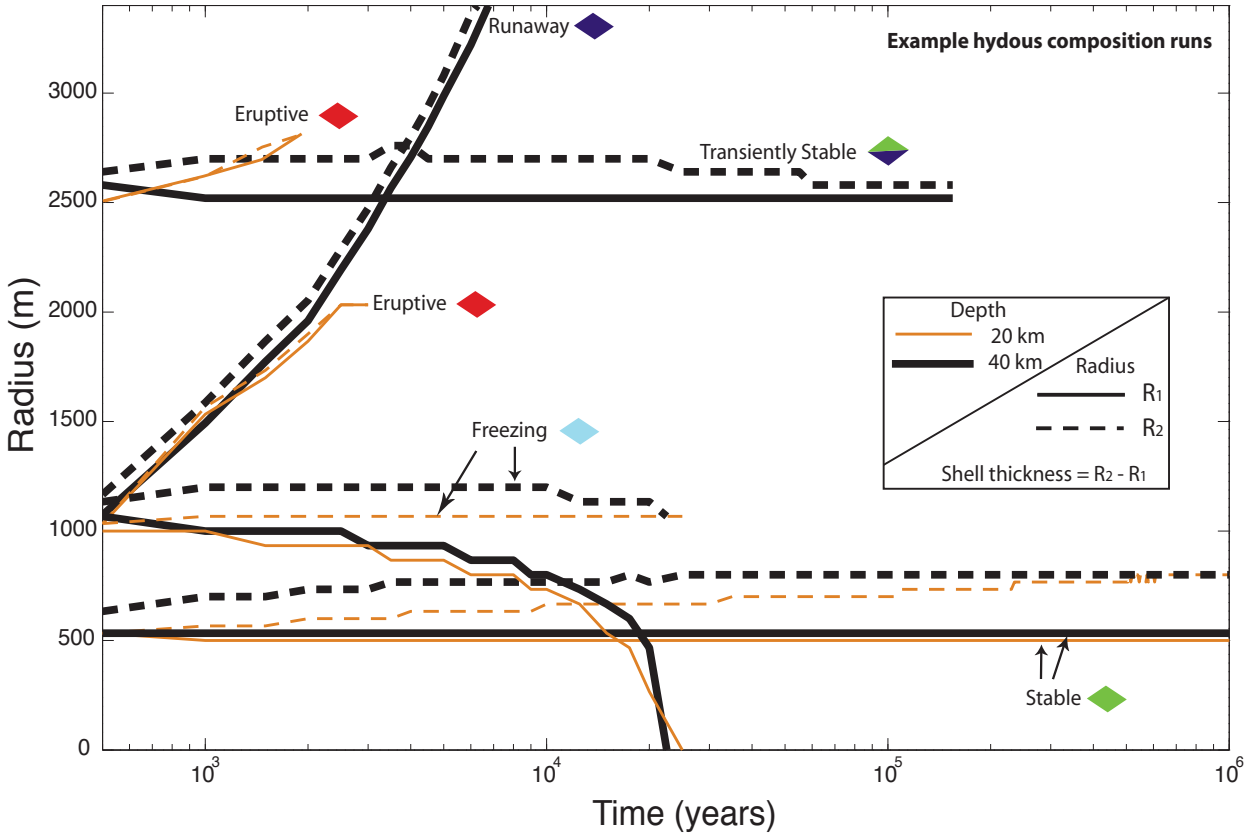

Figure 3.5: Time evolution of inner and outer chamber radii (R_1 and R_2 in figure 3.1) for selected pairs of "wet" composition runs at 20 and 40 km depths (circled in Figure 3.6). Growth of a viscoelastic shell ($R_2 - R_1 > 0$) is necessary for chamber stability, and chambers in the "eruptive" regime often expand more quickly than this can occur. 40 km deep chambers (thick as opposed to thin lines) grow viscoelastic shells more quickly than their 20 km depth counterparts. Labels indicate dynamic regime.

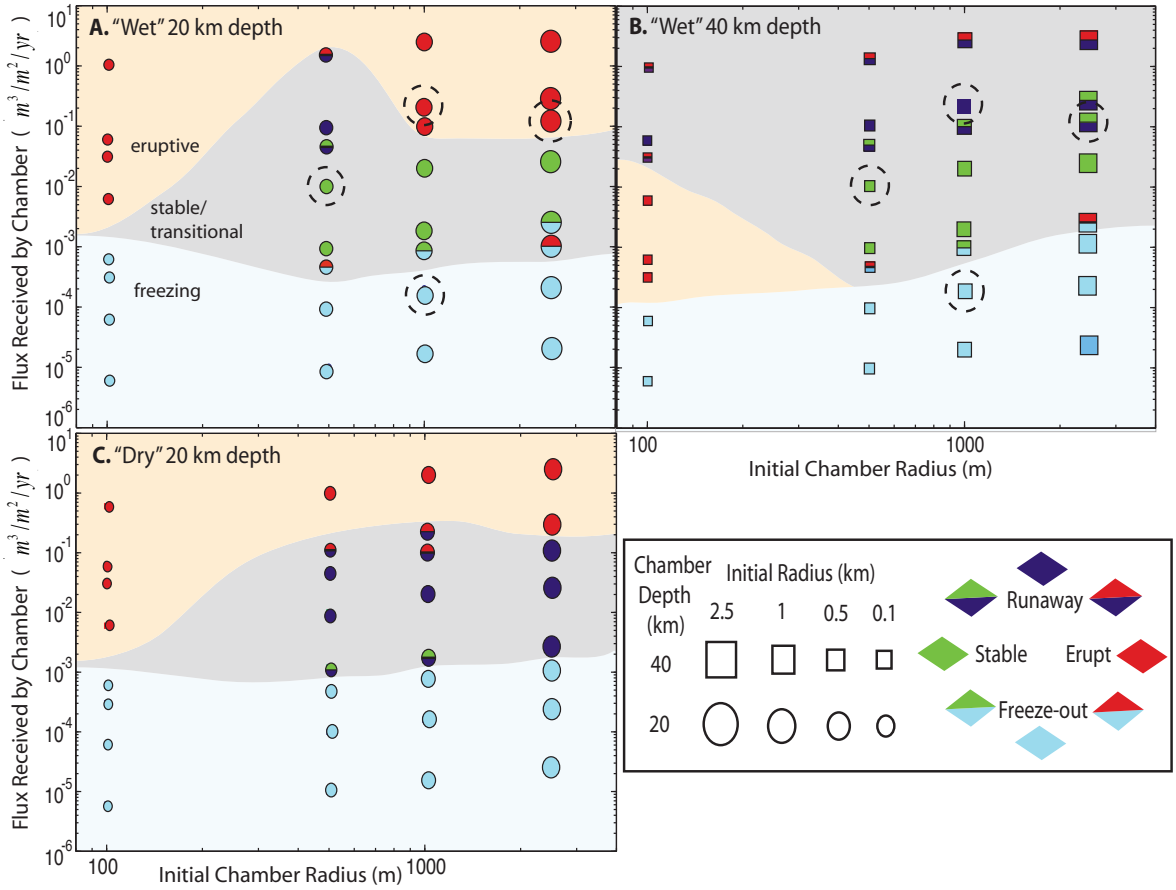

Figure 3.6: Stability field representation of the parameter space, with initial chamber volume plotted against lower crustal melt flux. (a) 20 km depth "wet" chambers. (b) 40 km depth "wet" chambers. c) 20 km "dry" chambers. Solid colors represent results in which one dynamical regime dominates, while two-toned points represent runs in which the outcome was influenced by two interacting processes or was run-dependent (due to the stochastic simulations). These two-toned points sample the transitional states of the system, where competing physical processes are balanced. Circled points are plotted in Figure 3.5, while shaded regions sketch qualitative boundaries between eruptive, stable/transitional and freezing regimes.

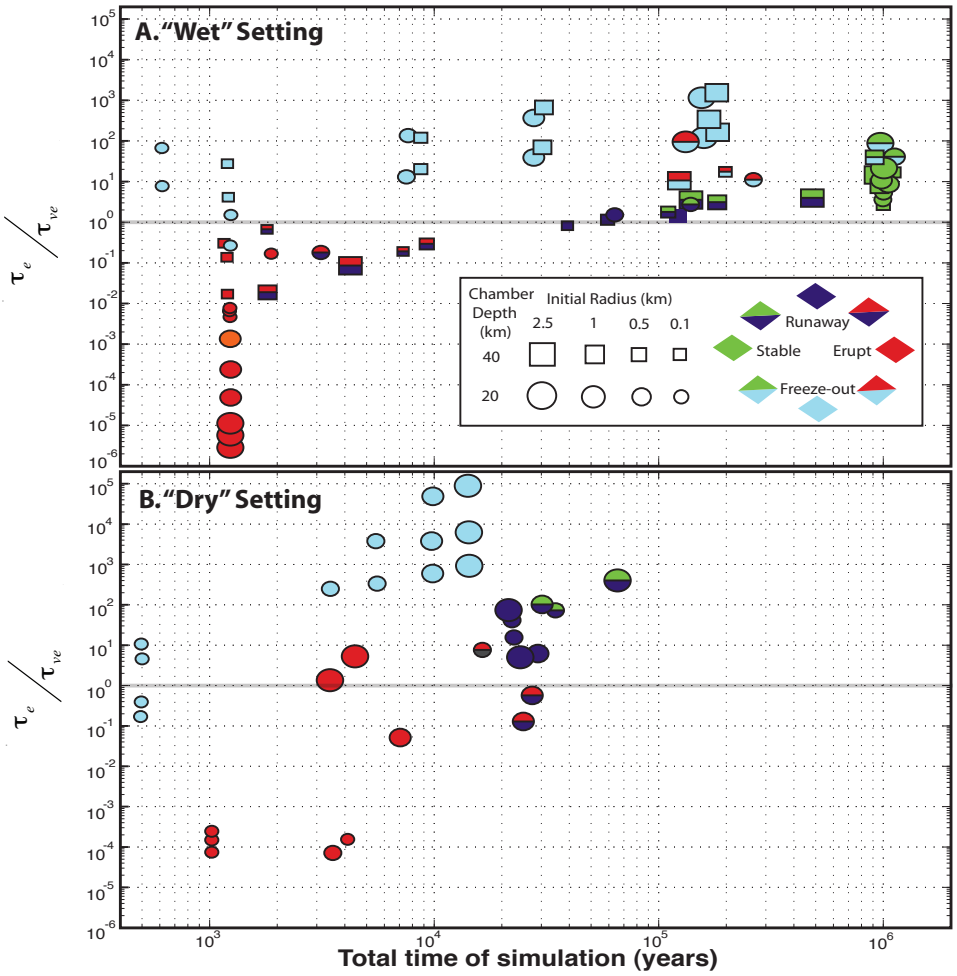

Figure 3.7: Stability field representation of the parameter space, in terms of dimensionless physical timescales. The system's thermal stability (total run time) is plotted against a ratio of the chamber's average elastic (τ_e) and viscolelastic (τ_{ve}) timescales (Table 3.1). Chambers in different dynamical regimes (defined in the legend) separate in this representation. This indicating that rheology and long-term stability are strongly coupled with a major dynamical transition occurring when $\tau_e/\tau_{ve} \sim 1$ (marked with a thick grey line), with deviations a result of the different nonlinear melt fraction curves (Appendix B). (a) Hydrous "arc" setting runs (64 total). (b) Anhydrous "continental" setting runs (32 total).

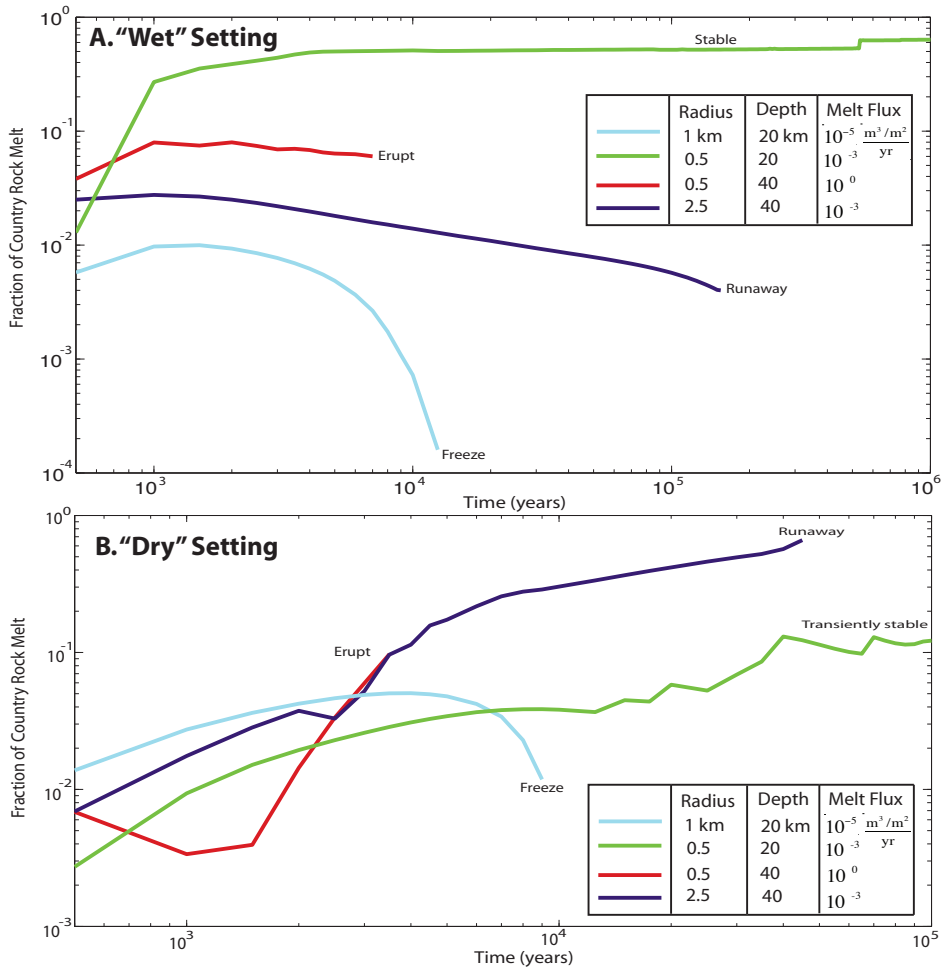

Figure 3.8: (a) Four examples from hydrous "arc" setting runs, to illustrate the degree of crustal anatexis and assimilation associated with each dynamical regime. Maximum country rock melt for this compositional suite occurs for chambers that are in the "stable equilibrium" regime, and is $\sim 40 - 50\%$ of the liquid chamber volume. (b) The same examples, but from anhydrous "continental" setting runs. In this case, much more melting and assimilation can occur (see melt fraction curves equations 3.58 - 3.62), especially in the "runaway growth" regime. These chambers may assimilate up to $\sim 60 - 70\%$ by volume crustal melt.

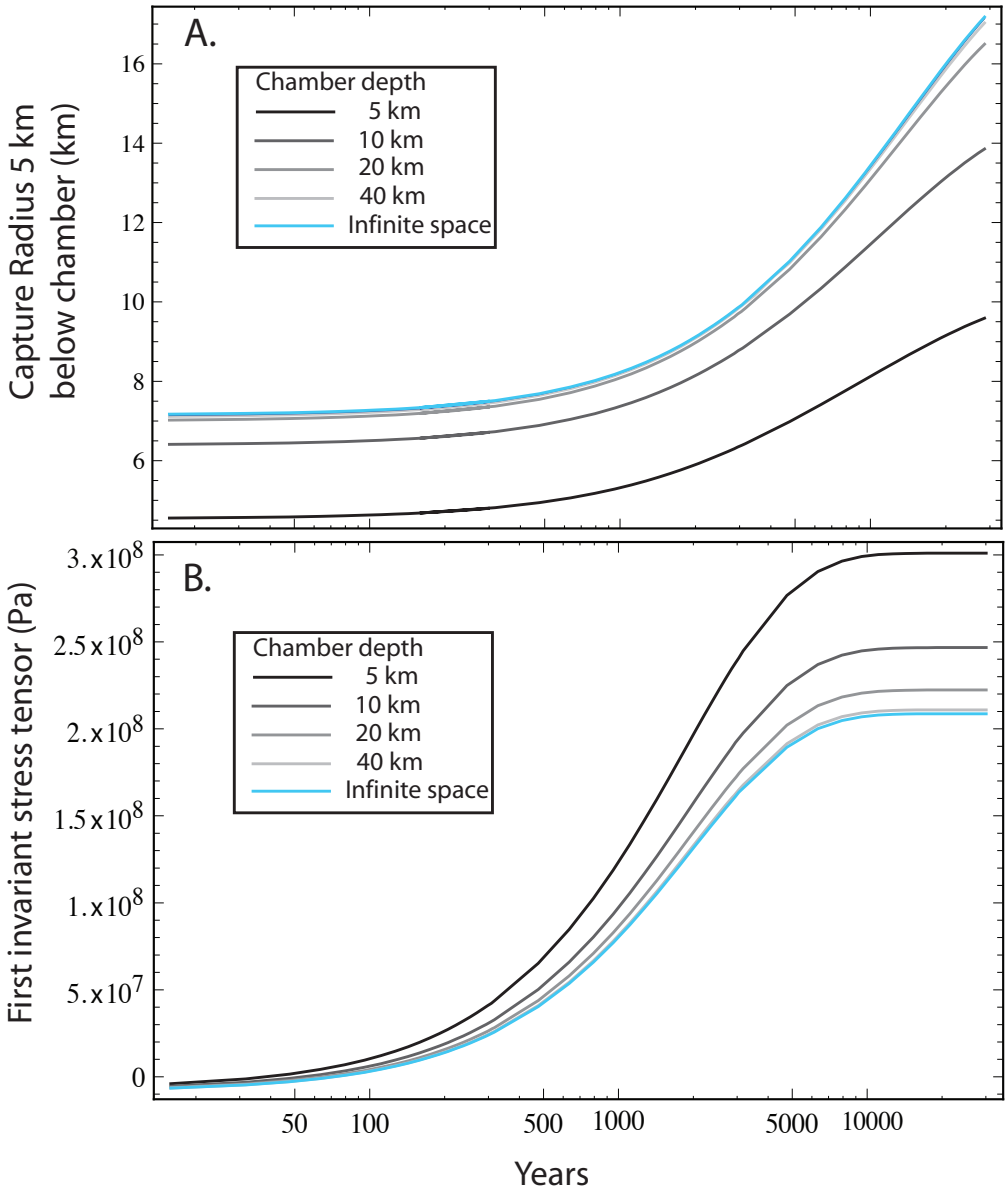

Figure 3.9: (a) Time evolution of capture radius (Figure 3.1)for chambers at different depths. Note that the capture radius increases in time due to viscous creep in the shell, and that the half space solutions approach the infinite space solution as depth increases. (b) Time evolution of the maximum first invariant of the stress tensor evaluated at R_1, comparing normal stresses between the half space and infinite space solutions in a coordinate-independent way. Normal stresses around shallow chambers are markedly higher in magnitude than deep chambers, and we note that the position of maximum stress on the boundary R_1 shifts with depth as well (Grosfils [2007]).

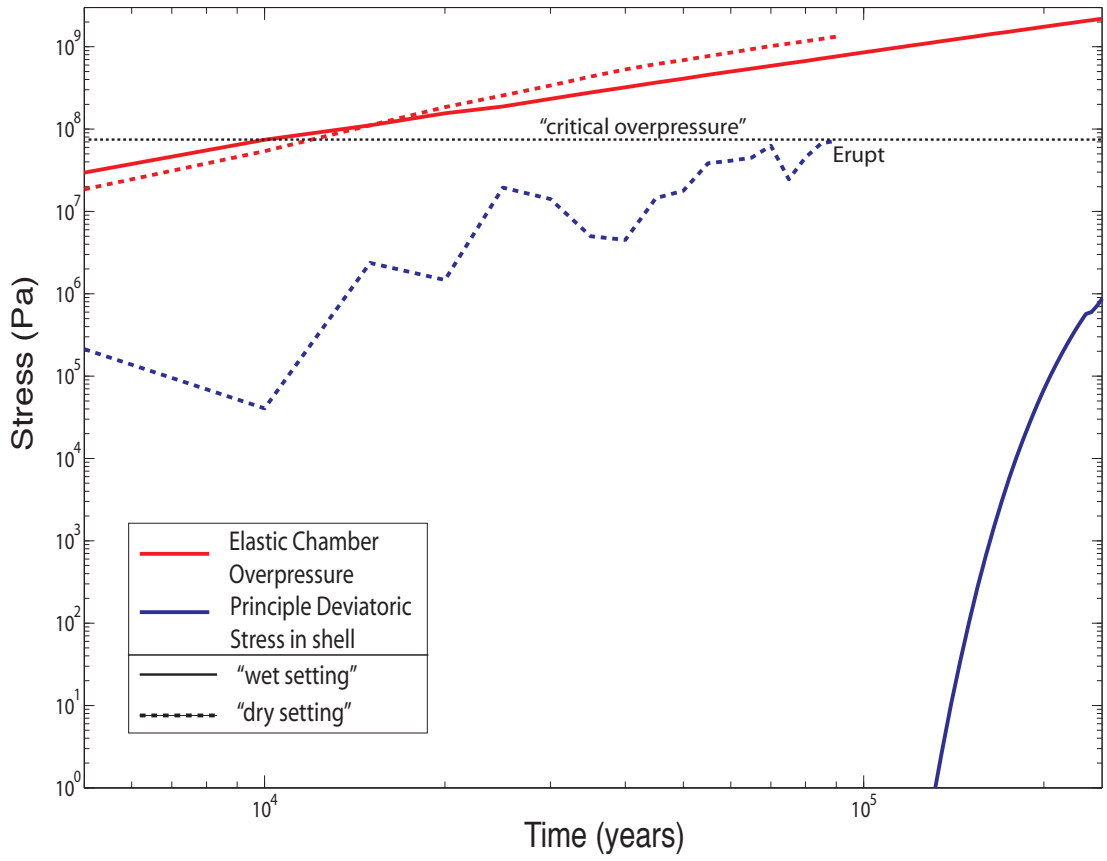

Figure 3.10: Example time evolution of principle deviatoric stresses in the viscoelastic shell and "elastic" stresses for two chambers. Elastic stresses are presented for reference only, and are not used in our model. Composition is the only difference between the two cases, which begin with radii of 2.5 km and depths of 20 km. Variations in deviatoric stress for the "dry" setting run (dashed blue line) in part reflect the stochastic input of melt and enthalpy from dikes. These contributions may be negative (positive) for net chamber solidification (melting). The "wet" setting run gradually builds up deviatoric stresses over the course of the run, and thus represents a "runaway growth" regime.

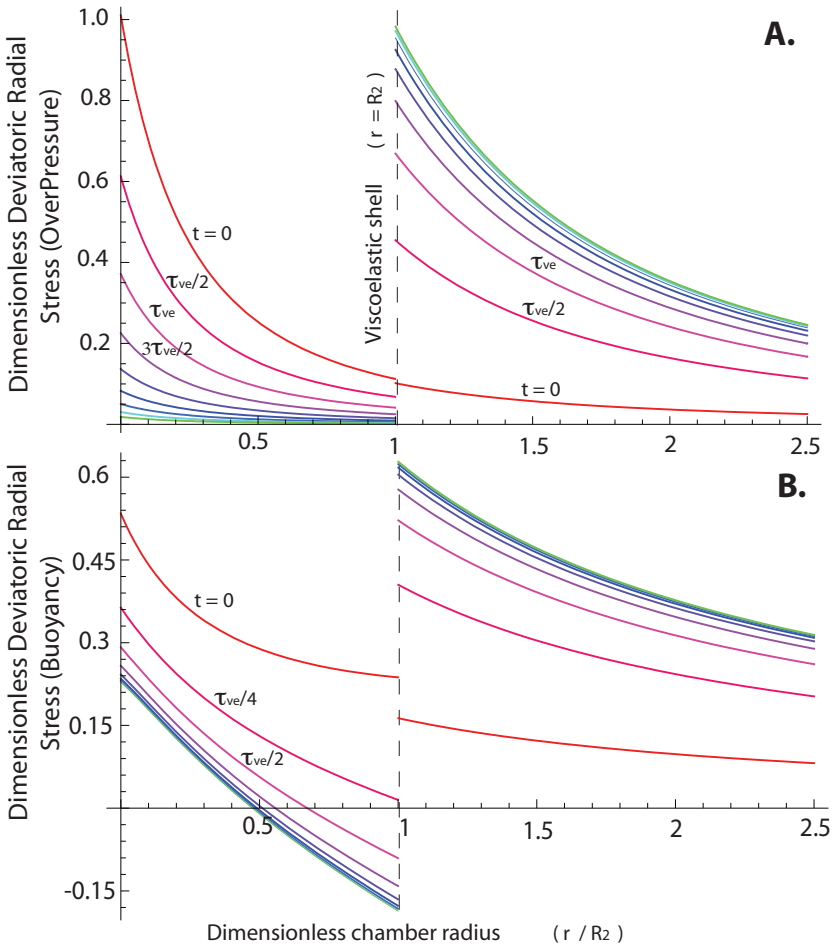

Figure 3.11: (a) Time evolution of greatest principle deviatoric stresses around a circular overpressured chamber in an infinite space (equations 3.12-3.17). Colored curves indicate time in increments of one half the Maxwell time ($\tau_{ve}/2$, Table 3.1), for a shell viscosity of 10^{19} Pas. (b) Time evolution of deviatoric stresses around a buoyant circular chamber. In this case, asymmetry in the boundary conditions induces incomplete relaxation of deviatoric stresses in the shell. Colored curves are time in increments of $\tau_{ve}/4$. Stresses in this case are evaluated at the top of the chamber $\phi = 0$ (the angle of maximum stress maximum for infinite space solutions of positive buoyancy). Normal stress boundary conditions are normalized to one in both panels.

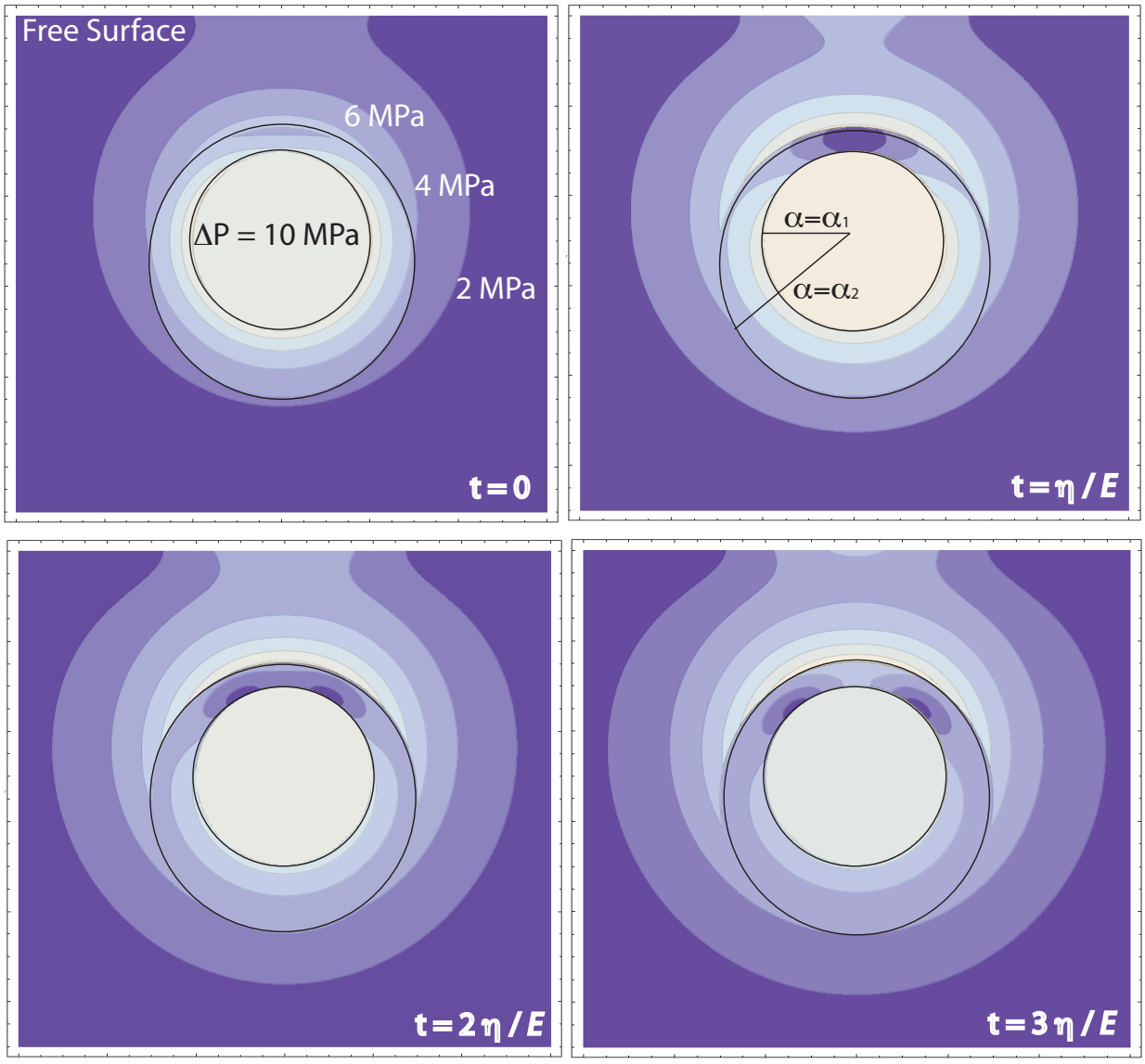

Figure 3.12: Time evolution of greatest principle deviatoric stress field in the half-space solutions (equations 3.41-3.46). Chamber depth is 5 km, $R_1 = 2$ km, $R_2 = 3$ km (equation 3.38), panel sizes are 12 km wide and 11 km high, with the stress free surface at the top. The up-down asymmetry in shell thickness is a feature of the bipolar coordinate system used to obtain the analytic solution, plotted here in cartesian coordinates. Overpressure is set to 10 MPa, and stress contours are 2 MPa apart. Time between panels is multiples of the "Maxwell Time" η_{wr}/E, where η_{wr} is the shell viscosity, and E is Young's Modulus. Note the topological change from one minima to two in the shell as deviatoric stresses are relaxed. This is a result of shear stresses induced on the chamber by the free surface.

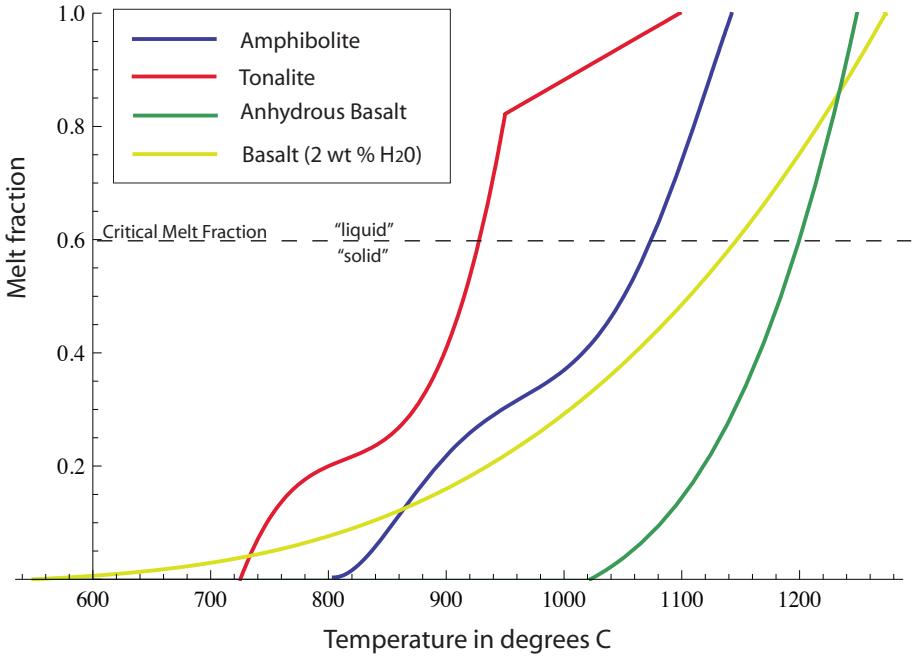

Figure 3.13: Meltfraction vs. temperature curves used in this study. We use a piecewise continuous curve for tonalite that better represents melting of biotite at low melt fractions. Higher melt fractions are less well constrained experimentally, and hence do not warrant a more detailed fit. Note that these curves are paramaterizations of melting experiments on "generic" but independent samples.

and outside the shell, in the assumed elastic medium

$$\sigma_{rr,out}(r,\phi) = \frac{\bar{B}_2}{r^2} + \frac{\bar{C}_2(2\nu_2 - 3)\cos(\phi)}{r} \tag{3.15}$$

$$\sigma_{\phi\phi,out}(r,\phi) = -\frac{\bar{B}_2}{r^2} + \frac{\bar{C}_2(1 - 2\nu_2)\cos(\phi)}{r} \tag{3.16}$$

$$\sigma_{r\phi,out}(r,\phi) = -\frac{\bar{C}_2(1 - 2\nu_2)\sin(\phi)}{r}. \tag{3.17}$$

Here $\bar{A}_1, \bar{B}_1, \bar{C}_1, \bar{D}_1, \bar{E}_1, \bar{B}_2, \bar{C}_2$ are constants evaluated to satisfy the boundary conditions, equations 3.1-3.4, and are found to be

$$\bar{A}_1 = \left(\Delta P(\nu_2 - \nu_1)R_1^2\right)/\mathcal{D} \tag{3.18}$$

$$\bar{B}_1 = \left(\Delta P R_1^2 R_2^2(-2 + \nu_1 + 2\nu_2^2 - \nu_2)\right)/\mathcal{D} \tag{3.19}$$

$$\begin{aligned}\bar{C}_1 \;=\; & (R_1^2\Delta\rho g(2\nu_1 - 3)((R_1^4 + R_2^4(1 - 4\nu_1))(1 + \nu_1)(3 + 4\nu_1(\nu_2 - 1) \\ & -4\nu_2) + 2(R_1^4 - R_2^4)(4\nu_1 - 3)(2\nu_2^2 + \nu_2 - 1)\log(R_2)))/\mathcal{G}\end{aligned} \tag{3.20}$$

$$\begin{aligned}\bar{D}_1 \;=\; & -(R_1^4 R_2^2\Delta\rho g(R_2^2(1 + \nu_1(-5 + 2\nu_1 + 8\nu_1^2))(3 + 4\nu_1(\nu_2 - 1) - 4\nu_2) + \\ & 2(4\nu_1 - 3)(-R_1^2(1 + 4\nu_1(\nu_2 - 1) - 6\nu_2)(\nu - \nu_2) + R_2^2(2\nu_1 - 1) \\ & (-1 + \nu_2 + 2\nu_2^2))\log(R_2)))/\mathcal{G}\end{aligned} \tag{3.21}$$

$$\begin{aligned}\bar{E}_1 \;=\; & -(R_1^2\Delta\rho g(R_1^2(1 - 2\nu_1)(1 + \nu_1)(3 + 4\nu_1(\nu_2 - 1) - 4\nu_2) - 2(4\nu_1 - 3) \\ & (-R_2^2(1 + 4\nu_1(\nu_2 - 1) - 6\nu_2)(\nu_1 - \nu_2) + R_1^2(2\nu_1 - 1)(-1 + \nu_2 + 2\nu_2^2)) \\ & \log(R_2))/\mathcal{G}\end{aligned} \tag{3.22}$$

$$\bar{B}_2 = \left(2\Delta P R_1^2 R_2^2(\nu_1^2 - 1)\right)/\mathcal{D} \tag{3.23}$$

$$\begin{aligned}\bar{D}_2 \;=\; & -(R_1^2\Delta\rho g(1 + \nu_1)(3 + 4\nu_1(\nu_2 - 1) - 4\nu_2)(2R_1^2 R_2^2(1 - 2\nu_1)^2 + \\ & R_1^4(3 - 2\nu_1) + R_2^4(3 + 2\nu_1(-7 + 4\nu_1)) - 2(R_1^4 - R_2^4) \\ & (-3 + 4\nu_1)\log(R_2))\mathcal{G}\end{aligned} \tag{3.24}$$

where

$$\mathcal{D} = \mathrm{R}_2^2(2\nu_1^2 - \nu_2 - \nu_1 - 2) + R_1^2(\nu_2 - \nu_1) \tag{3.25}$$

$$\begin{aligned}\mathcal{G} \;=\; & 4(\nu_1 - 1)((R_1^4 + R_2^4(1 - 4\nu_1))(1 + \nu)(3 + 4\nu(\nu_2 - 1) - 4\nu_2) + \\ & 2(R_1^4 - R_2^4)(4\nu_1 - 3)(2\nu_2^2 + \nu_2 - 1)\log(R_2)).\end{aligned} \tag{3.26}$$

These stresses are the two dimensional equivalent of the spherically symmetric viscoelastic solutions of Dragoni and Magnanensi [1989], but include buoyancy effects. Given these purely elastic solutions, it is possible to find viscoelastic solutions via the correspondence principle

(Fung [1965]), in which we assume that the material in the region $R_1 < r < R_2$ behaves as a maxwell solid only with respect to deviatoric stresses (e.g. Dragoni and Magnanensi [1989]):

$$\frac{1}{\eta_{wr}}\sigma_{\mathbf{dev}} + \frac{1}{E}\frac{d\sigma_{\mathbf{dev}}}{dt} = \frac{d\epsilon_{\mathbf{dev}}}{dt} \tag{3.27}$$

$$tr\sigma = 3K\ tr\epsilon \tag{3.28}$$

where K is the bulk modulus, ϵ is the strain tensor, and η_{wr} is the shell viscosity. The correspondence principle then entails making the substitution

$$\mu_1 = \frac{E}{2(1+\nu_1)} = \mu_1(s) = \frac{\mu_1\eta_{wr}s}{\mu_1 + \eta_{wr}s} \tag{3.29}$$

where s is the Laplace domain variable, and where use of the rigidity μ_1 as the sole time-varying material property indicates that only deviatoric components of the stress are subject to creep (Dragoni and Magnanensi [1989]).

Viscoelastic solutions are then found by taking the inverse Laplace transform of the stress components found by making the substitutions (3.29):

$$\sigma_{ij,VE} = \mathcal{L}^{-1}[\sigma_{ij,E}(s)]. \tag{3.30}$$

Here $\sigma_{ij,VE}$ are viscoelastic stresses, $\sigma_{ij,E}(s)$ are the Laplace-domain transformed elastic stresses, and $\mathcal{L}$ is the Laplace tranform operator

$$\mathcal{L}\left[f(t)\right] = \int_0^\infty e^{-st} f(t) ds. \tag{3.31}$$

The expressions obtained by performing the Laplace transforms are unwieldy and are not presented here. Cumbersome algebraic manipulations and inverse Laplace Transforms are performed with the symbolic mathematics software package Mathematica (Wolfram 2008).

Principle deviatoric viscoelastic stresses used in the model are then found by solving for the eigenvalues of the matrix defined by

$$\sigma_{\mathbf{dev,VE}} = \sigma_{\mathbf{VE}} - tr\sigma_{\mathbf{VE}} \tag{3.32}$$

and are even more complicated expressions.

Of the two boundary conditions considered in this study, overpressure ΔP and magma buoyancy $\Delta\rho g$, overpressure is the most important, generating stresses that are 3-5 orders of magnitude greater than buoyancy effects. However, magma buoyancy is a first-order mechanism for magma transport in many situations. It is therefore of note that viscoelastic solutions for a uniformly pressurized circular cavity differ in important respects from corresponding buoyant solutions. The viscous response to an overpressured inclusion is isotropic, and a constant overpressure boundary condition in a viscous medium requires a constant divergence of mass from the center of the inclusion. Buoyancy effects are, however, not isotropic and generate flow around the inclusion.

Our model considers a circular chamber with a viscoelastic shell in an elastic medium, which acts as a rigid container on the maxwell timescale of the shell. Deviatoric stresses due to chamber overpressure relax in time because of the isotropic nature of the viscous response - in fact, this property defines pressure. However, deviatoric stresses due to buoyancy do not. This is illustrated in Figure 3.10, where the time-dependent deviatoric radial stress at the top of the chamber ($\phi = 0$) is plotted for the overpressure and buoyancy boundary conditions. While stresses due to overpressure decay to zero in time within the shell, buoyancy stresses approach the stresses expected for Stokes flow around a buoyant inclusion rising toward a rigid boundary: stresses change sign toward the rigid boundary. Exactly opposite stresses occur at the bottom of the inclusion ($\phi = \pi$).

To test the effects of a free surface on viscoelastic stress relaxation, we solve a half-space viscoelastic chamber problem using stress functions Fung [1965], subject to overpressure boundary conditions. We use the bipolar coordinate system defined in terms of Cartesian coordinates by the complex mapping

$$x + iy = \frac{k(\sinh(\alpha) + i\sin(\beta))}{\cosh(\alpha) - \cos(\beta)} \tag{3.33}$$

where α and β are spatial coordinates, $i = \sqrt{-1}$, and k is a dimensional scaling factor that relates curves of constant α. For more details about this coordinate system and the method of stress functions, see e.g., Jeffery [1921], Karlstrom et al. [2009]. We merely state the main results here. For this problem, boundary conditions are

$$\sigma^{in}_{\alpha\alpha}|_{\alpha=\alpha_1} = \Delta P \tag{3.34}$$

$$\sigma^{in}_{\alpha\alpha}|_{\alpha=\alpha_2} = \sigma^{out}_{\alpha\alpha}|_{\alpha=\alpha_2} \tag{3.35}$$

$$u^{in}_{\alpha}|_{\alpha=\alpha_2} = u^{out}_{\alpha}|_{\alpha=\alpha_2} \tag{3.36}$$

$$\sigma_{\alpha\beta}|_{\alpha=\alpha_0} = \sigma_{\alpha\alpha}|_{\alpha=0} = \sigma_{\alpha\beta}|_{\alpha=0} = 0, \tag{3.37}$$

where α_1 and α_2 are related to R_1 and R_2 in the polar coordinate system through

$$R_i = k\ \mathrm{csch}(\alpha_i) \tag{3.38}$$

for $i = 1, 2$.

Stress functions that satisfy the appropriate equilibrium equations and these boundary conditions take the form

$$\begin{aligned}\chi^{in}(\alpha,\beta) &= \tfrac{k}{\cosh(\alpha)-\cos(\beta)}(A_1\cosh(\alpha) + B_1\sinh(\alpha) + C_1\alpha(\cosh(\alpha)-\cos(\beta)) + \\ &\quad (D_1\cosh(2\alpha) + E_1\sinh(2\alpha))\cos(\beta)),\end{aligned} \tag{3.39}$$

$$\begin{aligned}\chi^{out}(\alpha,\beta) &= \tfrac{k}{\cosh(\alpha)-\cos(\beta)}(A_2\cosh(\alpha) + B_2\alpha(\cosh(\alpha)-\cos(\beta)) + \\ &\quad (C_2\cosh(2\alpha) + D_2\sinh(2\alpha))\cos(\beta)).\end{aligned} \tag{3.40}$$

Stresses that correspond to these functions are

$$\begin{aligned}\sigma_{\alpha\alpha,in}(\alpha,\beta) &= \tfrac{1}{k}(A_1 + C_1(\cos(\beta)-\cosh(\alpha))\sinh(\alpha)+ \\ &\quad \cosh(2\alpha)(D_1 - 2E_1\cos(\beta)\sinh(\alpha))+ \\ &\quad (E_1 - 2D_1\cos(\beta)\sinh(\alpha))\sinh(2\alpha)),\end{aligned} \tag{3.41}$$

$$\begin{aligned}\sigma_{\beta\beta,in}(\alpha,\beta) &= \tfrac{1}{k}(A_1 + 4D_1\cos(\beta)\cosh^3(\alpha) - D_1\cosh(2\alpha)+ \\ &\quad (C_1 - 2E_1)\cosh(\alpha)\sinh(\alpha) + \cos(\beta)(-C_1 + 4E_1 + 2E_1\cosh(2\alpha)) \\ &\quad \sinh(\alpha))2\cos(2\beta)(D_1\cosh(2\alpha) + E_1\sinh(2\alpha))),\end{aligned} \tag{3.42}$$

$$\sigma_{\alpha\beta,in}(\alpha,\beta) = \frac{1}{k}\left(\cos(\beta)-\cosh(\alpha)\right)\sin(\beta)(C_1 - 2E_1\cosh(2\alpha) - 2D_1\sinh(2\alpha))), \tag{3.43}$$

$$\begin{aligned}\sigma_{\alpha\alpha,out}(\alpha,\beta) &= \tfrac{1}{k}(A_2 + B_2(\cos(\beta)-\cosh(\alpha))\sinh(\alpha)+ \\ &\quad \cosh(2\alpha)(C_2 - 2D_2\cos(\beta)\sinh(\alpha))+ \\ &\quad (D_2 - 2C_2\cos(\beta)\sinh(\alpha))\sinh(2\alpha))),\end{aligned} \tag{3.44}$$

$$\begin{aligned}\sigma_{\beta\beta,out}(\alpha,\beta) &= \tfrac{1}{k}(A_2 + 4C_2\cos(\beta)\cosh^3(\alpha) - C_2\cosh(2\alpha)+ \\ &\quad (B_2 - 2D_2)\cosh(\alpha)\sinh(\alpha) + \cos(\beta)(-B_2 + 4D_2 + 2D_2\cosh(2\alpha)) \\ &\quad \sinh(\alpha) - 2\cos(2\beta)(C_2\cosh(2\alpha) + D_2\sinh(2\alpha))),\end{aligned} \tag{3.45}$$

$$\sigma_{\alpha\beta,out}(\alpha,\beta) = \frac{1}{k}\left(\left(\cos(\beta)-\cosh(\alpha)\right)\sin(\beta)(B_2 - 2D_2\cosh(2\alpha) - C_2\sinh(2\alpha))\right), \tag{3.46}$$

and displacements outside the shell are

$$\begin{aligned}U_{\alpha,out}(\alpha,\beta) &= (\cos(\beta)((D_2(\lambda_2-\mu_2) - 4B_2(\lambda_2+\mu_2))\cosh(\alpha)D_2(\lambda_2+\mu_2) \\ &\quad \cosh(3\alpha) + 2(C_2\lambda_2 + A_2\mu_2 + C_2(\lambda_2+\mu_2)\cosh(2\alpha))\sinh(\alpha) + (\lambda_2+\mu_2) \\ &\quad (2B_2 + (-2D_2 + B_2)\cosh(2\alpha) - 2C_2\sinh(2\alpha)) + \cos(2\beta) \\ &\quad (B_2(\lambda_2+\mu_2) + 2D_2\mu_2\cosh(2\alpha) + 2C_2\mu_2\sinh(2\alpha)))/ \\ &\quad (4\mu_2(\lambda_2+\mu_2)(\cos(\beta)-\cosh(\alpha)))\end{aligned} \tag{3.47}$$

$$\begin{aligned}U_{\beta,out}(\alpha,\beta) &= (\sin(\beta)((\lambda_2+2\mu_2)(\cosh(2\alpha)(2C_2\cos(\beta) + D_2\sinh(\alpha))+ \\ &\quad (2D_2\cos(\beta) + C_2\sinh(\alpha))\sinh(2\alpha)) + \cosh(\alpha)(A_2\mu_2 - (2\lambda_2+3\mu_2) \\ &\quad (C_2\cosh(2\alpha) + D_2\sinh(2\alpha)))))/(2\mu_2(\lambda_2+\mu_2)(\cos(\beta)-\cosh(\alpha))).\end{aligned} \tag{3.48}$$

The constants $A_1, B_1, C_1, D_1, E_1, A_2, B_2, C_2, D_2$ are evaluated to satisfy boundary conditions 3.34-3.37, and are

$$
\begin{aligned}
A_1 = & -(2k\Delta P(-\operatorname{csch}(\alpha_1-\alpha_2)(\lambda_1+2\mu_1)\mu_2(\lambda_2+\mu_2)\sinh^2(\alpha_2) \\
& +\cosh(\alpha_1)\cosh(2\alpha_2)(\lambda_1+\mu_1)(\cosh(2\alpha_2)(\mu_1-\mu_2)(\lambda_2+\mu_2)+ \\
& \mu_2(\lambda_2+\mu_1+\mu_2))\sinh(\alpha_2)-\cosh(\alpha_2)(\cosh(2\alpha_2)-2)\sinh(\alpha_1) \\
& (\lambda_1+\mu_1)(\cosh(2\alpha_2)(\mu_1-\mu_2)(\lambda_2+\mu_2)+\mu_2(\lambda_2+\mu_1+\mu_2))))/ \\
& (\mu_1(2\mu_2((\sinh(\alpha_1-3\alpha_2)-4\sinh(\alpha_1-\alpha_2)+\sinh(3\alpha_1-\alpha_2))\mu_1\cosh^2(\alpha_2)+ \\
& 4\cosh^2(\alpha_1-\alpha_2)\sinh^2(\alpha_2)\sinh(\alpha_1+\alpha_2)\mu_2)+\lambda_2(8\cosh^2(\alpha_1-\alpha_2) \\
& \sinh(\alpha_1+\alpha_2)\mu_2\sinh^2(\alpha_2)+\cosh(2\alpha_2)(\sinh(\alpha_1-3\alpha_2) \\
& -4\sinh(\alpha_1-\alpha_2)+\sinh(3\alpha_1-\alpha_2))\mu_1))+\lambda_1(2\mu_2((\sinh(\alpha_1-3\alpha_2)- \\
& 4\sinh(\alpha_1-\alpha_2)+\sinh(3\alpha_1-\alpha_2))\mu_1\cosh^2(\alpha_2)+\sinh^2(\alpha_2)(-\sinh(\alpha_1-3\alpha_2)+ \\
& 2\sinh(\alpha_1-\alpha_2)+\sinh(\alpha_1+\alpha_2))\mu_2)+\lambda_2(2(-\sinh(\alpha_1-3\alpha_2)+2\sinh(\alpha_1-\alpha_2)+ \\
& \sinh(\alpha_1+\alpha_2))\mu_2\sinh^2(\alpha_2)+\cosh(2\alpha_2)(\sinh(\alpha_1-3\alpha_2)- \\
& 4\sinh(\alpha_1-\alpha_2)+\sinh(3\alpha_1-\alpha_2))\mu_1)))
\end{aligned}
\tag{3.49}
$$

$$
\begin{aligned}
B_1 = & (k\Delta P\cosh(\alpha_1-\alpha_2)(\lambda_1+\mu_1)(4\lambda_1(\sinh^2(\alpha_2)\lambda_2(\mu_1-\mu_2)- \\
& \mu_2(\mu_2\sinh^2(\alpha_2)+\mu_1))+\mu_1(4(\cosh(2\alpha_2)+3)(\mu_1-\mu_2)\mu_2\sinh^2(\alpha_2)+ \\
& \lambda_2((6\cosh(2\alpha_2)+\cosh(4\alpha_2)-3)\mu_1-4(\cosh(2\alpha_2)+3)\sinh^2(\alpha_2)\mu_2))))/ \\
& (\mu_1(\mu_1(2\mu_2((\sinh(\alpha_1-3\alpha_2)-4\sinh(\alpha_1-\alpha_2)+\sinh(3\alpha_1-\alpha_2))\mu_1\cosh^2(\alpha_2)+ \\
& 4\cosh^2(\alpha_1-\alpha_2)\sinh^2(\alpha_2)\sinh(\alpha_1+\alpha_2)\mu_2)+\lambda_2(8\cosh^2(\alpha_1-\alpha_2) \\
& \sinh(\alpha_1+\alpha_2)\mu_2\sinh^2(\alpha_2)+\cosh(2\alpha_2)(\sinh(\alpha_1-3\alpha_2)-4\sinh(\alpha_1-\alpha_2)+ \\
& \sinh(3\alpha_1-\alpha_2))\mu_1))+\lambda_1(2\mu_2((\sinh(\alpha_1-3\alpha_2)-4\sinh(\alpha_1-\alpha_2)+ \\
& \sinh(3\alpha_1-\alpha_2))\mu_1\cosh^2(\alpha_2)+\sinh^2(\alpha_2)(-\sinh(\alpha_1-3\alpha_2)+2\sinh(\alpha_1-\alpha_2)+ \\
& \sinh(\alpha_1+\alpha_2))\mu_2)+\lambda_2(2(-\sinh(\alpha_1-3\alpha_2)+2\sinh(\alpha_1-\alpha_2)+\sinh(\alpha_1+\alpha_2)) \\
& \mu_2\sinh^2(\alpha_2)+\cosh(2\alpha_2)(\sinh(\alpha_1-3\alpha_2)-4\sinh(\alpha_1-\alpha_2)+\sinh(3\alpha_1-\alpha_2))\mu_1))))
\end{aligned}
\tag{3.50}
$$

$$
\begin{aligned}
C_1 = & (-4k\Delta P\cosh(\alpha_1-\alpha_2)\mu_1((\lambda_1-\lambda_2+\mu_1-\mu_2)\mu_2+ \\
& \cosh(2\alpha_2)(\lambda_2+\mu_2)(\lambda_1+\mu_1+\mu_2)))/ \\
& (\mu_1(2\mu_2((\sinh(\alpha_1-3\alpha_2)-4\sinh(\alpha_1-\alpha_2)+\sinh(3\alpha_1-\alpha_2))\mu_1\cosh^2(\alpha_2)+ \\
& 4\cosh^2(\alpha_1-\alpha_2)\sinh^2(\alpha_2)\sinh(\alpha_1+\alpha_2)\mu_2)+\lambda_2(8\cosh^2(\alpha_1-\alpha_2) \\
& \sinh(\alpha_1+\alpha_2)\mu_2\sinh^2(\alpha_2)+\cosh(2\alpha_2)(\sinh(\alpha_1-3\alpha_2)-4\sinh(\alpha_1-\alpha_2)+ \\
& \sinh(3\alpha_1-\alpha_2))\mu_1))+\lambda_1(2\mu_2((\sinh(\alpha_1-3\alpha_2)-4\sinh(\alpha_1-\alpha_2)+ \\
& \sinh(3\alpha_1-\alpha_2))\mu_1\cosh^2(\alpha_2)+\sinh^2(\alpha_2)(-\sinh(\alpha_1-3\alpha_2)+2\sinh(\alpha_1-\alpha_2)+ \\
& \sinh(\alpha_1+\alpha_2))\mu_2)+\lambda_2(2(-\sinh(\alpha_1-3\alpha_2)+2\sinh(\alpha_1-\alpha_2)+\sinh(\alpha_1+\alpha_2)) \\
& \mu_2\sinh^2(\alpha_2)+\cosh(2\alpha_2)(\sinh(\alpha_1-3\alpha_2)-4\sinh(\alpha_1-\alpha_2)+\sinh(3\alpha_1-\alpha_2))\mu_1)))
\end{aligned}
\tag{3.51}
$$

$$\begin{aligned} D_1 = {} & (-k\Delta P\operatorname{csch}(\alpha_1-\alpha_2)(\cosh(2\alpha_2)\mu_1((\lambda_1-\lambda_2+\mu_1-\mu_2)\mu_2+\cosh(2\alpha_2) \\ & (\lambda_2+\mu_2)(\lambda_1+\mu_1+\mu_2))+\cosh(2\alpha_1)(-\lambda_1-\mu_1)(\cosh(2\alpha_2)(\mu_1-\mu_2)(\lambda_2+\mu_2)+ \\ & \mu_2(\lambda_2+\mu_1+\mu_2))))/(\mu_1(2\mu_2((\sinh(\alpha_1-3\alpha_2)-4\sinh(\alpha_1-\alpha_2)+ \\ & \sinh(3\alpha_1-\alpha_2))\mu_1\cosh^2(\alpha_2)+4\cosh^2(\alpha_1-\alpha_2)\sinh^2(\alpha_2)\sinh(\alpha_1+\alpha_2)\mu_2)+ \\ & \lambda_2(8\cosh^2(\alpha_1-\alpha_2)\sinh(\alpha_1+\alpha_2)\mu_2\sinh^2(\alpha_2)+ \\ & \cosh(2\alpha_2)(\sinh(\alpha_1-3\alpha_2)-4\sinh(\alpha_1-\alpha_2)+\sinh(3\alpha_1-\alpha_2))\mu_1))+ \\ & \lambda_1(2\mu_2((\sinh(\alpha_1-3\alpha_2)-4\sinh(\alpha_1-\alpha_2)+\sinh(3\alpha_1-\alpha_2))\mu_1\cosh^2(\alpha_2)+ \\ & \sinh^2(\alpha_2)(-\sinh(\alpha_1-3\alpha_2)+2\sinh(\alpha_1-\alpha_2)+ \\ & \sinh(\alpha_1+\alpha_2))\mu_2)+\lambda_2(2(-\sinh(\alpha_1-3\alpha_2)+2\sinh(\alpha_1-\alpha_2)+ \\ & \sinh(\alpha_1+\alpha_2))\mu_2\sinh^2(\alpha_2)+\cosh(2\alpha_2)(\sinh(\alpha_1-3\alpha_2)-4\sinh(\alpha_1-\alpha_2)+ \\ & \sinh(3\alpha_1-\alpha_2))\mu_1))) \end{aligned} \tag{3.52}$$

$$\begin{aligned} E_1 = {} & (k\Delta P\operatorname{csch}(\alpha_1-\alpha_2)(2\sinh(2\alpha_2)\mu_1(\lambda_1-\lambda_2+\mu_1-\mu_2)\mu_2- \\ & 2\sinh(2\alpha_1)(\lambda_1+\mu_1)(\lambda_2+\mu_1+\mu_2)\mu_2-2\cosh(2\alpha_2)\sinh(2\alpha_1) \\ & (\lambda_1+\mu_1)(\mu_1-\mu_2)(\lambda_2+\mu_2)+\sinh(4\alpha_2)\mu_1(\lambda_2+\mu_2)(\lambda_1+\mu_1+\mu_2)))/ \\ & (2(\mu_1(2\mu_2((\sinh(\alpha_1-3\alpha_2)-4\sinh(\alpha_1-\alpha_2)+\sinh(3\alpha_1-\alpha_2))\mu_1\cosh^2(\alpha_2)+ \\ & 4\cosh^2(\alpha_1-\alpha_2)\sinh^2(\alpha_2)\sinh(\alpha_1+\alpha_2)\mu_2)+\lambda_2(8\cosh^2(\alpha_1-\alpha_2)\sinh(\alpha_1+\alpha_2) \\ & \mu_2\sinh^2(\alpha_2)+\cosh(2\alpha_2)(\sinh(\alpha_1-3\alpha_2)-4\sinh(\alpha_1-\alpha_2)+\sinh(3\alpha_1-\alpha_2))\mu_1))+ \\ & \lambda_1(2\mu_2((\sinh(\alpha_1-3\alpha_2)-4\sinh(\alpha_1-\alpha_2)+\sinh(3\alpha_1-\alpha_2))\mu_1\cosh^2(\alpha_2)+\sinh^2(\alpha_2) \\ & (-\sinh(\alpha_1-3\alpha_2)+2\sinh(\alpha_1-\alpha_2)+\sinh(\alpha_1+\alpha_2))\mu_2)+\lambda_2(2(-\sinh(\alpha_1-3\alpha_2)+ \\ & 2\sinh(\alpha_1-\alpha_2)+\sinh(\alpha_1+\alpha_2))\mu_2\sinh^2(\alpha_2)+\cosh(2\alpha_2)(\sinh(\alpha_1-3\alpha_2)- \\ & 4\sinh(\alpha_1-\alpha_2)+\sinh(3\alpha_1-\alpha_2))\mu_1)))) \end{aligned} \tag{3.53}$$

$$A_2 = -C_2 \tag{3.54}$$

$$B_2 = 2D_2 \tag{3.55}$$

$$\begin{aligned} C_2 = {} & (2k\Delta P\cosh(\alpha_1-\alpha_2)\sinh(2\alpha_2)(\lambda_1+2\mu_1)\mu_2(\lambda_2+\mu_2)) \\ & (\mu_1(2\mu_2((\sinh(\alpha_1-3\alpha_2)-4\sinh(\alpha_1-\alpha_2)+\sinh(3\alpha_1-\alpha_2))\mu_1\cosh^2(\alpha_2)+ \\ & 4\cosh^2(\alpha_1-\alpha_2)\sinh^2(\alpha_2)\sinh(\alpha_1+\alpha_2)\mu_2)+\lambda_2(8\cosh^2(\alpha_1-\alpha_2)\sinh(\alpha_1+\alpha_2) \\ & \mu_2\sinh^2(\alpha_2)+\cosh(2\alpha_2)(\sinh(\alpha_1-3\alpha_2)-4\sinh(\alpha_1-\alpha_2)+ \\ & \sinh(3\alpha_1-\alpha_2))\mu_1))+\lambda_1(2\mu_2((\sinh(\alpha_1-3\alpha_2)-4\sinh(\alpha_1-\alpha_2)+ \\ & \sinh(3\alpha_1-\alpha_2))\mu_1\cosh^2(\alpha_2)+\sinh^2(\alpha_2)(-\sinh(\alpha_1-3\alpha_2)+2\sinh(\alpha_1-\alpha_2)+ \\ & \sinh(\alpha_1+\alpha_2))\mu_2)+\lambda_2(2(-\sinh(\alpha_1-3\alpha_2)+2\sinh(\alpha_1-\alpha_2)+\sinh(\alpha_1+\alpha_2))\mu_2 \\ & \sinh^2(\alpha_2)+\cosh(2\alpha_2)(\sinh(\alpha_1-3\alpha_2)-4\sinh(\alpha_1-\alpha_2)+\sinh(3\alpha_1-\alpha_2))\mu_1))) \end{aligned} \tag{3.56}$$

$$
\begin{aligned}
D_2 \;=\; & (-2k\Delta P\cosh(\alpha_1-\alpha_2)\cosh(2\alpha_2)(\lambda_1+2\mu_1)\mu_2(\lambda_2+\mu_2))/ \\
& (\mu_1(2\mu_2((\sinh(\alpha_1-3\alpha_2)-4\sinh(\alpha_1-\alpha_2)+\sinh(3\alpha_1-\alpha_2))\mu_1\cosh^2(\alpha_2)+ \\
& 4\cosh^2(\alpha_1-\alpha_2)\sinh^2(\alpha_2)\sinh(\alpha_1+\alpha_2)\mu_2)+\lambda_2(8\cosh^2(\alpha_1-\alpha_2)\sinh(\alpha_1+\alpha_2)\mu_2 \\
& \sinh^2(\alpha_2)+\cosh(2\alpha_2)(\sinh(\alpha_1-3\alpha_2)-4\sinh(\alpha_1-\alpha_2)+\sinh(3\alpha_1-\alpha_2))\mu_1))+ \\
& \lambda_1(2\mu_2((\sinh(\alpha_1-3\alpha_2)-4\sinh(\alpha_1-\alpha_2)+\sinh(3\alpha_1-\alpha_2))\mu_1\cosh^2(\alpha_2)+ \\
& \sinh^2(\alpha_2)(-\sinh(\alpha_1-3\alpha_2)+2\sinh(\alpha_1-\alpha_2)+\sinh(\alpha_1+\alpha_2))\mu_2)+ \\
& \lambda_2(2(-\sinh(\alpha_1-3\alpha_2)+2\sinh(\alpha_1-\alpha_2)+\sinh(\alpha_1+\alpha_2))\mu_2\sinh^2(\alpha_2)+ \\
& \cosh(2\alpha_2)(\sinh(\alpha_1-3\alpha_2)-4\sinh(\alpha_1-\alpha_2)+\sinh(3\alpha_1-\alpha_2))\mu_1)))
\end{aligned}
\tag{3.57}
$$

The above expressions are then Laplace Transformed using equations 3.29 - 3.31, to obtain viscoelastic stresses and displacements.

The elastic stresses in this case differ significantly from the infinite space solutions in general, although they are asymptotically similar in the appropriate limiting conditions (Figure 3.9). Deviatoric stresses around chambers at shallow depths are affected strongly by the free surface, and shell stresses exhibit an interesting change in topology as time progresses (Figure 3.12). This change reflects the shear stresses induced on the chamber by the free surface, which gradually becomes dominant as isotropic deviatoric stresses relax away.

Thermal Model

The melt fraction of a magma determines its rheological properties, and mixtures of magmas with different compositions are expected in chambers that grow through the discrete injection of basaltic dike melt. We use one-parameter functions to relate melt fraction to temperature in our model. For amphibolite, we use the parameterization of Dufek and Bergantz [2005]:

$$
\begin{aligned}
f(\mathbf{x},t) \;=\; & -2.0968e^{-12}\mathcal{T}^5+1.09308e^{-8}\mathcal{T}^4-2.26718e^{-5}\mathcal{T}^3 \\
& +2.33912e^{-2}\mathcal{T}^2-12.0048\mathcal{T}+2451.69,
\end{aligned}
\tag{3.58}
$$

where

$$
\mathcal{T}=T(\mathbf{x},t)+12(15\text{ k}bar-P) \tag{3.59}
$$

and we pick a pressure of $P=10$ kbar to evaluate $\mathcal{T}$. For tonalite, we use a parameterization drawn from Petcovic and Dufek [2005]:

$$
\begin{aligned}
f(\mathbf{x},t) \;=\; & 1.9852e^{-7}T^3(\mathbf{x},t)-4.8481e^{-4}T^2(\mathbf{x},t)+0.39547T(\mathbf{x},t) \\
& -107.54
\end{aligned}
\tag{3.60}
$$

This parameterization fits the data of Piwinskii and Wyllie [1968] well below melt fractions $f(\mathbf{x},t)\sim 0.8$. Higher melt fractions, which are more more poorly constrained by experiment, are parameterized by a linear segment with slope 0.18.

Basaltic melt fraction curves follow from the parameterizations in Dufek and Bergantz [2005], Petcovic and Dufek [2005] and the references therein. Anhydrous basalt follows the

relation

$$\begin{aligned} f(\mathbf{x},t) &= 2.79672e^{-11}T^4(\mathbf{x},t) - 8.79939e^{-8}T^3(\mathbf{x},t) + 1.01622e^{-4}T^2(\mathbf{x},t) \\ &\quad -5.02861e^{-2}T(\mathbf{x},t) + 8.6693, \end{aligned} \tag{3.61}$$

whereas basalt with 2 wt % H_2O has a melt fraction curve that accounts for the lower the solidus

$$f(\mathbf{x},t) = 2.039e^{-9}T^3(\mathbf{x},t) - 3.07e^{-6}T^2(\mathbf{x},t) + 1.63e^{-3}T(\mathbf{x},t) - 0.307. \tag{3.62}$$

Figure 3.13 plots the four melt fraction curves used in this study, and the "critical melt fraction" of 0.6. As discussed in the Results section, it is the different forms of these curves (determined by the melting temperatures of modal mineral components) that account for the degree of crustal anatexis in our model runs.

The viscoelastic shell is defined on the basis of equations (3.58) - (3.62), and the critical melt fraction of 0.6 that defines the transition from liquid-like to solid-like behavior. In calculating viscoelastic stresses, we use a constant viscosity throughout the shell, determined by the highest temperature material in the shell and an Arhennius Law

$$\eta_{wr} = A\ exp(Q/nRT) \tag{3.63}$$

where $A = exp(15.4)$ MPa, $Q = 515$ kJ/mol, $n = 3.5$, and R is the molar gas constant. This viscosity law overpredicts shell viscosities, and it contains no model for crystal connectivity (e.g., Scaillet et al. [1998]), but is nevertheless a commonly used formulation. The highest temperature in the shell results in a lower bound on shell viscosity in our model. Other choices (for example using the average temperature in shell) do affect details of the regime diagrams (Figures 3.6 - 3.7), but the four dynamic regimes themselves are a robust result.

Inside the 'liquid' region of the magma chamber, we use a linear mixing law to determine bulk material properties of the magma. Following Dufek and Bergantz [2005], we define a parameter $\gamma \in [0,1]$ that defines the local volume fraction of intruded basalt or crustal melt. The mixture density is then defined by

$$\rho_{mix} = \gamma f_c \rho_c^l + \gamma(1-f_c)\rho_c^s + (1-\gamma)f_b\rho_b^l + (1-\gamma)(1-f_b)\rho_b^s, \tag{3.64}$$

mixture heat capacity by

$$c_{mix} = \gamma f_c c_c^l + \gamma(1-f_c)c_c^s + (1-\gamma)f_b c_b^l + (1-\gamma)(1-f_b)c_b^s, \tag{3.65}$$

and mixture conductivity by

$$k_{mix} = \gamma f_c k_c^l + \gamma(1-f_c)k_c^s + (1-\gamma)f_b k_b^l + (1-\gamma)(1-f_b)k_b^s. \tag{3.66}$$

Here superscripts l and s refer to solid and liquid, while subscripts c and s stand for basalt and crust.

A number of factors in our model make keeping track of numerical errors important. The local nature of melting and solidification, along with the multiphase nature of the domain,

create a spatially discontinuous and nonlinear heat conduction problem. We have performed tests to ensure that the predictor-corrector method used in our thermal calculation (Voller and Swaminathan [1991]) does in fact converge to the correct solution at each time step. Additional errors might occur during the discretization of melt into rings. Finite numerical resolution means that it is possible for small incoming melt flux to fall within grid resolution, so that the chamber does not conserve mass. This problem is overcome with sufficient spatial resolution.

Chapter 4

On the Evolution of Large Ultramafic Magma Chambers and Timescales for Flood Basalt Eruptions

4.1 Introduction

The emplacement of large igneous provinces (LIPs) is a poorly understood process. Endogenous hypotheses for the large eruptive volumes associated with LIPs include mantle plume heads, or starting plumes, impinging upon the lithosphere [e.g., Morgan, 1971, Richards et al., 1989, Campbell and Griffiths, 1990], asthenospheric convection [e.g., King and Anderson, 1995] and lithospheric delamination [e.g., Tanton and Hager, 2000, Hales et al., 2005], suggesting source regions for these events at a range of depths. Exogenic origins for LIPs have also been proposed [e.g., Jones et al., 2002]. Most existing endogenous models for the genesis of flood basalt provinces do not explain the geologically short durations (1 Ma or less) of the "main-stage" eruptions that usually account for most of the erupted basalt volumes for LIPs [Courtillot and Renne, 2003].

Other important aspects of LIPs awaiting satisfactory explanation, include the magnitude of coevolving dynamic topography, the common (although not exclusive) association of LIPs with continental rifting events, and the remarkably uniform compositions of the main–stage basalts. There seems to be little consensus regarding the nature of magma chambers that appear necessary to fractionate and homogenize the large quantities of basaltic melt before eruption, despite the existence of extensive seismic evidence for large volumes of deep ultramafic intrusive/cumulate bodies underlying LIPs [Cox, 1980, Ridley and Richards, 2010], and extensive sills at more shallow depths [Elliot and Fleming, 2008]. These problems may be largely attributed to our lack of understanding of what happens to the primary melts produced in the mantle as they rise and interact with the overlying lithosphere and crust.

In our view there are a number of important questions related to the plumbing of LIP magmatism. What are the melt production rates predicted by the various LIP generation

hypotheses, and how might this melt accumulate in chambers? At what depths would these magma bodies form, and what factors govern their emplacement? Are there multiple stages or depths of fractionation and melt storage in the crust?

Other open questions are more directly linked to the geologic record: Why are the main–stage eruptions so brief and so uniform in individual flow characteristics (erupted volumes, major- and trace-element compositions)? How do inflation and deflation of intrusions affect uplift and subsidence at the surface? To what extent can exposed large intra–crustal mafic intrusions, and continental diking events be related to the eruption of flood basalts?

Of these questions, we are particularly drawn to that of the remarkably short duration of the main-stage eruptions of flood basalts. The largest volumes of basalts are erupted within $\sim 0.5 - 1.0$ Ma, but primary mantle melting events during LIPs are expected to be of duration > 10 Ma [e.g., Farnetani and Richards, 1994, Leitch and Davies, 2001]. Could primary melt be ponded in deep sills or magma chambers for an extended period before eruptions occur? This seems highly unlikely as such long–term storage is known not to occur in the oceanic lithosphere and crust beneath modern hotspots [Hauri et al., 1996]. A more attractive hypothesis is that large scale eruptions are controlled by the ability of the overlying crust to propagate fractures (dikes) to feed eruptions, limited by the onset of viscous flow as the crust surrounding the magma body heats up in time [Jellinek and DePaolo, 2003, de Silva and Gosnold, 2007].

We explore the latter hypothesis first by summarizing several independent lines of evidence that connect deep magmatic processes with eruptive processes in LIPs. We then formulate a model for the evolution of melt within and elastic deviatoric stresses surrounding a deep magma chamber. Finally, we apply these ideas to certain observational aspects of LIPs, thereby beginning to address the processes that occur between primary melting in the mantle and the eruption of flood basalts in both continental and oceanic settings.

4.2 The observed time progression of LIP magmatism

From radiometric and magnetostratigraphic dating it appears that many flood basalt provinces have a similar time progression of eruptive style and cumulative output. Across the spectrum of Phanerozoic LIPs recognized so far, in nearly every case there is a punctuated early phase of flood basalt volcanism in which $\sim 80 - 95\%$ of the total volume of lavas are extruded [e.g., Courtillot and Renne, 2003], often an order of magnitude shorter than the total duration of the event, during which the style and composition of erupted lavas can vary greatly [Jerram and Widdowson, 2005]. This trend has been shown for, among others, the Columbia River Basalts [Barry et al., 2010], the Parana-Etendeka province [Melluso et al., 1999], the North Atlantic province [Storey et al., 2007], and the Deccan traps [Allegre et al., 1999].

Most LIPs are underlain by large mafic–ultramafic intrusive bodies, widely observed in the seismic record [Ridley and Richards, 2010]. This observation is not unexpected, in fact the existence of cumulate bodies may be predicted from the fact that sublithospheric melting of mantle plumes results in primary magmas of ultramafic, not basaltic, composition that

are too dense to rise above the Moho or erupt [Farnetani et al., 1996]. Magma derived from 20% partial melting of a model pyrolite at 2 GPa results in a melt composition that includes 18% MgO and a corresponding melt density of about 2.9 kg/m^3 at Moho depths, more dense than the lowermost (gabbroic) oceanic crust. Thus we envision a 3-stage process of (1) magma genesis in the mantle, (2) crystal fractionation (mainly olivine and pyroxene) at near-Moho depths in large sill complexes, and (3) eruption (or higher level intrusion) of basaltic magmas, as summarized in Figure 4.1. In fact, Cox [1980] inferred essentially the same sequence of events from largely petrological considerations.

Explicit petrogenic models for the thickened crust of the Ontong–Java plateau, the largest LIP known [Coffin and Eldholm, 1994], show that the seismic velocity structure underlying the plateau can be explained in terms of sublithospheric mantle melting, deep fractionation, and ultimately eruption of residual basaltic magma [Farnetani et al., 1996]. These petrological models suggest that of order 2/3 the total melt volume is intruded material, with maximum crustal thicknesses reaching up to 40 km, and representing more than 30 km of crustal thickening relative to normal oceanic crust. Where high–quality seismic data are available beneath continental flood basalt provinces (Emeishan, Columbia River, Deccan, Siberia), high–velocity structures (Vp $\sim$ 6.9–7.5 km/sec) are typically found immediately overlying the Moho in layers 5–15 km thick [Ridley and Richards, 2010]. Oceanic plateau LIPs exhibit similar high velocity layers. These structures are similar to inferred ultramafic underplating structures seen beneath active hotspots such as Hawaii, the Marquesas and others [e.g., Watts and Brink, 1989, McNutt and Bonneville, 2000, Kopp et al., 2003, Contreras-Reyes et al., 2010], suggesting that lower crustal ultramafic intrusive bodies are a common feature of hotspot magmatism. Radiometric dating of uplift markers also provides some evidence that intrusions may be, at least in part, responsible for the broad bathymetric swells around hotspot islands [Ramalho et al., 2010].

Petrogenetic models for flood basalt volcanism based on hot plume material melting beneath mature lithosphere suggest that these deep seismic structures consist in large part of olivine and clinopyroxene cumulates [Cox, 1980, Furlong and Fountain, 1986, Farnetani et al., 1996]. Such fractionation is necessary to produce basalts with typical MgO contents of $\sim 3-6\%$, as in the vast bulk of observed flood basalts, from primary melts with MgO of $\sim 20\%$ such as result from hot, deep melting beneath the lithosphere.

4.3 Post–eruption Uplift and Doming

The overall question of uplift and subsidence associated with LIPs is controversial, complicated by the non–unique transfer function linking mantle dynamics and surface topography. Traditional mantle plume head models predict up to several kilometers of precursory uplift, and similar post–emplacement subsidence for LIPs [e.g., Campbell and Griffiths, 1990, Farnetani and Richards, 1994, Saunders et al., 2007]. Evidence for general large–amplitude uplift is present in some cases and lacking in others, however, and thermochemical plume models [Farnetani and Samuel, 2005, Burov et al., 2007] suggest that uplift associated with

plume impingement on the lithosphere may be much more complex.

Regardless of the melt generation mechanism, if the 10 Ma timescale for post main–stage eruptions is accompanied by intrusion rather than eruptions, we would expect dynamic topography of similar duration. And there is geologic evidence for continued uplift long after the main–stage flood basalt eruptions occur. Ito and Clift [1998] studied Deep Sea Drilling Project and Ocean Drilling Program data to constrain the uplift and subsidence histories of the three largest Pacific plateaus, Ontong-Java, Manihiki, and Shatsky Rise. In all three cases, subsidence post–dating the onset of eruptions is recorded by marine sedimentary sequences overlying the basaltic basement rocks. Similar histories are confirmed for the Ontong–Java plateau [Roberge et al., 2005] and the Kerguelen plateau [Coffin and Eldholm, 1994]. Notably, in all three cases studied by Ito and Clift [1998] there is a subsidence deficit: purely thermal models for plume generated magmatism predict post–emplacement subsidence at least $\sim$ 1 km more than observed. This deficit has been attributed to large volume intrusions that continue for 10–30 Ma following the initial short lived outburst of basaltic eruptions [Ito and Clift, 1998, Coffin and Eldholm, 1994].

LIP–related doming is also reported along the coast of southeastern Greenland in the Kangerdlugssuaq area [Brooks, 1973, Nielsen and Brooks, 1981, Brooks, 1982]. This region along the Denmark Strait was covered with up to 9 km of basalt at the onset of the North Atlantic Tertiary flood basalt event, with flows apparently accommodated by simultaneous subsidence as they were emplaced. Following these eruptions, and accompanying the opening of the North Atlantic basin, an area of horizontal dimension $\sim$300 km along the Kangerdlugssuaq coastline experienced a broad domal uplift of amplitude at least 4 km, estimated to have occurred within 10 Ma of the flood basalt eruptions. Continued intrusion of ultramafic magmas into the deep crust [e.g., White et al., 2008] provides a plausible explanation for this doming. Indeed, abundant shallow–crustal intrusive activity followed the basalt eruptions in this area, including the Skaergaard and other gabbroic intrusions shortly following the main extrusive episode, with more evolved syenitic intrusions 5 Myrs later [Tegner et al., 2008].

Finally, we note an additional observation from the Galapagos Archipelago that appears relevant to the question of deep intrusion. The Galapagos Islands are formed upon a broad platform of anomalously thick oceanic crust bounded on its SSW side by a steep escarpment of unknown origin. The SSW escarpment of the Galapagos Platform is now understood to be composed of many small topographic shelves that must predate the subsequent formation of the multiple shield complexes that have formed the islands and seamounts of the Galapagos Archipelago [Geist et al., 2005]. The crustal thickness of the platform approaches 14–15 km [Feighner and Richards, 1994], and modeling suggests that about one third of this material must be mafic–ultramafic bodies intruded as the oceanic lithosphere passed over the Galapagos mantle plume. We believe the Galapagos Platform and similar oceanic islands may also represent a case of massive igneous intrusion in the wake of initial basaltic eruption and shield formation.

4.4 Evolving Density of Primary Melt

We are interested in what factors other than the timescale for mantle melting may control the timescale for flood basalt eruptions. Our modeling thus considers the end member scenario in which extraction of partial melt from a plume head impinging upon the lithosphere occurs rapidly, generating a supply of magma that rises towards the base of the crust for the lifetime of decompression melting. This is assumed to be longer than the duration of main phase eruptions [e.g., Farnetani and Richards, 1994]. Assuming that individual main stage eruptions are controlled by rupture of a single magma reservoir, there are two possibilities to consider. Failure may initiate internally from the chamber, as stresses accumulate through recharge and buoyancy evolution driving dikes to the surface. Alternatively, there may be some external trigger that destabilizes the chamber and drives dike propagation.

Initial melting of a pyroxenite upper mantle will generate ultramafic magma that is more dense than the overlying crust, so that the density and rigidity contrast at the Moho will trap melt until it evolves sufficient buoyancy to erupt. This buoyancy is generated by a combination of fractional crystallization and progressive concentration of incompatible volatile species such as H_2O and CO_2 in the liquid. Depending on the depth and volatile concentration, and neglecting phase separation between bubbles and melt, exsolution of CO_2 may occur at Moho depths causing dramatically decreasing magma density and increasing compressibility. We explore these effects in numerical experiments combining the petrological modeling program pMELTS [Ghiorso and Sack, 1995, Asimow and Ghiorso, 1998, Ghiorso et al., 2002] with a joint H_2O and CO_2 solubility model calibrated for ultramafic magmas [Papale, 1999a]. We assume a mantle pyrolite at 2 GPa (∼60 km depth), and raise the temperature about 200 °C above the normal mantle adiabat, sufficient to cause 10% partial melting. Primary volatile contents are estimated based on solubility experiments at mantle temperatures and pressures, which suggest upper mantle water contents of ~ 0.1 wt % up to nearly 1 wt% and CO_2 contents of ~ 0.01 to ~ 0.1 wt% [Dasgupta and Hirschmann, 2006, Smith et al., 2006]. We do not attempt to explore this parameter range here, instead choosing a mantle concentration of 0.1 wt% H_2O and 0.05 wt% CO_2 to illustrate the effect of volatiles on melt evolution.

The extraction and fractionation simulation then progresses as follows. Melt rises adiabatically to a pressure of either 300 MPa ($\sim$ 10 km depth) or 8 MPa ($\sim$ 30 km depth) to approximate a typical Moho depth in oceanic or continental settings. The melt at this stage is ultramafic, with 20% MgO, a density of 2.75–2.85 kg/m^3 (depending on depth and volatile content), and volatile contents of 0.5 wt % CO_2 and 1 wt % H_2O. These volatile contents are similar to Hawaiian lavas [Gerlach et al., 2002], but might be underestimates for LIP events [Lange, 2002].

We then simulate the storage and crystallization of this melt in a magma chamber. Cooling simulations are performed isochorically and isobarically, as end member fractionation scenarios [Fowler and Spera, 2008]. Isochoric crystallization assumes a rigid container, letting pressure adjust to the volume changes induced by phase change. Isobaric crystallization instead fixes pressure, leaving the container volume to adjust freely. Either case is

an idealization of crystallization dynamics, as pMELTS calculations are all done at thermodynamic equilibrium (no time), and we do not model the separation of crystals and melt that becomes increasingly difficult at high crystal fraction [e.g., Dufek and Bachmann, 2010]. Pressure and volume changes implied by pure isobaric and isochoric crystallization are also often large enough to induce wall rock failure [e.g., Fowler and Spera, 2008], implying that other dynamics are also important. However this procedure does provide bounds for the expected chemical evolution of LIP magma. Keeping track of the progressive concentration of volatiles in the melt phase, we test the solubility of volatiles at each temperature step (2 degrees). If saturation is reached, we calculate a mixture density of the melt phase via

$$\rho_{mix} = \left(\frac{n}{\rho_m} + \frac{1-n}{\rho_f} \right)^{-1}, \tag{4.1}$$

where n is the mass fraction of volatiles in the melt phase, ρ_m is the density of the melt calculated from pMELTS, and ρ_f is the density of the exsolved volatile phase (CO_2) as a supercritical fluid calculated via the MRK equation of state [Kerrick and Jacobs, 1981]. We vary the temperature and pressure (isochoric cases) according to the output of pMELTS to calculate H_2O+CO_2 solubility throughout the simulations, but use the initial melt composition throughout. This introduces errors in the solubility of order $\sim 1\%$, negligible compared to other model approximations. Solid phases crystallizing from the melt are initially olivines and feldspars, with increasing amounts of plagioclase and pyroxene as crystallization progresses. We do not fractionate exsolved volatile phases, but note that the observation of diffuse CO_2 flux at ocean islands such as Hawaii [Gerlach et al., 2002] implies that some phase separation does occur naturally.

It is evident that significant melt buoyancy, calculated with respect to a fixed reference density of 2700 kg/m^3, is generated as fractionation proceeds (Figure 4.2.a). At 800 MPa exsolution of CO_2 may not become a dominant control on density until roughly 35% crystallinity (isobaric upper bound), but the shallower 300 MPa experiment results in CO_2 exsolution even for zero crystallinity as the exsolution surface is at greater depth. This implies that magma reaching the Moho at shallow depths will be buoyant, with destabilization and eruption possible on a timescale proportional to the influx of primary melt. At greater depths the concentration of volatiles in the melt phase due to progressive fractionation will dictate the critical crystal fraction necessary to transition from ponding of magma to eruption. Isobaric experiments performed for volatile–free primitive magmas (blue and orange curves in Figure 4.2.a) do not exhibit the same buoyancy production during crystallization and may stably pond even at shallow depths.

LIP lava major element chemistry is another constraint on melt evolution, requiring some melt differentiation before eruption to generate basalt. We therefore use the liquid composition calculated from pMELTS to identify an additional possible threshold crystallinity for eruption. As Figure 4.2.b illustrates, sufficiently evolved melts with basaltic MgO contents $< 10\%$ [e.g., Cox, 1980, Lange, 2002] does not occur until $\sim 25\%$ crystallinity for both 300 MPa and 800 MPa.

Given these bounds on the thermodynamic evolution of ponded primitive melts, we take 30% crystallinity to represent the transition from ponded to eruptible magmas based on buoyancy considerations, but experiment with a range of critical crystal fractions up to 80% to match the range of MgO contents observed in LIPs. We will show that the choice of critical crystal fraction is not a major control on the eruptibility of LIP magmas. However, lower choices of critical crystal fraction do imply additional fractionation during ascent or assimilation of surrounding crust to produce basalts. Sufficiently large influx of magma will cause net melting and assimilation to occur even at Moho depths. This latter effect may control the transition from dynamically stable to eruptible magma chambers at mid to upper crustal levels [Karlstrom et al., 2010a], facilitating intrusion of mafic melt into the lower crust. If assimilation does not contribute much to the buoyancy of these primitive melts, mantle melt influx will simply expand the chamber. When heat loss outpaces heat input to the chamber, fractional crystallization towards basaltic composition can occur.

In summary, if the Moho acts as a mechanical trap for rising melts, primary magma reaching Moho depths is less dense than primary pyrolite but requires additional buoyancy production to continue rising through the lower crust. The timescale for this to occur depends on an interplay between crystal fractionation and volatile exsolution. At depths greater than the CO_2 saturation depth, the rate limiting process is volatile concentration through fractional crystallization of magma. At more shallow depths the rate limiting step is the accumulation of bubbly melt.

Buoyancy production due to recharge of bubbly magma occurs on the filling timescale of the magma chamber, V_{ch}/Q, where V_{ch} is the chamber volume and Q is the melt influx. Chamber volumes are likely on the order of single eruptive volumes ($10^3 - 10^4$ km^3) [Barry et al., 2010]. Melt flux (assuming rapid extraction of 10% partial melt from a plume head) scales with the ascent velocity V_{plume} of plume material across the rheological boundary layer of thickness Z at the base of the lithosphere as [e.g., Sleep, 2007] $Q \approx 0.1 V_{plume} A_{plume} \approx 0.1\rho g \alpha \Delta T Z^2 \pi R_{plume}^2/\mu$. Influx ranges from $10^1 - 10^{-3}$ km^3/yr for $\Delta T = 100$ K, $\rho = 3000$ kg/m^3, $g = 10$ m/s^2, $\alpha = 10^{-5}$ K^{-1}, $Z = 10$ km, $\mu = 10^{17} - 10^{19}$ Pas and $R_{plume} = 100$ km (plume cross sectional area is $A_{plume} = \pi R_{plume}^2$), thus the filling timescale is $\sim 10^2 - 10^6$ yr. We assume that filling times on the lower end of this range are reasonable for the present model.

The timescale for fractional crystallization may also be simply estimated, by constructing the energy balance at the chamber walls that dictates the crystallization rate Q_{xtal},

$$Q_{xtal} = \frac{q(\Delta T) S_{ch}}{\rho_{mix} L} - \frac{Q c_p \Delta T}{L}. \tag{4.2}$$

Here $q(\Delta T)$ is the heat flux at the walls, written explicitly as a function of temperature difference between chamber and country rocks, Q is the influx rate of magma into the chamber, and $Q_{xtal} = V_{xtal}/t_{xtal}$ is the rate of solidification in the chamber. S_{ch} the surface area of the chamber, taken to resemble an oblate spheroid, $c_p = 1.5$ KJ/kg K the specific heat capacity, ΔT a drop in temperature below the magma liquidus, and $L = 400$ KJ/kg the latent heat of fusion. Because the crystallized volume is a fraction of the total chamber

volume ($V_{xtal} = \Phi V_{ch}$), we can rearrange equation 4.2 to find the time required to crystallize a fraction of the chamber volume at a given magma influx rate, plotted in Figure 4.3

$$t_{xtal} = \Phi V_{ch} \left(\frac{q(\Delta T) S_{ch}}{\rho_{mix} L} - \frac{Q c_p \Delta T}{L} \right)^{-1}. \tag{4.3}$$

In equation 4.3 we experiment with $\Phi = 0.3 - 0.8$, the critical crystal fraction for eruptible magma as derived from our melt evolution calculations. This crystal fraction sets the melt mixture density ρ_{mix} and temperature drop ΔT between melt and country rocks. Larger ΔT corresponds to lower densities and shallower depths, while large mixture densities correspond to volatile poor, primitive melts at greater depth with smaller ΔT. The crystallization time t_{xtal} becomes large as input of enthalpy through magma influx approaches the dissipation of heat to the surroundings, which scales with the surface area of the chamber S_{ch} (Figure 4.3) . This can be seen in equation 4.3, where the crystallization time becomes singular as $q(\Delta T) S_{ch}/\rho_{mix} L \sim Q c_p \Delta T/L$.

We estimate heat flux at the chamber walls using a steady state solution for a constant temperature oblate spheroid. Assuming large melt influx, this will underestimate heat transfer as it neglects the transient heating of an initially cool lower crust by the intrusion. It is an upper bound to the buoyancy evolution timescale. Steady state temperature around the chamber follows a simple expression in the oblate spheroidal coordinate system [Moon and Spencer, 1988]

$$T(\mathbf{x}) = T(\xi) = T_0 + \Delta T \frac{\cot^{-1}(\xi)}{\cot^{-1}(\xi_0)}, \tag{4.4}$$

where $\xi \in [\xi_0, \infty)$ is a nondimensional distance from the chamber wall, and $\xi_0 = \sqrt{e^2 - 1}$ defines the boundary of an oblate spheroid with semimajor axis a, semiminor axis c and eccentricity $e = 1/a\sqrt{a^2 - c^2}$. T_0 is the background temperature, and ΔT is the temperature difference between the magma and country rocks. Heat flux is then, with $k = 3 - 4$ W/m^2 the thermal conductivity [Whittington et al., 2009],

$$q(\xi) = k \nabla T(\xi) = \frac{k \Delta T}{\cot^{-1}(\xi_0)(1 + \xi^2)} \left[\frac{1 + \xi^2}{(a^2 - c^2)(\xi^2 + \eta^2)} \right]^{1/2}, \tag{4.5}$$

where $\eta \in [-1, 1)$ is the polar angle in the oblate spheroidal coordinate system. This heat flux closely approximates a heated sphere at large distances, but reflects geometrical differences in the near field and is larger at the poles than at the equator (Figure 4.4.a). Using surface area

$$S_{ch} = 2\pi a^2 + \pi \frac{c^2}{e} \ln \left(\frac{1 + e}{1 - e} \right) \tag{4.6}$$

and volume $V_{ch} = 4/3\pi a^2 c$ we can then use equation 4.3 to estimate the time required to obtain an eruptible, basaltic composition magma. After this time, magma can rise through the lower crust, driven by a combination of buoyancy and overpressure. However, as Figure 4.3 illustrates, the ultimate choice of critical crystal fraction for which buoyant melts is fairly

unimportant. Comparing calculations for $\Phi = 0.3, \rho_{mix} = 2700$ kg/m^3 (solid curves) with those for $\Phi = 0.8, \rho_{mix} = 1500$ kg/m^3 (dotted curves), we find that the predicted timescales are roughly linear in Φ. The timescale for buoyancy evolution will be less than 1 Ma for all reasonable parameter choices.

4.5 Magma chamber dynamics

We now consider the eruptive evolution of an LIP magma chamber. Assuming that isotropic overpressure is the dominant stress boundary condition, we follow the conceptual magma chamber model of [Jellinek and DePaolo, 2003], who proposed that prolonged heating of country rocks produces a shell of viscoelastic material that may undergo viscous creep on the timescale of chamber pressurization, relaxing away deviatoric stresses in the country rocks. These stresses are responsible for fracture and dike generation, so viscoelastic relaxation is a mechanism by which chambers may grow and remain stable at temperatures above the solidus without eruption for extended timescales [Jellinek and DePaolo, 2003, Karlstrom et al., 2010a].

We assume a threshold propagation criterion for dike propagation in which dikes may form if deviatoric stresses in the country rocks exceed a critical value of 1 MPa [Rubin, 1995b]. This is a crude approximation to dike propagation mechanics, but it does allow us to explore the relevant timescales for stress relaxation and dike shut-off implicit in our hypothesis. Initial deviatoric stresses in the country rocks larger than 1 MPa are spatially concentrated around the chamber in a rupture envelope (Figure 4.5), bounded by the geometric falloff and relaxation of deviatoric stresses. The region of viscous creep expands in time as heat diffuses from the chamber, so effective viscoelastic relaxation is time–dependent and the rupture envelope progressively shrinks. The time at which deviatoric stresses everywhere relax below 1 MPa is taken to be the maximum timescale over which dike propagation can occur.

Magma chambers are often idealized as pressurized cavities in elastic or viscoelastic media [Gudmundsson, 2006]. Stresses generated by a pressurized oblate spheroidal magma chamber are modeled with the equations of linear elasticity with no body force [e.g., Fung, 1965], subject to the normal stress boundary conditions at the boundary of the chamber R. We use a numerical implementation of the exact solution to this problem [Eshelby, 1957, Healy, 2009], illustrated in Figure 4.4.b.

Stresses are then related to the thermal evolution of rocks around the magma chamber, through a Maxwell viscoelastic constitutive equation for the country rocks. Maxwell viscoelastic stress solutions are available for pressurized chambers with simple geometry [e.g., Dragoni and Magnanensi, 1989, Karlstrom et al., 2010a], and exhibit exponential relaxation of deviatoric stresses on a characteristic (Maxwell) timescale $\tau = C\mu/Y$, where μ is the viscosity of the wall rocks, Y is the Young's Modulus, and C is a geometrical factor (of order unity) related to the size and shape of the viscoelastic shell. We assume that time dependent deviatoric stresses $\sigma_{dev}(x,t)$ for our problem take the form

$$\sigma_{dev}(x,t) \approx \sigma_{dev}(x) \exp\left(-\frac{t}{\tau}\right). \tag{4.7}$$

and that we can use the static Eshelby solution to calculate $\sigma_{dev}(x)$.

Viscosity follows an Arrhenius Law

$$\mu = A^{-1/n} \exp\left(\frac{E}{nRT(\mathbf{x},t)}\right), \tag{4.8}$$

in which A depends on the particular stress-strain relation used, R is the ideal gas constant, E is an activation energy, and n is the power law exponent. E and n depend upon confining pressure and rock type, while A in our parameterization depends on grain size (taken to be constant at 100 μm). We refer to several sets of laboratory dislocation creep measurements on mantle lithosphere and lower crustal rocks to bracket the rheological behavior at Moho depths (Table 4.7), including data on pyroxenite, olivine and anorthite. Rheology is of critical importance to our results, although there is significant uncertainty in the appropriate Arrhenius parameters n, E, and A for the lower crust [Bürgmann and Dresen, 2008].

We cannot assume steady state heat transfer, as we did to estimate a crystallization time of the magma chamber. However, the available asymptotic analytic solutions [Norminton and Blackwell, 1964, Blackwell, 1972] are not sufficient. We assume an idealized temperature evolution, the sudden heating of a sphere with radius equal to the semi–major axis of our ellipse:

$$T(\mathbf{x},t) = T(r,t) = T_0 + \Delta T \frac{R_c}{r} \mathrm{erfc}\left(\frac{r - R_c}{2\sqrt{\kappa t}}\right), \tag{4.9}$$

where T_0 is the initial temperature of the wall rocks, ΔT is the temperature change imposed by the magma chamber, R_c is the radius and r is distance from the of the sphere , $\kappa = 0.5\text{x}10^{-6}\text{m}^2/\text{s}$ [Whittington et al., 2009] is the thermal diffusivity and t is time. This solution overestimates thermal diffusion near the midplane of a spheroidal magma chamber (see the steady state temperatures in Figure 4.4.a). Given our neglect of other important transient heat transfer processes such as crystallization and convection within the chamber [e.g., Marsh, 1989], however, this model is sufficient.

We combine equations 4.7-4.9 to estimate the temporal evolution of the temperature and stresses surrounding the magma chamber. Effective deviatoric stresses are doubly exponential functions of temperature

$$\sigma_{dev}(x,t) \approx \sigma_{dev}(x) \exp\left[-t\ Y A^{1/n} \exp\left(\frac{-E}{nRT(\mathbf{x},t)}\right)\right]. \tag{4.10}$$

In general viscosity depends on stress as well as temperature [e.g., Jull and Kelemen, 2001], but the doubly exponential temperature dependence should dominate the relaxation behavior, and this fact leads to rather robust limits on the timescale over which deviatoric stresses around a heated and pressurized magma body are effectively dissipated.

External triggers

Finally, we consider the possibility that Large Igneous Province magma chambers might be destabilized by stresses imposed externally. There are two sources for these stresses. First, background tectonics or flexure of the lithosphere due to plume emplacement may generate stress concentration around a magma chamber, and may facilitate transport of magma to higher crustal levels or the surface. We neglect tectonic forcing here, but note that plume-related flexural stresses should induce sill emplacement and horizontal transport of magma rather than surface eruption, due to the sub-horizontal orientations of principle stresses in the bottom half of the plate [Galgana et al., 2011]. This could be a source of large scale sill emplacement if dynamic topography increases throughout the eruptive process.

An additional source of external stresses is the Earth's free surface: as is well known, a pressurized cavity beneath a free surface incurs shear stresses that concentrate along the margins of the chamber. This effect is often invoked as the source of ring fractures during caldera collapse [Gudmundsson, 1998], and becomes pronounced when the ratio of chamber size to chamber depth approaches unity [Grosfils, 2007]. Free surface stresses may also be important for the dynamic organization of deeper crustal melt transport [e.g., Karlstrom et al., 2009].

It is possible that LIP magma reservoirs, despite their depth, may grow laterally large enough for free surface stresses to become important. In this case, free surface stresses place a fundamental limit on the size (and eruptible volume) of these chambers. We assume here for simplicity that dike formation occurs when the lateral chamber dimension is equal to the depth. These shear stresses will not be relaxed away through viscous creep unless the entire crust behaves as a Newtonian fluid on the timescale of magma transport, hence there is a basic mechanistic limit on the size of a continuous overpressured body at depth.

4.6 Results

Shutoff timescales implied by equation 4.10 are evaluated for a range of magma chamber sizes and rheological parameters using Newton–Raphson iteration. The maximum stress occurs at the midplane of the oblate spheroid, where curvature is highest. We calculate the maximum deviatoric stress as a function of distance from the chamber, and evolve time forward to find the longest time for which stresses around the chamber exceed 1 MPa (Figure 4.5). Magma chamber overpressure may be estimated in a variety of ways, but is in general a major uncertainty in the modeling of magma dynamics. We choose an overpressure of 100 MPa in all models. Although transient stresses larger than this value might be possible, 100 MPa exceeds most estimates of maximum magma chamber failure strength [e.g., Jellinek and DePaolo, 2003, Traversa et al., 2010] and will result in the redistribution of melt through diking rather than prolonged storage in a central reservoir. The influx rates implied by this overpressure are a function of chamber volume, but generally fall in the range of $10^0 - 10^{-3}$ km^3/yr.

To close the thermal part of the model, we have assumed a Moho–level emplacement in continental and oceanic crust. These endmember scenarios provide a guide for the expected background temperatures, pressures, and country rock rheologies. Although there is considerable controversy over the dominant structure and deformation mechanisms of the lower (particularly continental) crust [e.g., Bürgmann and Dresen, 2008], different hypotheses may be simplified into two scenarios: hot and dry or cool and wet lower crustal rheologies. We perform calculations for both cases, assuming experimentally determined power law parameters for anorthite, clinopyroxene and olivine to explore the likely parameter space (Table 4.7).

The maximum time over which stresses anywhere outside the chamber exceed 1 MPa is found by testing a range of Moho temperatures and chamber sizes (fixing chamber aspect ratio = 0.1). As a consequence of the doubly exponential dependence of deviatoric stresses on temperature, initial Moho temperature exerts the strongest control on this timescale. Continental crust is represented by an initial temperature difference of 600–800 °C between Moho and intruding magma depending on choices of intrusion depth and surface heat flow in the conductive geothermal gradient (Figure 4.6.a). Using a typical conductive geothermal gradient, these temperatures map onto crustal thicknesses of 30–50 km. High velocity layers commonly exist at $\sim$ 40 km depths beneath continental provinces (Moho temperatures of $\sim$ 530°C) [Ridley and Richards, 2010]. Oceanic crust is thinner (average thickness 7 km), with higher heat flow and an error function geothermal gradient, resulting in larger temperature differences of 700-900 °C between melt and country rocks (Figure 4.6.b) corresponding to Moho depths of 10–30 km. High velocity layers are commonly observed at $\sim$ 20 km depths under oceanic LIPs [Ridley and Richards, 2010].

As Figure 4.6 emphasizes, country rock rheology (as expressed through the Arhennius parameters n, E, and A in Table 4.7) has first order effects on relaxation times. While the list of plausible crustal rheological parameters in either case is long [Bürgmann and Dresen, 2008], the range of relaxation times for single mineralogies provide a rough guide to effects of composition. We also model the effect of water in both cases (dotted curves in Figure 4.6), illustrating that hydrated mineral assemblages will relax away deviatoric stresses with greater ease than their dry counterparts. Overall, we find that hotter emplacement temperatures and hydrated mineralogies are most consistent with relaxation times of order 10^6 years for both continental (some combination of anorthite and anorthite and clinopyroxene) and oceanic (clinopyroxene and olivine) settings. Chamber size exerts some control on the relaxation timescale, with smaller chambers representing smaller stress perturbations than larger chambers, but overall this is a secondary effect compared to environmental conditions.

Controls on critical chamber size

We now assess which of the three mechanisms for chamber destabilization presented here (elastic pressurization, buoyancy evolution, free surface effects) may be important for LIPs. Chemical evolution must occur before main–stage eruptions can begin, as LIPs are often predominately basalt. By comparing Figures 4.3 and 4.6, it is evident that under many cir-

cumstances chemical evolution occurs rapidly, followed by chamber failure that is eventually shut off due to relaxation of deviatoric stresses on a timescale similar to the main stage of many LIPs. Crustal relaxation times vary considerably depending on lower crustal rheology (Figure 4.6), however assuming hot, dry continental lower crust and cool, wet oceanic crust, it is quite reasonable to infer a relaxation (or equivalently an eruptive) timescale of $\sim 10^6$ years in both cases.

Nonetheless, there are also clearly cases for which isotropic stresses may be relaxed much more quickly. It is possible in some circumstances that buoyancy evolution is outpaced by viscous relaxation of stresses, and other mechanisms for destabilizing LIP magma chambers must operate. In a viscous regime in which continued influx does not induce eruptions through diking, LIP chambers will spread out along the Moho as gravity currents. Recharge related deviatoric stresses decay quickly in this regime, and the chamber will continue to stably expand until free surface shear stresses begin to accumulate around the chamber. For an axisymmetric viscous gravity current, the semi major axis a will scale with time as $a \approx Kt^n$, with K, n positive constants that depend on the boundary conditions, material properties and input flux [Lister and Kerr, 1989]. $n = 1/2$ for steady axisymmetric flow along a rigid boundary fed by constant flux Q, while $K = (g'Q^3/\mu)^{1/8}$ with μ the viscosity of the surrounding liquid (the warmed wall rocks), and g' gravity scaled by the density difference between the fluid and the surroundings.

Assuming a density difference of 300 kg/m^3, ambient viscosities of $\mu = 10^{16} - 10^{20}$ Pas, and a range of melt influx $Q = 10^0 - 10^{-3}$ km^3/yr, this scaling suggests that in a viscous regime, magma spreading at the Moho will attain a lengthscale comparable to its depth in $\sim 0.1 - 1$ million years. At this point we assume that elastic stresses due to free surface effects accumulate, initiating melt redistribution and eruptions. Progressive warming will lead to increased viscous response of the country rock, thus this mechanism provides a limit to the stable size of magma chambers, redistributing stored melt through diking or surface eruptions. However, there is no simple way to shut off eruptions via this mechanism, so surface eruptions would continue unimpeded for the duration of mantle melting. Based on the evidence for crustal modulation of mantle melting represented by distinct main phase eruptions, we rule out a purely viscous response to lower crustal melt flux. But such considerations do suggest the possibility of entirely intrusive LIPs that never erupt large volumes of lava.

4.7 Discussion

Provided melt extraction from the mantle is rapid, our analysis suggests that modulation of magma transport by the crust controls the progression of Large Igneous Province eruptions. The other end–member hypothesis, that surface emplacement of lavas tracks decompression melting evolution, is hard to reconcile with the observed timing and volume of main phase eruptions [e.g., Hooper et al., 2007] and the presence of cumulate layers at Moho depths beneath most flood basalt provinces [Ridley and Richards, 2010]. However we recognize

that the dynamics of plume/lithosphere interaction are significantly more complex than we assume here. Possible multiple maxima in plume head melting due to thermochemical effects [Leitch and Davies, 2001, Lin and van Keken, 2005], and deflection of plume material by Moho–level topography due to cratonic keels [Sleep et al., 2002] or passive continental margins [Sleep, 2007] may modulate the evolution of pressure–release melting during plume emplacement. Low matrix permeabilities will slow melt extraction and induce buoyant convective instabilities in the melting region [Hernlund et al., 2008] providing a possible melting feedback in the dynamics of plume–lithosphere interactions and well as possible episodic supply [Schmeling, 2006].

These processes are beyond the scope of this work, but may be important in a more complete integration of LIP phenomenology. We assume that decompression melting follows a simple single maximum trend, and that the scaling of section 4.4 for supply of ultramafic melt from the plume source to the lower crust holds over the timescale of many eruptions. This then provides the background supply for cyclic magma chamber filling and draining and controls the episodicity of surface eruptions.

Our analysis suggests two fundamental destabilization mechanisms for LIP magma reservoirs, given sufficient buoyancy to make the magmas eruptible. After the emplacement of magma at the Moho, the elastic response of country rocks initially allows fracture and dike propagation that accommodates the overpressure of rising melts. The length of this period of elastic behavior depends on country rock rheology, background stresses and the initial geothermal gradient, which varies between continental and oceanic settings. We propose that the main phase of LIP emplacement occurs during this time window, constraining the rheology of the lower crust to mineral assemblages that, upon heating, may relax away deviatoric stresses in ~ 1 Ma. For continental crust we find that either cool and wet or hot and dry combinations of anorthite and clinopyroxene will satisfy this constraint (Figure 4.6.a - b). For thinner oceanic crust hydrated mafic mineralogy is more suitable (Figure 4.6.b - c). The record of large–scale igneous events may in this way reflect the rheological structure and evolution of the crust.

After prolonged warming has occurred viscous relaxation of stresses dominates and magma chambers will grow stably without erupting. Limits to this growth may come from more rapid differentiation of magma in time, or from external sources of stress such as those exerted on the chamber by the free surface. This latter mechanism places a constraint on the size of a magma reservoir set by the lengthscale over which stable growth can occur (section 4.5): lateral size will scale with the depth of the reservoir, and implies that magma chambers residing below crust of different thickness, such as oceanic versus continental settings, have different maximum sizes. If individual LIP eruption volumes scale with magma chamber size, this predicts larger flows in continental provinces. Large background stresses may also be important for LIPs: preserved surface feeder dikes are largely linear in nature perhaps implying local extension in some provinces [Ray et al., 2007], while deep radial dike swarms perhaps associated with plume head emplacement can be thousands of kilometers long [Ernst and Buchan, 1997] and might broadly distribute primary melt.

Model for LIP crustal magma transport

In our model the progression of LIP emplacement begins with intrusive early magmatism, transitioning to a short largely extrusive main stage, then back to an intrusion–dominated regime that lasts for the duration of melt supply. Figure 4.7 illustrates this model qualitatively, through comparison of simulated plume head melting rates (modified from Leitch and Davies [2001]) and the inferred extrusion rate from the Columbia River Flood Basalt Province [Hooper et al., 2007]. These curves are qualitative, meant to illustrate the transitions in style of magmatism during LIPs in the framework of starting plume–lithosphere interactions.

Upon emplacement, chemical evolution from ultramafic to basaltic melt occurs. Mantle plume melts formed at sublithospheric depths will be more dense than typical mafic lower crustal rocks, and should therefore pond at the Moho or within the lower crust, undergoing extensive fractionation of mainly olivine and pyroxene before evolving large volumes of basaltic liquids able to rise to the surface. The duration of this fractionation phase depends on the melt flux and heat transfer out of the lower crust. There may be a period of melting and assimilation during high flux phases of melt emplacement before fractional crystallization can occur to further evolve the bulk of the melt (upper left of figure 4.7).

Next, brittle fracture of the lower crust due to stresses generated by the lower crustal basaltic magma reservoir induces dike emplacement and the main phase of LIP surface eruptions. This elastic phase depends strongly on the rheology of the lower crust; for sufficiently warm and/or weak country rocks it may be absent (top of Figure 4.7), suggesting the possibility of non–eruptive LIPs. This phase is relatively insensitive to the flux of magma, however, assuming that large reservoirs of basaltic melt exist.

Finally, viscous response of the lower crust stabilizes magma chambers, and they spread gravitationally until buoyancy or external triggers cause local disruption and elastic failure. We hypothesize that the accumulation of free surface stresses for laterally extensive LIP chambers limits their size. The viscous regime lasts the lifetime of melt supply, likely accompanied by dynamic surface topography as intrusions accumulate in the lower crust.

Throughout the lifetime of continued primitive melt flux, progressively more buoyant melt will move upward from the Moho, directed by the continued background stresses of plume impingement on the lithosphere. Emplaced through elastic failure of country rocks on short timescales, they will form a dense network of intrusions that, once frozen, put the lower crust into compression that is only relaxed through plate–scale spreading or viscous creep. This induces horizontal magma transport and sill emplacement that likely moves upward through time [Parsons et al., 1992] (Figure 4.1). Examples of such intrusion networks are observed, e.g., in the Ferrar LIP dolerite sills of Antarctica [Elliot and Fleming, 2008].

Individual LIP eruptions (which may reach volumes of $\leq 10^4$ km^3) are discrete in space and time, although the total erupted volumes are not well constrained in many cases [e.g., Mangan et al., 1986, Bryan et al., 2010]. The model here is consistent with a scenario in which individual eruptions tap individual magma chambers during the main phase. The timescale between eruptions would reflect the timescale for build-up of significant deviatoric

Mineralogy	log A ($MPa^{-n}\mu m^m\ s^{-1}$)	G (kJ/mol)	n	m
Dry Anorthite[a]	$10^{12.1}$	467	1	3
Wet Anorthite[a]	$10^{1.7}$	170	1	3
Dry Clinopyroxene[b]	$10^{15.1}$	560	1	3
Wet Clinopyroxene[c]	$10^{6.1}$	340	1	3
Dry Olivine[d]	$10^{6.1}$	510	3	0
Wet Olivine[d]	$10^{2.9}$	470	3	0

Table 4.1: Rheological parameters, taken from the experiments of a. Rybacki and Dresen [2000], b. Bystricky and Mackwell [2001], c. Hier-Majumder et al. [2005], d. Karato and Jung [2003]. For those cases where m$>$ 0, we take a nominal grainsize of 100 μm.

stress in the lower crust, set by the recharge timescale and the production of buoyancy due to volatile exsolution. Deep exsolution of CO_2 can destabilize chambers at relatively low crystal fractions ($< 35\%$) even at 30–40 km depths as magma differentiation proceeds (Figure 4.2).

Massive ultramafic intrusive complexes at Moho depths suggest that the largest fraction of magmas from the mantle may never rise above the lower most crust. Models for LIPs must directly address the processes associated with these deep magma bodies, especially the possible modes by which more evolved magmas may escape to generate surface eruptions and, perhaps, shallower magma bodies. We have shown that simple scaling considerations for viscoelastic deviatoric stress relaxation around a sill–like magma chamber due to progressive heating can explain a main stage eruptive timescale of $\sim$ 1 Ma, with continued magma emplacement over the $\sim$ 10 Ma mantle melting timescale.

Because the rheology of lower crustal rocks plays a fundamental role in setting the viscoelastic relaxation timescale (Figure 4.6), reconstructions of surface lava output through the cessation of main-phase eruptions [e.g., Barry et al., 2010] might provide a means of constraining lower crustal rheology. It is possible even that the spatial heterogeneity in lower crustal rocks may account for much of the variability observed among flood basalt provinces, between oceanic and continental settings and between continental LIPs emplaced through accreted terrains or stable cratonic settings [Wolff et al., 2008].

Our model offers three distinct hypotheses for the evolution and distribution of LIP magmas: (1) Main phase eruptions are shut off when viscous creep overwhelms elastic failure as the primary mechanism of relieving stresses in the lower crust (2) The lateral extent of individual high melt fraction, mafic magma chambers is limited by their depth of emplacement (3) The magmatic plumbing of LIPs moves upward in time, forming a network of individual sills that populate the lower crust. This causes continued dynamic topography over the lifetime of melt supply, as the rheology of the lower crust responds to magmatic input of heat and stress.

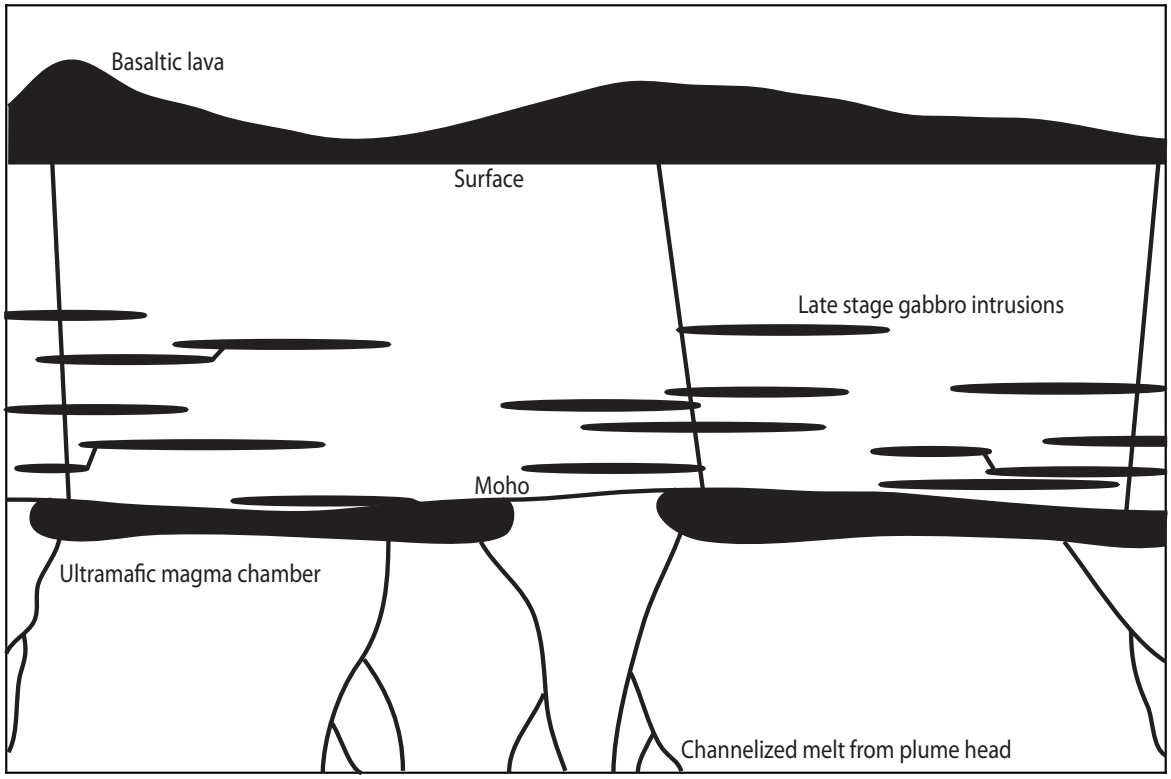

Figure 4.1: Conceptual model for LIP plumbing. Channelized melt from the upper mantle ponds at the base of the crust, forming large continuous magma reservoirs that differentiate to make basalts. These chambers inflate until destabilization occurs, erupting flood basalts on the surface and intruding gabbroic sills into higher crustal levels.

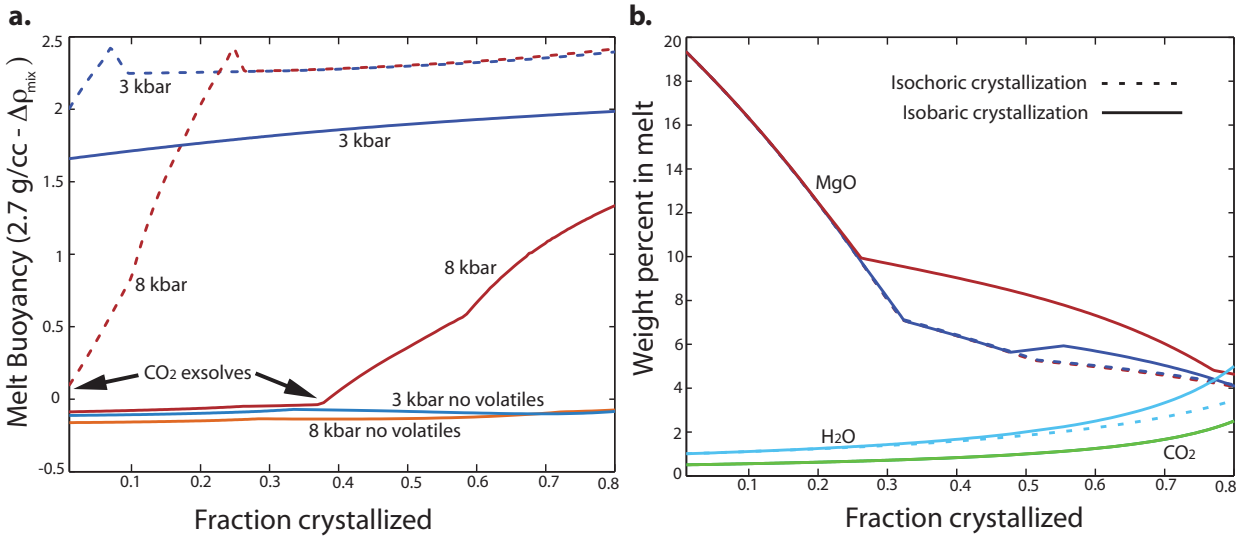

Figure 4.2: (*a*) Evolution of melt buoyancy during crystallization, with progressive volatile concentration and exsolution, at 300 MPa (blue curves, color in online version) and 800 MPa (red curves). Dashed lines are for isochoric crystallization, while solid lines are for isobaric crystallization. Buoyancy is calculated relative to 2700 kg/m^3, with exsolution of CO_2 at 800 MPa indicated by arrows. 300 MPa melts have exsolved CO_2 even at zero crystallinity. Mantle volatile contents of 0.1 wt% H_2O, 0.05 wt% CO_2 and ascent path described in the text are assumed. (*b*) Evolution of concentration for MgO in melt phase as a proxy for the chemical evolution of primitive magma. Concentration of CO_2 (green curve) and H_2O (blue curve) in the melt is similar at 3 and 800 MPa, but does vary slightly if crystallization is isochoric or isobaric.

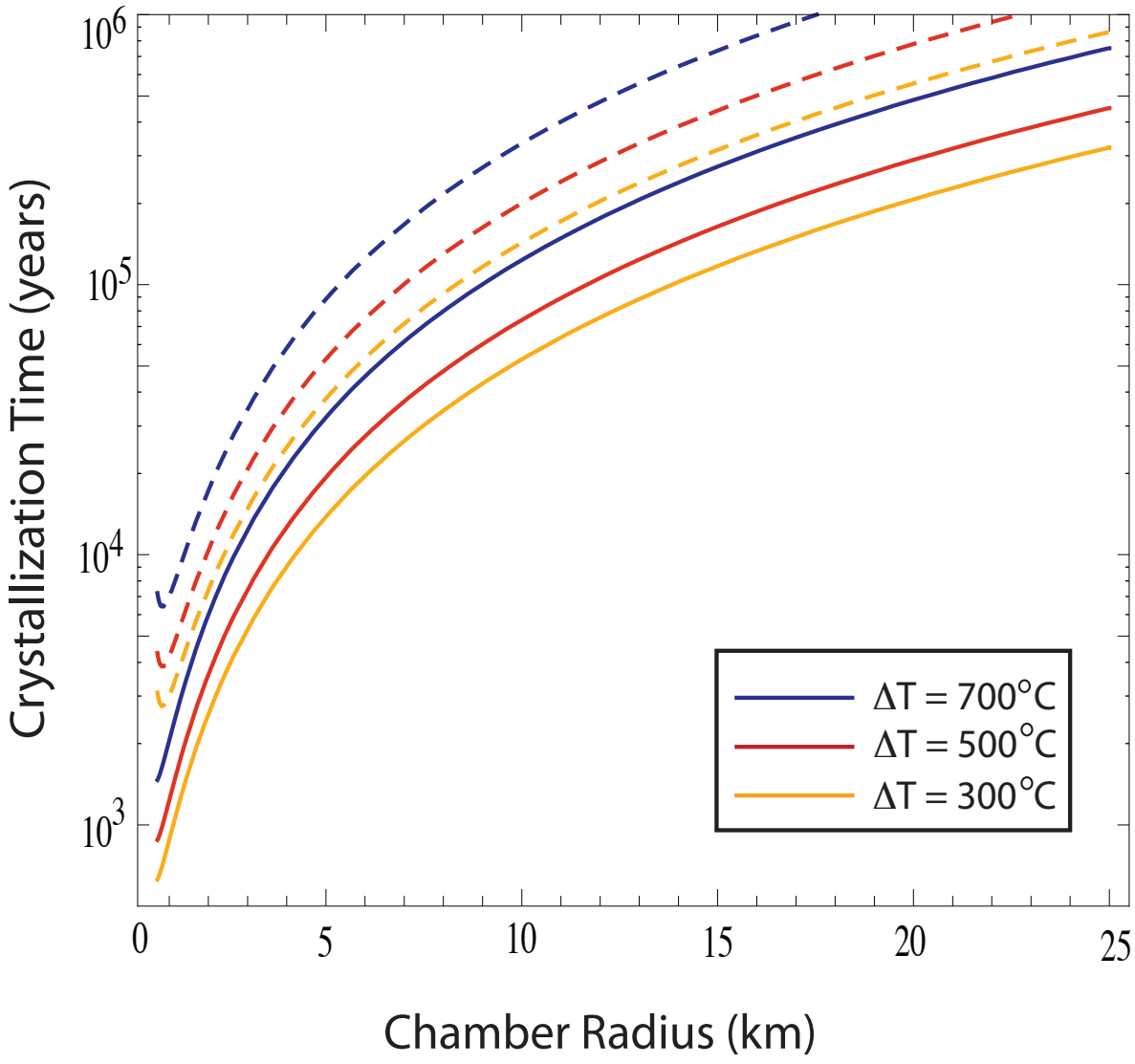

Figure 4.3: Buoyancy evolution timescale, taken to be the time until a critical fraction of the chamber has crystallized. Curves derive from equation 4.3 in the text, varying temperature difference between chamber and country rock. Magma influx is set to 10^{-2} km^3/yr. Larger magma influx values increase the incoming heat flux and thus increase the minimum chamber size required for crystallization. As discussed in the text, bounds for the critical crystal fraction are $\Phi = 0.8$ (dashed curves) in which fluid density $\rho_{mix} = 1500$ kg/m^3, and $\Phi = 0.3$ (solid curves) where $\rho_{mix} = 2700$ kg/m^3.

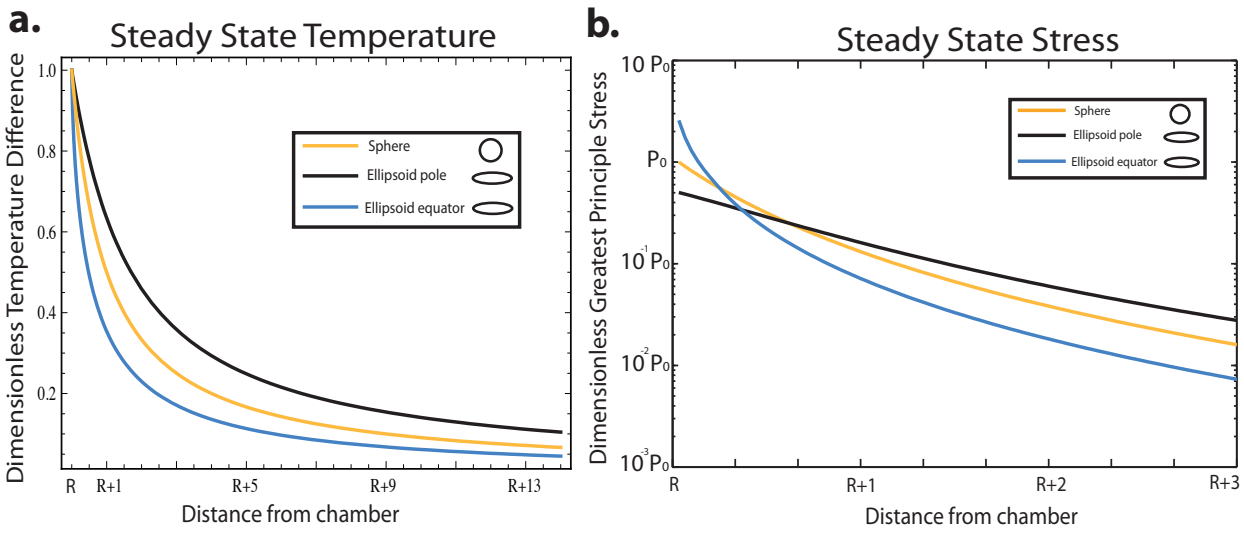

Figure 4.4: Comparison between a sphere and oblate spheroid with aspect ratio = 0.1 (a) Steady state temperatures in an infinite medium. For the spheroid polar heat transfer is enhanced relative to a sphere, while equatorial heat transfer is diminished. (b) Steady state greatest principle deviatoric stress in an infinite medium. Overpressure is set to P_0 at the chamber wall.

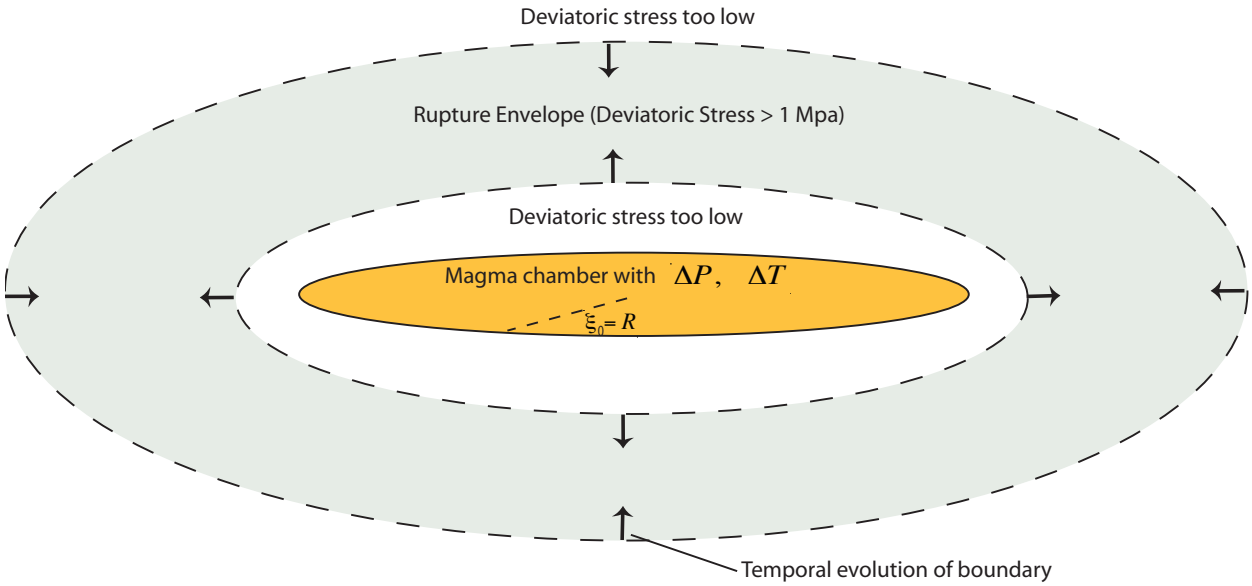

Figure 4.5: Thermomechanical model for time dependent stresses around a hot, pressurized magma chamber, defined by the curve $\xi_0 = R$. Initial deviatoric stresses from overpressured magma create a rupture envelope that surrounds the chamber, in which the critical stress required for dike formation is exceeded. Viscous creep induced by gradual heating of country rocks relaxes away deviatoric stresses and eventually inhibits dike formation.

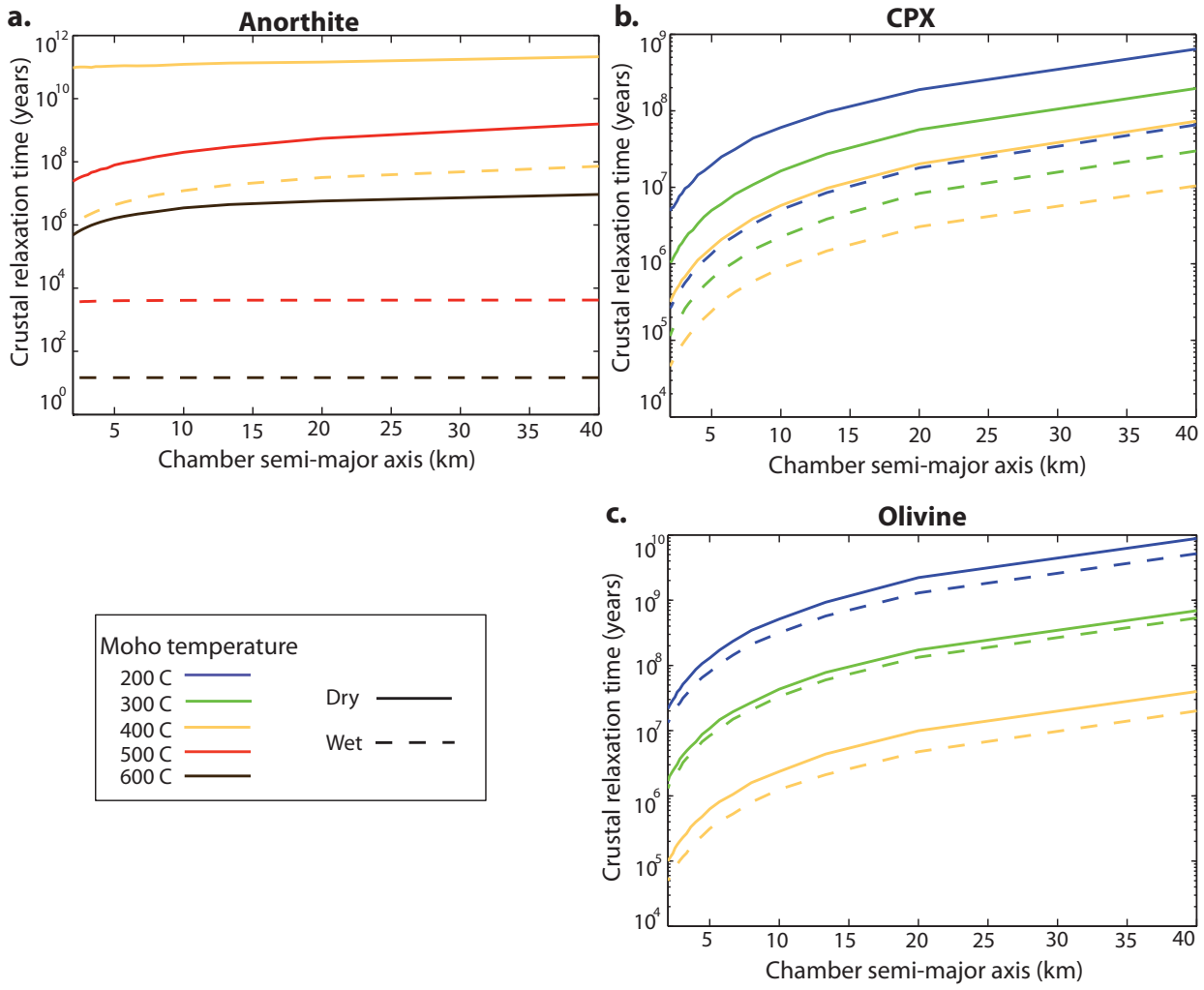

Figure 4.6: Time until deviatoric stresses relax below 1 MPa everywhere around the chamber, as evaluated from Equation 4.10. Curves are for different temperature contrast between intruded magma and crust (as proxy for varying Moho temperatures in continental and oceanic settings), calculated for power law rheological parameters of (a) anorthite, (b) clinopyroxene, and (c) olivine. Dashed curves correspond to equivalent but hydrated mineralology (Table 4.7).

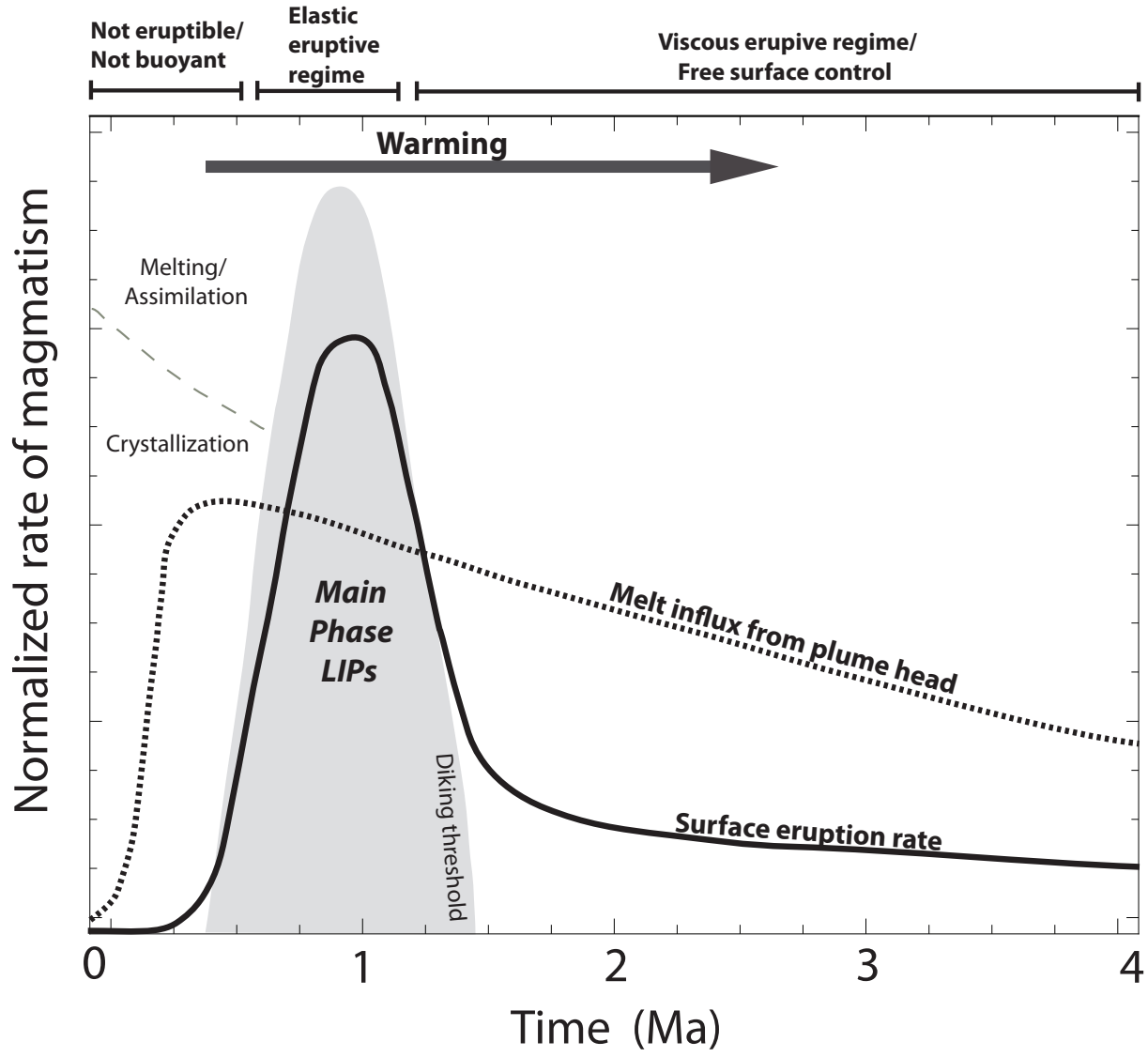

Figure 4.7: Qualitative regimes of LIP magmatism, with curves illustrating inferred eruption rate of the Columbia River Flood Basalt province [Hooper et al., 2007] and simplified evolution for generic LIP primary melt generation [Leitch and Davies, 2001]. Initial intrusive magmatism is associated with chemical evolution of Moho–level primary melts along with possible assimilation of crustal material, while the transition between largely extrusive and intrusive magmatism after $\sim$ 1 Ma of main phase eruptions reflects the onset of viscous creep in the lower crust. Free surface control provides a destabilizing trigger for eruptions in the viscous regime. Shaded gray region denotes a regime in which sufficiently cool crust promotes dike propagation and surface eruption of stored magma.

Chapter 5

Magma chamber growth during caldera–forming volcanic eruptions

5.1 Introduction

Magma chambers function both as repositories for melt rising through the crust and as reservoirs that feed individual volcanic eruptions. During the large volume silicic caldera–forming eruptions common in the geologic record, these functions occur on vastly different timescales as many hundred cubic kilometers of magma assembled and distilled in the crust over $10^4 - 10^6$ years are likely erupted in hours to days Self [2006], Turner and Costa [2007], Bryan et al. [2010]. Such eruptions perturb global climate, disperse ash over thousands of kilometers, and leave behind 10–100 km diameter calderas as evidence of contiguous magma chambers at shallow depths Lipman [2007]. Despite their considerable geologic importance, constraints on the mechanics of caldera forming eruptions are scarce. Here we propose that high crystal volume fractions of 30–60% in many erupted lavas Lindsay et al. [2001], Bachmann et al. [2002] impart stored magma with a yield stress that may modulate the progression of eruption and ultimately affect caldera size, the most characteristic feature of these events. We present a coupled conduit flow and magma chamber drainage model in which yield strength magma results in a multimodal distribution of erupted volumes, as is observed in the geologic record. After surface eruption initiates, magma near the conduit is mobilized and behaves as a fluid. However magma further away can remain locked and support elastic stresses while maintaining high fluid pore pressures. Eruption causes the yield surface separating mobile and locked magma to expand through the chamber. A rheological transition then defines the effective magma chamber boundary. Mobilization buffers chamber pressure, so progressive concentration of stresses during chamber growth may cause caldera collapse prior to the complete mobilization of stored magma. Our model implies that caldera size may not always reflect the spatial extent of magma storage, and provides constraints on the conditions necessary for and dynamics of extreme explosive eruptions.

The largest silicic volcanic eruptions in the geologic record have no historical analog.

They are known only through their eruptive products, leaving behind calderas that form as the surface collapses when erupting magma evacuates chambers at 5–15 km depths Lipman [2007]. It is generally assumed that calderas reflect the spatial dimensions of underlying magma storage. Petrologic evidence from "super–eruptions" (> 500 km^3 erupted Self [2006]) as well as smaller recent eruptions such as Pinatubo suggest that these magma reservoirs are incrementally assembled over $10^4 - 10^6$ years Halliday et al. [1989], Turner and Costa [2007]. Models indicate that mobilization of this reservoir and eruption triggering may be caused by injection of hot, volatile rich, mafic magma to the base of the locked crystal mush Pallister et al. [1992], Bachmann et al. [2002], Burgisser and Bergantz [2011]. However the relationship between geologic observables and the pre–eruptive development of these systems remains unconstrained.

Our study is motivated by the observation that many magmas from caldera forming eruptions, such as the Fish Canyon Tuff Bachmann et al. [2002] and Atana Ignimbrite Lindsay et al. [2001] are crystal rich. Crystal fractions in these ignimbrites approach the maximum packing limit Stickel and Powell [2005] where a rheological phase transition from liquid to solid–like behavior occurs. Many other smaller deposits have crystal fractions in the 10–30% range, in which connected networks of crystals may impart the suspension with an effective yield strength Philpotts et al. [1998], Saar et al. [2001]. We focus on caldera–forming silicic eruptions because these events have significant impact on other Earth systems Rampino and Self [1992], and because large erupted volumes minimize the nonlinear feedbacks between chamber and conduit processes exhibited by smaller silicic eruptions Jaupart and Allègre [1991] (Supplementary Methods).

The yielding behavior of highly viscous and crystal rich fluid has two important consequences for erupting stored magma. Foremost, it creates an evolving partition between mobile and locked portions of the magma chamber set by the position of the yield surface. Second, the yield surface maintains a pore pressure difference between the rheologically locked and mobilized portions of the magma chamber. Thus the differential stress state on eruptive timescales (set by magma over–pressure relative to lithostatic pressure) in country rocks may differ from that of locked magma, which may itself differ from mobilized magma (Figure 5.1).

It is unlikely that complete mobilization always occurs prior to eruption for mechanical reasons. Elastic deviatoric stresses induced by the free surface become significant when the lateral extent of a pressurized magma chamber approaches its depth Gudmundsson [1998], providing the pathways and impetus for caldera collapse. Calderas with lateral dimensions that exceed their depth by up to an order of magnitude (such as La Garita caldera of the Fish Canyon Tuff Lipman [2007]) are proxies for magma chambers that, fully mobile, would be extremely mechanically unstable. Mobilization as a result of mafic intrusion proceeds much more slowly than eruption and is prone to buoyancy instabilities Burgisser and Bergantz [2011], implying that free surface stresses will facilitate eruption before chamber–wide mixing is complete. This is corroborated by evidence that many silicic eruptions were sourced through central vents prior to caldera collapse Self et al. [1986], Geyer and Marti [2008]. Finally, available historical analogs indicate that a significant fraction of the total eruptive

output (> 50% for Pinatubo and Katmai Stix and Kobayashi [2008]) may be emplaced prior to caldera formation. The syn–eruptive progression of caldera formation into a fully mobile chamber is important after fractures decouple the caldera roof from country rocks Kennedy et al. [2008]. However it does not necessarilly represent the majority of erupted magma or the primary vehicle of mass transfer during many large caldera–forming eruptions.

Yielding represents an alternative way to understand progression towards caldera formation in these systems. Eruption begins with evacuation of initially mobilized magma from a shallow, low aspect ratio chamber. Pressure gradients are homogenized across mobile magma by viscous flow, but low suspension permeability and high melt viscosity Bachmann [2004] maintain high pressures in locked magma. As the yield surface expands (Figure 5.3a), mobilization of material buffers pressure in the fluid chamber towards its initial value (Figure 5.3b). If crustal strength is similar to the initial over–pressure triggering eruption, caldera collapse may occur during growth of the mobilized chamber as aspect ratio and hence stress concentration increases. However if the crust can sustain this stress accumulation around the growing chamber, all available magma will be mobilized and decompression continues until mechanical failure of roof rocks occurs.

To gain insight into the consequences of yielding rheology on eruption dynamics, we developed a numerical model that couples flow in a conduit with evacuation of a laterally extensive magma chamber located beneath a free surface. We model time–dependent magma chamber evacuation and steady, isothermal flow through a cylindrical conduit (Figure 5.1). Chamber deformation is calculated with an equation of state that relates mass removal by eruption to deformation of the (assumed elastic) surroundings, while yielding and chamber growth proceed according to the von Mises criterion. Processes that occur on magma mixing rather than much shorter eruptive timescales, such as magma recharge, are neglected. We assume that over–pressure gradually develops during magma chamber construction, producing elastic stresses smaller than the crust failure strength but larger than lithostatic stress. Surface eruption is then triggered by some combination of rapid recharge, crystallization, and volatile exsolution Tait et al. [1989] that mobilize a subset of the reservoir and pressurize it past a crust failure threshold (Figure 5.1).

5.2 Model derivation

We model an (assumed isothermal) magma chamber whose pressure P_C evolves in time due to material transfer (Figure 5.1) as

$$\eta \frac{dP_C}{dt} = \frac{1}{\rho_{mix}} \left(Q_I - Q_O \right) \tag{5.1}$$

where Q_I and Q_O are the mass fluxes of magma into and out of the chamber, ρ_{mix} is a mixture magma density and η an effective chamber volume divided by a bulk modulusHuppert and Woods [2002] that accounts for deformation of the host rock as well as the three–phase mixture of bubbles, crystals and melt in the chamber. During explosive eruptions $Q_O >> Q_I$,

so we consider only extraction from a fixed reservoir. Similar simplifications may be made by comparing the timescale for chamber pressure change

$$\tau_{chamber} \sim \frac{\Delta P_C V_C \rho_{mix}}{K_{mix} Q_O}, \tag{5.2}$$

with the timescale for magma ascent

$$\tau_{ascent} \sim \frac{H}{\bar{u}}, \tag{5.3}$$

where $\Delta P_C = P_C - \rho_s g H$ is the chamber over–pressure with g = 9.8 m/s^2, ρ_s the density of crustal rocks, H the conduit length, V_C the chamber volume and K_{mix} the effective bulk modulus.

For large eruptions we take representative values of $V_C \sim 10^{12}$ m^3, $\Delta P_{ch} = 10^7$ Pa, $r = 10 - 100$ m, $Q_O = \pi r^2 \bar{u} \rho_{mix}$, $K_{mix} = 10^7 - 10^9$ Pa to account for the important effect of bubbles on magma compressibility Huppert and Woods [2002], $H = 7500$ m, and representative velocity $\bar{u} = 1 - 10$ m/s (below fragmentation). $\tau_{chamber} >> \tau_{ascent}$ for these parameter choices, so we assume steady conduit flow and time–dependent chamber evacuation.

Our model considers chamber evolution of the form

$$\rho_0 V_{0,C} + \int_0^t \dot{M}(\tau) d\tau = V_C(P_C)/v_S(P_C), \tag{5.4}$$

$$\nabla \cdot \underline{\sigma} = \underline{0}, \tag{5.5}$$

$$\sigma_{ij} = \lambda \epsilon_{kk} \delta_{ij} + 2\mu \epsilon_{ij}, \tag{5.6}$$

where λ and μ are the Lamé constants, subject to boundary conditions on the chamber boundary ∂S

$$\sigma_n|_{\partial S} = \Delta P_C, \tag{5.7}$$

the free surface

$$\sigma_n|_{z=H} = \sigma_t|_{z=H} = 0, \tag{5.8}$$

and an initial condition on the contact between locked magma and country rocks ∂R

$$\sigma_n|_{\partial R} = \Delta P_0. \tag{5.9}$$

This reference state accounts for the development of over–pressure $\Delta P_0 = P_0 - \rho_s g H$ in the locked magma prior to the onset of eruption. The condition that $0 \leq \Delta P_0 \leq \Delta P_C$ holds initially, but in the case of large magma yield stress $\Delta P_C \leq 0 \leq \Delta P_0$ may occur during chamber growth.

Equation 5.4 is an equation of state for mobile fluid in the magma chamber, relating a reference (initial) undeformed chamber volume $V_{0,C}$, initial bulk density ρ_0, the deformed volume of the cavity V_C, the specific volume v_S (volume per unit mass) of the 3-phase fluid inside the chamber, the time derivative of chamber mass $\dot{M}$ and the chamber pressure P_C.

Deformed chamber volumes are calculated assuming that the chamber surroundings are a linear elastic solid (Equation 5.5), with possibly differing elastic moduli in the immobile portions of the chamber (Figure 1) and the country rocks. σ_n and σ_t are normal and tangential stresses.

We model steady one–dimensional isothermal conduit flow of magma, solid particles and gas, in which conservation of mass and momentum can be expressed as Mastin [2002]

$$\frac{\partial P}{\partial z} = \frac{-\left(\rho_{mix} g + f\right)}{1 - \frac{u^2}{c_s^2}}, \tag{5.10}$$

$$\rho_{mix} = \left(\frac{n}{\rho_g} + \frac{1-n}{\left(\frac{\chi}{\rho_s} + \frac{1-\chi}{\rho_l}\right)^{-1}} \right)^{-1} \tag{5.11}$$

where u is the cross–section averaged mixture velocity at height z above the magma chamber and P is pressure. Equation 5.11 is the density of a mixture of solid, liquid and gas with densities ρ_s, ρ_l, ρ_g, with n the mass fraction of gas (water and CO_2) calculated as a function of pressure from Papale (1999)Papale [1999b] assuming Fish Canyon Tuff compositions Bachmann et al. [2002]. $\chi = 0.4$ is the mass fraction of solids, taken to be constant. Although χ may vary as magma yield stress in the chamber varies (a parameter in our model) varies, we hold it constant for simplicity. We will show that the presence of choked flow at the vent prevents variation in all conduit flow parameters from affecting the end result of chamber evacuation, although they will affect eruptive timescales. The assumption of yielding (Bingham) rheology in the magma chamber does not conflict with equation 5.10, as choked–flow induced strain rates ensure mobilization (at least in near wall regions of the conduit) throughout eruption. Fragmentation occurs at a critical strain rate Papale [1999a] , at which point the friction factor f and mixture sound speed c_s are calculated from turbulent approximations Mastin [2002]. Below the fragmentation depth $c_s^2 = (\partial P/\partial \rho_{mix})$ is calculated numerically to conserve mass, while the friction factor due to laminar flow through a cylindrical pipe is

$$f = 8\Lambda \frac{\mu_m(n,\chi) u}{r^2} \tag{5.12}$$

with $\mu_m(n,\chi)$ the apparent viscosity. We note that f may be simply represented for other conduit geometries. Non-circular or fissure-like conduits require corrections only to this friction term.

$$\Lambda = \frac{1}{1 + a\left(\frac{\mathrm{Na}}{\sqrt{\mathrm{Gz}}}\right)^{1.5}} \tag{5.13}$$

is an empirical correction to the friction factor due to viscous heating Costa et al. [2007] with $a = 0.3$. $\mathrm{Na} = b\mu_r \bar{u}^2/k$ is the Nahme–Griffith number measuring the relative importance of viscous heating and conduction with dimensionless $b = 0.05$; $\mathrm{Gz} = \rho_{mix} c_p \bar{u} r^2/kH$ is the Graetz number measuring vertical advective heat transport versus lateral conduction. For

representative values as before and $\mu_r = \mu_m(n = 0, \chi = 0) \sim 10^7$ Pas (Fish Canyon Tuff melt composition viscosity at 750° C Bachmann et al. [2002]), Na $= 10^6 - 10^8$ and Gz $= 10^7 - 10^9$. Here c_p is specific heat capacity, and k is thermal conductivity. While likely important for silicic eruptions, the viscous heating parameterized by Λ does not significantly affect our results, which are dictated by the conduit boundary conditions (in particular choked flow).

Viscosity in our model thus depends on magma composition, water content and temperature Hui and Zhang [2007], bubble Pal [2003] as well as crystal Caricchi et al. [2007] volume fraction, strain rate Caricchi et al. [2007], and viscous heating Costa et al. [2007], Hess et al. [2008]. We neglect wall–localized heating and radial viscosity variation due to lateral variations in strain rate (although these are parameterized through Λ, which decreases the reference apparent viscosity by up to 3 orders of magnitude for the conditions of interest). We similarly neglect explicit treatment of temperature variations with height Mastin and Ghiorso [2001], but note that non–adiabatic temperatures and radial variation in heat transfer in the conduit during silicic super-eruptions may be reflected in textural features of erupted lavas Blundy et al. [2006] and could account for heating comparable to that attributed to magma chamber rejuvenation Bachmann et al. [2002].

Equations 5.10-5.11 are subject to boundary conditions that couple time evolving chamber pressure to the conduit:

$$P|_{z=0} = \Delta P_C \tag{5.14}$$

and choked flow $u = c_s$ at the surface, a condition that is likely realized during most explosive eruptions Dufek and Bergantz [2005]

$$u|_{z=H} = c_s. \tag{5.15}$$

We adopt a von Mises criterion for mobilizing locked magma during eruption, calculated as

$$\sigma_v = \sqrt{3J_2} \tag{5.16}$$

where J_2 is the second deviatoric stress invariant. If decompression induces elastic stresses in rheologically locked magma σ_v such that the von Mises yield stress σ_{magma} is exceeded, this locked magma mobilizes. The result is a larger chamber radius and increased chamber pressure. Pressure increase (buffering) occurs as incorporated material has the initial locked magma pressure P_0. The small difference in specific volume between locked magma at the initial over–pressure and that of mobilized magma is also accounted for in this step. It is assumed that within the locked, unmobilized magma there is no deviatoric stress at onset of eruption.

We solve for the expanding chamber radius iteratively, beginning with a spherical chamber of radius 2 km, such that von Mises stresses outside the new chamber radius are everywhere lower than σ_{magma}. Our chamber is confined to a layer of half–thickness 2 km, so that there is one degree of freedom for chamber expansion. While this geometrical constraint is imposed for simplicity, we expect it to be approximately realized in nature, as large aspect ratio chambers and stress concentration in regions of high boundary curvature will promote

lateral rather than vertical expansion. The position of the yield surface in unsteady flow of yielding fluids is a free–boundary problem with generally more structure and subtlety than our treatment. By analogy to Bingham channel flows Taylor and Wilson [1997] and Saffman-Taylor problems Alexandrou and Entov [1997], we expect that boundary layers of unyielded fluid may develop during syn–eruptive mobilization of locked magma. Preferential yielding in a stratified chamber is a natural extension of this model, although it is beyond the scope of our efforts here. Magma yield stress functions only to modulate eruption time (similar to conduit flow processes) in cases where complete chamber mobilization occurs.

At each time step we evaluate maximum von Mises stress between the chamber (defined by the yield surface) and the surface, using a critical crustal yield strength σ_{cr} as a crustal failure metric. Deviatoric stresses are calculated as a departure from the reference stress distribution set by specifying the size of the locked magma reservoir and its over–pressure ΔP_0 (equation 5.9). Locked zone over–pressures approaching the initial mobilized chamber over–pressure represent a reference von Mises stress state that is not perturbed significantly until large under–pressures are reached. This situation progresses to caldera failure only after complete mobilization of the reservoir and chamber underpressuring. Conversely, small locked zone over–pressures allow significant von Mises stresses to accumulate during chamber growth and hence caldera formation before complete mobilization is possible.

Elastic stresses and strains (equations 5.5–5.8) are calculated numerically using the axisymmetric program mode in FEAP, version 8.3 Taylor [2008]. The two–point conduit boundary value problem of equation 5.11 is solved with a bisection and shooting method and 4th order Runge Kutta integration with adaptive step size control. Newton–Raphson iteration is performed at each timestep to ensure the chamber pressure remains consistent both with the elastic deformation of the chamber and the withdrawal of material through the conduit.

5.3 Yielding rheology of magma

The existence and magnitude of a yield stress for crystal rich silicate melts is controversial. Although a number of experiments Ryerson et al. [1988], Lejeune and Richet [1995], Caricchi et al. [2007], Champallier et al. [2008aa] and theoretical studies Kerr and Lister [1991], Saar et al. [2001], Walsh and Saar [2008] concern magmatic yield strength, it has been difficult to determine experimentally for the high crystal fractions and apparent viscosities of interest Champallier et al. [2008aa]. It is complicated by the likelihood that yield stress may vary as a function of crystal fraction and shear rate Heymann et al. [2002]. The withdrawal of crystal rich magma at eruptive rates may also push the suspension through a jamming transition Cates et al. [1998], Liu and Nagel [1998], in which an effective yield stress exist at crystal volume fractions that are much lower than the maximum packing fraction. For example, flattened prismatic crystals form a percolating network at volume fractions in the range of 0.08 – 0.29 Saar et al. [2001], that may sustain elastic stresses over eruptive timescales.

In the absence of predictions for yield stress that are directly applicable to silicic crystal rich magmas, we use the model of Gay et al. (1969) Gay et al. [1969] to estimate a range of

yield stresses that may be reasonable for crystal rich silicic magmas. This model is empirical, but allows us to explore yield strength as a function of parameters that can be estimated from field deposits, experiments or predicted theoretically. It also provides a comparison with the work of Burgisser and Bergantz (2011) Burgisser and Bergantz [2011], whose mechanism for chamber–wide mobilization before eruption relies on low suspension yield stress as calculated from the Gay et al. (1969) model.

Yield stress in the Gay et al. (1969) model requires estimates of the mean crystal size D_p, crystal volume fraction Φ, maximum packing fraction Φ_m, shape factor ξ and geometric standard deviation Σ. Crystal sizes in large ash–flow tuffs range considerably, from 0.1 mm – 10 mm. Mean crystal sizes are in general correlated with the crystallinity of the magmas Bindeman [2003], and are > 1 mm for many large eruptions. We take $D_p = 10$ mm as an upper bound from published crystal size distributions Bindeman [2003], Mock and Jerram [2005], although we experiment with sizes down to $D_p = 0.1$ mm for comparison with Burgisser and Bergantz (2011). We expect that crystal sizes as measured from erupted lavas under–represent the mean crystal size in the magma chamber as many crystals exhibit evidence of melting, fracture or breaking during eruption Hess et al. [2008], and numerous small microlite crystals may form upon ascent Hammer et al. [1999].

Figure 5.2 shows yield stresses σ_{magma} as a function of crystal volume fraction Φ predicted by this model, using shape factor $\xi = 0.5$, along with curves that represent bounds defined by $D_p = 0.1 - 10$ mm, $\Sigma = 1.25$ (a low proportion of small crystals), and $\Phi_m = 0.6 - 0.84$ Pinkerton and Stevenson [1992], Burgisser and Bergantz [2011]. Grey boxes represent the range of Φ estimated for magma with $30 - 60\%$ crystals and $D_p = 0.5 - 10$ mm in the two cases where $\Phi_m = 0.6$ (light) and $\Phi_m = 0.84$ (dark), although we recognize that the Gay et al. model may not be valid as Φ approaches Φ_m [Pinkerton and Stevenson, 1992]. $\Phi_m = 0.6$ is the classical maximum packing for geological fluids Marsh [1981], while 0.84 exceeds the hexagonal close packing of mono–dispersed spheres (0.74) but is used to compare with Burgisser and Bergantz [2011]. Predicted yield stress for this range of crystallinity lies in the range of $\sigma_{magma} = 10^1 - 10^7$ Pa. We use these values in our model, with the recognition that better characterization of yield stress is required to constrain this aspect of our model. We also note that yield stress is a quantity defined before flow occurs, i.e., the stress required to initiate motion. Once yielding occurs, magma deforms viscously. Small yield strengths measured in lavas after mobilization (e.g., Pinkerton and Stevenson, 1992[Pinkerton and Stevenson, 1992]) thus do not characterize the quantity of interest in our model and are lower bounds to magma yield stress.

5.4 Results

The eruptive dynamics predicted by this model are straightforward. Rather than exponentially decreasing discharge during decompression–controlled eruptions Huppert and Woods [2002], buffering of the chamber pressure and thus discharge occurs throughout the mobilization period (Figure 5.3b). Decompression and vesiculation of ascending magma induces

acceleration to choked flow near the surface, so poorly known parameters of conduit flow (magma volatile content, conduit geometry, mixture viscosity) play no role in average eruption dynamics and do not affect total volume erupted. If chamber mobilization is complete or magma yield stress is large enough to allow chamber underpressure during yielding, the eruption is a siphon–like flow driven primarily by gas exsolution with a lower limit to basal pressure given by the potential energy of dissolved gas in the chamber rather than lithostatic pressure Druitt and Sparks [1984]. After caldera collapse begins, eruption dynamics are driven by interaction with the subsiding caldera roof Kennedy et al. [2008] and are not modeled here.

Important but unknown parameters in our model include the depth and lateral extent of the locked magma reservoir, over–pressure in locked magma as well as the initial eruption triggering pressure, yield strength of immobile magma and that of the overlying roof rocks. Although unknown in general, constraints on these parameters come from field, laboratory and petrologic work Lipman [2007], Geyer and Marti [2008], Caricchi et al. [2007]. We vary magma volatile content, chamber crystallinity (yield stress), magma viscosity, chamber depth, the caldera scale strength of roof rocks (the critical von Mises stress σ_{cr}), conduit radius, and difference in elastic moduli (Young's Modulus $E_{cr} - E_{magma}$ and Poisson's Ratio $\nu_{cr} - \nu_{magma}$) between locked magma and country rocks, lateral extent (aspect ratio) of locked magma reservoir. Geometrical parameters are better constrained than evolving intensive variables such as pressure or the rheology of crystal rich, bubbly magma. To deal with such uncertainty we assume a uniform distribution of all parameters, and perform a suite of Monte Carlo eruption simulations.

We fix the volume of the crystal rich reservoir to be a disk with rounded edges of half–thickness 2 km, situated at 7.5 km depth (Figure 5.1). This depth is similar to estimates for magma emplacement pressures (2–3 kbar Lipman [2007]). We vary the lateral radius of stored magma between 5 and 30 km, which corresponds to roof aspect ratios (depth/diameter) of 0.75–0.125. Aspect ratio may exert primary control on the final geometry of collapse calderas Acocella [2007], Marti et al. [2008], however studies to date do not consider the mechanical consequences of only partially fluid reservoirs during collapse. We assume a fixed CO_2 mass fraction of $n_{CO2} = 0.1$, but a uniform prior distribution of all other parameters (Table 5.1).

Despite this uniform prior we find a bimodal distribution of eruption volumes, reflecting caldera failure before and after complete mobilization of locked magma (green and blue symbols in Figure 5.3c). A small subset of eruptions (red symbols in Figure 5.3c) end without caldera formation, as country rocks strong enough to sustain under–pressure that exceeds the potential energy available for conduit flow. Eruptions in which the magma yield stress is $> 1\%$ of crust yield stress and is similar to the initial pressure difference between mobile and locked magmas exhibit caldera failure before complete mobilization (Figure 5.3b–c).

Figure 5.4a–f shows that caldera forming eruptive volumes are strongly bimodal, with different parameter dependence for the case of complete mobilization (blue symbols) versus partial mobilization (red symbols) at caldera collapse. Volumes comparable to super–eruptions (> 500 km^3) require full mobilization and depend in a meaningful way only on the strength of country rocks – the critical roof rock von Mises stress σ_{cr} – and locked zone

radius (roof aspect ratio). The yield strength of magma is constrained from below by the pressure difference between locked magma and initial mobile chamber, and the combination of these three parameters determine whether complete mobilization can occur (see also main text Figure 2c). Contrast in elastic parameters between locked magma and country rocks does not appear to affect erupted volumes, although we note that different choices of country rock Young's modulus affects the magnitude of strain in crustal rocks in response to chamber pressure changes and hence the likelihood of caldera failure. For our chosen $E_{crust} = 10$ GPa, we find a small subset of results ($\sim 1\%$) in which strains become large and unphysical displacements occur in finite element simulations. As the assumption of small strain linear elasticity breaks down as strains approach order unity, we discard simulations in which this occurs. Figure 5.4f shows that conduit radius does not affect the results, given choked flow at the surface. Variation in magma volatile content and Poisson's ratio contrast between crustal rocks and locked magma (not plotted) similarly do not affect the results.

5.5 Discussion

Long term reservoir assembly in the shallow crust likely buffers magma crystallinity near the maximum packing fraction Dufek and Bachmann [2010] while the reservoir grows and pressurizes, although magnitudes of magma over–pressure and yield stress are uncertain. Effective yield stresses similar to stresses that trigger the eruption thus seem reasonable, augmented on eruption timescales by a jamming phase transition which endows the suspension with additional elastic strength Liu and Nagel [1998]. This would imply that many caldera forming systems fail before complete mobilization. However volumes typical of super–eruptions generally cannot be attained in this regime. The largest eruptions require strong country rocks (a critical von Mises stress of $> \mathcal{O}(10^8)$ Pa) and large magma storage zones (radii of > 20 km) irrespective of other parameters (Figures 5.3, 5.4 and 5.5), ending always in an under–pressured state.

Our simulations generate a size distribution of caldera–forming eruptions that may be compared to the geologic record (Figure 5.6). Data come from two sources. For Holocene eruptions, we use the Smithsonian Institution Global Volcanism Program database. This database has been demonstrated to be complete through eruption of magnitude 4 and larger Coles and Sparks [2006]. Eruption magnitude is defined generally as a combination of data from plume height and volume erupted Newhall and Self [1982], Mason et al. [2004]. We use a formula based solely on erupted volume

$$\mathrm{M} = \log_{10}(DRE) - 7 \tag{5.17}$$

where DRE is the Dense Rock Equivalent magma mass in kilograms to calculate eruption magnitude for all our data.

For caldera forming eruptions, we use the worldwide Collapse Caldera Database Geyer and Marti [2008] to estimate magnitude and frequency of volcanic eruptions that are most similar to those we model. This database includes calderas that vary in age from historical

eruptions up to 500 Ma, although the age distribution peaks around 30 Ma Geyer and Marti [2008]. We expect that there are systematic preservation biases reflected in this wide age distribution. Therefore we used the upper limits reported for eruption volume to make the curves in Figure 3 of the main text.

Despite model assumptions and the incomplete nature of available data, the predicted magnitude–frequency distribution is statistically similar to that derived from available data on worldwide collapse calderas. The distribution of large eruptions aligns best with that of completely mobilized model runs (blue bars in Figure 5.6a, Supplementary Methods). However the data exhibit a more complex and multimodal distribution as erupted volume decreases. In our model, premature caldera failure leads to an increase in small eruptions as is observed in the data. Quantitative comparison is carried out using a Kolmogorov–Smirnov (KS) test with a significance level of 5%. Based on this test, both simulated and database derived caldera forming eruptions arise from a different underlying distribution than the complete Holocene eruption catalog at 95% confidence. The complete distribution of caldera forming eruptions and model results also fail this similarity test, however if we exclude caldera forming eruptions smaller than 3 km^3 from both datasets the two distributions pass the KS test indicating that the model results best align with data from larger eruptions.

We do not strive for quantitative agreement between modeled eruptions and data, as the true distribution of governing parameters is unknown. We expect that refining the prior distribution of input parameters would permit a better match to observational data, as would including smaller locked magma zones (the lower size limit considered here is 5 km radius). Nevertheless, similarity between modeled erupted volumes and the observational record is robust. Both modeled and real caldera distributions are distinct from that of recorded Holocene eruptions (Figure 5.6b). The conditions leading to and dynamics of caldera–forming eruptions are thus not common to all volcanic eruptions.

We suggest that basic observables of caldera forming eruptions such as erupted volume and caldera size reflect the natural variability of crustal strength and magma rheology. Yielding during eruption may generate calderas that do not reflect the lateral dimension of the underlying magma reservoir, leaving a significant fraction of magma locked as roof failure occurs. For caldera radii much less than that of the reservoir (Figure 5.5) residual magma may not be mobilized syn–collapse, providing a seed for future eruption and development of caldera complexes Lipman [2007]. Heterogeneity of phenocryst populations and inferred differentiation times within single eruptive units observed in multi–cycle caldera systems Cathey and Nash [2004] may be a consequence of similar episodic magmatic processes. Our work challenges models for silicic eruptions that require complete mobilization and chamber–wide convection prior to eruption triggering Burgisser and Bergantz [2011], however it does not preclude bulk chemical homogenization through recharge–driven stirring of silicic magma reservoirs Bachmann [2004]. Finally, recent eruptions may offer direct tests of this model, as yielding should be reflected in the eruptive stratigraphy of isotopic proxies for subsurface magma movement prior to and during eruption Kayzar et al. [2009].

The timescale–dependence of magma rheology plays a fundamental role in magma transport through the crust, as it does for controlling the style and magnitude of volcanic erup-

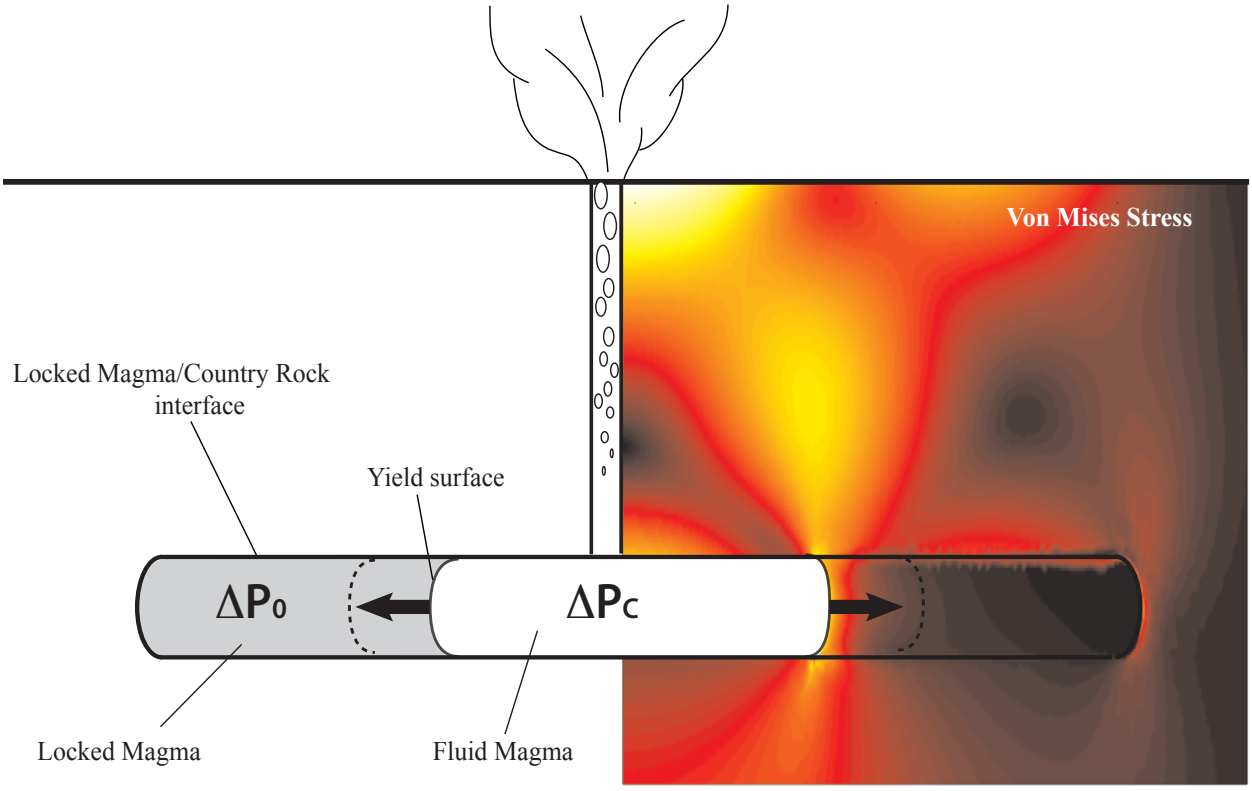

Figure 5.1: Schematic of the coupled conduit flow and chamber deformation model. Removal of magma through the conduit mobilizes locked magma in a reservoir at depth. The inner boundary of this magma chamber (the yield surface) grows in time as magma erupts, and is represented by an expanding pressurized cavity in an elastic half–space. The outer interface between locked magma and country rock remains fixed with initial over–pressure ΔP_0. This pre–stressed condition generates two zones of stress concentration around the reservoir during mobilization (shaded, warm colors indicate larger stress). In this case the locked magma overpressure is 10 times smaller than that of the mobile magma.

tions. This study views magma chambers dynamically, defined by a rheological transition that occurs on the timescale of eruptions. It is therefore separate from the dynamics of magma chamber convection and from the petrologic role of these structures in facilitating magma differentiation and ascent through the crust. Such a distinction is similar in spirit to the geodynamic and geochemical definitions of the lithosphere Anderson [1995], and highlights the general problem in Earth Science of relating static measurements and dynamics on human timescales to inaccessible domains of time and space.

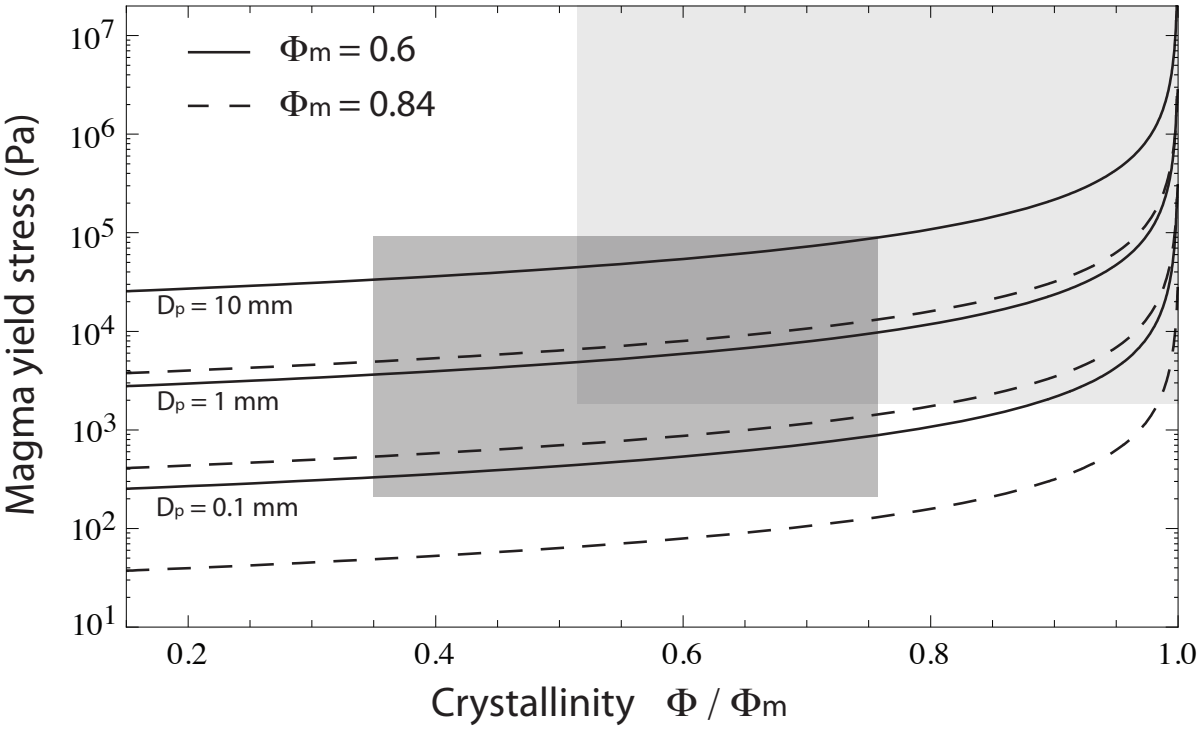

Figure 5.2: Yield stress as a function of crystallinity (normalized by the maximum packing fraction) predicted by the semi–empirical model of Gay et al. (1969) Gay et al. [1969]. Parameters used are described in the text. Boxes represent a range of crystal rich magmas $(30-60\%)$ with light grey assuming maximum packing $\Phi_m = 0.6$ and dark grey $\Phi_m = 0.84$.

Monte Carlo parameters

Parameter Name	Symbol	Range
Locked zone radius	R	$5-30$ km
Initial mobile magma over–pressure	ΔP_C	$5-50$ MPa
Locked zone over–pressure	ΔP_0	$0-\Delta P_C$
Magma yield stress	σ_{magma}	$(P_C-P_0)/4-4(P_C-P_0)$
Country rock yield stress	σ_{cr}	$\sigma_{magma}-10^{8.5}$ Pa
Conduit radius	r	$50-300$ m
Country rock Young's modulus	E_{cr}	10^{10} Pa
Magma Young's modulus	E_{magma}	10^8-10^{10} Pa
Country rock Poisson ratio	ν_{cr}	0.25
Magma Poisson ratio	ν_{magma}	$0.25-0.4$
Magma water content	$n-n_{CO2}$	$3-7$ weight percent

Table 5.1: Range of model parameters in Monte Carlo simulations. Uniform distributions are assumed.

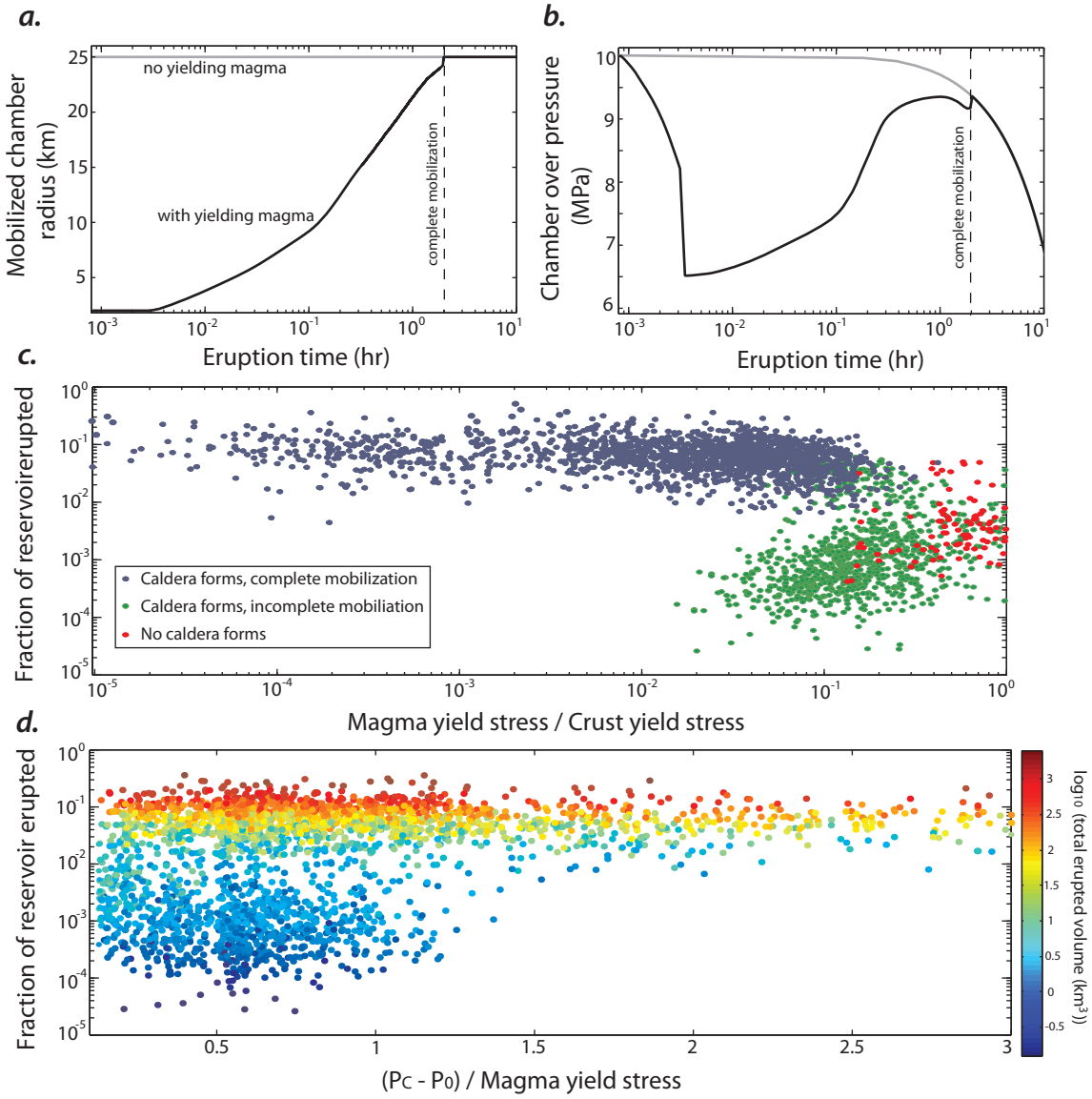

Figure 5.3: (a) Sample evolution of chamber growth during an eruption. Locked magma zone is a disk of thickness 4 km and radius of 25 km, conduit radius is 200 m, magma yield stress is 1 MPa, crust yield stress is 500 MPa, magma water content is 5 wt. pct., $P_C - P_0 = 0.1$ MPa, difference in Young's modulus between locked magma and crust is 10 fold. Initial mass flux is 13.6 Tg/s. (b) Evolution of chamber pressure, demonstrating the buffering effect of progressive magma mobilization. (c) Monte Carlo results (n=3000) illustrating dependences of simulation end condition (caldera collapse after full mobilization versus partial mobilization versus no caldera formation). Axes are dimensionless ratios of input yield stress and erupted fraction of total available magma. (d) The effect of overpressure (difference between locked magma overpressure and triggering overpressure ($P_C - P_0$)) normalized by magma yield stress versus fraction of magma erupted for Monte Carlo results. Coloring is log10 total erupted volume in km^3.

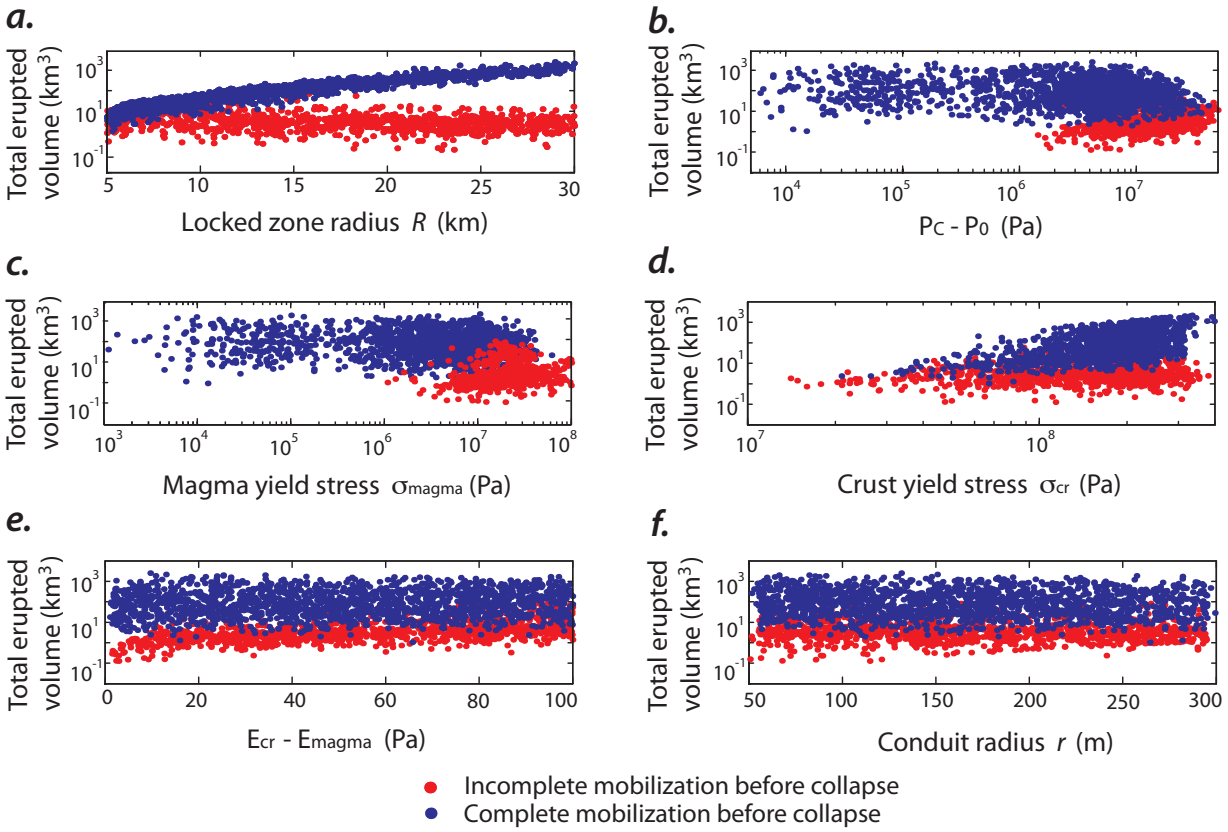

Figure 5.4: Monte Carlo results, plotting final discharge in km^3 as a function of (a) Locked zone radius (initial reservoir dimension) (b) Difference between initial triggering over–pressure in mobile magma and initial locked magma pressure. (c) Magma yield stress (d) Crust yield stress (e) Young's modulus difference between country rocks and locked magma (f) Conduit radius. Completely mobilized chambers (blue symbols) have different dependencies than incompletely mobilized chambers (red symbols).

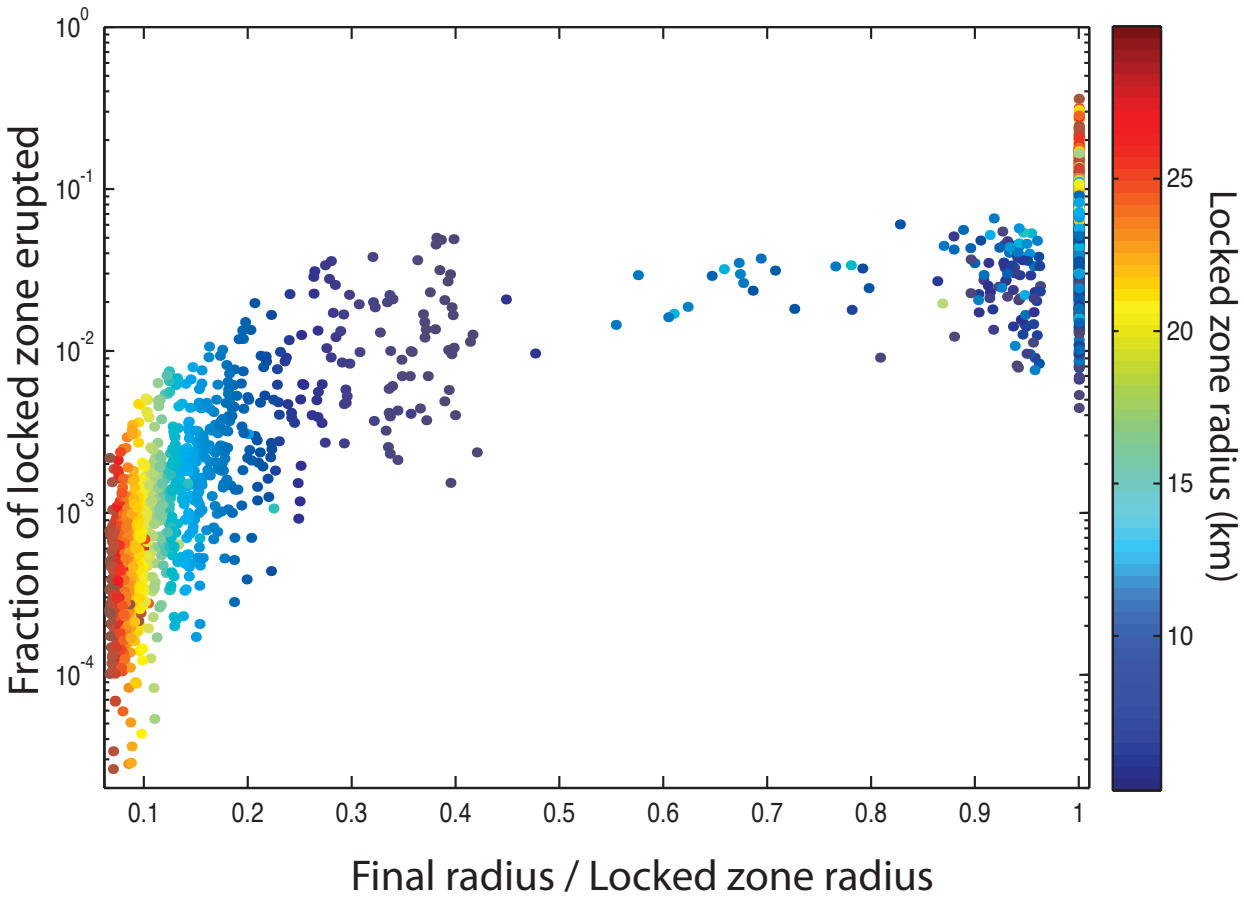

Figure 5.5: Fraction of locked zone erupted as a function of fractional radius mobilized at onset of caldera collapse. A significant fraction of calderas form with radius less than 50% the locked zone radius. For these there is a straightforward correlation with fraction of reservoir erupted. Only for completely mobilized chambers does the fraction erupted exceed 10% of the reservoir.

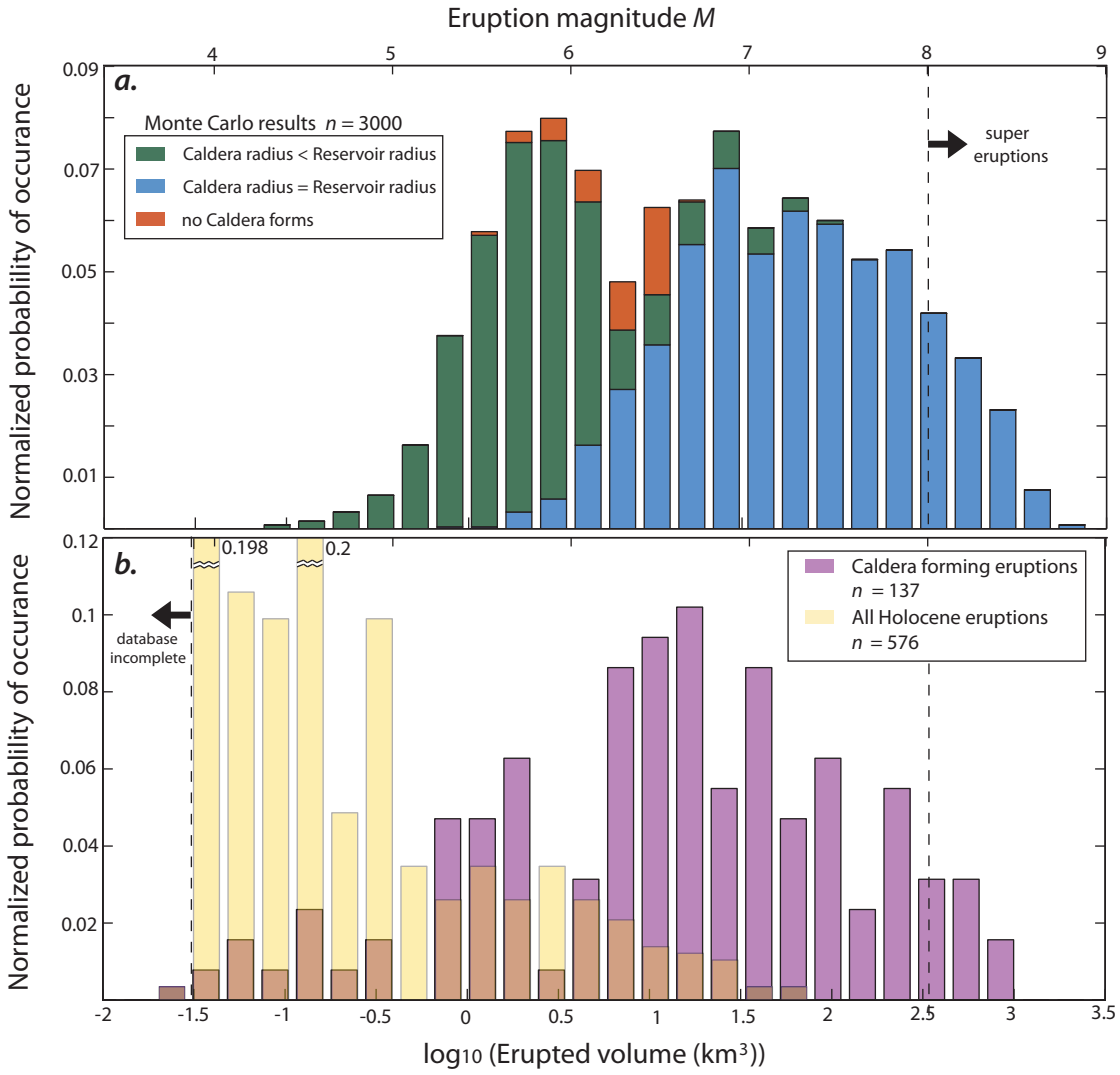

Figure 5.6: Comparison of modeled eruption magnitude and frequency with available data, bottom scale is log10 total erupted volume in km^3, while top scale is the eruption magnitude M. (a) Distribution of erupted volumes from Monte Carlo simulations. The bimodal distribution of volumes reflects whether the magma reservoir completely mobilizes before caldera formation. (b) Distribution of erupted volume estimates from worldwide collapse calderas-Geyer and Marti [2008] and all Holocene eruptions. The model distribution is similar to that observed for collapse calderas as eruption size increases. The magnitude and frequency of non caldera–forming eruptions is distinct, with small eruptions dominant (off the scale in two cases indicated).

Chapter 6

Meander formation in supraglacial streams

6.1 Introduction

Supraglacial streams are melt channels that form in the ablation zone of glaciers and icesheets during the summer season when surface melt water (sometimes augmented by rain water) thermally erodes channels into the glacial surface. These streams form networks that drain off the glacier or more often into moulins and supraglacial lakes, forming a primary link between surface, englacial, and subglacial hydrologic systems [Fountain and Walder, 1998]. Although there is likely some inheritance of channels from year to year, supraglacial hydrology re–evolves from initial channelization to large scale organization each year as surface melting waxes and wanes.

Supraglacial streams are mechanistically distinct from alluvial or bedrock rivers, in which sediment transport forms the principle mode of incision and channel slope regularization over much longer timescales [see for example Sklar and Dietrich, 2004]. Yet despite differences in substrate strength and lack of significant suspended sediment, supraglacial streams exhibit similar morphologic features such as meandering (including cutoff loops), multi–threaded channels, and propagating knickpoints [Knighton, 1981, Marston, 1983]. As is also the case for alluvial rivers [Leopold and Maddock, 1953], planform morphology and channel geometry of supraglacial streams provide a rough estimate for time–averaged discharge, and over the glacier as a whole albedo changes caused by such melt water channelization help set the fine structure of glacial surface ablation. In a broader sense, the morphology of these streams is a potential analog to fluvial systems observed on other terrestrial planets, where sinuous channels are observed but both the substrate characteristics and the melt composition are often poorly constrained.

This study focuses on meanders because of their ubiquity in supraglacial channels (figure 6.1), and because of the interesting analog to meandering in more well–understood alluvial settings [Seminara, 2006]. We develop a model for meander formation based on linear sta-

bility analysis of depth–integrated mass, momentum and energy conservation equations for a supraglacial stream. This work generalizes previous modeling of Parker [1975], and follows the more general approach taken in recent meandering models of alluvial rivers [Camporeale et al., 2007]. We end by comparing our model predictions to a compilation of supraglacial stream field data from the literature and our own field work.

6.2 Meander formation

In alluvial settings, variations in boundary shear stresses that exceed the threshold for sediment motion drive bank erosion and deposition. In supraglacial streams there is no similar mechanism for deposition of bank material, and generally little sediment (ice or rock) with which to mechanically erode the bed. Meandering supraglacial streams thus exemplify a problem long recognized in bedrock channels [Leopold and Wolman, 1960]: how does channel sinuosity evolve in the absence of bank deposition? In particular, how does a channel migrate with nearly constant width as is observed in most meandering systems?

We believe that supraglacial streams migrate through the interaction of two erosional processes: thermal erosion occuring over the entire glacial surface forced by solar radiation, and thermal erosion within the channel. Channelized melt water will attain a higher mean temperature than the surrounding ice due to its lower albedo and the heat dissipated by flow, providing a mechanism to establish long–lived channels that may last the duration of the melt season and possibly beyond. A balance between stream incision and large scale surface lowering will determine the channel morphology, such that the record of meander migration is erased to some degree as the melt season progresses.

Melting in supraglacial channels is analogous to sediment transport and mechanical erosion in alluvial settings as it provides the mechanism by which the channel incises and achieves an equilibrium shape. Melting is, in general, a better understood process than sediment transport, and the stability of melting/solidification fronts is well known [see for example Mullins and Sekerka, 1963]. Channel sinuosity provides a natural vehicle for streamwise variations in heat transfer, as bends in the channel centerline locally decrease the thickness of the boundary layer between melt water and glacial ice, increasing lateral temperature and velocity gradients. This mechanism increases heat transfer in regions of high channel curvature, enhancing initially small channel instabilities. Other sources of spatial variations in heat transfer are possible: for example, anisotropic shielding from solar radiation, nonuniform surface slope, small scale variations in glacial ice structure and composition, or input/subtraction of water from the system. However, given the ubiquity of meanders in supraglacial streams, we favor formative mechanisms that do not depend on the particulars of external forcing.

6.3 Model Formulation

Our modeling solves two problems, the flow field within a supraglacial stream and the migration due to melting of channel banks. Because the timescale for water advection is quite small compared to the timescale for melting, flow is effectively steady on bank migration timescales and these problems are to large extent decoupled. Spatially variable heat transfer must content with channel boundaries buffered at the ice melting temperature and hence isothermal, providing some coupling between streamflow and the thermal balance. The resulting flow field then provides thermal forcing for unsteady bank migration.

Parker [1975] developed a model for supraglacial stream meanders based on a linear stability analysis of a vertically integrated heat balance, assuming potential flow in an initially straight stream channel. Harmonic perturbations to the bed of the stream were found unstable, with a finite range of unstable wavenumbers. In particular, Parker [1975] predicts that supercritical flow (Froude number $\mathrm{Fr} > 1$) is a necessary condition for meander formation.

This approach is conceptually similar to "bar" models of alluvial meandering [Callander, 1969]: the modeled channel axis remains fixed, but it is assumed that small amplitude perturbations of the bed force eventual lateral channel migration. It has since been shown for alluvial rivers, however, that flow perturbations due to curvature in the channel axis are largely responsible for the primary lateral instability, which is re–enforced by bed perturbations in the form of point bars and overdeepenings [Ikeda, Parker, and Sawai, 1981, Blondeaux and Seminara, 1985, Johannesson and Parker, 1989]. We are interested in applying this more general treatment of meandering to the linear stability of supraglacial streams.

Coordinate system

We use "meandering coordinates" to express the appropriate conservation equations in a translating coordinate system that tracks the channel centerline described by coordinates $(X_0^*(s^*), Y_0^*(s^*), Z_0^*)$ (figure 6.2). This coordinate system, in which s^* and n^* represent downstream and cross-stream positions (stars indicate dimensional variables), is mapped to a fixed cartesian basis (X^*, Y^*, Z^*) via

$$(X^*, Y^*, Z^*) = (X_0^* - n^* \sin\phi, Y_0^* + n^* \cos\phi, Z^*), \tag{6.1}$$

from which we obtain the metric coefficients

$$(h_s^*, h_n^*, h_z^*) = (1 + n^*\kappa^*(s^*), 1, 1), \tag{6.2}$$

where $\kappa^*(s^*) = d\phi/ds^*$ is the curvature of the channel centerline, ϕ is the angle of the centerline from the X^* axis, and the slope of the channel axis is assumed to be small. More details about the derivation of this coordinate system and the resulting curvilinear differential operators may be found in, for example, Seminara and Turbino [1992]. The channel half–width B_0^* is assumed to be fixed, implicitly requiring a lowering of the glacial surface to enable lateral channel migration. This assumption is grounded observationally, as meanders

of nearly constant width are often observed with steep banks on the outside of bends and low angle banks on the inside (figure 6.1(b)). The radius of curvature scales with its typical lengthscale R_0^* as $1/\kappa^* = R_0^*/\kappa$.

Governing Equations

In the meandering coordinate system we employ the non–dimensionalization

$$(s, n) = \frac{(s^*, n^*)}{B_0^*}, \quad (u, v, w) = \frac{(u^*, v^*, w^*)}{U_0^*}, \quad (h, D, z) = \frac{(h^*, D^*, z^*)}{D_0^*}, \tag{6.3}$$

where (u, v, w) are velocity components taking characteristic value U_0^* and (h, D, z) are the water surface height, the water depth, and the height above a datum respectively (figure 6.2) that scale with the characteristic depth D_0^*. The Reynolds equations for mass and momentum are

$$N\frac{\partial}{\partial s}\left(u^2\right) + \frac{\partial}{\partial n}\left(uv\right) + \beta\frac{\partial}{\partial z}\left(uw\right) + 2\nu_0 N\kappa uv = -\frac{N}{\mathrm{Fr}^2}\frac{\partial h}{\partial s} + \beta\frac{\partial}{\partial z}\left(\nu_T\frac{\partial u}{\partial z}\right) \tag{6.4}$$

$$N\frac{\partial}{\partial s}\left(uv\right) + \frac{\partial}{\partial n}\left(v^2\right) + \beta\frac{\partial}{\partial z}\left(vw\right) + \nu_0 N\kappa\left(v^2 - u^2\right) = -\frac{1}{\mathrm{Fr}^2}\frac{\partial h}{\partial n} + \beta\frac{\partial}{\partial z}\left(\nu_T\frac{\partial v}{\partial z}\right) \tag{6.5}$$

$$N\frac{\partial u}{\partial s} + \left(\frac{\partial}{\partial n} + \nu_0 N\kappa\right)v + \beta\frac{\partial w}{\partial z} = 0, \tag{6.6}$$

where $N = [1 + \nu_0 n\kappa]^{-1}$ is the longitudinal metric coefficient of the co–ordinate system with $\nu_0 = B_0^*/R_0^*$, $\beta = B_0^*/D_0^*$ is the half–width to depth ratio, $\mathrm{Fr} = U_0^*/\sqrt{gD_0^*}$, is the Froude number, while $\nu_T = \nu_T^*/(U_0^* D_0^*)$ is a dimensionless eddy viscosity. Hydrostatic pressure is incorporated into (6.4–6.6), while the normal Reynolds stresses and lateral bed stress have been neglected.

After applying the depth averaging operation $\langle\cdot\rangle = 1/D\int_{h-D}^{h}(\cdot)\,dz$, the above equations become

$$NU\frac{\partial U}{\partial s} + V\frac{\partial U}{\partial n} + \nu_0 N\kappa\, UV + N\frac{\partial H}{\partial s} + \frac{\beta\tau_s}{D} = 0 \tag{6.7}$$

$$NU\frac{\partial V}{\partial s} + V\frac{\partial V}{\partial n} - \nu_0 N\kappa U^2 + \frac{\partial H}{\partial n} + \frac{\beta\tau_n}{D} = 0 \tag{6.8}$$

$$N\frac{\partial}{\partial s}\left(DU\right) + \frac{\partial}{\partial n}\left(DV\right) + \nu_0 N\kappa DV = 0. \tag{6.9}$$

Here $U = \langle u\rangle$, $V = \langle v\rangle$ and $H = h/\mathrm{Fr}^2$, while τ_s, τ_n are the downstream and cross-stream shear stresses. Equations (6.7–6.9) are identical to those of Blondeaux and Seminara [1985], who similarly neglect the vertical structure of the flow.

Equations (6.7)-(6.9) are coupled to the Reynolds–averaged heat equation, for which we scale the dimensional viscous dissipation a^*, turbulent diffusivity Γ_T^*, water temperature T^*, and boundary heat flux q^* as

$$a = \frac{D_0^*}{\rho U_0^{*3}} a^*, \quad \Gamma_T = \frac{\Gamma_T^*}{U_0^* D_0^*}, \quad T = \frac{T^*}{\Delta T_G^*}, \quad q = \frac{1}{\rho c_p \mathcal{U}^* \Delta T_G^*} q. \tag{6.10}$$

$\Delta T_G^* = T_w^* - T_g^*$ is the mean temperature difference between stream water and bulk glacier ice.

The dimensionless heat equation in meandering coordinates is

$$\begin{gathered} N\tfrac{\partial}{\partial s}(uT) + \nu_0 N\kappa(vT) + \tfrac{\partial}{\partial n}(vT) + \beta\tfrac{\partial}{\partial z}(wT) \\ -\tfrac{1}{\beta}\left[N\tfrac{\partial}{\partial s}\left(\Gamma_T\tfrac{\partial T}{\partial n}\right) + \tfrac{\partial}{\partial n}\left(\Gamma_T\tfrac{\partial T}{\partial n}\right) + N\nu_0\kappa\Gamma_T\tfrac{\partial T}{\partial n}\right] - \beta\tfrac{\partial}{\partial z}\left(\Gamma_T\tfrac{\partial T}{\partial n}\right) = E_c\beta a, \end{gathered} \tag{6.11}$$

where $E_c = U_0^{*2}/c_p\Delta T_G^*$ is the Eckert number measuring the relative importance of kinetic energy and enthalpy.

Equation (6.11) describes the temperature structure and full coupling between heat transfer and flow within supraglacial streams. Equation (6.11) could be analyzed by employing a temperature decomposition similar to the velocity decomposition of higher order alluvial models (Zolezzi and Seminara [2001], Gajjar [2010]). However, we take a simpler approach here and parameterize temperature fluctuations in terms of depth–averaged flow variables.

For straight channels we assume that the water temperature is well mixed by turbulence, buffered near 0 °C by the ice boundaries but nonzero in the bulk flow due to warming by solar radiation, downslope transport and frictional dissipation. Wall curvature and bed topography introduce cross–stream gradients in the mean temperature field as well as spatial variability in the frictional generation of heat (figure 6.3). We utilize a mixing length model for turbulent heat transport, so the Reynolds decomposition in equation 6.11 describes the interaction of fluctuating temperature T' and fluctuating velocity u' in the stream by $\overline{u'T'} \approx -\Gamma_T \partial T/\partial n$ (overbar donates time–average). Thus spatial gradients in stream temperature are driven solely by lateral gradients in velocity, and we assume that turbulent heat flux is isotropic. This assumption may be relaxed in future work.

The resulting depth average of equation (6.11) is

$$\begin{gathered} NUD\frac{\partial DT}{\partial s} + \nu_0 N\kappa\left(VDT - \Gamma_T D\frac{dT}{dn}\right) + VD\frac{\partial T}{\partial n} \\ -\frac{1}{\beta}\left[N\frac{\partial}{\partial s}\left(\Gamma_T\frac{\partial DT}{\partial n}\right) + \frac{\partial}{\partial n}\left(\Gamma_T\frac{\partial DT}{\partial n}\right)\right] = \beta(q|_{z=h-D} \; - \; q|_{z=h} + E_c\langle a\rangle D), \end{gathered} \tag{6.12}$$

where $q|_{z=h-D}$ is the vertical heat transport in the water at the water–ice interface, and $q|_{z=h}$ is the vertical heat transport in the water at the water–air interface. Boundary terms associated with turbulent advection of heat are neglected. Equation (6.12) expresses that the rate of heat generation by viscous dissipation at the smallest lengthscales in the stream

is balanced by heat transport at the top and bottom boundaries, as well as advection by the mean flow and turbulent eddies.

At the air–water interface, heat transport occurs by a combination of radiation (solar forcing) and advection by wind. This aspect of heat transfer is of great importance for large scale glacial mass balance as well as being a zeroth order requirement for supraglacial channel formation [Parker, 1975]. It implies that lowering of the channel through melting by the stream is in an approximate steady state with lowering of the entire glacier surface. This is in accord with our observation of supraglacial streams that persist throughout the melt season [as well as Knighton, 1981].We make the assumption that (using dimensional variables)

$$q^*|_{z=h} = \gamma^* \Delta T_A^* \tag{6.13}$$

with $\Delta T_A^* = T_a^* - T_w^*$ the temperature difference between water and air and γ_a^* a coefficient of heat transfer at the water–air interface that may be determined through field measurements, although we set it equal to unity here. A kinematic (Stefan) condition governs the position of the water–ice interface

$$|\mathbf{n_z}| \frac{\partial (h^* - D^*)}{\partial t^*} = q^*|_{z=h-D} - q_I^*, \tag{6.14}$$

where ρ is the density of ice (assumed equal to the density of water), and $|\mathbf{n_z}|$ is a unit vector perpendicular to the interface and heat fluxes $q^*|_{z=h-D}$ and q_I^* are scaled as in Equation 6.10. The basal melting time is scaled as $t^* = LD_0^*/U_0^{*3}t$ with L the latent heat of fusion. This timescale is large compared to the other obvious timescale of flow B_0^*/U_0^* (hence there is no time derivative in our continuity equation 6.9). We assume that the base level of our stream is in approximate steady state (i.e., melting of the walls occurs more slowly than melting of the base due to shallow flows) therefore set $\partial(h - D)/\partial t$ to zero while calculating the flow field.

$$q_I^* = -\frac{\kappa_I \Delta T_G^*}{W_b^*} \tag{6.15}$$

is the rate of vertical heat conduction through the ice at the ice–water boundary, with κ_I the thermal conductivity of ice. q_I^* occurs over a thermal boundary layer of constant thickness W_b^* that scales with D_0^*. Because supraglacial stream water is strongly buffered towards 0 °C [Isenko, Narus, and Mavlyudov, 2005], the water temperature is a good approximation to the ice melting temperature in equation 6.15. We thus neglect diurnal temperature fluctuation in stream water. ΔT_G^* in supraglacial streams will be a function of latitude, less than one degree in temperate glaciers but possibly larger in polar settings as the bulk temperature of glacier ice decreases.

Dissipation $\langle a \rangle$ in the stream is modeled following Parker [1975],

$$\langle a \rangle = \frac{\tau_s U + \tau_n V}{D}, \tag{6.16}$$

with near–bed shear stress terms (τ_s, τ_n) represented as

$$(\tau_s, \tau_n) = \frac{(\tau_s^*, \tau_n^*)}{\rho\, U_0^{*2}} = C_f\, \mathcal{U}(U, V), \tag{6.17}$$

using $\mathcal{U} = \mathcal{U}^*/U_0^* = \sqrt{U^2 + V^2}$ as the flow speed.

Additional contributions to shear stresses arise from secondary flow [Camporeale et al., 2007], and can be explicitly calculated in models that include depth–dependent velocity. We do not explicitly include vertical flow structure as most of these effects represent higher order corrections to our model [Johannesson and Parker, 1988], although Zolezzi and Seminara [2001] show that vertically variable momentum transfer in the secondary flow may induce a non–negligible enhancement of the cross–stream shear stress τ_n. We have found that imposition of such an enhancement does not change the qualitative behavior of our model, and hence neglect it.

The friction factor C_f is given by an empirical approximation for rough–walled pipe flow [ColeBrook, 1939, Parker, 1975]

$$(C_f)^{-1/2} = -2\log(\frac{\zeta^*}{3.7D^*} + \frac{2.5}{\mathrm{Re}\sqrt{C_f}}). \tag{6.18}$$

$\mathrm{Re} = \rho\,\mathcal{U}^* D^*/\mu$ is the Reynolds number of the flow with μ the water viscosity, and ζ^* is a characteristic roughness height of the channel walls.

The advective terms on the lefthand side of equation (6.12) are responsible for transporting the bulk temperature of the stream towards the outside wall around bends as the high velocity core of the stream approaches the wall [Whiting and Dietrich, 1993] (figure 6.3). We model the cross stream turbulent heat flux in terms of flow variables as

$$\frac{\partial}{\partial n}\left(\Gamma_T \frac{\partial T}{\partial n}\right) = \frac{\partial}{\partial n}\left(\mathcal{U} D \frac{\partial \mathcal{U}}{\partial n}\right) = \frac{\beta B_0^*}{U_0^{*2}\mathcal{J}^*\Delta T_G^*}\frac{\partial}{\partial n^*}\left(\mathcal{U}^* D^* \frac{\partial \mathcal{U}^*}{\partial n^*}\right). \tag{6.19}$$

This relation assumes strong coupling between heat and momentum transfer. $\mathcal{J}^*$ is an empirical and dimensional constant that measures the strength of coupling between velocity and temperature gradients in the Reynolds analogy $T^* = \mathcal{J}^*\Delta T_G^* \mathcal{U}^*$. For flow past a flat plate with Prandtl number Pr equal to unity $\mathcal{J}^* = 1/U_0^*$ [Schlichting, 1960], but we leave it as an adjustable parameter here.

Finally, we use the Reynolds analogy between temperature and velocity gradients to eliminate temperature in equation (6.12), giving

$$\begin{aligned}\beta\Pi_1\left(NUD\frac{\partial \mathcal{U}}{\partial s} + VD\frac{\partial \mathcal{U}}{\partial n}\right) - \Pi_1\left[N\frac{\partial}{\partial s}\left(\mathcal{U}D^2\frac{\partial D\mathcal{U}}{\partial n}\right) + \frac{\partial}{\partial n}\left(\mathcal{U}D^2\frac{\partial D\mathcal{U}}{\partial n}\right) + \beta\ \nu_0 N\kappa\mathcal{U}D\frac{\partial D\mathcal{U}}{\partial n}\right] \\ = \frac{\partial(Fr^2H - D)}{\partial t} + \Pi_2 - \frac{\Pi_3}{W_b} + C_f\mathcal{U}^3\end{aligned} \tag{6.20}$$

as the depth–averaged energy balance, where

$$\begin{aligned}\Pi_1 &= \frac{\mathcal{J}^* U_0^*}{\beta^2 E_c}, \\ \Pi_2 &= \frac{\gamma_a^* \Delta T_A^*}{\rho U_0^{*3}}, \\ \Pi_3 &= \frac{\kappa_I \Delta T_G^*}{\rho U_0^{*3} D_0^*}.\end{aligned} \tag{6.21}$$

The dimensionless groups that appear in equation (6.20) are variants on a turbulent Eckert number (Π_1), and turbulent Brinkman numbers (Π_2 and Π_3) that measure the relative importance of viscous heating and conductive heat transfer.

Boundary Conditions

Equations (6.7–6.9) and (6.20) form the basis of our model for flow in supraglacial streams. These equations, despite assuming no lateral wall effects, represent a finite channels with Dirichlet boundary conditions stating that the channel boundaries are impermeable to flow,

$$V = 0 \text{ at } n = \pm 1 \tag{6.22}$$

and that the temperature at the channel walls is equal to the ice melting temperature (0°C)

$$T = \mathcal{U} = 0 \text{ at } n = \pm 1. \tag{6.23}$$

We again have assumed that

$$T = \frac{T^*}{\Delta T_G^* \mathcal{J}^* U_0^*} = \mathcal{U}, \tag{6.24}$$

meaning that the (small) near–wall temperature variations are coupled directly to the flow field. Condition 6.23 is thus an additional constraint on the depth–averaged velocity structure.

Lateral channel migration

We close our mathematical formulation by modeling the thermal erosion and lateral migration of the channel walls. Boundary melting and bank migration require consideration of the unsteady terms in equation (6.20), where vertical downcutting of the channel occurs according to equation 6.14. A similar Stefan condition governs the lateral migration of the channel bank y_b^*

$$\beta \rho U_0^{*3} |\mathbf{n_y}| \frac{\partial y_b}{\partial t} = q_w^{l*} - q_I^{l*} \quad \text{at} \quad n^* = B_0^*, \tag{6.25}$$

where the unit vector $|\mathbf{n_y}|$ ensures that melting occurs perpendicular to the bank and q_w^{l*}, q_I^{l*} are the lateral heat fluxes at the ice–water interface through water and ice.

We focus here on lateral bank migration. Channel downcutting must outpace large–scale lowering of the glacier surface to maintain channelized flow of melt water [Parker, 1975]. These melting velocities will vary diurnally and throughout the melt season as the ablation rate of the glacier responds to the surface energy balance, resulting in unsteady vertical incision. However, the persistence of channels throughout the melt season is evidence that, on average, these two rates are balanced. Because we do not treat the details of unsteady solar forcing, we assume here a constant background vertical incision and model lateral migration of the channel only. In equation 6.25 our assumption of constant channel width is implicit in the statement that only one side of the channel melts and requires ablation of the glacier surface.

q_w^{l*} at lateral boundaries is spatially variable due to the generation of temperature fluctuations from frictional dissipation and advection of heat by the flow (equation 6.12). Boundary layer heat transfer at the water–ice interface is modeled as [Schlichting, 1960]

$$q_w^l = \frac{B_0^* \mathrm{Pr}_T}{\rho c_p \Delta T_G^* \nu_T'^* \mathcal{J}^* U_0^*} q_w^{l*} = -\frac{\partial \mathcal{U}}{\partial n}, \tag{6.26}$$

where $\mathrm{Pr}_T \geq 1$ is a turbulent Prandtl number, $\nu_T'^*$ is a near–wall eddy viscosity, and we have used the Reynold's analogy to relate temperature gradients to velocity gradients scaled by $\mathcal{J}^*$. We scale eddy viscosity with the lengthscale ℓ^* near the wall $\nu_T'^* = U_0^* \ell^*$ that scales with depth.

Heat transfer through the ice scales with the thermal boundary layer in the ice as in equation 6.15. The Stefan number $S = L/c_p \Delta T_G^*$ for supraglacial streams is large, so this thermal boundary layer adjusts rapidly to perturbations in the channel centerline. It will maintain a constant thickness, assumed (as with the boundary layer at the bottom of the channel) to scale with the water depth D_0^*. Combining terms we thus have

$$\frac{\partial y_b}{\partial t} = \frac{\Pi_3}{\beta} \frac{1}{W_b} - \frac{\Pi_1 \ell^* \beta}{B_0^* \mathrm{Pr}_T} \frac{\partial \mathcal{U}}{\partial n}. \tag{6.27}$$

6.4 Linear Stability Analysis

We now perform a linear stability analysis on equations (6.7–6.9) and (6.20), following Blondeaux and Seminara [1985]. We examine a channel whose centreline exhibits small–amplitude perturbations with respect to the straight configuration and investigate the conditions for these perturbations to grow in time. In this light we make the harmonic perturbation (using c.c. for complex conjugate)

$$\kappa(s) = \frac{1}{R_0} \left[e^{i(\lambda_m s - \omega t)} + \text{c.c.} \right], \tag{6.28}$$

where λ_m is a non–dimensional meander wavenumber scaled by the half–width B_0^*, and ω is a frequency that may be directly related to the propagation speed of the harmonic disturbances.

We perturb the channel centerline as

$$y_c = \epsilon(t) \left[e^{i(kx - \omega t)} + \text{c.c.} \right], \tag{6.29}$$

where y_c, ϵ, k and x are quantities normalized by the half width B_0^*, and $\epsilon \ll 1$. This approximation implies that

$$\nu_0 = k^2 \epsilon \tag{6.30}$$

$$\lambda_m = k + \mathcal{O}(\epsilon^2 k^2) \tag{6.31}$$

$$s = x + \mathcal{O}(\epsilon^2 k^2). \tag{6.32}$$

Hence the channel slope, the average depth D_0^*, the average speed U_0^* and thus the average Froude number all undergo variations due to the bend growth which are $\mathcal{O}(\epsilon^2 k^2)$ and so are negligible. Moreover the relationship (6.30) implies that in order for the amplitude ϵ to be small, ν_0 and k should satisfy the inequality

$$\lambda_m \sim k \gg \nu_0^{\frac{1}{2}}. \tag{6.33}$$

We assume the flow is fully developed in the s–direction, with no secondary flow at zeroth order. Perturbation of flow variables (U, V, H, D) is then performed as an expansion

$$(U, V, H, D) = (1, 0, h_0, 1) + \epsilon(t)(\mathcal{A}_1, \mathcal{B}_1, \mathcal{H}_1, \mathcal{D}_1)\left[e^{i(kx-\omega t)} + \text{c.c.}\right] + \mathcal{O}(\epsilon^2 k^2), \tag{6.34}$$

where $\mathcal{A}_1$, $\mathcal{B}_1$, $\mathcal{H}_1$, $\mathcal{D}_1$ are all functions of n alone and h_0 is the nondimensional unperturbed depth.

Expanding C_f as a function of $\mathcal{U}$ and D, in powers of ϵ, we have

$$C_f = C_0|_{\epsilon=0} + \epsilon \frac{\partial C_f}{\partial \mathcal{U}} \frac{\partial \mathcal{U}}{\partial \epsilon}|_{\epsilon=0} + \epsilon \frac{\partial C_f}{\partial D} \frac{\partial D}{\partial \epsilon}|_{\epsilon=0} + \mathcal{O}(\epsilon^2). \tag{6.35}$$

This gives

$$\begin{aligned} \tau_s &= C_0(1 + \epsilon s_1 \mathcal{A}_1 \left[(e^{i(\lambda_m s-\omega t)} + \text{c.c.}\right] + \epsilon s_2 \mathcal{D}_1 \left[e^{i(\lambda_m s-\omega t)} + \text{c.c.}\right] + \mathcal{O}(\epsilon^2)) \\ \tau_n &= \epsilon \mathcal{B}_1 C_0 \left[e^{i(\lambda_m s-\omega t)} + \text{c.c.}\right] + \mathcal{O}(\epsilon^2) \end{aligned} \tag{6.36}$$

where

$$s_1 = 2 + \tfrac{1}{C_0}\tfrac{\partial C_f}{\partial \mathcal{U}}, \qquad s_2 = \tfrac{1}{C_0}\tfrac{\partial C_f}{\partial D}. \tag{6.37}$$

C_0 as well as the derivatives $\partial C_f/\partial \mathcal{U}$ and $\partial C_f/\partial D$ may be evaluated in closed form using the principle solution for w in $z = we^w$.

The bottom thermal boundary layer W_b^* in ice around the stream will be perturbed by depth variations in the channel, but remains of constant thickness due to the large Stefan number. We assume that this boundary layer tracks the bottom interface $W_b^* \approx D^* \approx D_0^*\left(1 + \epsilon\, \mathcal{D}_1 \left[e^{i(kx-\omega t)} + \text{c.c.}\right]\right)$.

Finally, we need to ensure that perturbations to the flow variables do not greatly affect externally controlled aspects of this problem that are built into the governing equations. We require that the average discharge and surface slope are unaffected by the $\mathcal{O}(\epsilon^1)$ perturbations through two integral conditions:

$$\int_{-1}^{1} (\mathcal{A}_1 + \mathcal{D}_1) dn = 0 \tag{6.38}$$

and

$$\int_{-1}^{1} (\mathcal{H}_1 - \mathcal{D}_1) dn = 0. \tag{6.39}$$

Solution of the linearized problem

Substituting all the expansions into the governing differential system (6.7–6.9) and (6.20), at $\mathcal{O}(\epsilon^0)$ we find the uniform flow solution and energy balance within the stream,

$$\frac{dh_0}{ds} = -\beta C_0 \tag{6.40}$$

$$\frac{d(Fr^2 h_0)}{dt} = -\Pi_2 + \Pi_3 - C_0. \tag{6.41}$$

In equation (7.31), a nonzero RHS sets the time–averaged lowering rate of the stream. Comparison with the glacier surface lowering [Parker, 1975] yields vertical stream incision, but we note again that this rate is much larger than the rate of flow adjustment.

At $\mathcal{O}(\epsilon^1)$ we have

$$\mathcal{L}\begin{bmatrix}\mathcal{A}_1\\ \mathcal{B}_1\\ \mathcal{H}_1\\ \mathcal{D}_1\end{bmatrix} = \begin{bmatrix} i\lambda_m\mathcal{A}_1 + \frac{d\mathcal{B}_1}{dn} + i\lambda_m\mathcal{D}_1 \\ (i\lambda_m + \chi_0 s_1)\,\mathcal{A}_1 + i\lambda_m\mathcal{H}_1 + \chi_0(s_2-1)\mathcal{D}_1 \\ (i\lambda_m + \chi_0)\mathcal{B}_1 + \frac{d\mathcal{H}_1}{dn} \\ \left(C_0(s_1+1) + \Pi_1\left(-\beta i\lambda_m + i\lambda_m\frac{d}{dn} + \frac{d^2}{dn^2}\right)\right)\mathcal{A}_1 + (\Pi_3 + C_0 s_2)\,\mathcal{D}_1 \end{bmatrix}$$

$$= \begin{bmatrix} 0 \\ -n\lambda_m^2\chi_0 \\ \lambda_m^2 \\ 0 \end{bmatrix}. \tag{6.42}$$

The homogeneous ordinary differential operator $\mathcal{L}$ may be written in the form

$$\mathcal{L} = \begin{bmatrix} a_1 & \frac{d}{dn} & 0 & a_1 \\ a_2 & 0 & a_3 & a_4 \\ 0 & a_5 & a_6\frac{d}{dn} & 0 \\ a_6 + a_8\frac{d}{dn} + \Pi_1\frac{d^2}{dn^2} & 0 & 0 & a_7 \end{bmatrix}, \tag{6.43}$$

with $\chi_0 = \beta C_0$, and the coefficients $a_i (i = 1, 2, \ldots, 8)$ defined by

$$\left.\begin{array}{c} a_1 = i\lambda_m, \quad a_2 = i\lambda_m + \chi_0 s_1 \\ a_3 = i\lambda_m, \quad a_4 = \chi_0(s_2 - 1) \\ a_5 = i\lambda_m + \chi_0, \quad a_6 = C_0(s_2+1) - i\beta\lambda_m\Pi_1, \\ a_7 = \Pi_3 + C_0 s_2, \quad a_8 = i\lambda_m\Pi_1. \end{array}\right\} \tag{6.44}$$

By manipulating this system we can obtain a simpler 4th order equation

$$\Sigma_0\mathcal{A}_1 + \Sigma_1\frac{d\mathcal{A}_1}{dn} + \Sigma_2\frac{d^2\mathcal{A}_1}{dn^2} + \Sigma_3\frac{d^3\mathcal{A}_1}{dn^3} + \Sigma_4\frac{d^4\mathcal{A}_1}{dn^4} = 0 \tag{6.45}$$

where

$$\Sigma_0 = (1 - \frac{a_6}{a_7}) \tag{6.46}$$

$$\Sigma_1 = -\frac{a_8}{a_7} \tag{6.47}$$

$$\Sigma_2 = \frac{a_2 a_6}{a_1 a_3 a_5} - \frac{a_4 a_6 a_6}{a_1 a_3 a_5 a_7} - \frac{\Pi_1}{a_7} \tag{6.48}$$

$$\Sigma_3 = -\frac{a_4 a_6 a_8}{a_1 a_3 a_5 a_7} \tag{6.49}$$

$$\Sigma_4 = -\frac{a_4 a_6 \Pi_1}{a_1 a_3 a_5 a_7}, \tag{6.50}$$

along with coupled equations in the other variables. Equation (6.45) has the form of a forced linear oscillator, also characteristic of alluvial meander models.

The boundary conditions, equations (6.22) and (6.23), at $\mathcal{O}(\epsilon^1)$ become

$$\mathcal{B}_1 = \mathcal{A}_1 = 0 \qquad \text{at} \quad n = \pm 1. \tag{6.51}$$

The general solution to (6.45) is

$$\mathcal{A}_1(n) = C_1 e^{r_1 n} + C_2 e^{r_2 n} + C_3 e^{r_3 n} + C_4 e^{r_4 n} \tag{6.52}$$

where (r_1, r_2, r_3, r_4) are roots of the characteristic equation

$$0 = \Sigma_0 + \Sigma_1 r + \Sigma_2 r^2 + \Sigma_3 r^3 + \Sigma_4 r^4. \tag{6.53}$$

The constants (C_1, C_2, C_3, C_4) are unwieldy analytic expressions not presented here (available upon request to the authors), evaluated by substituting equation (6.52) into (6.42), from which $\mathcal{B}_1$, $\mathcal{D}_1$ and $\mathcal{H}_1$ follow.

Lateral channel instabilities

Perturbations to the flow field will lead to harmonic meandering instabilities on the timescale of melting, following equation (6.27). The linear contribution to this balance governs the amplification of perturbations to the channel centerline, and we note that because of the assumed fixed channel width

$$y_b = 1 + y_c + \mathcal{O}(\epsilon^2 k^2). \tag{6.54}$$

The $\mathcal{O}(\epsilon^1)$ contribution reads

$$\frac{\partial y_c}{\partial t} = -\left(\frac{\Pi_3}{\beta} \mathcal{D}_1 + \Pi_1 \frac{\ell}{D_0^*} \frac{\partial \mathcal{A}_1}{\partial n} \right), \tag{6.55}$$

where we have expressed the RHS in terms of thermal dimensionless parameters and assumed Pr_T=1, to illustrate that bank migration results from a competition between perturbations to water depth $\mathcal{D}_1$ and cross stream gradients in downstream velocity $\frac{\partial \mathcal{A}_1}{\partial n}$. We vary the lengthscale ℓ^* associated with boundary layer heat transport to explore sensitivity of results these competing terms.

6.5 Results

We have mapped parameter space of our linear model in the range of values consistent with available field data on supraglacial streams, based on our own work on the Juneau Icefield, Alaska, in 2009–2010 and published studies (table 1). We expect that characteristics of meandering instabilities will be sensitive to both geometric and hydraulic parameters readily measured, as well as thermal parameters that are less well known and harder to quantify. In evaluating the model we assume fixed heat transfer coefficients and thermal conductivities, exploring the sensitivity of meandering to mean temperature differences between bulk glacier ice and water ΔT_G^*, bed roughness height ζ^* and to the empirical constant $\mathcal{J}^*$ which relates cross–stream gradients in velocity to heat transfer.

Example evaluation of (6.55) is shown in figure 6.4(a). For reasonable parameter choices, the solution exhibits a well defined peak and positive celerity, indicating that meanders travel downstream. We also find a parameter regime in which all wavenumbers are unstable and meanders propagate upstream figure 6.4(b). We expect that the most unstable wavelength in our linear model approximates the meander wavelength chosen in nature, although there may be quantitative corrections due to processes that our model does not capture, such as the vertical structure within the flow [Camporeale et al., 2007] and finite amplitude effects.

Figure 6.5(a) illustrates the most unstable wavelength for a range of hydraulic parameters. We find that, contrary to the results of Parker [1975], meandering may occur for subcritical flows (Fr < 1). We thus do not find a stable regime. Meander wavelength becomes largely insensitive to Froude number as Fr increases, but is a strong function of channel aspect ratio. The regime of no selected wavenumber and upstream meander propagation occurs when the contribution of $\partial\mathcal{A}_1/\partial n$ is insignificant, and only at low Froude numbers. By varying ℓ^* as in figure 6.5.b, we see that $\mathcal{D}_1$ is dominant at low Fr when ℓ^* approaches D_0^*, creating distinct regimes of influence for these two variables. For values of $\ell^* \sim D_0^*$ (figure 6.5.a), finite wavenumber selection and downstream propagation at all values of Fr. For all choices of ℓ^* the U_0^{*-3} dependence of Π_3 ensures that $\mathcal{D}_1$ rapidly becomes unimportant as water speed U_0^* increases. Figure 6.5 demonstrates that the contribution to meandering instabilities by spatial variability in conduction through the walls (first term on the RHS of equation 6.55) is insignificant except at very low water velocity.

There is a discontinuous transition in the solution for $\frac{\partial\mathcal{A}_1}{\partial n}$ that accounts for the shift in behavior at low Fr (figure 6.4 and figure 6.5(b), dashed curve). This is a result of a sign change in the characteristic equation (6.53), and illustrates parameter dependencies of the solution. Although algebraically complex, for the parameters in Table 1 only two terms in equation (6.53) change sign, $a_6 = (\partial C_f/\partial D + C_0) - i\beta\lambda_m\Pi_1$ and $a_7 = \Pi_3 + \partial C_f/\partial D$. The derivative $\partial C_f/\partial D$ is uniformly negative, thus the relative magnitudes of C_0, U_0, D_0 and ΔT_G determine the sign of a_6 and a_7. For the parameter range in figure 6.5, sign change in the characteristic equation occurs precisely at the transition in $\frac{\partial\mathcal{A}_1}{\partial n}$ from a finite maxima to no selected wavenumber, and from downstream to upstream propagation.

Figure 6.6(a) illustrates the effect of varying the coupling parameter $\mathcal{J}^*$. Varying $\mathcal{J}^*$ affects the wavenumber selection and also shifts the balance between $\partial\mathcal{A}_1/\partial n$ and $\mathcal{D}_1$ in

equation (6.55). As $\mathcal{J}^*$ increases we find that the Froude number dependence of most unstable wavelength decreases. Our simple model for $\mathcal{J}^*$ thus suggests that increased coupling between flow and temperature stabilizes the selected wavelength of meandering.

As illustrated in figure 6.6(b) there is a width–dependence of selected wavelength that effectively does the opposite, increasing the Froude number dependence of selected wavelength. It is possible [Marston, 1983] but not well established whether supraglacial streams attain a hydraulic geometry similar to alluvial rivers that empirically relates water velocity, channel width and depth to discharge [Leopold and Maddock, 1953]. Available data suggest that $\beta \sim 3-5$ for many supraglacial streams (Isenko et al. [2005], present study). However, hydraulic geometry in this setting should reflect covariance of width not only with mean discharge (as is the case for alluvial rivers) but also the amplitude of diurnal discharge variations.

It is important to note differences in the assumptions between our study and that of Parker [1975]. Parker [1975] takes straight banks and potential flow, neglecting boundary effects and the coupling between channel curvature, streamflow and heat transfer. Time evolution of the bed is completely decoupled from the flow field as stream velocity is prescribed. Our study decouples flow and boundary melting, but treats the flow constraints imposed by isothermal channel walls and the cross stream advection of heat that is a result of thalweg perturbations due to channel curvature. We neglect spatial gradients in basal melting, as our focus is lateral channel instabilities. However it is possible that variability in basal melting may create ice bedforms, as we have observed in some supraglacial streams (presented elsewhere).

Cross–stream gradients in flow velocity produce spatial gradients in dissipation, which are largely responsible for deviations from the generally low water temperatures (generally 0.5°C or less [Isenko et al., 2005]) and therefore spatial variability in heat transfer to the boundaries. This can be demonstrated by estimating the heat transfer increase that occurs during thinning of the turbulent boundary layer an amount Δn^*. There are two contributions, an increase in dissipation Q^*_{dis} and increased heat transport across the turbulent boundary layer Q^*_{bdy} per unit wall area. For flat wall geometry these scale as [Schlichting, 1960]

$$\begin{array}{rcl} Q^*_{dis} & \sim & \rho\nu_T D^*_0 \left(\frac{\partial v^*}{\partial n^*}\right)^2, \\ Q^*_{bdy} & \sim & \frac{\rho c_p \nu_T \Delta T^*_G}{\mathrm{Pr_T} U^*_0} \frac{\partial v^*}{\partial n^*}. \end{array} \tag{6.56}$$

We approximate the velocity gradient as $\partial v^*/\partial n^* \sim U^*_0/\Delta n^*$, and can arrange (6.56) to find that

$$\frac{Q^*_{bdy}}{Q^*_{dis}} \sim \frac{c_p \Delta \ell^* \Delta T^*_G}{\mathrm{Pr_T} U^{*2}_0 D^*_0}. \tag{6.57}$$

For supraglacial streams $\mathrm{Pr_T} \geq 1, \Delta n^* < 0.01$ m, and ΔT^*_G, and U^*_0 are listed in table 1. We see that an increase in dissipation rather than enhanced transport of heat from the bulk flow generally dominates the heat flux increase incurred by thinning the turbulent boundary layer by Δn^* around a bend. This does not continue to hold for small discharge streams or

high melt water temperature, but dissipation dominates as the mean velocity increases and is thus likely to control the spatial variability in heat flux to the channel walls in supraglacial streams.

Mean temperature differences affect the lengthscales of instability through Π_3, and are explored in figure 6.7 (a). Increasing water temperature tends to increase meander wavelength at low temperatures, with a maximum that depends on velocity scale U_0^*. Low U_0^* results are sensitive to the lengthscale ℓ^*, with large ℓ^* resulting in a shutoff of single wavelength selection as water temperature increases (figure 6.7 (a) dashed curves). Increased magnitude of the friction coefficient C_f as expressed by the wall roughness height ζ^* shifts the wavelength of meandering to smaller values (figure 6.7 (b)), consistent with enhanced dissipation governing instability. There is a similar dependence on ℓ^* for low water velocities.

We solve for the migration direction of meanders (figure 6.4 dotted curves), and it appears that in regimes with a finite maximum in unstable wavenumber meanders always migrate downstream. Although previous modeling [Parker, 1975] predicts no migration of meanders, our field work on the Juneau Icefield (documented in more detail elsewhere) suggests downstream migration in at least some streams, as do the observations of Marston [1983]. This result also appears the most physically consistent with the channel migration mechanisms we propose.

6.6 Discussion

In our model, the origin of meandering in supraglacial channels is an instability driven by channel curvature enhancing heat transfer and hence melting along the outside of bends. Finite amplitude meanders are not a feature of our model, but we expect that this is attained in nature if the increase in surface area available to conductively transport heat due to enhanced curvature balances the excess. We expect that maximum meander amplitude is modulated by the glacial surface slope, which sets the total potential energy available for flow, a result suggested by some field studies [Ferguson, 1973]. A more complete treatment of this process could provide bounds for the fully three dimensional finite amplitude of ice channel sinuosity, as in the rich nonlinear theory for alluvial meanders.

Available data show a power–law relationship between channel width and meander wavelength for supraglacial streams over three orders of magnitude in channel width (figure 6.8). This is consistent with the power–law channel width versus meander wavelength relationship also found for alluvial and bedrock meanders, although the coefficients of these empirical relations appear to differ by up to an order of magnitude as the composition of the erodable substrate varies [Leopold et al., 1964]. The paucity of available data on supraglacial streams makes it premature to evaluate the significance of the data in figure 6.8 in the context of other fluvial systems. A direct comparison between our model and the observed channel widths and wavelengths seen in the field is also not attempted here, as the covariance of flow parameters (the hydraulic geometry) for supraglacial streams are not yet well constrained. However in the context of our linear model we can find a range of realistic parameters (figure

(6.5) for 1 m width channels) that reproduce the empirical scaling between channel width and meander wavelength in figure (6.8), making this comparison a promising direction of future work. Despite the number of model parameters that result in factors of 2–3 change in most unstable wavelength, it is quite likely that most parameters (e.g., water temperature, wall roughness, coupling between heat transfer and flow) are strongly buffered. Hence future field measurements may prove useful for constraining site–specific controls on meander wavelength, and deciphering the scatter in figure (6.8).

Supraglacial streams are distinct from other meandering fluvial channels in several important ways. First, the instability driving lateral channel migration is thermal rather than mechanical, such that hydrodynamics in the stream are coupled to bank erosion through forced spatial variations in heat flux at the channel wall. This is fundamentally different than the coupling of hydrodynamics to erosion through sediment transport that occurs in alluvial settings, although it may be more similar to dissolution meanders in Karst settings [Ford and Williams, 2007].

A second distinguishing feature of supraglacial streams is that the discharge is strongly diurnal, especially for streams in which rain or other stored meltwater does not constitute a large fraction of the total water mass. A supraglacial stream will experience a smoothly varying hydrograph each day, with the same period but slightly out of phase with solar forcing [Marston, 1983]. To attain a regular sinusoidal meandering planform, then, would imply that this pattern is either set early on or is set by the average daily maximum discharge. We believe that the latter case is more likely, because the timescale over which meanders adjust their planform geometry is extremely rapid [Marston, 1983]. It may also be the case that regular, single wavelength meander formation is the exception rather than the rule for this reason (for example, figure 6.1(a)).

The rate for meander development may be estimated from our model through the growth rate of linear perturbations (for example, the ordinate in figure 6.4). For the range of parameters listed in table 1, we can find maximum growth rates in range of 0.001-0.1 cm/hr. Despite the implicit neglect of time-dependent forcing in this estimate, this is roughly consistent with measured maximum supraglacial stream incision rates of several centimeters per day [Marston, 1983]. Such rapid incision raises the possibility that the drainage network as well as the planform geometry of supraglacial streams may evolve significantly over the course of one melt season. While there is limited data suggesting that this does occur on multi–year timescales [Leopold, Wolman, and Miller, 1964], intra–season reorganization of the supraglacial network may also occur. In the context of high volume systems such as on the Greenland Icesheet, this dynamic reorganization interacts with englacial and subglacial melt water routing through the drainage of supraglacial lakes [Box and Ski, 2007], which may affect the large-scale dynamics of icesheet movement [der Wal et al., 2008].

We conclude by emphasizing that supraglacial channels represent a mechanistic endmember in the spectrum of natural channelization features that exhibit meandering (only thermal erosion), which also includes lava tubes and flows, alluvial rivers, and dissolution channels. A metric relating supraglacial channel morphology to the rates and mechanisms of incision would be a useful remote means of monitoring seasonal melt water routing on icesheets,

Parameter	Range
B_0^*	$0.1 - 4$ m [a,b,c,d]
D_0^*	$.01 - 1$ m [a,b,c]
U_0^*	$0.25 - 3$ m/s [a,b,c,d]
T_g^*	$0 - (-5)$ °C [a,b]
T_w^*	$0 - 1$ °C [a,b,e]
T_a^*	$(-10) - 10$ °C [a,b,c]
ζ^*	$0.0001 - 0.01$ m [a]
γ_a^*	1 W/m^{2}K
γ_w	1 W/m^{2}K
κ_I	2 W/m K
L	334 kJ/kg
ρ	1000 kg/m^3
c_p	4 kJ/kg K

Table 6.1: Estimates for model parameters, taken from field studies of supraglacial streams. a. Present study, b. Parker [1975], c. Marston [1983], d. Knighton [1981], e. Isenko et al. [2005]

but may be applicable in a much broader planetary context as well. On Earth it has been suggested that sinuosity of bedrock channels varies as a function of underlying geology, and may contain a climate signature [Stark et al., 2010]. Some sinuous channels on Mars record meandering lava flows, as they do on the Moon [Hauber et al., 2009], but others may record fluvial activity from a wetter period of Martian history [Malin and Edgett, 2003]. On Titan, present day cycling of liquid methane is likely responsible for meandering channels on the icy surface [Lunine and Atreya, 2008], but the rates and mechanisms of incision are currently unknown. If it is possible to clearly separate thermally eroded channels from those formed through mechanical erosion, this can be used to better understand landscape evolution on terrestrial planets and moons in our solar system that exhibit sinuous channels.

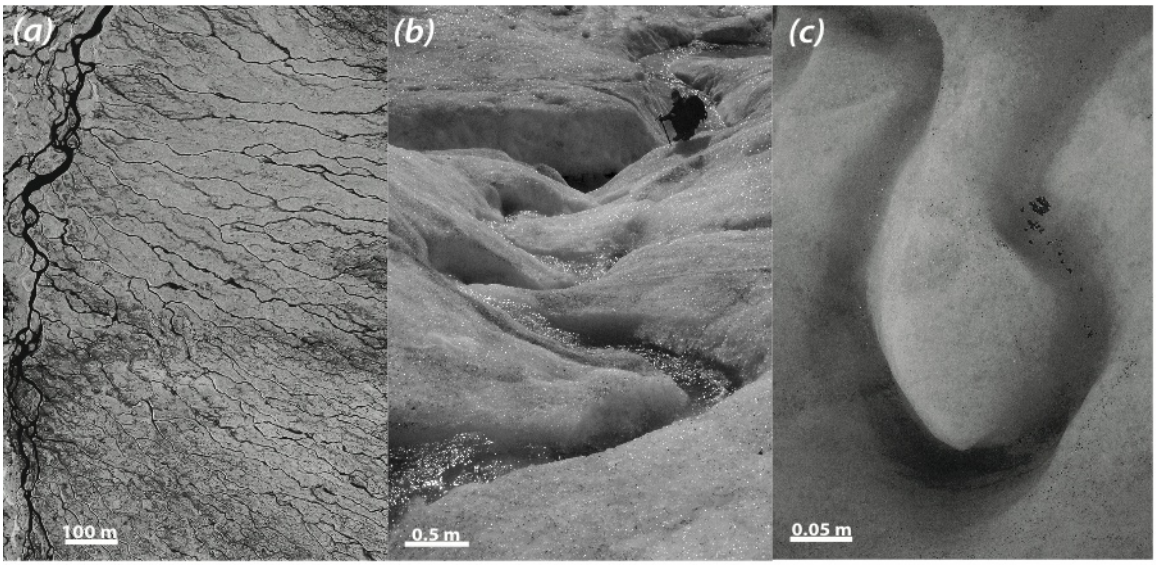

Figure 6.1: (a) Supraglacial stream network on the West Greenland Icesheet, from the near–infrared band of the IKONOS satellite. Image courtesy of Jason Box, Ohio State University, donated by Geoeye to Impossible Pictures UK. (b) Single wavelength meander sequence on the Mendenhall Glacier, Alaska, August 2010, person for scale. (c) Small well–developed meander bend on the Mendenhall Glacier, Alaska, August 2009.

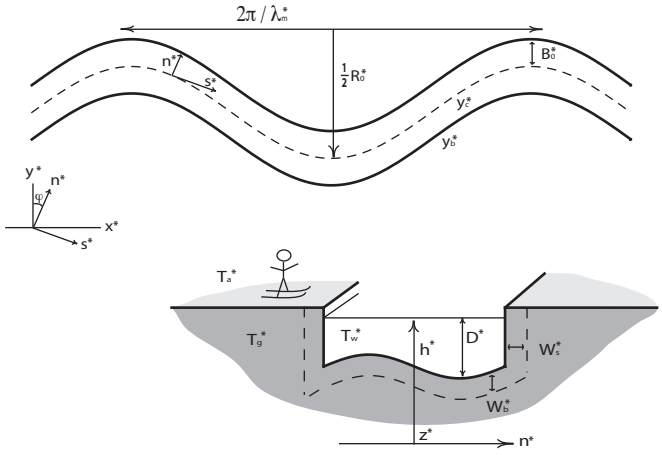

Figure 6.2: Model geometry and coordinate system definition.

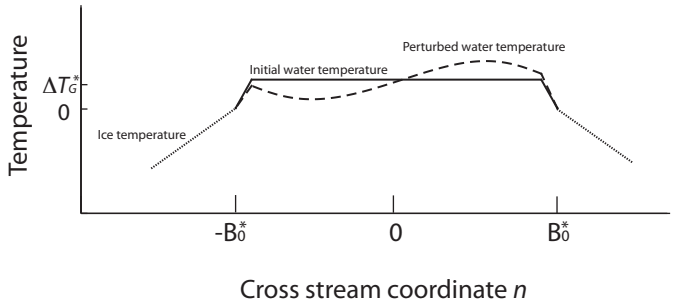

Figure 6.3: Model temperature profile in and around a supraglacial stream. Heating results in nonzero but uniform stream water temperature T^* in straight channels (solid curve), which drops to 0°C at the channel walls, while channel curvature results in a perturbed temperatures that are higher near the outer bank. Temperature in the ice falls to the bulk glacier temperature in the thermal boundary layer surrounding the channel (dotted curves). Solid and dotted curves are assumed, while dashed curve is the predicted temperature profile at the apex of a meander bend from our linear model.

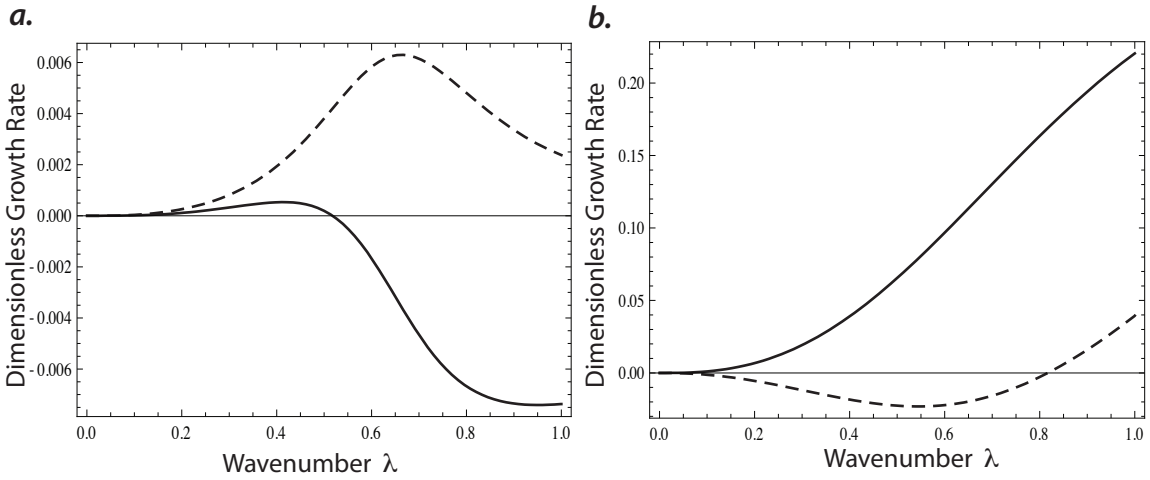

Figure 6.4: Evaluation of the linear model for lateral channel perturbations (equation 6.55), illustrating the two primary regimes. (a) The single maximum regime with downstream meander propagation. Heat transfer parameter $\mathcal{J}^* = 10^{-4}$ s/m, bulk temperature difference $\Delta T_G^* = 0.1°$C, channel width $2B_0^* = 1$ m, channel depth $D_0^* = 0.25$ m, velocity scale $U_0^* = 1$ m/s, roughness height $\zeta^* = 10^{-3}$ m and boundary scale $\ell^* = D_0^*$. (b) The regime of all unstable wavenumbers and downstream propagation. $\mathcal{J}^* = 10^{-4}$ s/m, $\Delta T_G^* = 0.1°$C, $2B_0^* = 1$ m, $D_0^* = 0.25$ m, $U_0^* = 0.1$ m/s, $\zeta^* = 10^{-3}$ m and $\ell^* = 0.1D_0^*$. Solid curves are dimensionless growth rate of perturbations (real part of equation 6.55) while dashed lines are wave celerity (imaginary part of equation 6.55).

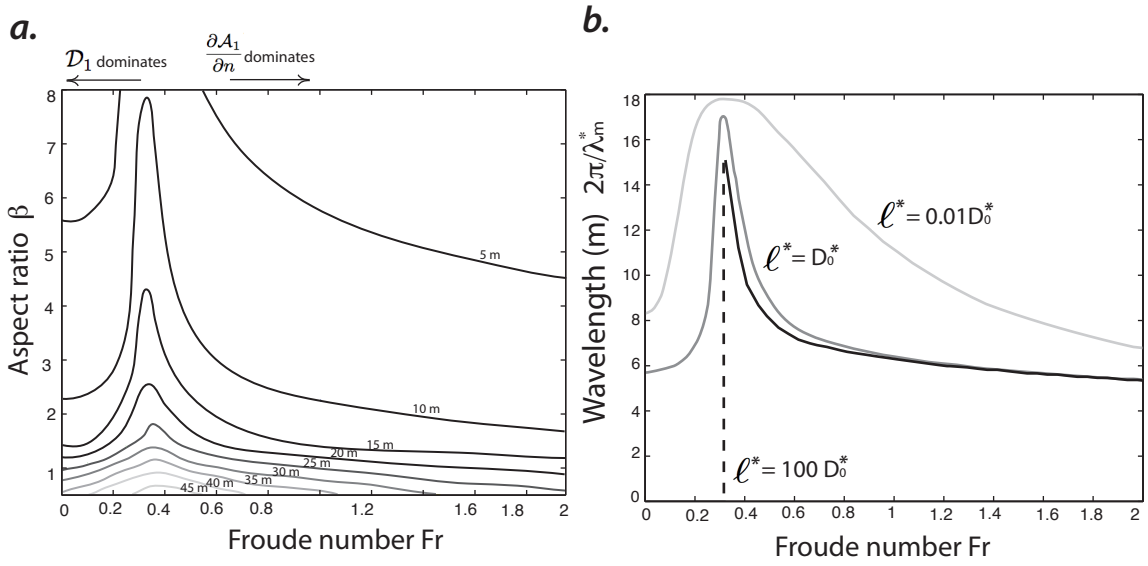

Figure 6.5: (a) Stability field for parameters in table 1, illustrating the range of (dimensional) selected unstable wavelengths in the linear model $2\pi/\lambda_m^*$ (contoured) as a function of channel aspect ratio and Froude number for fixed heat transfer parameter $\mathcal{J}^* = 10^{-4}$ s/m, bulk temperature difference $\Delta T_G^* = 0.1°$C, $\ell^* = D_0^*$, channel width $2B_0^* = 1$ m and roughness height $\zeta^* = 10^{-3}$ m. Regimes of influence for $\mathcal{D}_1$ and $\partial \mathcal{A}_1/\partial n$ are indicated by arrows. (b) Effect of varying scaling constant ℓ^* which determines the relative influence of depth perturbation $\mathcal{D}_1$ on selected wavenumber in equation (6.55). As ℓ^* increases, the contribution of $\mathcal{D}_1$ decreases until at $\ell^* = 100 D_0^*$ it has disappeared altogether and there is an abrupt transition to a completely unstable regime at low Fr (dashed line and figure 6.4.b).

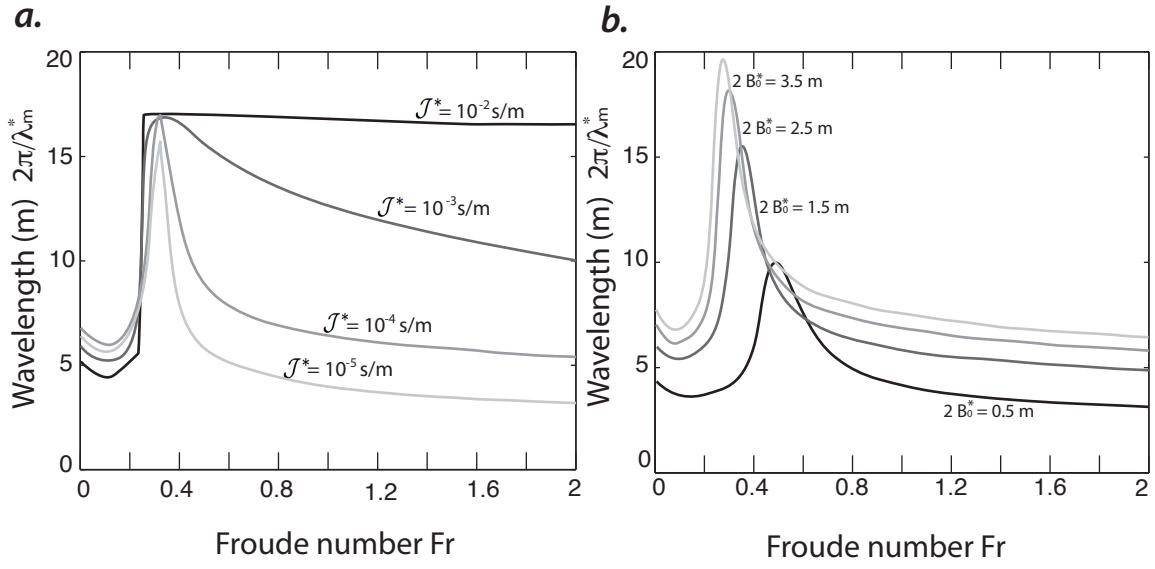

Figure 6.6: Selected most unstable meander wavelength as a function of Froude number, varying (a) Heat transfer parameter $\mathcal{J}^*$, with $B_0^* = 1$ m, $\beta = 4$, velocity scale $U_0^* = 1$ m/s, bulk temperature difference $\Delta T_G^* = 0.1°$C, roughness height $\zeta^* = 10^{-3}$ m, $\ell = D_0^*$, and (b) Channel width $2B_0^*$, with $\mathcal{J}^* = 10^{-4}$ s/m, and all other parameters are as in (a).

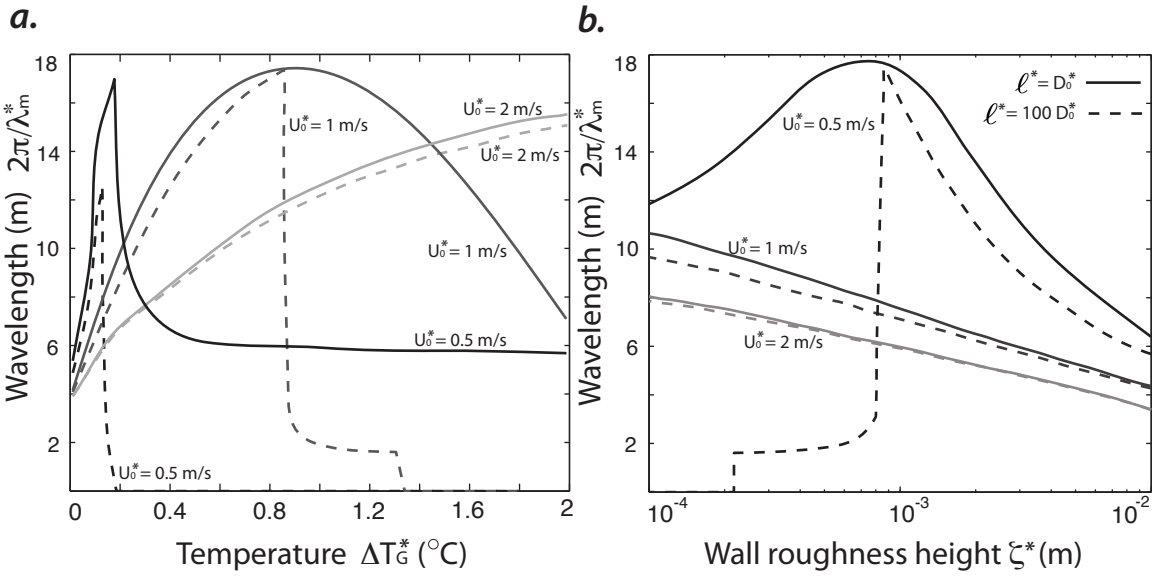

Figure 6.7: Most unstable wavelength as a function of (a) bulk temperature difference ΔT_G^* and (b) wall roughness height ζ^*. Curves illustrate three choices of velocity scale U_0^*, for $\ell^* = D_0^*$ (solid curves) and $\ell^* = 100 D_0^*$ (dashed curves). $\mathcal{J}^* = 10^{-4}$ s/m, $B_0^* = 1$ m, and all other parameters as in figure 6.6.

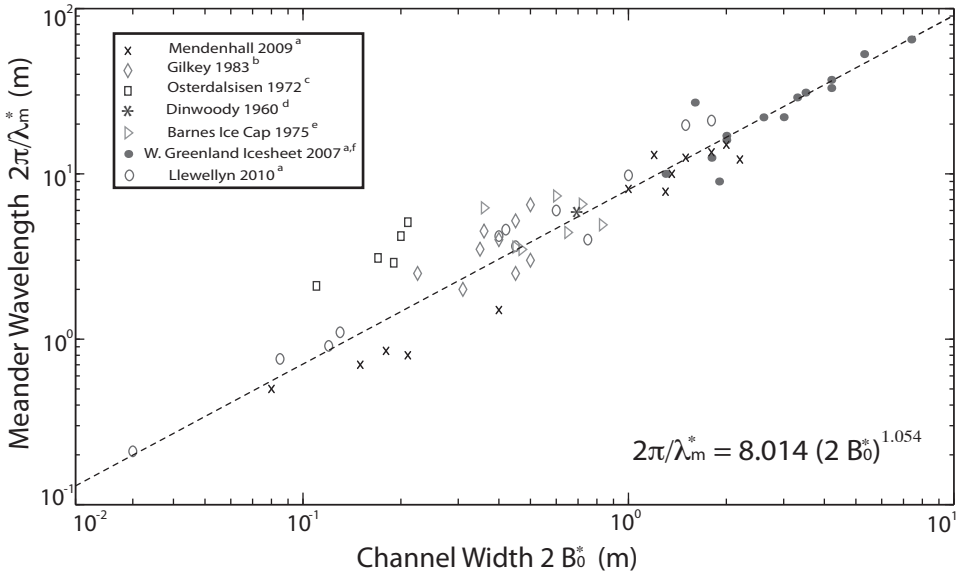

Figure 6.8: Compilation of supraglacial stream channel width vs. meander wavelength derived from field studies, along with a power law fit using the Levenberg-Marquardt algorithm. Standard error in the intercept is 0.517, and for the exponent is 0.043. Data sources: a. Authors' measurements, b. Marston [1983], c. Knighton [1981], d. Leopold and Wolman [1960], e. Parker [1975], f. pixel counting IKONOS 1 m resolution satellite images, taken July 2007.

Chapter 7

Meandering lava channels and tubes

7.1 Introduction

Lava channels and tubes are common features of basaltic lava flows on Earth [e.g,. Swanson, 1973, Hulme, 1974] and other terrestrial planets [e.g., Schubert et al., 1970, Schenk and Williams, 2004, Williams et al., 2005]. Channelization is a natural consequence of rapid (largely radiative) cooling and strongly temperature dependent viscosity [Morris, 1996, Wylie and Lister, 1995]: hotter lava has a lower viscosity, flows faster, and can cause thermal erosion, thus there is a feedback between cooling and channel formation. On steep slopes near the vent, where solidification of the lava surface is insufficient to produce a stable crust, these are open channel flows. However many exhibit an along–stream transition to tube flow [e.g., Macdonald, 1953] in which solidification of the surface decouples the bulk flow from the atmosphere through a channel–covering roof. Lava tubes are very thermally efficient because radiative heat loss is suppressed [Keszthelyi, 1995], and are sometimes travel 10s of kilometers from the vent [Swanson, 1973, Self, 1998]. In contrast, un–insulated open channel flows cool 2–4 times more quickly [Cashman et al., 1999] than their closed counterparts but also can travel long distances from the vent if discharge rates are sufficiently high [Riker et al., 2009].

While deposition through cooling and solidification is an inevitable consequence of lava emplacement in the surface environment, lava flows also have significant erosive potential [Carr, 1974]. Thermal erosion of the substrate, although inefficient, has been inferred from field observations and analog experiments [Huppert and Sparks, 1985, Kerr, 2001, 2009]. Mechanical erosion may also occur, as substrate material is either entrained into the flow [Siewert and Ferlito, 2008] or plastically indented by the surface load [Gioia et al., 2006]. Mechanical erosion is in general more efficient than thermal erosion, varying linearly with flow rate Q as opposed to a $Q^{1/3}$ dependence for thermal erosion [Siewert and Ferlito, 2008]. A combination of thermal and mechanical effects may also be important, as contraction and fracture of a freezing substrate create detachable blocks that are amenable to plucking. It is unknown in general the extent to which thermal or mechanical erosion dominates in lava

channels.

Regardless of erosion process, lava channels exhibit similarities to bedrock rivers and supraglacial streams where fluid instabilities coupled with bank erosion are reflected in channel morphology. As in other fluvial systems, lava channels exhibit standing waves (a feature of supercritical flow) [Geist et al., 2008], lava cascades [Peterson et al., 1994], and large amplitude along–stream channel sinuousity [Schubert et al., 1970]. In most other aspects they are unique: lava channels exhibit strongly temperature dependent viscosity that is large compared with water, high fluid temperature, and an inherently transient spatiotemporal nature set by rapid cooling and short eruption duration.

We focus here on the sinuosity of lava channels, applying theoretical tools developed for alluvial meanders [Blondeaux and Seminara, 1985, Camporeale et al., 2007] to study the possible meandering instabilities of lava channels. Meandering is a defining and robust feature in many fluvial settings, spanning systems in which the mechanisms of incision are fundamentally different. Supraglacial streams (thermal erosion), karst channels (chemical erosion), bedrock rivers (mechanical erosion of strong substrate), and alluvial rivers (mechanical erosion of granular substrate) all exhibit meandering, suggesting that this instability is a universal feature of erosion by channelized flow [Seminara, 2006]. Sinuousity is a common observation in lava tubes on Earth as well as the Moon and Mars, and although the amplitude of meandering is often less than that observed in other systems [Leopold and Wolman, 1960, Schubert et al., 1970, Karlstrom et al., 2011] we suspect that similar instabilities are responsible.

In general, we would like to understand meandering as a function of incision mechanism, substrate and fluid properties. Simple metrics of meandering such as the ratio of meander wavelength to channel width are distinct between settings (e.g., alluvial rivers versus supraglacial streams versus lava channels). A sufficiently general theory for meandering may offer predictive power in settings where macro scale morphology is observable but measuring flow properties is unrealistic, such as on other planets or remote locations on Earth. In what follows we develop a model for meandering lava channels that allows us to explore controls on channel sinuousity. The next step of comparing lava channel meanders to that of other channels is not attempted, but we do offer predictions that may be tested and refined in future work.

7.2 Model Development

Flow in lava channels is strongly coupled to heat transfer [Keszthelyi, 1995, Cashman et al., 1999], and thermally–insulated lava tube flow differs in this regard from open channel flow in which thermal radiation sets the cooling rate. To model this system we solve two problems, the flow field field within a lava channel and the migration due to melting and/or mechanical erosion of channel banks. In hydrologic settings these two problems are largely decoupled, as the timescale for water advection is quite small compared to the timescale for channel erosion so flow is effectively steady on bank migration timescales. Lava flows, despite their larger

viscosity, are rapidly moving flows (characteristic speed > 10 m/s in some cases [Geist et al., 2008]) so this decoupling also applies. Spatially variable shear stresses and heat transfer provide the coupling between steady streamflow and bank erosion.

Coordinate system

We use "meandering coordinates" to express the appropriate conservation equations in a translating coordinate system that tracks the channel centerline described by coordinates $(X_0^*(s^*), Y_0^*(s^*), Z_0^*)$ (figure 7.1). This coordinate system, in which s^* and n^* represent downstream and cross-stream positions (stars indicate dimensional variables), is mapped to a fixed cartesian basis (X^*, Y^*, Z^*) via

$$(X^*, Y^*, Z^*) = (X_0^* - n^* \sin\phi, Y_0^* + n^* \cos\phi, Z^*), \tag{7.1}$$

from which we obtain the metric coefficients

$$(h_s^*, h_n^*, h_z^*) = (1 + n^*\kappa^*(s^*), 1, 1), \tag{7.2}$$

where $\kappa^*(s^*) = d\phi/ds^*$ is the curvature of the channel centerline, ϕ is the angle of the centerline from the X^* axis, and the slope of the channel axis is assumed to be small. More details about the derivation of this coordinate system and the resulting curvilinear differential operators may be found in, for example, Seminara and Turbino [1992]. The channel half–width B_0^* is assumed to be fixed, implicitly requiring a lowering of the glacial surface to enable lateral channel migration. This assumption is grounded observationally, as meanders of nearly constant width are often observed with steep banks on the outside of bends and low angle banks on the inside (Figure 7.1(b)). The radius of curvature scales with its typical lengthscale R_0^* as $1/\kappa^* = R_0^*/\kappa$.

Governing Equations

In the meandering coordinate system we employ the non–dimensionalization

$$(s, n) = \frac{(s^*, n^*)}{B_0^*}, \quad (u, v, w) = \frac{(u^*, v^*, w^*)}{U_0^*}, \quad (h, D, z) = \frac{(h^*, D^*, z^*)}{D_0^*}, \tag{7.3}$$

where (u, v, w) are velocity components taking characteristic value U_0^* and (h, D, z) are the lava surface height, the lava depth, and the height above a datum respectively (figure 7.1) that scale with the characteristic depth D_0^*. After applying the depth averaging operation $\langle\cdot\rangle = 1/D \int_{h-D}^{h} (\cdot)\, dz$, the equations for mass and momentum are

$$NU\frac{\partial U}{\partial s} + V\frac{\partial U}{\partial n} + \nu_0 N\kappa\, UV + N\frac{\partial H}{\partial s} + \beta\, \mathrm{Fr}^2 \frac{\tau_{sz}}{D} - \frac{1}{\mathrm{Re}\beta}\frac{\partial \tau_{sn}}{\partial n} + \frac{1}{\mathrm{Re}\beta} N\kappa\tau_{sn} = 0 \tag{7.4}$$

$$NU\frac{\partial V}{\partial s} + V\frac{\partial V}{\partial n} - \nu_0 N\kappa U^2 + \frac{\partial H}{\partial n} + \beta\ \mathrm{Fr}^2\frac{\tau_{nz}}{D} - \frac{1}{\mathrm{Re}\beta}\frac{\partial \tau_{ns}}{\partial n} = 0 \tag{7.5}$$

$$N\frac{\partial}{\partial s}(DU) + \frac{\partial}{\partial n}(DV) + \nu_0 N\kappa DV = 0. \tag{7.6}$$

Here $U = \langle u\rangle$, $V = \langle v\rangle$ and $H = h/\mathrm{Fr}^2$, τ_{sz}, τ_{nz} are depth averaged downstream and cross-stream bed shear stresses, and τ_{ns} is the depth averaged lateral shear stress in the flow. Equations (7.4–7.6) are similar in structure to those of Blondeaux and Seminara [1985], who also neglect the vertical structure of the flow. However, we include additional shear stress terms (as derived in the appendix) to account for lateral gradients in viscosity. $N = [1+\nu_0 n\kappa]^{-1}$ is the longitudinal metric coefficient of the co–ordinate system with $\nu_0 = B_0^*/R_0^*$, $\beta = B_0^*/D_0^*$ is the half–width to depth ratio, $\mathrm{Fr} = U_0^*/\sqrt{gD_0^*}$, is the Froude number and $\mathrm{Re} = \rho U_0^* D_0^*/\mu_0$ is the Reynolds number based on reference viscosity μ_0.

Basal shear stresses are modeled as

$$\tau_{sz}^* = \tau_{nz}^* = \rho g D^*, \tag{7.7}$$

while lateral viscous stresses are

$$\tau_{sn}^* = \mu(T)\frac{\partial U^*}{\partial n^*}. \tag{7.8}$$

Equations (7.4)-(7.6) are coupled to a dimensionless and depth averaged heat balance for the flow, in meandering coordinates and after applying continuity

$$\rho c_p\left(NU^*D^*\frac{\partial T^*}{\partial s^*} + N\kappa V^*D^*T^* + V^*D^*\frac{\partial T^*}{\partial n^*}\right) = q|_{z=h-D}^* - q|_{z=h}^* + \langle a^*\rangle \tag{7.9}$$

where T^* is lava temperature, $q|_{z=h-D}^*, q|_{z=h}^*$ are heat transfer at the bottom and top interfaces of the flow, c_p is lava specific heat and $\langle a^*\rangle$ is the depth averaged viscous dissipation. We use a Reynolds analogy to parameterize temperature in terms of velocity, $T^* = T_l^* + \Delta T \mathcal{J}^* U_0^* \mathcal{U}^*$. This relation assumes strong coupling between heat and momentum transfer with T_l^* the temperature at which magma becomes locked due to cooling and crystallizing past a locking threshold [e.g., Harris and Allen, 2008] and ΔT^* the bulk flow temperature above T_l^*. All temperares in this work are scaled by ΔT^*. $\mathcal{J}^*$ is an empirical and dimensional constant that measures the strength of coupling between velocity and temperature gradients in the Reynolds analogy $T^* = \mathcal{J}^*\Delta T^*\mathcal{U}^*$. For flow past a flat plate with Prandtl number Pr equal to unity $\mathcal{J}^* = 1/U_0^*$ [Schlichting, 1960], but we consider it a variable parameter here.

Heat transfer at the upper interface is dominated by thermal radiation for open channel flow [Cashman et al., 1999], so that

$$q|_{z=h}^* = q_{radiative}^* = \sigma\left(T^{*4} - T_a^{*4}\right) = \sigma\left((T_l^* + \Delta T^*\mathcal{J}^*U_0^*\mathcal{U}^*)^4 + T_a^{*4}\right) \tag{7.10}$$

where $\sigma = 5.6\mathrm{x}10^{-8}$ W/m^{-2}K^{-4} is the Stefan–Boltzmann constant and T_a is the air temperature. For lava tubes, this upper interface is insulated from the atmosphere, and we assume

that heat transfer is conductive over a thermal boundary W^* that scales with channel depth D^*

$$q|^*_{z=h} = q^*_{conductive} = -k\left(T^*_l - T^*_g\right)/W^* \sim -k\left(T^*_l - T^*_g\right)/D^* \tag{7.11}$$

with T^*_g a far field steady temperature of the ground and k the thermal conductivity of magma or basalt.

Heat transfer through the bottom interface of the flow depends on interface position, a free boundary as phase change occurs. We are able to model both erosion and solidification, however we stick to a parameter range in which channel erosion outpaces channel construction.

The kinematic (Stefan) condition for the bottom boundary is

$$|\mathbf{n_z}|\frac{\partial(h^* - D^*)}{\partial t^*} = \frac{1}{\rho L}(q|^*_{z=h-D} - q^*_g) + \mathcal{S}\rho g\frac{\partial h}{\partial s}\mathcal{U}^* D^*, \tag{7.12}$$

accounting for lowering by thermal erosion (first two terms on the RHS) [Kerr, 2001] as well as mechanical erosion (last term on RHS) through wear [Siewert and Ferlito, 2008]. Our simple model for mechanical erosion assumes wear is proportional to the normal load and sliding distance, inversely proportional to substrate hardness as measured by $\mathcal{S}$ an empirical constant determined from experiment in the range of $10^{-7} - 10^{-11}$ Pa^{-1}, $\mathcal{U}^* = U^*_0\sqrt{U^2 + V^2}$ the flow speed and $\frac{\partial h}{\partial s}$ a small angle approximation to the basal slope. $|\mathbf{n_z}|$ is a unit vector perpendicular to the interface. The basal melting time is scaled as $t^* = LD^*_0/U^{*3}_0 t$ with L the latent heat of fusion. This timescale is large compared to the other obvious timescale of flow B^*_0/U^*_0 for the conditions we model here. Therefore we set $\partial(h - D)/\partial t$ to zero while calculating the flow field, but include it when considering boundary melting. $q^*_g = q^*_{conductive}$ is the vertical conductive heat loss obtained from equation 7.11.

Dissipation $\langle a\rangle$ in the stream is modeled as

$$\langle a\rangle = \mu(T)\langle\dot{\epsilon} : \dot{\epsilon}\rangle, \tag{7.13}$$

where in meandering coordinates contraction of strain rate tensor $\dot{\epsilon}$ (derived in appendix) reduces to $\langle\dot{\epsilon^*} : \dot{\epsilon^*}\rangle = \mathcal{U}^{*2}/D^{*2}$. Viscosity of basaltic lava is often modeled with an Arrenhius or power law dependence on temperature (also accounting for crystallization below the liquidus) [Harris and Allen, 2008]. We assume that cooling near the banks defines the channel, but in the bulk flow rapid advection maintains high temperatures and thus roughly constant viscosity. We thus take viscosity $\mu(T) = \mu_0 = const$ while solving the flow equations, acknowledging that this is most valid in the limit of large channel aspect ratio β. Dissipation is then

$$\langle a\rangle = \frac{\mu_0 U^{*2}_0}{D^{*2}_0}\frac{\mathcal{U}^2}{D^2}, \tag{7.14}$$

and we can write the final dimensionless energy balance for lava flows as

$$\begin{aligned} NDU\frac{\partial\mathcal{U}}{\partial s} + DV\frac{\partial\mathcal{U}}{\partial n} &= \Pi_1\frac{\partial(h-D)}{\partial t} - \Pi_2\frac{T_l - T_g}{D} - \Pi_3\frac{\partial h}{\partial s}\mathcal{U}D \\ &\quad -\Pi_4\left((T_l + \Delta T\mathcal{J}U^*_0\mathcal{U})^4 + T^4_a\right) + \Pi_5\frac{\mathcal{U}^2}{D^2} \end{aligned} \tag{7.15}$$

where the dimensionless numbers $\Pi_1 - \Pi_5$ are the explicit control parameters measuring the relative importance of advection versus basal lowering (Π_1), conduction (Π_2), mechanical wear (Π_3), thermal radiation (Π_4) and viscous dissipation (Π_5). These take the form:

$$\begin{aligned} \Pi_1 &= \frac{\beta U_0^*}{\mathcal{J}^* \Delta T c_p}, & \frac{\text{Basal lowering}}{\text{Heat advection}} \\ \Pi_2 &= \frac{\beta^2 k}{\mathcal{J}^* D_0^* U_0^{*2} \rho c_p}, & \frac{\text{Conductive heat loss}}{\text{Heat advection}} \\ \Pi_3 &= \frac{\beta \mathcal{S} \rho g L D_0^*}{\mathcal{J}^* \Delta T U_0^* c_p}, & \frac{\text{Mechanical wear}}{\text{Heat advection}} \\ \Pi_4 &= \frac{\beta^2 \sigma \Delta T^3}{\mathcal{J}^* U_0^{*2} \rho c_p}, & \frac{\text{Thermal Radiation}}{\text{Heat advection}} \\ \Pi_5 &= \frac{\beta \mu_0}{2 \rho c_p \mathcal{J}^* \Delta T D_0^*}. & \frac{\text{Viscous dissipation}}{\text{Heat advection}} \end{aligned} \tag{7.16}$$

We also note that open channel flow differs from lava tube flow only in the relative importance of Π_4 and Π_2 in this model. For tube flow we set $\Pi_4 = 0$ and double Π_2. These thermal dimensionless parameters, along with the channel aspect ratio β, Froude number Fr and Reynolds number Re from the momentum balance (equations 7.4 - 7.6) set the parameter space and dynamical behavior in our model.

Boundary Conditions

Equations (7.4–7.6) and (7.15) have Dirichlet boundary conditions stating that the channel walls are impermeable to flow,

$$V = 0 \text{ at } n = \pm 1 \tag{7.17}$$

and that the temperature at the channel walls is equal to the locking temperature $T = T_l$. This isothermal boundary condition implicitly assumes that magma viscosity rapidly increases near the boundary. With our parameterization of temperature this condition implies that flow speed drops to zero at the boundaries:

$$\mathcal{U} = 0 \text{ at } n = \pm 1. \tag{7.18}$$

Lateral channel migration

We close our mathematical formulation by modeling lateral migration of the channel walls. Bank migration may reflect both mechanical and thermal erosion, and may be additionally influenced by the rate of downcutting on similar timescales. A Stefan condition governs thermal erosion, while mechanical wear is set by lateral shear stresses τ_{sn}^* rather than the normal load as in equation 7.12. The rate of lateral migration of the channel bank is a condition on y_b^*

$$|\mathbf{n_y}| \frac{\partial y_b^*}{\partial t^*} = \frac{1}{\rho L} \left(q_m^{l*} - q_{conductive}^{l*} - \rho L \frac{\partial (h^* - D^*)}{\partial t^*} \right) + \mu_0 U^* \frac{\partial U^*}{\partial n^*} \quad \text{at} \quad n^* = B_0^*, \tag{7.19}$$

where the unit vector $|\mathbf{n_y}|$ ensures that erosion occurs perpendicular to the bank and q_m^{l*}, q_{cond}^{l*} are the lateral heat fluxes at the locked lava interface. $q^*_{conductive}$ is given by equation 7.11, and we calculate q_m^* from the flow field via

$$q_m^* = k\frac{\partial T^*}{\partial n^*} = \frac{k\Delta T U_0^* \mathcal{J}}{B_0^*}\frac{\partial U}{\partial n}. \tag{7.20}$$

Equation 7.19 is somewhat more general than similar models for bank migration in alluvial [Blondeaux and Seminara, 1985] and supraglacial [Parker, 1975, Karlstrom et al., 2011] settings, allowing for variable influence of vertical incision rate on lateral incision and a combination of thermal and mechanical mechanisms for bank erosion. In what follows we explore the dependence of meandering instabilities on these parameters, with the goal of constraining the mechanisms of lava channel incision through observation.

7.3 Linear Stability Analysis

We perform a linear stability analysis on equations (7.4–7.6) and (7.15), examining a channel whose centreline exhibits small–amplitude perturbations with respect to the straight configuration. We are interested in the conditions for which these perturbations grow in time, with the largest growth rate assumed to determine the finite amplitude behavior of the instability. We study harmonic perturbations (using c.c. for complex conjugate)

$$\kappa(s) = \frac{1}{R_0}\left[e^{i(\lambda_m s - \omega t)} + \text{c.c.}\right], \tag{7.21}$$

where λ_m is a non–dimensional meander wavenumber scaled by the half–width B_0^*, and ω is a frequency that may be directly related to the propagation speed of the disturbances.

We perturb the channel centerline as

$$y_c = \epsilon(t)\left[e^{i(kx - \omega t)} + \text{c.c.}\right], \tag{7.22}$$

where y_c, ϵ, k and x are quantities normalized by the half width B_0^*, and $\epsilon \ll 1$. This approximation implies that

$$\nu_0 = k^2\epsilon \tag{7.23}$$
$$\lambda_m = k + \mathcal{O}(\epsilon^2 k^2) \tag{7.24}$$
$$s = x + \mathcal{O}(\epsilon^2 k^2). \tag{7.25}$$

Hence the channel slope, the average depth D_0^*, the average speed U_0^* and thus the average Froude number all undergo variations due to the bend growth which are $\mathcal{O}(\epsilon^2 k^2)$ and so are negligible. Moreover the relationship (7.23) implies that in order for the amplitude ϵ to be small, ν_0 and k should satisfy the inequality

$$\lambda_m \sim k \gg \nu_0^{\frac{1}{2}}. \tag{7.26}$$

Perturbation of flow variables (U, V, H, D) is performed as an expansion

$$(U, V, H, D) = (1, 0, h_0, 1) + \epsilon(t)(\mathcal{A}_1, \mathcal{B}_1, \mathcal{H}_1, \mathcal{D}_1)\left[e^{i(kx-\omega t)} + \text{c.c.}\right] + \mathcal{O}(\epsilon^2 k^2), \tag{7.27}$$

where $\mathcal{A}_1$, $\mathcal{B}_1$, $\mathcal{H}_1$, $\mathcal{D}_1$ are all functions of n alone and h_0 is the nondimensional unperturbed depth.

We ensure that perturbations to the flow variables do not greatly affect externally controlled aspects of this problem that are built into the governing equations. Thus the average discharge and surface slope must remain unaffected by the $\mathcal{O}(\epsilon^1)$ perturbations as expressed by the integral conditions

$$\int_{-1}^{1} (\mathcal{A}_1 + \mathcal{D}_1) dn = 0 \tag{7.28}$$

and

$$\int_{-1}^{1} (\mathcal{H}_1 - \mathcal{D}_1) dn = 0. \tag{7.29}$$

Solution of the linearized problem

Substituting all the expansions into the governing differential system (7.4–7.6) and (7.15), at $\mathcal{O}(\epsilon^0)$ we find the uniform flow solution and energy balance within the channel,

$$\frac{dh_0}{ds} = -\frac{\text{Fr}^2}{\text{Re}} \tag{7.30}$$

$$-\Pi_2 \frac{d(\text{Fr}^2 h_0)}{dt} = -\Pi_3 \frac{T_l - T_g}{\Delta T} + \frac{\Pi_4 \text{Fr}^2}{\text{Re}} - \Pi_5 \left(\left(\frac{T_l}{\Delta T} + \mathcal{J} U_0^* \right)^4 - \left(\frac{T_a}{\Delta T} \right)^4 \right) + \frac{1}{4}\Pi_6. \tag{7.31}$$

These equations express the basic momentum balance of the unperturbed channel – that surface slope is set by viscous stresses – and the basic energy balance that determines channel lowering as a function of heat sources and sinks from the top and bottom interfaces as well as heat generation by viscous dissipation.

At $\mathcal{O}(\epsilon^1)$ we have the following system of linear equations

$$\begin{bmatrix} a_1 & \frac{d}{dn} & 0 & a_1 \\ a_2 \frac{d^2}{dn^2} + a_3 & 0 & a_4 & a_2 \frac{d^2}{dn^2} + a_5 \\ a_6 \frac{d}{dn} & a_7 & a_8 \frac{d}{dn} & a_6 \frac{d}{dn} \\ a_9 & 0 & a_{10} & a_{11} \end{bmatrix} \begin{bmatrix} \mathcal{A}_1 \\ \mathcal{B}_1 \\ \mathcal{H}_1 \\ \mathcal{D}_1 \end{bmatrix} = \begin{bmatrix} 0 \\ \beta n \lambda_m^2 \frac{1}{\text{Re}} \\ \lambda_m^2 \\ 0 \end{bmatrix}. \tag{7.32}$$

with the coefficients $a_i (i = 1, 2, \ldots, 11)$ defined by

$$\left.\begin{array}{c} a_1 = i\lambda_m, \quad a_2 = \frac{1}{\mathrm{Re}\beta} \\ a_3 = i\lambda_m + \frac{1}{\mathrm{Re}}, \quad a_4 = \frac{i\lambda_m}{\mathrm{Fr}^2} \\ a_5 = -\frac{1}{\mathrm{Re}}, \quad a_6 = -i\lambda_m \frac{1}{\mathrm{Re}\beta}, \\ a_7 = i\lambda_m + \frac{1}{\mathrm{Re}}, \quad a_8 = \frac{1}{\mathrm{Fr}^2}, \\ a_9 = -i\lambda_m + \Pi_3 \frac{\mathrm{Fr}^2}{\mathrm{Re}} - \Pi_4 4\mathcal{J}U_0^*(\mathcal{J}U_0^* + \frac{T_l}{\Delta T})^3 + \frac{\Pi_5}{2}, \\ a_{10} = i\Pi_1\omega - i\Pi_3\lambda_m, \\ a_{11} = -i\Pi_1\omega + \Pi_2\left(\frac{T_l}{\Delta T} - \frac{T_g}{\Delta T}\right) - \Pi_3 \frac{1}{\mathrm{Re}}\mathrm{Fr}^2 - \frac{\Pi_5}{2}, \end{array}\right\} \tag{7.33}$$

By manipulating this system we can obtain a simpler 4th order equation

$$\Sigma_1 \mathcal{A}_1 + \Sigma_2 \frac{d\mathcal{A}_1}{dn} + \Sigma_3 \frac{d^2\mathcal{A}_1}{dn^2} + \Sigma_4 \frac{d^4\mathcal{A}_1}{dn^4} = \Sigma_0 \tag{7.34}$$

where

$$\Sigma_0 = \lambda_m^2 \left(1 - \frac{a_8}{a_4 \mathrm{Re}} \left(1 + a_{10} \frac{a_5 - a_3}{\sigma}\right)\right) \tag{7.35}$$

$$\Sigma_1 = a_7 \tag{7.36}$$

$$\Sigma_2 = \frac{-a_7}{a_1} \tag{7.37}$$

$$\Sigma_3 = \frac{a_3 a_8}{a_1 a_4} + \frac{a_8(a_5 - a_3)(\frac{a_3 a_{10}}{a_4} - a_9)}{a_1 a_4 \sigma} \tag{7.38}$$

$$\Sigma_4 = \frac{a_2 a_8}{a_1 a_4} \left(1 + \frac{a_{10}(a_5 - a_3)}{a_4 \sigma}\right), \tag{7.39}$$

with $\sigma = a_{11} - a_9 - a_{10}(a_5 - a_3)/a_4$ along with coupled equations in the other variables. Equation (7.34) has the form of a forced linear oscillator, also characteristic of alluvial meander models.

The boundary conditions, equations (7.17) and (7.18), at $\mathcal{O}(\epsilon^1)$ become

$$\mathcal{B}_1 = \mathcal{A}_1 = 0 \qquad \text{at} \quad n = \pm 1. \tag{7.40}$$

The general solution to (7.34) is

$$\mathcal{A}_1(n) = C_1 e^{r_1 n} + C_2 e^{r_2 n} + C_3\, e^{r_3 n} + C_4\, e^{r_4 n} \tag{7.41}$$

where (r_1, r_2, r_3, r_4) are the four linearly independent roots of the characteristic equation

$$0 = \Sigma_1 + \Sigma_2 r + \Sigma_3 r^2 + \Sigma_4 r^4. \tag{7.42}$$

The constants (C_1, C_2, C_3, C_4) are unwieldy analytic expressions not presented here (available upon request to the authors), evaluated by substituting equation (7.41) into (7.32), from which $\mathcal{B}_1$, $\mathcal{D}_1$ and $\mathcal{H}_1$ follow.

Lateral channel instabilities

Perturbations to the flow field will lead to harmonic meandering instabilities on the timescale of melting, following equation (7.19). The linear contribution to this balance governs the amplification of perturbations to the channel centerline, and we note that because of the assumed fixed channel width

$$y_b = 1 + y_c + \mathcal{O}(\epsilon^2 k^2). \tag{7.43}$$

The $\mathcal{O}(\epsilon^1)$ contribution reads

$$\frac{\partial y_c}{\partial t} = \left(\frac{k\Delta T \mathcal{J}}{\beta \rho U_0^{*2}} + \frac{\mu_0 L \mathcal{S}}{\beta U_0^* B_0^*} \right) \frac{\partial \mathcal{A}_1}{\partial n} + \left(\frac{k\Delta T}{\beta \rho U_0^{*3}} (T_l - T_g) + \frac{i\omega}{\beta} \right) \mathcal{D}_1 - \frac{i\omega}{\beta} \mathcal{H}_1, \tag{7.44}$$

where we scale the time variation of perturbations $\omega^* = LD_0^*/U_0^{*3}\omega$ as we do time. This balance explicitly illustrates the competition between conductive heat loss, mechanical wear and vertical downcutting in setting the lateral bank migration rate.

7.4 Results

We find a wide range of parameters for which our model produces a meandering instability with unique wavelength (Figure 7.3). Both the amplitude and wavelength of this instability vary quite strongly over the range of parameters we consider reasonable, and transitions to stability (perturbation amplitudes are negative so become damped in time) and high frequency instability (perturbation amplitudes become increasingly unstable at small wave lengths) are predicted for some parameters. We find that, for finite amplitude meanders, the instability generally propagates upstream (celerity, the imaginary part of the solution, is negative). This is in contrast to meandering instabilities for supraglacial streams [Karlstrom et al., 2011] and most alluvial models [Seminara, 2006]. However, we also find stationary meanders (e.g., Figure 7.3.c) and cases in which downstream propagation occurs.

There are a large number of dimensionless parameters in our solution, and many dimensional parameters that are poorly constrained. A complete exploration of the parameter space is not attempted here, but we do wish to demonstrate which parameters control meander instabilities in specific cases that are relevant for real lava channels, and rationalize the physical controls on meandering implied by model behavior. Sinuousity provides information about substrate strength and erosion processes in other settings [Seminara, 2006], and we anticipate that a fit of our model to data may inform the debate on lava channel erosion. However, before attempting this we must first demonstrate that our model makes predictions that are reasonable.

To this end we pick two end member cases, a channel with width similar to Lunar sinuous rilles ($B_0^* = 100$ m, Schubert et al. [1970]) and a channel similar to typical those observed during terrestrial basaltic eruptions (e.g., Hawaii and Mount Etna) ($B_0^* = 1$ m) [e.g., Peterson et al., 1994, Siewert and Ferlito, 2008] as illustrated in Figure 7.1. Many unknown parameters in our problem covary, as they do in setting the hydraulic geometry

of alluvial rivers [Leopold and Maddock, 1953], but this covariance is poorly constrained for lava flows. Dimensional parameters chosen for each of these cases are listed in Table 1, along with the corresponding dimensionless numbers in Table 2. Selected variation of dimensional parameters is shown in Figure 7.4.

For the large channel we choose a mean flow velocity (10 m/s) and channel width (100 m) similar to that estimated for the original width (before erosion of channel walls) of lunar rilles. We then explore the selected wavelength of the meander instability as a function of channel aspect ratio varying 4 other parameters: the magma viscosity μ_0, bulk temperature difference ΔT, downcutting rate of perturbation ω, and efficacy of mechanical erosion $\mathcal{S}$. It is evident that quite different model behavior results from varying these parameters, and finite amplitude meandering is not a feature of all parameter choices (note the transitions to instability at small wavelengths – a high frequency instability that is not realistic – and stability in Figure 7.4).

In terms of dimensional parameters, it appears that lowering rate ω and lava viscosity μ_0 have the largest effect on selected wavelength, with finite lowering rate resulting in a much reduced meander wavelength irrespective of other parameters. Mechanical erosion appears to have only modest control on the solution for these parameters, while temperature difference between the bulk flow and locking temperature ΔT exerts greater influence. However dimensional quantites affect the solution through the 8 dimensionless governing parameters in equation 7.4-7.6 and 7.15, and more complete physical insight follows from examining the relative magnitudes of these numbers for the parameter choices in figure 7.4. These ranges are listed in Table 2.

Influence of the dimensionless numbers in our problem follows the governing equations, and thus they may be easily interpreted physically. Reynolds number Re appears in inverse in the governing equations. Increasing Re generally decreases the viscous stresses and results in a larger meander wavelength. Viscous stresses introduce a stabilization of the meander instability that is increasingly suppressed as Reynolds number increases. Vertical shear stresses will increase with Froude number, and directly correlate with increase wavelength. Thermal parameters exhibit trends that match their sign in the heat balance – increasing Π_1 (downcutting energy) and Π_5 (viscous dissipation) result in increased meander wavelength, while Π_2, Π_3 and Π_4 are inversely correlated with meander wavelength.

The smaller channel that we explore, with half-width $B_0^* = 1$ m, exhibits quite different behavior. In this case, typical values for flow parameters (U_0^* and D_0^*) result in stable channels for significant range of the parameter space, irrespective of thermal parameters. This results from the fact that Reynolds numbers for these flows are much smaller, so the stabilizing effect of viscous stresses in enhanced relative to the large channel. This reduced range of instability is exhibited in Figure 7.5 for select parameter choices. It is evident from this figure that thermal parameters exert a second order influence on selected wavelength compared to flow parameters. In cases that thermal parameters dominate the Reynolds number effect, we see similar dynamic trends as with the larger channel.

We can also explore the transition from open channel flow to tube flow. Our model for the transition between these flow types consists of turning on and off the radiative heat loss

at the top interface of the channel in our energy balance (equation 7.15). We find that for some parameter choices there are quantitative differences between the selected wavelength and stability of perturbations with and without radiative heat transfer. Examples for a large channel ($B_0^* = 100$ m) are plotted in Figure 7.6. We see in this case that, all else constant, for large flow velocities ($U_0^* = 10$ m/s) meanders result over a greater range of aspect ratio with greater wavelength in channels for which radiation is suppressed (tube flow). However, we also show that varying other parameters in the problem (for example, the magnitude of mechanical erosion in Figure 7.6) may suppress this difference.

The selected wavelengths produced by our model are linear solutions, and finite amplitude effects may modulated the initial instabilities that we model here. Still, these linear perturbations are expected to most closely represent true meander wavelengths. While there is little published quantitative data on the sinuousity of lava channels, Schubert et al. [1970] provide measurements of Lunar sinuous rilles that we can use to provide some constraints on our model. Their Figure 12 shows measure meander wavelength to width ratios of 2–10, and we overlay this measurement on Figures 7.4 and 7.6. If we compare this quantity to the dimensionless wavelengths plotted in figure 7.4, we would infer that downcutting occurred during rille formation in order to produce small wavelength to width ratios. We also rule out cool flows with only thermal erosion (curve excluded from the shaded box in Figure 7.4). Further constraints on channel aspect ration may inform whether lunar rilles are tube or open channel flows (Figure 7.6) or whether we can rule out particular erosion mechanisms. However, even without this more detailed comparison we have demonstrated that meandering is a common instability in lava channels. This model makes testable predictions that may inform other studies of these flows, and illustrates that meandering lava channels share a common origin with meandering in other fluvial systems.

7.5 Appendix

Derivation of the governing equations for alluvial meandering has been presented in detail in, e.g., Smith and McLean [1984] and Seminara and Turbino [1992], however these models are not appropriate for viscous flow. We therefore present in detail the shear stress terms in equations 7.4-7.5 and viscous dissipation in equation 7.15.

Shear stress in meandering coordinates

In meandering coordinate with metric coefficients given by $(h_s^*, h_n^*, h_z^*) = (1 + n^*\kappa^*(s^*), 1, 1)$, divergence of the general stress tensor is given by

$$\left.\begin{array}{rcl} \nabla \cdot \tau & = & \left[N\frac{\partial \tau_{ss}}{\partial s} + \frac{\partial \tau_{ns}}{\partial n} - \kappa N \tau_{ns} + \frac{\partial \tau_{sz}}{\partial z}\right]\mathbf{e_s} \\ & + & \left[N\frac{\partial \tau_{sn}}{\partial s} + \frac{\partial \tau_{nn}}{\partial n} + \kappa N(\tau_{ss} - \tau_{nn}) + \frac{\partial \tau_{nz}}{\partial z}\right]\mathbf{e_n} \\ & + & \left[N\frac{\partial \tau_{sz}}{\partial s} + \frac{\partial \tau_{nz}}{\partial n} - \kappa N\frac{\partial \tau_{sz}}{\partial s} + \frac{\partial \tau_{zz}}{\partial z}\right]\mathbf{e_z} \end{array}\right\} \tag{7.45}$$

with N and κ defined in the main text and $(\mathbf{e_s}, \mathbf{e_n}, \mathbf{e_z})$ unit vectors in downstream, cross stream and vertical directions respectively. Models for meandering alluvial streams simplify this general expression considerably, arguing that in large aspect ratio rivers the dominant boundary layer shear flow of low viscosity fluid implies vertical stresses dominate. τ_{sz}, τ_{nz} are then the only nonzero components of the stress tensor.

Lava channels are likewise dominantly shear flows, but strongly temperature dependent viscosity and lower aspect ratios than alluvial systems imply that wall cooling may significantly affect viscous stresses. For example, assuming that the lava channel boundary is set by the locking temperature $T_l = 800 - 1000°C$, lava viscosity increases roughly 3 orders of magnitude (roughly $\mathcal{O}(10)$ Pas to $\mathcal{O}(10^4)$ Pas) from conditions likely found in the bulk flow ($T = 1200 - 1300C$) near to the vent [Harris and Allen, 2008]. Therefor we include lateral shear stresses τ_{ns} that arise from viscosity variations in our modeling as well as bed shear stresses. All other components vanish upon depth averaging or are negligible.

Viscous dissipation in meandering coordinates

Viscous dissipitaion occurs at the smallest length scales in a flow as fluid viscosity turns momentum into heat. It may be expressed as a contraction of the stress tensor τ with the strain rate tensor $\dot{\epsilon}$ of the flow which for the (thermo) viscous flow considered here takes the form

$$a = 2\mu(T)\ \dot{\epsilon} : \dot{\epsilon}, \tag{7.46}$$

where $\dot{\epsilon} = (\nabla u + \nabla u^T)/2$ is the strain rate tensor.

In meandering coordinates strain rate is

$$\nabla u = \begin{bmatrix} N\left(\frac{\partial u}{\partial s} - \kappa v\right) & N\left(\frac{\partial v}{\partial s} + \kappa u\right) & N\frac{\partial w}{\partial z} \\ \frac{\partial u}{\partial n} & \frac{\partial v}{\partial n} & \frac{\partial w}{\partial n} \\ \frac{\partial u}{\partial z} & \frac{\partial v}{\partial z} & \frac{\partial w}{\partial z} \end{bmatrix}, \tag{7.47}$$

and the contraction $\dot{\epsilon} : \dot{\epsilon}$ may be expressed (after applying continuity) as

$$\dot{\epsilon} : \dot{\epsilon} = 2\left[\frac{\partial u_n}{\partial n}\right]^2 + \frac{1}{2}\left[N\left(\frac{\partial u_n}{\partial s} + \kappa u_s\right) + \frac{\partial u_s}{\partial n}\right]^2 + \left[\frac{1}{2}\frac{\partial u_s}{\partial z}\right]^2 + \left[\frac{1}{2}\frac{\partial u_n}{\partial z}\right]^2. \tag{7.48}$$

after a depth averaging operation assuming $\langle\phi\psi\rangle \approx \langle\phi\rangle\langle\psi\rangle$, two terms arise that do not involve derivatives with respect to n or s and thus will dominate the expression, leaving

$$\langle\dot{\epsilon} : \dot{\epsilon}\rangle = \frac{U^2 + V^2}{4D^2} \tag{7.49}$$

as the viscous dissipation in our model.

Parameter	Large Channel	Small Channel
B_0^*	$100 \quad m$	$1 \quad m$
D_0^*	$1 - 10 \quad$ m/s	$0.01 - 1 \quad$ m
U_0^*	$1 - 5 \quad$ m/s	$0.01 - 2 \quad$ m/s
ΔT^*	$100, 500 \quad ^\circ$C	$100, 500 \quad ^\circ$C
μ_0^*	$1, 100 \quad$ Pas	$1, 100 \quad$ Pas
$\mathcal{S}^*$	$10^{-7}, 10^{-10} \quad$ Pa^{-1}	$10^{-7}, 10^{-10} \quad$ Pa^{-1}
T_l^*	$700 \quad ^\circ$C	$700 \quad ^\circ$C
κ_I	$1 \quad$ W/m K	$1 \quad$ W/m K
L	$400 \quad$ kJ/kg	$400 \quad$ kJ/kg
ρ	$3000 \quad$ kg/m^3	$3000 \quad$ kg/m^3
c_p	$4 \quad$ kJ/kg K	$4 \quad$ kJ/kg K

Table 7.1: Estimates for model parameters, for case of large and small channel.

Symbol	Physical ratio	Large Channel	Small Channel
β	Channel width to depth	$5 - 100$	$1 - 100$
Fr	Inertia to gravity	$0.05 - 4$	0.003–4
Re	Viscous stresses to inertia	$10^0 - 10^5$	$10^{-4} - 10^{2.5}$
Π_1	Latent heat to advection	$10^{-5} - 10^0$	$10^{-8} - 10^{-1}$
Π_2	Conduction to advection	$10^{-9} - 10^{-3}$	$10^{-7} - 10^2$
Π_3	Mechanical erosion to advection	$10^{-8} - 10^{-1}$	$10^{-6} - 10^{1/2}$
Π_4	Radiation to advection	$10^{-9} - 10^{-2}$	$10^{-8} - 10^2$
Π_5	Viscous dissipation to advection	$10^{-10} - 10^{-6}$	$10^{-9} - 10^{-3}$

Table 7.2: Dimensionless numbers, their meaning, and ranges for the two example cases of a large channel ($B_0^* = 100$ m) and a small channel ($B_0^* = 1$ m)

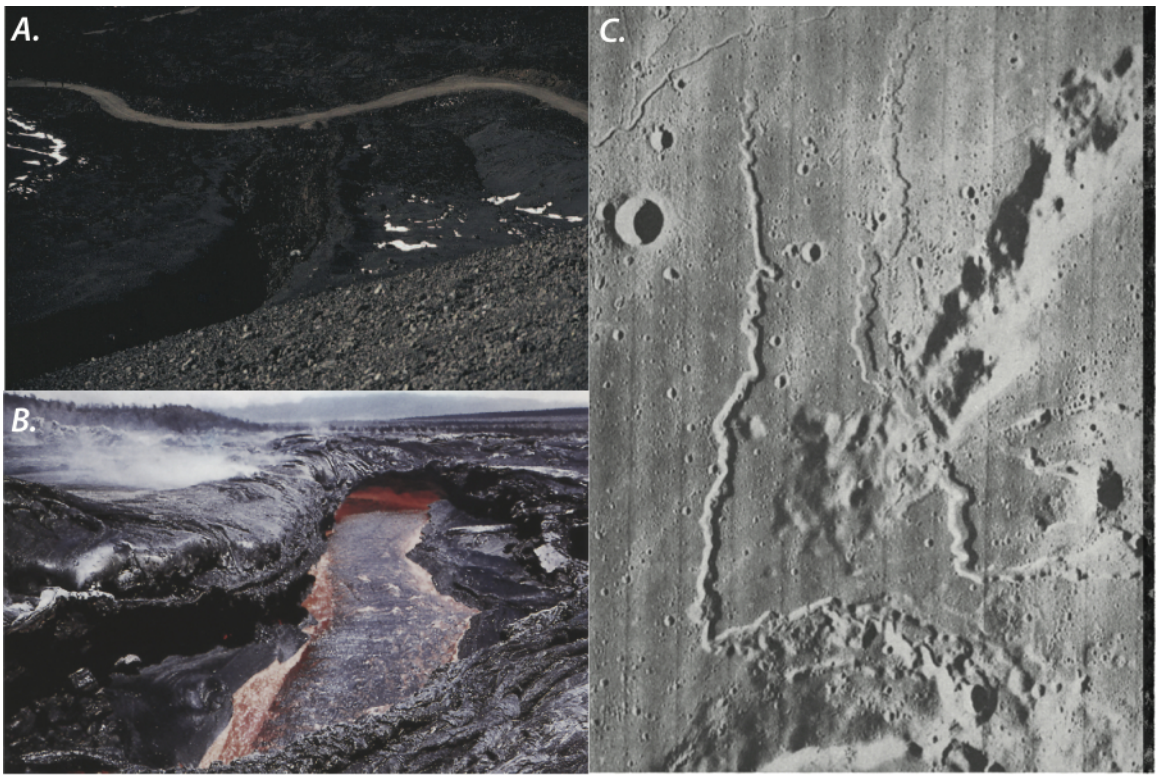

Figure 7.1: (a) Example of a sinuous (frozen) lava channel on Mt Etna, with width between 8 and 16 m [from Siewert and Ferlito, 2008]. (b) Transition from open channel flow to tube flow through roof building during the 1970 Mauna Ulu eruption, Hawaii [from Peterson et al., 1994] (c). Sinuous rilles on the Moon [from Schubert et al., 1970]. Width of this photo is 50 km.

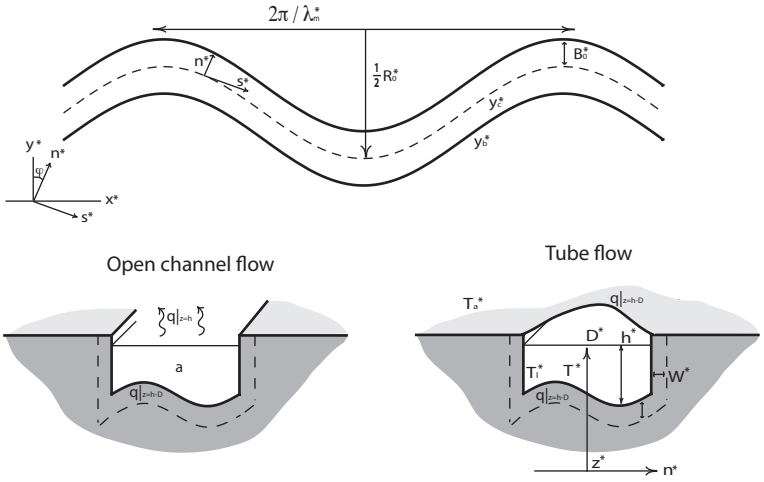

Figure 7.2: Model geometry and coordinate system definition, illustrating the heat balance differences between open lava channels and tube flow.

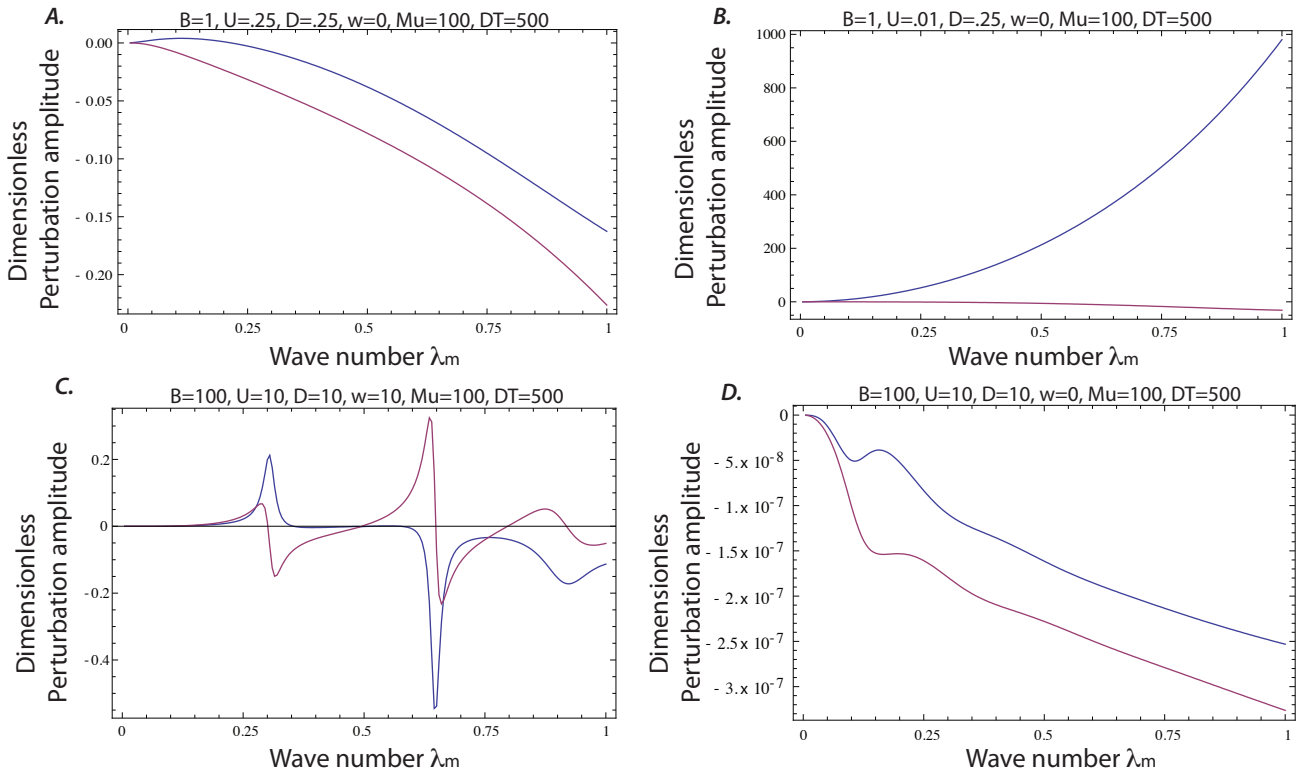

Figure 7.3: Dimensionless lateral bank perturbation amplitude (equation 7.44) versus wavenumber for selected cases to demonstrate typical model output. Blue cruves are the growth rate (real part of perturbation) while red curves are the propagation direction (imaginary part of perturbation). Variable parameters are listed at the top of each panel. We assume a locking temperature $T_l = 700$ C, and $\mathcal{J} = 1$ s/m for all cases.

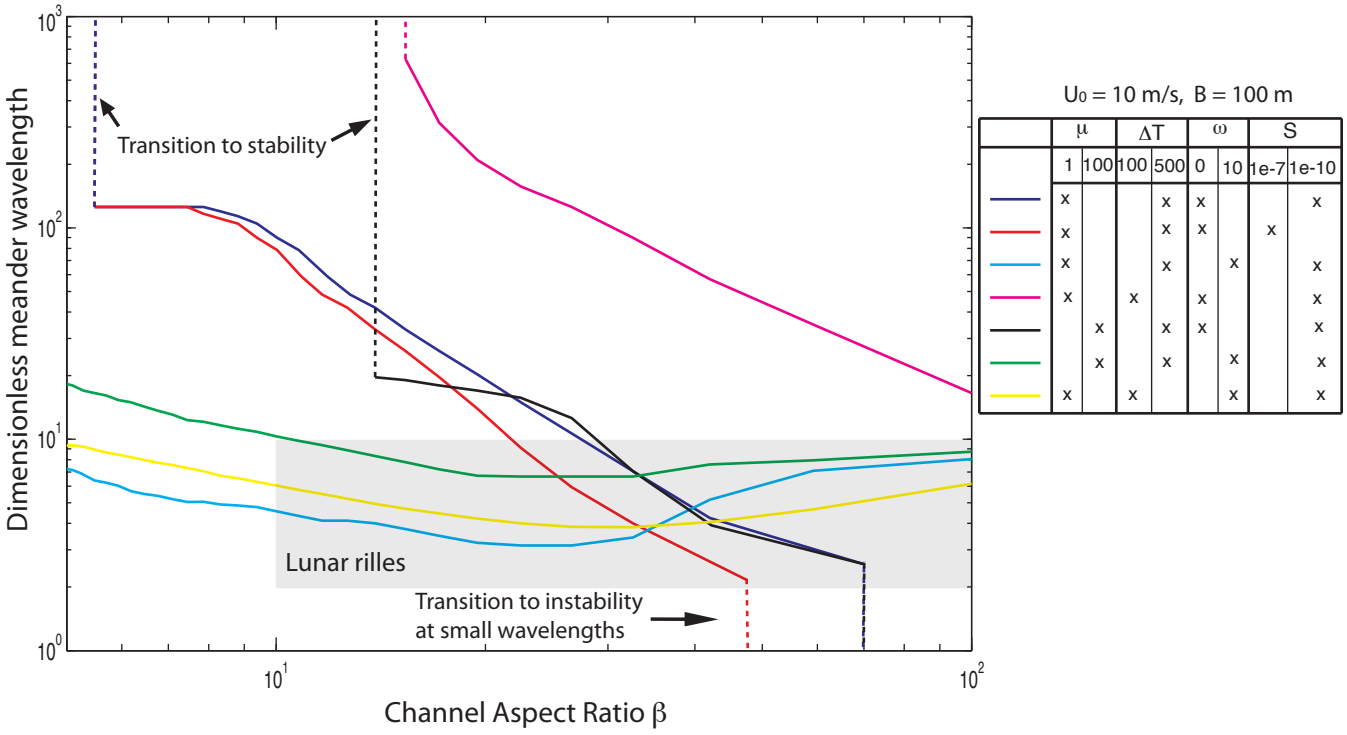

Figure 7.4: Variation of selected meander wavelength as a function of channel aspect ratio β for a wide ($B_0^* = 100$ m) lava channel. Curves are for selected parameters listed in the table. Transitions to stability (perturbation amplitude is negative) and to uniform instability (perturbation amplitude grows with wavenumber) are labeled. The gray box is the range of dimensionless wavelength measured for Lunar rilles by Schubert et al. [1970].

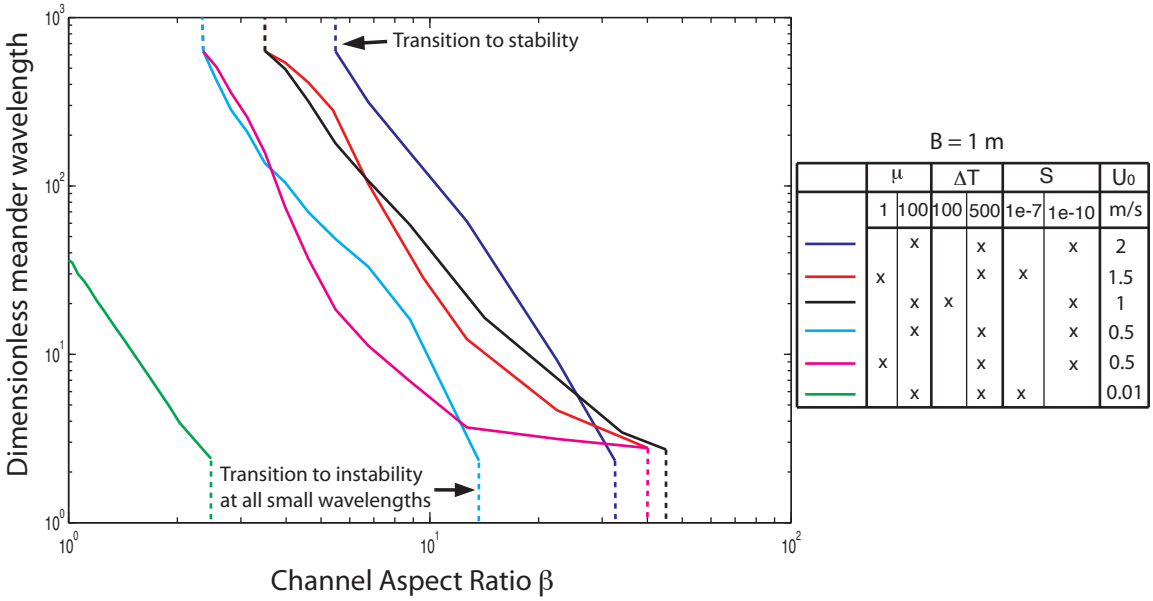

Figure 7.5: Variation of selected meander wavelength as a function of channel aspect ratio β for a small ($B_0^* = 1$ m) lava channel. Curves are for selected parameters listed in the table. Transitions to stability (perturbation amplitude is negative) and to uniform instability (perturbation amplitude grows with wavenumber) are labeled.

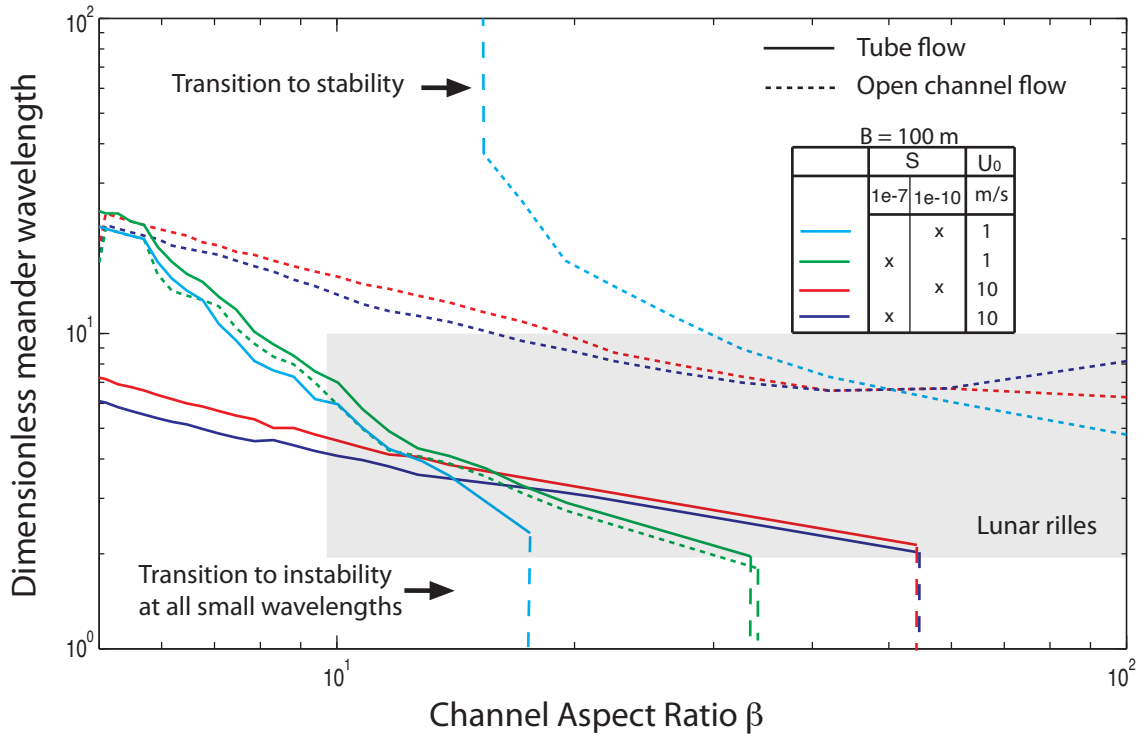

Figure 7.6: Differences in meander wavelength for open channel versus tube fed flows in the case that $B_0^* = 100$ m. For these examples ($\mu = 100$ Pas $\Delta T = 500$ C) eliminating radiation from the heat balance (our model for the tube transition) results in smaller meanders at a restricted range of aspect ratios. Mechanical erosion eliminates differences between meander wavelength in tube versus channel flows as velocity U_0^* goes down. The gray box is the range of dimensionless wavelength measured for Lunar rilles by Schubert et al. [1970]. Further constraints on channel aspect ratio would appear to provide constraints on whether Lunar rilles were open channel or tube flows.

Chapter 8

Conclusion

Crustal magma transport integrates processes that occur over 12–15 orders of magnitude in space and time, culminating in volcanic eruptions and intrusions that build and chemically evolve the crust. Magma transport is relevant both for understanding Earth history and volcano–human interactions, but it is largely inaccessible to direct observation. Constraints come both from observations of active magma transport and from study of the frozen record of intruded magmas, erupted lavas, ash and volcanic landforms. Integrating active monitoring with the geologic record is of primary importance for understanding the variability and consequences of magma transport over geologic time. However, as with other Earth Science disciplines [e..g., Oskin et al., 2007], it is not always easy to reconcile observed modern observations with the partial preservation and time–averaged nature of geologic data.

Extreme volcanic eruptions with erupted volume > 1000 km^3 [Self, 2006] are a prime example and have no historical analog. Their infrequence relative to human timescales ($10^5 - 10^6$ year recurrence [Miller and Wark, 2008], compared to 30–100 year global recurrence of great earthquakes [McCaffery, 2008]) provides us with little direct evidence for their assembly, eruption or global impact. Yet these large events are preferentially preserved in the geologic record and represent the largest perturbations to other Earth Systems (e.g., climate, ecology). There are a variety of indirect means to reconstruct evolving eruption cycles, but we lack an unambiguous observational record. Thus for both the study of short–term volcanic hazards and longer–term coupling of eruption cycles to tectonics and climate it is necessary to extrapolate from modern to geologic constraints. Integration of such diverse data benefits from quantitative models for magma transport.

This thesis develops models for the time–evolving dynamics of individual magma transport components, dikes, magma chambers and volcanic conduits. Modeling demonstrates that these internal components exert significant control on the episodic nature of surface volcanism. Applications to stratovolcano spacing in arc settings, to the distribution of caldera forming eruptions in the geologic record, and to the duration of "main phase" eruptions of Large Igneous Provinces, suggest that these models provide a consistent explanation for a range of volcanic phenomena on large scales.

Chapters five and six model meander formation in the channels of water on glaciers

and lava from effusive eruptions. These features, while distinct in transported fluid, substrate, and mechanisms of erosion, nonetheless exhibit similar morphological instabilities. A mathematical framework developed for alluvial meanders [Blondeaux and Seminara, 1985] demonstrates that the instability responsible for meander formation is a generic feature of flow over an erodable substrate. This work provides general justification for developing mechanistic rather than empirical models for transport processes: large scale features, while differing in detail, are often controlled by processes that are independent of setting. Applied to subsurface magmatic plumbing this perspective suggests that, despite an enormous range of environmental conditions, primary transport features reflect emergent organization from underlying nonlinear thermodynamic and mechanistic controls.

Of course, similarity does not necessarily imply universality [e.g., Stanley et al., 2000], and important mechanistic information may be obtained by focusing on differences between similar phenomena in different environments. The scaling between meander wavelength and channel width, for example, is slightly different between meanders on gravel, bedrock, ice, and lava. This likely reflects differences in erosion mechanism between these settings, and has geological applications to planetary settings in which meanders are observed but the nature of the substrate and eroding fluid is unknown. Future directions towards this goal will synthesize data from lava channels [e.g., Schubert et al., 1970], supraglacial streams [e.g., Parker, 1975, Karlstrom et al., 2011], bedrock and alluvial rivers [e.g., Leopold and Wolman, 1960] to constrain the parameters of erosion in different settings. The models in this thesis also predict a time evolution of meanders that can be tested.

Connecting frozen magma transport to other Earth systems that have evolved over geologic time (e.g., climate, mantle circulation) requires understanding these couplings and the effect of background forcing on the transport processes. Testing of models presented here will require subtracting background signals due to tectonics, climate, and mantle dynamics. Planetary analogs, such as the Tharsis magmatic province on Mars, provide examples of volcano spacing in non–plate tectonic settings with which to test magmatic lensing [Karlstrom et al., 2010b] and thus a control on tectonic forcing. To address other influences, settings with many well–characterized volcanic centers are required to provide a statistical basis for removing background signals. Volcanic zones such as the Cascades may provide sufficient data to accomplish this task.

The Cascades have been a continuous and well–defined arc since the Eocene, with slab- and mantle wedge-derived melt available to drive crustal magma transport [Hildreth, 2007]. However, the distribution of Cascades volcanism is far from uniform in space or time [Guffanti and Weaver, 1988]. Eruptive output concentrates at evolved, long–lived volcanic centers for parts of the arc, but significant contributions come also from broadly distributed and largely mafic monogenetic cones. These monogenetic eruptions most directly sample the mantle source regions, with little modulation or storage in the crust. Roughly 75% of erupted lavas come from individual edifices versus distributed cones in the segment of the arc from Washington to British Columbia, dropping to 10% in the Oregon Cascades but up to $65-80\%$ for the Lassen and Shasta segments in California [Hildreth, 2007]. All eruptive centers evolve in output over time. Eruption rates (as constrained by dating and mapping of flows) vary

widely, from 0.01 - 100 km^3/yr at individual centers throughout the Quaternary [Hildreth, 2007]. Although partial preservation dictates that the geologic portrait of Cascades magmatism will never be complete, this may be a suitable setting to test dynamic models for magma transport.

A primary goal in volcanology, as in many branches of Earth Science, is to understand natural systems well enough to mitigate human hazards. As with many branches of Earth Science, the extreme range of interacting nonlinear components involved in magma transport makes hazard forecasting difficult. However, relative to other hazards such as earthquakes that provide seconds at most of warning before strong ground motion occurs, volcanic eruptions are often preceded by prolonged precursors, in the form of seismicity [Voight and Cornelius, 1991, Chouet, 1996], ground inflation [Mogi, 1958, Geist et al., 2008], and changes in gas discharge [e.g., Swanson et al., 1983, Spilliaert et al., 2006]. Combined with models for magma transport, these precursors provide complicated but far–reaching information about the subsequent surface eruption [e.g., Anderson and Segall, 2011].

Further refinements to these models make true eruption forecasting a real possibility, and it is likely that within 50 years there will be an effective short–term eruption early warning system similar to weather forecasting. On longer time scales magmatism is likely chaotic, so in the absence of knowledge about all relevant initial conditions true prediction is impossible. However, extreme volcanic events such as Large Igneous Provinces that represent anomalous perturbations to the magma transport system are more tractable, and represent opportunities to invert the frozen igneous record for drivers and consequences of volcanism. The models provided here represent a template both for hazard mitigation on human timescales and a probe of Earth history through prehistoric eruptions. This follows in the rich Earth Science tradition of extrapolating processes understood on human scales to inaccessible domains of time and space.

Bibliography

V. Acocella. Understanding caldera structure and development: An overview of analogue models compared to natural calderas. *Earth-Science Reviews*, 85:125–160, 2007.

J. J. Ague and G. H. Brimhall. Magmatic arc asymmetry and distribution of anomalous plutonic belts in the batholiths of california: Effects of assimilation, crustal thickness, and depth of crystallization. *GSA Bulletin*, 100:912–927, 1988.

M. Albertz. Relationships between melt-induced rheological transitions and finite strain: Observations from host rock pendants of the tuolumne intrusive suite, sierra nevada, california. *Journal of Structural Geology*, 28:1422–1444, 2005.

A. N. Alexandrou and V. Entov. On the steady-state advancement of fingers and bubbles in a hele-shaw cell filled by a non-newtonian fluid. *European Journal of Applied Mathematics*, 8:73–87, 1997.

C. Allegre, J. Birck, F. Capmas, and V. Courtillot. Age of the deccan traps using 187re-187os systematics. *Earth and Planetary Science Letters*, Jan 1999.

D. Anderson. Lithosphere, asthenosphere, and perisphere. *Reviews of Geophysics*, 33(1): 125–149, 1995.

E. M. Anderson. *The dynamics of faulting and dyke formation with applications to britain*. Oliver and Boyd, White Plains, N.Y., 1951.

K. Anderson and P. Segall. Physics-based models of ground deformation and extrusion rate at effusively erupting volcanoes. *Journal of Geophysical Research*, 116(B07204), 2011.

K. Anderson, M. Lisowski, and P. Segall. Cyclic ground tilit associated with the 2004-2008 eruption of mount st. helens. *Journal of Geophysical Research*, B11201, 2010.

C. Annen and R. S. J. Sparks. Effects of repetitice emplacement of basaltic intrusions on thermal evolution and melt generation in the crust. *Earth and Planetary Science Letters*, 203:937–955, 2002.

P. Asimow and M. Ghiorso. Algorithmic modifications extending melts to calculate subsolidus phase relations. *American Mineralogist*, Jan 1998.

B. K. Atkinson and P. G. Meredith. The theory of subcritical crack growth with application to minerals and rocks. In B. K. Atkinson, editor, *Fracture Mechanics of Rock*, Academic Press Geology Series. Academic Press, New York, 1987.

E. Auger, P. Gasparini, J. Virieux, and A. Zollo. Seismic evidence of an extended magmatic sill under mt. vesuvius. *Science*, 294:1510–1512, 2001.

O. Bachmann. On the origin of crystal-poor rhyolites: Extracted from batholithic crystal mushes. *Journal of Petrology*, 45(8):1565–1582, 2004.

O. Bachmann and G. W. Bergantz. Rejuvenation of the fish canyon magma body: a window into the evolution of high-volume silicic magma systems. *Geology*, 31(9):789–792, doi:10.1130/G19764.1 2003.

O. Bachmann, M. Dungan, and P. Lipman. The fish canyon magma body, san juan volcanic field, colorado: rejuvenation and eruption of an upper-crustal batholith. *Journal of Petrology*, 43(8):1469, 2002.

O. Bachmann, C. Miller, and S. de Silva. The volcanic-plutonic connection as a stage for understanding crustal magmatism. *Journal of Volcanology and Geothermal Research*, 167: 1–23, 2007.

C. Bacon and M. Lanphere. Eruptive history and geochronology of mount mazama abd crater lake region, oregon. *Geological Society of America Bulletin*, 118(11-12):1331–1359, 2006.

M. Ban and T. Yamamoto. Petrological study of nasu-chausudake volcano (ca. 16 ka to present) northeastern japan. *Bulletin of Volcanology*, 64:100–116, 2002.

S. A. Barboza and G. W. Bergantz. Metamorphism and anatexis in the mafic complex contact aureole, ivrea zone, northern italy. *Journal of Petrology*, 41(8):1307–1327, 2000.

S. E. Barker and S. D. Malone. Magmatic system geometry at mount st. helens modeled from the stress field associated with posteruptive earthquakes. *Journal of Geophysical Research*, 96(B7):11883–11894, July 1991.

T. Barry, S. Self, S. Kelley, S. Reidel, and P. Hooper. New 40ar/39ar dating of the grande ronde lavas, columbia river basalts, usa: Implications for duration of flood basalt eruption episodes. *Lithos*, Jan 2010.

I. N. Bindeman. Crystal sizes in evolving silicic magma chambers. *Geology*, 31(4):367–370, 2003.

J. Blackwell. Transient heat flow from a thin circular disk—small-time solution. *Journal of the Australian Mathematical Society*, 14(04):433–442, 1972.

P. Blondeaux and G. Seminara. A unified bar-bend theory of river meanders. *Journal of Fluid Mechanics*, 157:449–470, 1985.

J. Blundy and K. Cashman. Rapid decompression-driven crystallization recorded by melt inclusions from mount st. helens volcano. *Geology*, 33(10):793–797, 2005.

J. Blundy, K. Cashman, and M. Humphreys. Magma heating by decompression-driven crystallization beneath andesite volcanoes. *Nature*, 443:76–80, 2006.

M. Bonafede, M. Dragoni, and F. Quareni. Displacement and stress produced by a center of dilation and by a pressure source in a viscoelastic half-space: application to the study of ground deformation and seismicity at campi flegeri, italy. *The Geophysical Journal of the Royal Astronomical Society*, 87(2):455–485, 1986.

J. E. Box and K. Ski. Remote sounding of greenland supraglacial melt lakes and implications for subglacial hydraulics. *Journal of Glaciology*, 53(181):257–265, 2007.

C. Brooks. Rifting and doming in southern east greenland. *Nature*, 244(132):23–25, 1973.

C. Brooks. The e. greenland continental-margin - a transition between oceanic and continental magmatism. *Journal of the Geological Society*, 139:265–175, 1982.

P. M. Bruce and H. E. Huppert. Thermal controls of basaltic fissure eruptions. *Nature*, 342, 1989.

S. E. Bryan, I. U. Peate, D. W. Peat, S. Self, D. A. Jerram, M. R. Mawby, J. S. Marsh, and J. A. Miller. The largest volcanic eruptions on earth. *Earth-Science Reviews*, 102:207–229, 2010.

A. Burgisser and G. W. Bergantz. A rapid mechanism to remobilize and homogenize highly crystalline magma bodies. *Nature*, 471(7337):212–215, 2011.

R. Bürgmann and G. Dresen. Rheology of the lower crust and upper mantle: Evidence from rock mechanics, geodesy, and field observations. *Annual Review of Earth and Planetary Sciences*, 36:531–567, 2008.

E. Burov, L. Guillou-Frottier, E. d'Acremont, L. L. Pourhiet, and S. Cloetingh. Plume head-lithosphere interactions near intra-continental plate boundaries. *Tectonophysics*, 434 (1-4):15–38, 2007.

M. Bystricky and S. Mackwell. Creep of dry clinopyroxen aggregates. *Journal of Geophysical Research*, 106:13443–54, 2001.

R. A. Callander. Instability and river channels. *Journal of Fluid Mechanics*, 36(3):465–480, 1969.

I. Campbell and R. Griffiths. Implications of mantle plume structure for the evolution of flood basalts. *Earth and Planetary Science Letters*, 99(1-2):79–93, 1990.

C. Camporeale, P. Perona, A. Porporato, and L. Ridolfi. Hierarchy of models for meandering rivers and related morphodynamic processes. *Reviews of Geophysics*, 45(1), 2007.

E. Canon-Tapia and G. P. Walker. Global aspects of volcanism: the perspectives of "plate tectonics" and "volcanic systems". *Earth-Science Reviews*, 66:163–182, 2004.

L. Caricchi, L. Builini, P. Ulmer, T. Gerya, M. Vassalli, and P. Papale. Non-newtonian rheology of cyrstal-bearing magmas and implications for magma ascent dynamics. *Earth and Planetary Science Letters*, 264:402–419, 2007.

M. Carr. The role of lava erosion in the formation of lunar rilles and martian channels. *Icarus*, 22:1–23, 1974.

C. R. Carrigan. Biot number and thermos bottle effect: Implications for magma-chamber convection. *Geology*, 16:771–774, 1988.

K. Cashman, C. Thornber, and J. Kauahikaua. Cooling and crystallization of lava in open channels, and the transition of pahoehoe lava to 'a'a. *Bullentin of Volcanology*, 61:306–323, 1999.

M. E. Cates, J. P. Wittmer, J.-P. Bouchaud, and P. Claudin. Jamming, force chains, and fragile matter. *Physical Review Letters*, 81(9):1841–1844, 1998.

H. E. Cathey and B. P. Nash. The cougar point tuff: Implications for thermochemical zonation and longevity of high-temperature, large-volume silicic magmas of the miocene yellowstone hotspot. *Journal of Petrology*, 45(1):27–58, 2004.

R. G. Cawthorn and F. Walraven. Emplacement and crystallization time for the bushveld complex. *Journal of Petrology*, 39(9):1669–1687, 1998.

R. Champallier, M. Bystricky, and L. Arbaret. Experimental investigation of magma rheology at 300 mpa: From pure hydrous melt tp 76 vol. % of crystals. *Earth and Planetary Science Letters*, 267:571–583, 2008aa.

Y. J. Chen. Constraints on melt production rate beneath the mid-ocean ridges based on passive flow models. *Pure and Applied Geophysics*, 146(3/4):586–620, 1996.

Z. Chen and Z.-H. Jin. Magma-driven subcritical crack growth and implications for dike initiation from a magma chamber. *Geophysical Research Letters*, 33 (doi:10.1029/2006GL026979):L19307, 2006.

B. A. Chouet. Long-period volcano seismicity: its source and use in eruption forecasting. *Nature*, 380:309–317, March 1996.

N. I. Christensen and W. Mooney. Seismic velocity structure and composition of the continental crust: a global view. *Journal of Geophysical Research*, 100(B7):9761–9788, 1995.

J. D. Clemens and C. K. Mawer. Granitic magma transport by fracture propagation. *Tectonophysics*, 204:339–360, 1992.

M. Coffin and O. Eldholm. Large igneous provinces: crustal structure, dimensions, and external consequences. *Rev. Geophys*, 32(1):1–36, 1994.

C. F. ColeBrook. Turbulent flow in pipes, with particular reference to the transition between smooth and rough pipe laws. *Journal of the Institution of Civil Engineers*, 1939.

D. S. Coleman, W. Gray, and A. F. Glazner. Rethinking the emplacement and evolution of zoned plutons: Geochronologic for incremental assembly of the tuolomne intrusive suite, california. *Geology*, 32(5):433–436, May 2004.

S. Coles and R. Sparks. Extreme value methods for modelling historical series of large volcanic magntiudes. In H. Mader, S. Coles, C. Connor, and L. Connor, editors, *Statistics in volcanology*, volume 1 of *Special Publication of IAVCEI*. London: Geologocal Society, 2006.

E. Contreras-Reyes, I. Grevemeyer, and A. Watts. Crustal intrusion beneath the louisville hotspot track. *Earth and Planetary Science Letters*, Jan 2010.

K. M. Cooper and M. R. Reid. Re-examination of crystal ages in recent mount st. helens lavas: implications for magma reservoir processes. *Earth and Planetary Science Letters*, 213:149–167, 2003.

R. Cooper and D. Kohlstedt. Solution-precipitation enhanced diffusional creep of partially molten olivine-basalt aggregates during hot-pressing. *Tectonophysics*, 107:207–233, 1984.

A. Costa, O. Melnik, and E. Vedeneeva. Thermal effects during magma ascent in conduits. *Journal of Geophysical Research*, 112(B12205), 2007.

V. Courtillot and P. Renne. On the ages of flood basalt events. *Comptes Rendus Geosciences*, Jan 2003.

K. Cox. A model for flood basalt vulcanism. *Journal of Petrology*, 21(4):629, 1980.

K. G. Cox. Continental magmatic underplating. *Philosophical Transaction of the Royal Society of London A*, 342:155–166, 1993.

R. Dasgupta and M. M. Hirschmann. Melting in the earth's deep upper mantle caused by carbon dioxide. *Nature*, 440:659–662, 2006.

J. H. Davies and M. J. Bickle. A physical model for the volume and composition of melt produced by hydrous fluxing above subduction zones. *Philosophical Transaction of the Royal Society of London*, 335:355–364, 1991.

J. de Bremond d'Ars, C. Jaupart, and R. S. J. Sparks. Distribution of volcanoes in active margins. *Journal of Geophysical Research*, 100(B10):20421–20432, 1995.

S. L. de Silva and W. D. Gosnold. Episodic construction of batholiths: Insights from the spatiotemporal development of an ignimbrite flare-up. *Journal of Volcanology and Geothermal Research*, 167:320–335, 2007.

C. DeMets, R. G. Gordon, D. F. Argus, and S. Stein. Current plate motions. *Geophysical Journal International*, 101:425–478, 1990.

D. J. DePaolo. Trace element and isotopic effects of combined wallrock assimilation and fractional crystallization. *Earth and Planetary Science Letters*, 53:189–202, 1981.

R. S. W. V. der Wal, W. Boot, M. R. van den Broeke, C. J. P. P. Smeets, C. H. Reijmer, J. J. A. Donker, and J. Oerlemans. Large and rapid melt-induced velocity changes in the ablation zone of the greenland icesheet. *Science*, 321(111), 2008.

C. Dimalanta, A. Taira, G. P. J. Yumul, H. Tokuyama, and K. Mochizuki. New rates of western pacific island arc magmatism from seismic and gravity data. *Earth and Planetary Science Letters*, 202:105–115, 2002.

F. Dobran. *Volcanic Processes: Mechanisms in Material Transport.* Kluwer Academic/Plenum, 2001.

M. Dragoni and C. Magnanensi. Displacement and stress produced by a pressurized, spherical magma chamber, surrounded by a viscoelastic shell. *Physics of the Earth and Planetary Interiors*, 56:316–328, 1989.

T. H. Druitt and R. S. J. Sparks. On the formation of calderas during ignimbrite eruptions. *Nature*, 310:679–681, 1984.

J. Dufek and O. Bachmann. Quantum magmatism: Magmatic compositional gaps generated by melt-crystal dynamics. *Geology*, 38(8):687–690, 2010.

J. Dufek and G. W. Bergantz. Transient two-dimensional dynamics in the upper conduit of a rhyolitic eruption: A comparison of closure models for the granular stress. *Journal of Volcanology and Geothermal Research*, 143:113–132, 2005.

J. Dufek, L. Karlstrom, and C. Huber. Magma chamber dynamics and thermodynamics. In S. Fagent, T. Gregg, and R. Lopes, editors, *Modeling Volcanic Processes: The physics and mathematics of volcanism*, chapter 2. Cambridge University Press, 2011.

G. Dumond, K. H. Mahan, M. L. Williams, and K. E. Karlstrom. Crustal segmentation, composite looping pressure-temperature paths, and magma-enhanced metamorphic field gradients: Upper granite gorge, grand canyon, usa. *GSA Bulletin*, 119(1/2):202–220, January/February 2007.

D. Elliot and T. Fleming. Physical volcanology and geological relationships of the jurassic ferrar large igneous province, antarctica. *Journal of Volcanology and Geothermal Research*, 172(1-2):20–37, 2008.

R. E. Ernst and K. L. Buchan. Layered mafic intrusions: A model for their feeder systems and relationship with giant dyke swarms and mantle plume centres. *South African Journal of Geology*, 100(4):319–334, 1997.

R. E. Ernst, J. W. Head, E. Parfitt, E. B. Grosfils, and L. Wilson. Giant radiating dyke swarms on earth and venus. *Earth-Science Reviews*, 39, 1995.

J. Eshelby. The determination of the elastic field of an ellipsoidal inclusion, and related problems. *Proceedings of the Royal Society of London. Series A, Mathematical and Physical Sciences*, pages 376–396, 1957.

C. Farnetani and H. Samuel. Beyond the thermal plume paradigm. *Geophysical Research Letters*, Jan 2005.

C. Farnetani, M. Richards, and M. Ghiorso. Petrological models of magma evolution and deep crustal structure beneath hotspots and flood basalt provinces. *Earth and Planetary Science Letters*, 143(1-4):81–94, 1996.

C. G. Farnetani and M. A. Richards. Numerical investigations of the mantle plume initiation model for flood basalt events. *Journal of Geophysical Research*, 99(B7):13813–13833, 1994.

D. Farnetani and M. Richards. Thermal entrainment and melting in mantle plumes. *Earth and Planetary Science Letters*, 136(3-4):251–267, 1995.

M. Feighner and M. Richards. Lithospheric structure and compensation mechanisms of the galapagos archipelago. *Journal of Geophysical Research*, Jan 1994.

R. I. Ferguson. Sinuosity of supraglacial streams. *Geological Society of America Bulletin*, 84:251–256, 1973.

A. Folch and J. Marti. The generation of overpressure in felsic magma chambers by replenishment. *Earth and Planetary Science Letters*, 163:301–314, 1998.

D. C. Ford and P. Williams. *Karst Hydrogeology and Geomorphology*. John Wylie and Sons, 2007.

A. G. Fountain and J. S. Walder. Water flow through temperature glaciers. *Reviews of Geophysics*, 36(3):299–328, 1998.

S. J. Fowler and F. J. Spera. Phase equilibria trigger for explosive volcanic eruptions. *Geophysical Research Letters*, 35(L08309), 2008.

P. Fryer. Evolution of the mariana convergent plate margin system. *Reviews of Geophysics*, 34(1):89–125, 1996.

Y. C. Fung. *Foundations of Solid Mechanics*. Prentice-Hall, Englewood Cliffs, N.J., 1965.

K. P. Furlong and D. M. Fountain. Continental crustal underplating: Thermal considerations and seismic-petrologic consequences. *Journal of Geophysical Research*, 91(B8):8285–8294, 1986.

E. S. Gaffney, B. Damjanac, and G. A. Valentine. Localization of volcanic activity: 2. effects of pre-existing structure. *Earth and Planetary Science Letters*, 263:323–338, doi:10.1016/j.epsl.2007.09.002 2007.

P. Gajjar. Meandering rivers. *Step 3 paper, Sidney Sussex College, Cambridge, CB2 3HU, UK*, University of Cambridge 2010.

G. A. Galgana, P. J. McGovern, and E. B. Grosfils. Evolution of large venusian volcanoes: Insights from coupled models of lithospheric flexure and magma reservoir pressurization. *Journal of Geophysical Research*, 116(E03009), 2011.

O. Galland, P. R. Cobbold, J. de Bremond d'Ars, and E. Hallot. Rise and emplacement of magma during horizontal shortening of the brittle crust: Insights from experimental modeling. *Journal of Geophysical Research*, 112(B06402), June 2007.

X.-W. Gao and T. G. Davies. *Boundary element programming in mechanics*. Cambridge University Press, 2002.

E. C. Gay, P. A. Nelson, and W. P. Armstrong. Flow properties of suspensions with high solids concentration. *AlChE Journal*, 15(6):815–822, 1969.

D. Geist, T. Naumann, and J. Standish. Wolf volcano, galápagos archipelago: Melting and magmatic evolution at the margins of a mantle plume. *Journal of Petrology*, 46(11): 2197–2224, 2005.

D. Geist, K. Harpp, T. Naumann, M. Poland, W. Chadwick, M. Hall, and E. Rader. The 2005 eruption of sierra negra volcano, galapagos, ecuador. *Bullentin of Volcanology*, 70: 655–673, 2008.

T. M. Gerlach, K. A. McGee, T. Elias, A. J. Sutton, and M. P. Doukas. Carbon dioxide emission rate of kilauea volcano: Implications for primary magma and the summit reservoir. *Journal of Geophysical Research*, 107(B9), 2002.

T. V. Gerya, D. A. Yuen, and E. O. D. Sevre. Dynamical causes for incipient magma chambers above slabs. *Geology*, 32(1):89–92, January 2004.

A. Geyer and J. Marti. The new worldwide collapse caldera database (ccdb): A tool for studying and understanding caldera processes. *Journal of Volcanology and Geothermal Research*, 175(3):334–354, 2008.

M. Ghiorso and R. Sack. Chemical mass transfer in magmatic processes iv: A revised and internally consistent thermodynamic mondel for the interpolation and extrapolation of liquid-solid equilibria in magmatic systems at elevated temperatures and pressures. *Contributions to Mineralogy and Petrology*, 119:197–212, 1995.

M. Ghiorso, M. Hirschmann, and P. Reiners. The pmelts: a revision of melts for improved calculation of phase relations and major element partitioning related to partial melting of the mantle to 3 gpa. *Geochemistry Geophysics Geosystems*, 3(5), Jan 2002.

M. S. Ghiorso and I. S. E. Carmichael. Modeling magmatic systems: Petrologic applications. In I. S. E. Carmichael and H. P. Eugster, editors, *Thermodynamic Modeling of Geological Materias: Minerals, Fluids and Melts, Reviews in Mineralogy*, volume 17, pages 467–499. Mineralogical Society of America, Washington DC, 1987.

G. Gioia, P. Chakraborty, and S. Kieffer. Lava channel formation via the viscoplastic indentation of hot substrates. *Geophysical Research Letters*, 33(L19305), 2006.

A. F. Glazner, D. S. Coleman, and J. M. Bartley. The tenuous connection between high-silica rhyolites and granodiorite plutons. *Geology*, 36(2):183–186, doi:10.1130/G24496A.1 2008.

H. Gonnermann and M. Manga. The fluid mechanics inside a volcano. *Annual Reviews of Fluid Mechanics*, 39:321–355, 2007.

H. Gonnermann and M. Manga. Dynamics of magma ascent in the volcanic conduit. In S. Fagents, T. Gregg, and R. Lopes, editors, *Modeling Volcanic Processes: The physics and mathematics of volcanism*, chapter 4. Cambridge University Press, 2011.

J. Gottsmann, Y. Lavallee, J. Marti, and A. Aguirre-Diaz. Magma-tectonic interaction and the eruption of silicic batholiths. *Earth and Planetary Science Letters*, 284:426–434, 2009.

A. A. Griffith. The phenomena of rupture and flow in solids. *Philosophical Transaction of the Royal Society of London*, 221:163–197, 1920.

R. Griffiths. The dynamics of lava flows. *Annual Reviews of Fluid Mechanics*, 32:477–518, 2000.

E. B. Grosfils. Magma reservoir failure on the terrestrial planets: Assesing the importance of gravitational loading in simple elastic models. *Journal of Volcanology and Geothermal Research*, 166:47–75, 2007.

A. Gudmundsson. Effect of tensile stress concentration around magma chambers on intrusion and extrusion frequencies. *Journal of Volcanology and Geothermal Research*, 35:179–194, 1988.

A. Gudmundsson. Formation and development of normal-fault calderas and the initiation of large explosive eruptions. *Bulletin of Volcanology*, 60:160–170, 1998.

A. Gudmundsson. How local stresses control magma-chamber ruptures, dyke injections, and eruptions in composite volcanoes. *Earth-Science Reviews*, 79:1–31, 2006.

M. Guffanti and C. S. Weaver. Distribution of late cenozoic volcanic vents in the cascade range: Volcanic arc segmentation and regional tectonic considerations. *Journal of Geophysical Research*, 93(B6):6513–6529, 1988.

L. Gurioli, B. Houghton, K. Cashman, and R. Cioni. Complex changes in eruption dynamics during the 79 ad eruption vesuvius. *Bulletin of Volcanology*, 67(2):144–159, 2003.

B. R. Hacker, L. Mehl, P. B. Kelemen, M. Rioux, M. D. Behn, and P. Luffi. Reconstruction of the talkeetna intraoceanic arc of alaska through thermobarometry. *Journal of Geophysical Research*, 113(B03204):doi:10.1029/2007JB005208, 2008.

T. Hales, D. Abt, E. Humphreys, and J. Roering. A lithospheric instability origin for columbia river flood basalts and wallowa mountains uplift in northeast oregon. *Nature*, 438(7069):842–845, 2005.

A. N. Halliday, G. A. Mahood, P. Holden, J. M. Metz, T. J. Dempster, and F. P. Davidson. Evidence for long residence times of rhyolitic magma in the long valley magmatic system: the isotopic record in precaldera lavas of glass mountain. *Earth and Planetary Science Letters*, 94:274–290, 1989.

J. Hammer, K. Cashman, R. Hoblitt, and S. Newman. Degassing and microlite crystallization during pre-climactic events of the 1991 eruption of mt. pinatubo, philippines. *Bulletin of Volcanology*, 60(5):355–380, 1999.

R. B. Hanson and A. F. Glazner. Thermal requirements for extensional emplacements of granitoids. *Geology*, 23(3):213–216, 1995.

A. Harris and J. Allen. One-, two- and three-phase viscosity treatments for basaltic lava flows. *Journal of Geophysical Research*, 113, 2008.

C. Harris, J. J. M. Pronost, L. D. Ashwal, and R. G. Cawthorn. Oxygen and hydrogen isotope stratigraphy if the rstenburg layered suite, bushveld complex: Constraints on crustal contamination. *Journal of Petrology*, 46(3):579–601, 2005.

C. J. Hatton. Mantle plume origin for the bushveld and ventersdorp magmatic provinces. *Journal of African Earth Sciences*, 21(4):571–577, 1995.

E. Hauber, J. Bleacher, K. Gwinner, D. Williams, and R. Greeley. The topography and morphology of low shields and associated landforms of plains volcanism in the tharsis region of mars. *Journal of Volcanology and Geothermal Research*, 185:69–95, 2009.

E. Hauri, J. Lassiter, and D. DePaolo. Osmium isotope systematics of drilled lavas from mauna loa, hawaii. *Journal of Geophysical Research*, 1996.

D. Healy. Short note: Elastic field in 3d due to a spheroidal inclusion-matlab® code for eshelby's solution. *Computers & Geosciences*, 2009.

R. T. Helz. *Reviews in Mineralogy*, volume 9B, chapter Phase relations and compositions of amphiboles produced in studies of the melting behavior of rocks, pages 279–347. Mineralogical Society of America, Washington DC, 1982.

J. W. Hernlund, P. J. Tackley, and D. J. Stevenson. Bouyant melting instabilities beneath extending lithosphere: 1. numerical models. *Journal of Geophysical Research*, 113(B04405), 2008.

K.-U. Hess, B. Cordonnier, Y. Lavallée, and D. B. Dingwell. Viscous heating in rhyolite: An in situ experimental determination. *Earth and Planetary Science Letters*, 275:121–126, 2008.

L. Heymann, S. Peukert, and N. Aksel. On the solid-liquid transition of concentrated suspension in transient shear flow. *Rheologica Acta*, 41:307–315, 2002.

S. Hier-Majumder, S. Mei, and D. L. Kohlstedt. Water weakening in clinopyroxen in diffusion creep. *Journal of Geophysical Research*, 110, 2005.

C. F. Hieronymus and D. Bercovici. Discrete alternating hotspot islands formed by interaction of magma transport and lithospheric flexure. *Nature*, 397(18):604–607, February 1999.

W. Hildreth. Quaternary magmatism in the cascades - geologic perspectives. Professional Paper 1744, US Geological Survey, http://pubs.usgs.gov/pp/pp1744/, 2007.

W. Hildreth and S. Moorbath. Crustal contributions to arc magmatism in the andes of central chile. *Contributions to Mineralogy and Petrology*, 98:455–489, 1988.

B. K. Holtzman, N. J. Groebner, M. E. Zimmerman, S. B. Ginsber, and D. L. Kohlstedt. Stress-driven melt segregation in partially molten rocks. *Geochemistry Geophysics Geosystems*, 4(5), 2003.

P. R. Hooper, V. E. Camp, S. P. Reidel, and M. E. Ross. The origin of the columbia river flood basalt province: Plume versus nonplume models. *The Geological Society of America Special Paper*, 430, 2007.

M. Hort. Cooling and crystallization in sheet-like magma bodies revisited. *Journal of Volcanology and Geothermal Research*, 76:297–317, 1997.

M. Hort. Abrupt change in magma liquidus temperature because of volatile loss or magma mixing: effects on nucleation, crystal growth and thermal history of the magma. *Journal of Petrology*, 39(5):1063–1076, 1998.

B. Houghton, C. Wilson, P. Carlo, M. Coltelli, J. Sable, and R. Carey. The influence of conduit processes on changes in style of basaltic plinian eruptions: Tarawere 1886 and etna 122 bc. *Journal of Volcanology and Geothermal Research*, 137:1–14, 2004.

N. Houlie, J.-C. Komorowski, and J. Dufek. Stress preconditioning and magma chamber pressure evolution at piton de la fournaise. *In review by Earth and Planetary Science Letters*, 2009.

C. Huber, O. Bachmann, and M. Manga. Homogenization processes in silicic magma chambers by stirring and mushification (latent heat buffering). *Earth and Planetary Science Letters*, 283:38–43, doi:10.1016/j.epsl.2009.03.029 2009.

G. R. Hughes and G. A. Mahood. Tectonic controls on the nature of large silicic calderas in volcanic arcs. *Geology*, 36(8):627–630, doi:10.1130/G24796A.1 2008.

H. Hui and Y. Zhang. Toward a general viscosity equation for natural anhydrous and hydrous silicate melts. *Geochimica et Cosmochimica Acta*, 71:403–416, 2007.

G. Hulme. The interpretation of lava flow morphology. *Journal of Geophysical Research*, 39: 361–383, 1974.

H. Huppert and R. Sparks. Komatiites i: Eruption and flow. *Journal of Petrology*, 26(3): 694–725, 1985.

H. Huppert and A. Woods. The role of volatiles in magma chamber dynamics. *Nature*, 420 (6915):493–495, 2002.

P. Huybers and C. Langmuir. Feedback between deglaciation, volcanism, and atmospheric co2. *Earth and Planetary Science Letters*, 286:479–491, 2009.

P. D. Ihinger. Mantle flow beneath the pacific plate – evidence from seamount segments in the hawaiian-emperor chain. *The American Journal of Science*, 295(9):1035–1057, 1995.

S. Ikeda, G. Parker, and K. Sawai. Bend theory of river meanders. part 1. linear development. *Journal of Fluid Mechanics*, 112:363–377, 1981.

E. Isenko, R. Narus, and B. Mavlyudov. Water temperature in englacial and supraglacial channels: Change along the flow and contribution to ice melting on the channel wall. *Cold Regions Science and Technology*, 42:53–62, 2005.

G. Ito and P. Clift. Subsidence and growth of pacific cretaceous plateaus. *Earth and Planetary Science Letters*, 161(1-4):85–100, 1998.

G. Ito and S. J. Martel. Focusing of magma in the upper mantle through dike interaction. *Journal of Geophysical Research*, 107(B10):2223–2241, 2002.

J. C. Jaeger and N. G. W. Cook. *Fundamentals of Rock Mechanics*, volume 513 pp. Methuen, London, 1969.

O. Jagoutz, O. Muntener, J.-P. Burg, P. Ulmer, and E. Jagoutz. Lower continental crust formation through focused flow in km-scale melt conduits: The zoned ultramafic bodies of the chilas complex in the kohistan island arc (nw pakistan). *Earth and Planetary Science Letters*, 242:320–342, 2006.

O. Jagoutz, O. Muntener, P. Ulmer, T. Pettke, and J. Burg. Petrology and mineral chemistry of lower crust intrusions: the chilas complex, kohistan (nw pakistan). *Journal of Petrology*, 48(10):1895–1953, 2007.

C. Jaupart and C. J. Allègre. Gas content, eruption rate and instabilities of eruption regime in silicic volcanoes. *Earth and Planetary Science Letters*, 102:413–429, 1991.

G. B. Jeffery. Plain stress and plane strain in bipolar co-ordinates. *Philosophical Transaction of the Royal Society of London A*, 221:265–293, 1921.

A. Jellinek, M. Manga, and M. Saar. Did melting glaciers cause volcanic eruptions in eastern california? probing the mechanics of dike formation. *Journal of Geophysical Research*, 109: 1–10, 2004.

A. M. Jellinek and D. J. DePaolo. A model for the origin of large silicic magma chambers: precursprs of caldera-forming eruptions. *Bulletin of Volcanology*, 65:363–381, doi:10.1007/s0045-003-0277-y 2003.

D. Jerram and M. Widdowson. The anatomy of continental flood basalt provinces: geological constraints on the processes and products of flood volcanism. *Lithos*, 79(3-4):385–405, 2005.

H. Johannesson and G. Parker. Secondary flow in a mildy sinuous channel. *Journal of Hydraulic Engineering, American Society of Civil Engineers*, 115(3):289–308, 1988.

H. Johannesson and G. Parker. Linear theory of river meanders. In S. Ikeda and G. Parker, editors, *River Meandering*, volume 12, pages 181–214. American Geophysical Union, 1989.

T. E. Johnson, R. L. Gibson, M. Brown, I. S. Buick, and I. Cartwright. Partial melting of metapelitic rocks beneath the bushveld complex, south africa. *Journal of Petrology*, 44 (5):789–813, 2003.

Jones, G. Price, N. Price, and P. DeCarli. Impact induced melting and the development of large igneous provinces. *Earth and Planetary Science Letters*, Jan 2002.

M. Jull and P. Kelemen. On the conditions for lower crustal convective instability. *Journal of Geophysical Research*, 106(B4):6423–6446, 2001.

S.-I. Karato and H. Jung. Effects of pressure on high-temperature disclocation creep in olivine. *Philosophical Magazine*, 83:401–414, 2003.

L. Karlstrom, J. Dufek, and M. Manga. Organization of volcanic plumbing through magmatic lensing by magma chambers and volcanic loads. *Journal of Geophysical Research*, 114 (B10):B10204, Oct 2009. doi: 10.1029/2009JB006339.

L. Karlstrom, J. Dufek, and M. Manga. Magma chamber stability in arc and continental crust. *Journal of Volcanology and Geothermal Research*, 190:249–270, 2010a.

L. Karlstrom, M. Manga, and I. Matsuyama. Martian magmatic plumbing and the spacing between tharsis montes shield volcanoes. *Lunar and Planetary Science Conference abstract*, 2010b.

L. Karlstrom, P. Gajjar, and M. Manga. Meander formation in supraglacial streams. *in review at Journal of Fluid Mechanics*, 2011.

J. L. Kavanagh, T. Menand, and R. S. J. Sparks. An experimental investigation of sill formation and propagation in layered elastic media. *Earth and Planetary Science Letters*, 245:799–813, 2006.

T. M. Kayzar, K. M. Cooper, M. K. Reagan, and A. J. Kent. Gas transport model for the magmatic system at mount pinatubo, philippines: Insights from (^{210}pb)/(^{226}ra). *Journal of Volcanology and Geothermal Research*, 181:124–140, 2009.

B. M. Kennedy, A. M. Jellinek, and J. Stix. Coupled caldera subsidence and stirring inferred from analogue models. *Nature Geoscience*, 1:385–389, 2008.

R. Kerr. Thermal erosion by laminar lava flows. *Journal of Geophysical Research*, 106(B11): 26453–26465, 2001.

R. Kerr. Thermal erosion of felsic ground by the laminar flow of a basaltic lava, with application to the cave basalt, mount st. helens, washington. *Journal of Geophysical Research*, 114(B09204), 2009.

R. C. Kerr and J. R. Lister. The effects of shape on crystal settling and on the rheology of magmas. *The Journal of Geology*, 99(3):457–467, 1991.

D. M. Kerrick and G. K. Jacobs. A modified redlich-kwong equation for h2o, co2, and h2o-co2 mixtures at elevated pressures and temperatures. *American Journal of Science*, 281: 755–767, 1981.

M. Kervyn, G. G. J. Ernst, B. van Wyk de Vries, L. Mathieu, and P. Jacobs. Volcano load control on dyke propagation and vent distribution: Insights from analogue modeling. *Journal of Geophysical Research*, 114(B03401, doi:10.1029/2008JB005653), 2009.

L. Keszthelyi. A preliminary thermal budget for lava tubes on the earth and planets. *Journal of Geophysical Research*, 100(B10):20411–20420, 1995.

S. King and D. Anderson. An alternative mechanism of flood basalt formation. *Earth and Planetary Science Letters*, 136:269–279, 1995.

A. D. Knighton. Channel form and flow characteristics of supraglacial streams, austre okstindbreen, norway. *Arctic and Alpine Research*, 13(3):295–306, 1981.

H. Kopp, C. Kopp, J. Morgan, and E. Flueh. Fossil hot spot-ridge interaction in the musicians seamount province: Geophysical investigations of hot spot volcanism at volcanic elongated ridges. *Journal of Geophysical Research*, 108(B3), 2003.

F. J. Kruger. Filling the bushveld complex magma chamber: lateral expansion, roof and floor interaction, magmatic unconformities, and the formation of giant chromitite, pge and ti-v-magnetitite deposits. *Mineralium Deposita*, 40:451–472, 2005.

D. Kühn and T. Dahm. Numerical modelling of dyke interaction and its influence on oceanic crust formation. *Tectonophysics*, 447:53–65, doi:10.1016/j.tecto.2006.09.018 2008.

R. A. Lange. Constraints on the preeruptive volatile concentrations in the columbia river flood basalts. *Geology*, 30(2):179–182, 2002.

J. M. Lees. Seismic tomography of magmatic systems. *Journal of Volcanology and Geothermal Research*, 167:37–56, 2007.

A. Leitch and G. Davies. Mantle plumes and flood basalts: enhanced melting from plume ascent and an eclogite component. *Journal of Geophysical Research*, 106(B2), 2001.

A.-M. Lejeune and P. Richet. Rheology of crystal-bearing silicate melts: An experimental study at high viscosities. *Journal of Geophysical Research*, 100(B3):4215–4229, 1995.

O. Lengline, D. Marsan, J.-L. Got, V. Pinel, V. Ferrazzini, and P. G. Okubo. Seismicity and deformation induced by magma accumulation at three basaltic volcanoes. *Journal of Geophysical Research*, 113(B12305), doi:10.1029/2008JB005937 2008.

L. B. Leopold and T. Maddock. The hydraulic geometry of stream channels and some physiographic implications. *Geological Survey Professional Paper 252*, 1953.

L. B. Leopold and M. G. Wolman. River meanders. *Geological Society of America Bulletin*, 71:769–793, 1960.

L. B. Leopold, M. G. Wolman, and J. P. Miller. *Fluvial Processes in Geomorphology*. W. H. Freeman and Company, 1964.

H.-C. Lin and P. E. van Keken. Multiple volcanic episodes of flood basalts caused by thermochemical mantle plumes. *Nature*, 436:250–252, 2005.

J. M. Lindsay, A. K. Schmitt, R. B. Trumbull, S. L. de Silva, W. Siebel, and R. Emmermann. Magmatic evolution of the la pacana caldera system, central andes, chile: Compositional variation of two cogenetic large–volume felsic ignimbrites. *Journal of Petrology*, 42(3): 459–486, 2001.

P. Lipman. Incremental assembly and prolonged consolidation of cordilleran magma chambers: Evidence from the southern rocky mountain volcanic field. *Geosphere*, 3(1):42, 2007.

P. W. Lipman. The roots of ash flow calderas in western north america: Windows into the tops of granitic batholiths. *Journal of Geophysical Research*, 89(B10):8801–8841, September 1984.

J. Lister and R. Kerr. The propagation of two-dimensional and axisymmetric viscous gravity currents at a fluid interface. *J. Fluid Mech*, 203:215–249, 1989.

A. J. Liu and S. R. Nagel. Jamming is not just cool any more. *Nature*, 396:21–22, 1998.

A. E. H. Love. *Treatise on the Mathematical Theory of Elasticity*. Dover Publications Inc., NewYork, 1944.

J. Lunine and S. K. Atreya. The methane cycle on titan. *Nature Geoscience*, 1:159–164, 2008.

G. Macdonald. Pahoehoe, aa, and block lava. *American Journal of Science*, 251:169–191, 1953.

W. D. Majer, N. T. Arndt, and E. A. Curl. Progressive crustal contamination of the bushveld complex: evidence from nd isotopic analyses of the cumulate rocks. *Contributions to Mineralogy and Petrology*, 140:316–327, 2000.

M. C. Malin and K. S. Edgett. Evidence for persistent flow and aqueous sedimentation on early mars. *Science*, 302:1931–1934, 2003.

M. Manga and E. Brodsky. Seismic triggering of eruptions in the far field: Volcanoes and geysers. *Annual Reviews of Earth and Planetary Sciences*, 34(1):263–291, 2006.

M. Manga, J. Castro, K. Cashman, and M. Loewenberg. Rheology of bubble-bearing magmas. *Journal of Volcanology and Geothermal Research*, 87(15-28), 1998.

M. Mangan, T. Wright, D. Swanson, and G. Byerly. Regional correlation of grande ronde basalt flows, columbia river basalt group, washington, oregon, and idaho. *Bulletin of the Geological Society of America*, 97(11):1300, 1986.

I. Manno. *Introduction to the Monte-Carlo Method*. Akademiai Kiado, Budapest, 1999.

B. Marsh. On convective style and vigor in sheet-like magma chambers. *Journal of Petrology*, 30(3):479–530, 1989.

B. D. Marsh. On the crystallinity, probability of occurence, and rheology of lava and magma. *Contributions to Mineralogy and Petrology*, 78:85–98, 1981.

B. D. Marsh and I. S. Carmichael. Benioff-zone magmatism. *Journal of Geophysical Research*, 79(8):1196–1206, 1974.

R. A. Marston. Supraglacial stream dynamics on the juneau icefield. *Annals of the Association of American Geographers*, 73(4):597–608, 1983.

J. Marti, A. Geyer, A. Folch, and J. Gottsmann. *A review on collapse caldera modelling*, volume 10, chapter 6. Elsevier, 2008.

B. G. Mason, D. Pyle, and C. Oppenheimer. The size and frequency of the largest explosive eruptions on earth. *Bulletin of Volcanology*, 66:735–748, 2004.

D. Massonnet, P. Briole, and A. Arnaud. Deflation of mount etna monitored by spaceborne radar interferometry. *Nature*, 375(15):567–570, June 1995.

L. G. Mastin. Insights into volcanic conduit flow from an open-source numerical model. *Geochemistry Geophysics Geosystems*, 3(7), 2002.

L. G. Mastin and M. S. Ghiorso. Adiabatic temperature changes of magma-gas mixtures during ascent and eruption. *Contributions to Mineralogy and Petrology*, 141:307–321, 2001.

J. E. P. Matzel, S. A. Bowring, and R. B. Miller. Time scales of pluton construction at differing crustal levels: Examples from the mount stuart and tenpeak intrusions, north cascades, washington. *GSA Bulletin*, 118(11/12):1412–1430, 2006.

R. McCaffery. Global frequency of magnitude 9 earthquakes. *Geology*, 36(3):263–266, 2008.

D. McKenzie. The generation and compaction of partially molten rock. *Journal of Petrology*, 25:713–765, 1984.

B. A. McNulty, W. Tong, and O. T. Tobisch. Assembly of a dike-fed magma chamber: The jackass lakes pluton, central sierra nevada, california. *GSA Bulletin*, 108(8):926–940, August 1996.

M. McNutt and A. Bonneville. A shallow, chemical origin for the marguesas swell. *Geochemistry Geophysics Geosystems*, 1, 2000.

D. F. McTigue. Elastic stress and deformation near a finite spherical magma body - resolution of the point-source paradox. *Journal of Geophysical Research*, 92(B12):12931–12940, 1987.

L. Melluso, V. Morra, P. Renne, I. Sgrosso, and M. D. .... Geochronology and petrology of cretaceous basaltic magmatism in the kwanza basin (western angola), and relationships with the paranā-etendeka continental flood .... *Journal of Geodynamics*, 28:341–356, Jan 1999.

O. Melnik and R. S. J. Sparks. Controls on magma flow dynamics during lava dome building eruptions. *Journal of Geophysical Research*, 110(B02209), doi:10.1029/2004JB003183 2005.

Meriaux and Lister. Calculation of dike trajectories from volcanic centers. *Journal of Geophysical Research*, 107(B4):2077–2087, 2002.

C. F. Miller and D. A. Wark. Supervolcanoes and their explosive supereruptions. *Elements*, 4(1):11–15, 2008.

J. S. Miller, J. E. P. Matzel, C. F. Miller, S. D. Burgess, and R. B. Miller. Zircon growth and recycling during the assembly of large, composite arc plutons. *Journal of Volcanology and Geothermal Research*, 167:282–299, 2007.

R. B. Miller and S. Paterson. Construction of mid-crustal sheeted plutons: Examples from the north cascades, washington. *Geological Society of America Bulletin*, 113(11):1423–1442, 2001.

R. B. Miller and S. R. Paterson. In defense of magmatic diapirs. *Journal of Structural Geology*, 21:1161–1173, 1999.

A. Mock and D. A. Jerram. Crystal size distributions (csd) in three dimensions: Insights from the 3d reconstruction of a highly porphyritic rhyolite. *Journal of Petrology*, pages 1–17, 2005.

K. Mogi. Relations between the eruptions of various volcanoes and the deformations of the ground suurfaces around them. *Bulletin of the Earthquake Research Institute*, 36:99–134, 1958.

P. A. Mohr and C. A. Wood. Volcano spacings and lithospheric attenuation in the eastern rift of africa. *Earth and Planetary Science Letters*, 33:126–144, 1976.

P. Moon and D. Spencer. *Field Theory Handbook, Including Coordinate Systems, Differential Equations, and Their Solutions*. New York: Springer Verlag, 2 edition, 1988.

W. Morgan. Convection plumes in the lower mantle. *Nature*, 230:42–43, 1971.

S. Morris. Stability of thermoviscous hele-shaw flow. *Journal of Fluid Mechanics*, 308: 111–128, 1996.

J. R. Muller, G. Ito, and S. J. Martel. Effects of volcano loading on dike propagation in an elastic half-space. *Journal of Geophysical Research*, 106(B6):11101–11113, 2001.

W. W. Mullins and R. F. Sekerka. Morphological stability of a particle growing by diffusion of heat. *Journal of Applied Physics*, 34:323–328, 1963.

K. Nakamura, K. H. Jacob, and J. N. Davies. Volcanoes as possible indicators of tectonic stress orientation - aleutians and alaska. *Pure and Applied Geophysics*, 115(1-2):87–112, 1977.

C. G. Newhall and S. Self. The volcanic explosivity index (vei): An estimate of explosive magnitude for historical volcanism. *Journal of Geophysical Research*, 87(C2):1231–1238, 1982.

A. V. Newman, T. H. Dixon, G. I. Ofoegbu, and J. E. Dixon. Geodetic and seismic constraints on recent activity at long valley caldera, california: evidence for viscoelastic rheology. *Journal of Volcanology and Geothermal Research*, 105:183–206, 2001.

A. V. Newman, T. H. Dixon, and N. Gourmelen. A four-dimensional viscoelastic deformation model for long valley caldera, california, between 1995 and 2000. *Journal of Volcanology and Geothermal Research*, 150:244–269, 2006.

T. Nielsen and C. Brooks. The e. greenland rifted continental-margin - an examination of the coastal flexure. *Journal of the Geological Society*, 138:559–568, 1981.

E. Norminton and J. Blackwell. Transient heat flow from constant temperature spheroids and the thin circular disk. *The Quarterly Journal of Mechanics and Applied Mathematics*, 17(1):65, 1964.

H. Odé. Mechanical analysis of the dike pattern of the spanish peaks area, colorado. *Geological Society of America Bulletin*, 68:567–576, 1957.

P. G. Okubo, H. M. Benz, and B. A. Chouet. Imaging the crstal magma sources benarth mauna loa and kilauea volcanoes, hawaii. *Geology*, 25(10):867–870, 1997.

P. Olson. *Magmatic Systems*, chapter Mechanics of flood bassalt magmatism, pages 1–18. Academic Press, New York, 1994.

P. Olson and H. Singer. Creeping plumes. *Journal of Fluid Mechanics*, 158:511–531, 1985.

C. O'Neill, A. Lenardic, A. M. Jellinek, and W. S. Kiefer. Melt propagation and volcanism in mantle convection simulations, with applications for martian volcanic and atmospheric evolution. *Journal of Geophysical Research*, 112(E07003), doi:10.1029/2006JE002799 2007.

M. Oskin, L. Perg, D. Blumentritt, S. Mukhopadhyay, and A. Iriondo. Slip rate of the calico fault: Implications for geologic versus geodetic rate discrepency in the eastern california shear zone. *Journal of Geophysical Research*, 112:16, 2007.

R. Pal. Rheological behavior of bubble-bearing magmas. *Earth and Planetary Science Letters*, 207:165–179, 2003.

J. S. Pallister, R. P. Hoblitt, and A. G. Reyes. A basaltic trigger for the 1991 eruptions of pinatubo volcano? *Nature*, 356:426–428, 1992.

P. Papale. Strain-induced magma fragmentation in explosive eruptions. *Nature*, 397:425–428, 1999a.

P. Papale. Modeling of the solubility of a two-component h2o + co2 fluid in silicate liquids. *American Mineralogist*, 84:477–492, 1999b.

G. Parker. Meandering of supraglacial melt streams. *Water Resources Research*, 11(4): 551–552, 1975.

T. Parsons, N. H. Sleep, and G. H. Thompson. Host rock rheology controls on the emplacement of tabular intrusions: implications for underplating of extending crust. *Tectonics*, 11(6):1348–1356, 1992.

S. R. Paterson, T. K. Fowler, and R. B. Miller. Pluton emplacement in arcs: A crustal-scale exchange process. *Transations of the Royal Society of Edinburgh, Earth Sciences*, 87:115–123, 1995.

H. L. Petcovic and J. Dufek. Modeling magma flow and cooling in dikes: Implications for emplacement of columbia river flood basalts. *Journal of Geophysical Research*, 110 (B10201):doi:10.1029/2004JB003432, 2005.

D. Peterson, R. Holccomb, R. Tilling, and R. Christiansen. Development of lava tubes in the light of observations at mauna ulu, kilauea volcano, hawaii. *Bullentin of Volcanology*, 56:343–360, 1994.

N. Petford. Dykes or diapirs? *Transations of the Royal Society of Edinburgh, Earth Sciences*, 87:105–114, 1996.

A. Philpotts, J. Shi, and C. Brustman. Role of plagioclase crystal chains in the differentiation of partly crystallized basaltic magma. *Nature*, 395(6700):343–346, 1998.

D. A. Pickett and L. B. Saleeby. Thermobarometric constraints on the depth of exposure and conditions of plutonism and metamorphism at deep levels of the sierra-nevada batholith, tehachapi mountains, california. *Journal of Geophysical Research-Solid Earth*, 98(B1): 609–629, 1993.

V. Pinel and C. Jaupart. The effect of edifice load on magma ascent beneath a volcano. *Philosophical Transaction of the Royal Society of London A*, 358:1515–1532, 2000.

V. Pinel and C. Jaupart. Magma chamber behvaior beneath a volcanic edifice. *Journal of Geophysical Research*, 108(B2, doi: 10.1029/2002JB001751), 2003.

V. Pinel and C. Jaupart. Caldera formation by magma withdrawl from a reservoir beneath a volcanic edifice. *Earth and Planetary Science Letters*, 230:273–287, doi:10.1016/j.epsl.2004.11.016 2005.

H. Pinkerton and R. J. Stevenson. Methods of determining the rheological properties of magmas at sub-liquidus temperatures. *Journal of Volcanology and Geothermal Research*, 53:47–66, 1992.

A. J. Piwinskii and P. J. Wyllie. Experimental studies of igneous rock series; a zoned pluton in the wallowa batholith, oregon. *Journal of Geology*, 76:483–499, 1968.

D. D. Pollard. derivation and evaluation of a mechanical model for sheet intrusions. *Tectonophysics*, 19:233–269, 1973.

M. E. Pritchard and M. Simons. An insar-based survey of volcanic deformation in the central andes. *Geochemistry Geophysics Geosystems*, 5(2), February 2004.

R. Ramalho, G. Helffrich, M. Costa, D. Vance, D. Hoffmann, and D. N. Schmidt. Episodic swell growth inferred from variable uplift of the cape verde hotspot islands. *Nature Geoscience*, 3:774–777, 2010.

M. R. Rampino and S. Self. Volcanic winter and accelerated glaciation following the toba super-eruption. *Nature*, 359(50-52), 1992.

R. P. Rapp and E. B. Watson. Dehydration melting of metabasalt at 8-32 kbar: Implications for continental growth and crust-mantle recycling. *Journal of Petrology*, 36(4):891–931, 1995.

R. Ray, H. C. Sheth, and J. Mallik. Structure and emplacement of the nandurdar-dhule mafic dyke swarm, deccan traps, and the tectonomagmatic evolution of flood basalts. *Bulletin of Volcanology*, 69:537–551, 2007.

M. E. Reid. Massice collapse of volcano edifices triggered by hydrothermal pressurization. *Geology*, 39(12), 2011.

M. Richards, R. Duncan, and V. Courtillot. Flood basalts and hot-spot tracks: plume heads and tails. *Science*, 246(4926):103–107, 1989.

V. Ridley and M. Richards. Deep crustal structure beneath large igneous provinces and the petrologic evolution of flood basalts. *Geochemistry Geophysics Geosystems*, 11(9), 2010.

J. Riker, K. Cashman, and J. Kauahikaua. The length of channelized lava flows: Insight from the 1859 eruption of mauna loa volcano, hawai'i. *Journal of Volcanology and Geothermal Research*, 183:139–156, 2009.

J. Roberge, P. J. Wallace, R. V. White, and M. F. Coffin. Anomalous uplift and subsidence of the ontong java plateau inferred from co2 contents of submarine basaltic glasses. *Geology*, 33(6):501–504, 2005.

O. Roche and T. H. Druitt. Onset of caldera collapse during ignimbrite eruptions. *Earth and Planetary Science Letters*, 191:191–202, 2001.

S. M. Roper and J. R. Lister. Buoyancy-driven crack propagation from an over-pressured source. *Journal of Fluid Mechanics*, 536:79–98, 2005.

A. M. Rubin. Getting granite dikes out of the source region. *Journal of Geophysical Research*, B4:5911–5929, 1995a.

A. M. Rubin. Propagation of magma-filled cracks. *Annual Reviews of Earth and Planetary Sciences*, 23:287–336, 1995b.

R. L. Rudnick, W. E. McDonough, and R. J. O'Connell. Thermal structure, thickness and composition of continental lithosphere. *Chemical Geology*, 145:395–411, 1998.

P. Ruprecht, G. W. Bergantz, and J. Dufek. Modeling of gas-driven magmatic overturn: Tracking of phenocryst dispersal and gathering during magma mixing. *Geochemistry Geophysics Geosystems*, 9(Q07017), doi:10.1029/2008GC002022 2008.

E. Rybacki and G. Dresen. Dislocation and diffusion creep of synthetic anorthie aggregates. *Journal of Geophysical Research*, 105(26017-36), 2000.

F. J. Ryerson, H. C. Weed, and A. J. Piwinskii. Rheology of subliquidus magmas 1. picritic compositions. *Journal of Geophysical Research*, 93(B4):3421–3436, 1988.

M. O. Saar, M. Manga, K. V. Cashman, and S. Fremouw. Numerical models of the onset of yield strength in crystal-melt suspensions. *Earth and Planetary Science Letters*, 187: 367–379, 2001.

G. Sartoris, J. P. Pozzi, C. Phillippe, and J. L. L. Mouel. Mechanial stability of shallow magma chambers. *Journal of Geophysical Research*, 95(B4):5141–5151, 1990.

A. Saunders, S. Jones, L. Morgan, K. Pierce, M. Widdowson, and Y. Xu. Regional uplift associated with continental large igneous provinces: The roles of mantle plumes and the lithosphere. *Chemical Geology*, 241(3-4):282–318, 2007.

S. S. Savant and S. L. de Silva. A gis-based spatial analysis of volcanoes in the central andes: Insights into factors controlling volcano spacing. *EOS Transactions of AGU Fall Meeting Suppliment, Abstract V21D-0648*, 86(52), December 2005.

B. Scaillet, F. Holtz, and M. Pichavant. Phase equilibrium constraints on the viscosity of silicic magmas; 1. volcanic-plutonic comparison. *Journal of Geophysical Research*, 103 (B1):27257–27266, 1998.

B. Scaillet, M. Pichavant, and R. Cioni. Upward migration of vesuvius magma chamber over the past 20,000 years. *Nature*, 455:216–219, September 2008.

P. M. Schenk and D. Williams. A potential thermal erosion lava channel on io. *Geophysical Research Letters*, 31(L23702), 2004.

H. Schlichting. *Boundary Layer Theory*. McGraw-Hill Book Company, 4th edition, 1960.

H. Schmeling. A model of episodic melt extraction for plumes. *Journal of Geophysical Research*, 111(B03202), 2006.

G. Schubert, R. Lingenfelter, and S. Peale. The morphology, distribution, and origin of lunar sinuous rilles. *Reviews of geophysics and space physics*, 8(1), 1970.

S. Self. The importance of pahoehoe. *Annual Reviews of Earth and Planetary Science*, 26: 81–110, 1998.

S. Self. The effects and consequences of very large explosive volcanic eruptions. *Philosophical Transaction of the Royal Society of London A*, 364:2073–2097, 2006.

S. Self, F. Goff, J. Gardner, J. V. Wright, and W. M. Kite. Explosive rhyolitic volcanism in the jemez mountains: Vent locations, caldera development and relation to regional structure. *Journal of Geophysical Research*, 91(B2):1779–1798, 1986.

G. Seminara. Meanders. *Journal of Fluid Mechanics*, 554:271–297, 2006.

G. Seminara and M. Turbino. Weakly nonlinear theory of regular meanders. *Journal of Fluid Mechanics*, 244:257–288, 1992.

S. T. Siebert. Volcanoes of the world: an illustrated catalog of holocene volcanoes and their eruptions. Smithsonian Institution, Global Volcanism Program Digital Information Series, GVP-3, (http://www.volcano.si.edu/world), 2002.

J. Siewert and C. Ferlito. Mechanical erosion by flowing lava. *Contemporary Physics*, 49(1): 43–54, 2008.

J. I. Simon and M. R. Reid. The pace of rhyolite differentiation and storage in an 'archetypical' silicic magma system, long valley, california. *Earth and Planetary Science Letters*, 235:123–140, 2005.

J. I. Simon, P. R. Renne, and R. Mundil. Implications of pre-eruptive magmatic histories of zircons for u-pb geochronology of silicic extrusions. *Earth and Planetary Science Letters*, 266:182–194, doi:10.1016/j.epsl.2007.11.014 2008.

L. S. Sklar and W. E. Dietrich. A mechanistic model for river incision into bedrock by saltating bedload. *Water Resources Research*, 40(W06301), 2004.

N. H. Sleep. Edge-modulated stagnant-lid convection and volcanic passive margins. *Geochemistry Geophysics Geosystems*, 8(12), 2007.

N. H. Sleep, C. J. Ebinger, and J. M. Kendell. *Deflection of mantle plume material by cratonic keels*, volume 199, pages 135–150. The geological society of London, 2002.

J. D. Smith and S. R. McLean. A model for flow in meandering streams. *Water Resources Research*, 20(9):1301–1315, 1984.

J. R. Smith, D. J. Frost, F. Nestola, C. M. Holl, and G. Bromiley. Olivine hydration in the deep upper mantle: Effects of temperature and silica activity. *Geophysical Research Letters*, 33(L15301), 2006.

R. Smith, M. Jordan, B. Stienberger, C. Puskas, J. Farrell, G. Whaite, S. Husen, W. Chang, and R. O'Connell. Geodynamics of the yellowstone hotspot and mantle plume: Seismic and gps imaging, kinematics, and mantle flow. *Journal of Volcanology and Geothermal Research*, 188(1-7):26–56, 2009.

F. Spera. Thermal evolution of plutons: a parameterized approah. *Science*, 207(4428): 299–301, 1980.

F. Spera and W. A. Bohrson. Energy-constrained open-system magmatic processes i: General model and energy-constrained assimilation and fractional crystallization (ec-afc) formulation. *Journal of Petrology*, 42(5):999–1018, 2001.

M. Spiegelman. Flow in deformable porous media. part 1 simple analysis. *Journal of Fluid Mechanics*, 247:17–38, 1993.

M. Spiegelman and P. Kenyon. The requirements for chemical disequilibrium during magma migration. *Earth and Planetary Science Letters*, 109:611–620, 1992.

N. Spilliaert, N. Metrich, and P. Allard. S-cl-f degassing pattern of water-rich alkali basalt: Modelling and relationship with eruption styles on mount etna volcano. *Earth and Planetary Science Letters*, 248(772-786), 2006.

H. Stanley, L. Amaral, P. Gopikrishnan, P. Ivanov, T. Keitt, and V. Plerou. Scale invariance and universalityl organizing principles in complex systems. *Physica AL Statistical Mechanics and its applications*, 281(1-4):60–68, 2000.

C. P. Stark, J. R. Barbour, Y. S. Hayakawa, T. Hattanji, N. Hovius, H. Chen, C.-W. Lin, M.-J. Horng, K.-Q. Xu, and Y. Fukahata. The climatic signature of incised river meanders. *Science*, 327:1497–1500, 2010.

M. V. Stasuik, C. Jaupart, and R. S. J. Sparks. On the variation of lava flow rate in non-explosive lava eruptions. *Earth and Planetary Science Letters*, 114:505–516, 1993.

G. Stevens, R. L. Gibson, and G. T. R. Droop. Mid-crustal granulite facies metamorphism in the central kaapvaal craton: the bushveld complex connection. *Precambrian Research*, 82:113–132, 1997.

J. J. Stickel and R. L. Powell. Fluid mechanics and rheology of dense suspensions. *Annual Reviews of Fluid Mechanics*, 37:129–149, 2005.

J. Stix and T. Kobayashi. Magma dynamics and collapse mechanisms during four historic caldera-forming events. *Journal of Geophysical Research*, 113(B09205), 2008.

M. Storey, R. Duncan, and C. Tegner. Timing and duration of volcanism in the north atlantic igneous province: Implications for geodynamics and links to the iceland hotspot. *Chemical Geology*, 241:264–281, 2007.

D. Swanson. Pahoehoe flows from the 1969-1971 mauna ulu eruption, kilauea volcano, hawaii. *Geological Society of America Bulletin*, 84(2):615–626, 1973.

D. Swanson, T. Casadevall, D. Dzurisin, S. Malone, C. Newhall, and C. Weaver. Predicting eruptions at mount st. helens, june 1980 through december 1982. *Science*, 221(4618): 1369–1376, 1983.

S. Tait, C. Jaupart, and S. Vergniolle. Pressure, gas content and eruption periodicity of a shallow, crystallizing magma chamber. *Earth and Planetary Science Letters*, 92:107–123, 1989.

Y. Tamura, Y. Tatsumi, D. Zhao, Y. Kido, and H. Shukuno. Hot fingers in the mantle wedge: new insights into magma genesis in subduction zones. *Earth and Planetary Science Letters*, 197:105–116, 2002.

L. Tanton and B. Hager. Melt intrusion as a trigger for lithospheric foundering and the eruption of the siberian flood basalts. *Geophys. Res. Lett*, 27(23):3937–3940, 2000.

A. J. Taylor and S. D. Wilson. Conduit flow of an incompressible, yield-stress fluid. *Journal of Rheology*, 41(1):93–101, 1997.

R. L. Taylor. Feap: A finite element analysis program. *User Manual*, 2008.

C. Tegner, C. Brooks, R. Duncan, L. Heister, and S. Bernstein. 40ar-39ar ages of intrusions in east greenland: Rift-to-drift transition over the iceland hotspot. *Lithos*, 101(3-4):480–500, 2008.

U. ten Brink. Volcano spacing and plate rigidity. *Geology*, 19:397–400, April 1991.

P. Traversa, V. Pinel, and J. R. Grasso. A constant influx model for dike propagation: Implications for magma reservoir dynamics. *Journal of Geophysical Research*, 115(B01201), 2010.

D. Turcotte and G. Schubert. *Geodynamics*. Cambridge University Press, 2002.

J. Turner and I. Campbell. Convection and mixing in magma chambers. *Earth Sci. Rev*, 23 (4):255–352, 1986.

S. Turner and F. Costa. Measuring timescales of magmatic evolution. *Elements*, 3:267–272, 2007.

G. A. Valentine and K. E. C. Krogh. Emplacement of shallow dikes and sills beneath a small basaltic volcano - the role of pre-existing structure (paiute ridge, southern nevada, usa). *Earth and Planetary Science Letters*, 246(3-4):217–230, doi:10.1016/j.epsl.2006.04.031 2006.

J.-L. Vigneresse, B. Tikoff, and L. Ameglio. Modification of the regional stress field by magma intrusion and formation of tabular granitic plutons. *Tectonophysics*, 302:203–224, 1999.

D. R. Villagomez, D. Toomey, E. Hooft, and S. Solomon. Upper mantle structure beneath the galapagos archipelago from surface wave tomography. *Journal of Geophysical Research*, 112(B07303), 2007.

P. R. Vogt. Volcano spacing, fractures, and thickness of the lithosphere. *Earth and Planetary Science Letters*, 21:235–252, 1974.

B. Voight and R. R. Cornelius. Prospects for eruption prediction in near-real-time. *Nature*, 350:695–698, 1991.

V. R. Voller and C. R. Swaminathan. General source-based method for solidification phase change. *Numerical Heat Transfer, Part B*, 19:175–189, 1991.

P. J. Wallace. Volatiles in subduction zone magmas: concentrations and fluxes based on melt inclusion and volcanic gas data. *Journal of Volcanology and Geothermal Research*, 140:217–240, doi:10.1016/j.jvolgeores.2004.07.023 2005.

S. D. C. Walsh and M. O. Saar. Numerical models of stiffness and yield stress growth in crystal-melt suspensions. *Earth and Planetary Science Letters*, 267:32–44, 2008.

A. Watts and U. T. Brink. Crustal structure, flexure, and subsidence history of the hawaiian islands. *Journal of Geophysical Research*, 94(B8):10473–10500, Jan 1989.

R. S. White, L. K. Smith, A. W. Roberts, P. A. F. Christie, N. J. Kusznir, A. M. Roberts, D. Healy, R. Spitzer, A. Chappel, and J. D. Eccles. Lower-crustal intrusion on the north atlantic continental margin. *Nature*, 452:460–464, 2008.

P. J. Whiting and W. E. Dietrich. Experimental studies of bed topography and flow patterns in large amplitude meanders: 1. observations. *Water Resources Research*, 29:3605–3614, 1993.

A. Whittington, A. Hofmeister, and P. Nabelek. Temperature-dependent thermal diffusivity of the earth's crust and implications for magmatism. *Nature*, Jan 2009.

D. Williams, R. Greeley, E. Hauber, K. Gwinner, and G. Neukum. Erosion by flowing martian lava: New insights for hecates tholus from mars express and mer data. *Journal of Geophysical Research*, 110(E05006), 2005.

M. L. Williams, K. E. Karlstrom, G. Dumond, and K. H. Mahan. Perspectives on the architecture of continental crust from integrated field studies of exposed isobaric sections. *Geological Society of America Special Paper 456*, 2009.

M. B. Wolf and P. J. Wyllie. Dehydration-melting of amphibolite at 10 kbar: the effects of temperature and time. *Contributions to Mineralogy and Petrology*, 115:369–383, 1994.

J. A. Wolff, F. C. Ramos, G. L. Hart, J. D. Patterson, and A. D. Brandon. Columbia river flood basalts from a centralized crustal magma system. *Nature Geoscience*, 1(3):177–180, 2008.

A. Woods, R. Sparks, L. Ritchie, J. Batey, C. Gladstone, and M. Bursik. The explosive decompression of a pressurized volcanic dome: the 26 december 1997 collapse and explosion of soufriere hills volcano, montserrat. *Geological Society, London, Memoirs*, 21:457–465, 2002.

J. Wylie and J. Lister. The effects of temperature-dependent viscosity on flow in a cooled channel with application to basaltic fissure eruptions. *Journal of Fluid Mechanics*, 305: 239–261, 1995.

L. W. Younker and T. A. Vogel. Plutonism and plate tectonics; the origin of circum-pacific batholiths. *Canadian Mineralogist*, 14:238–244, 1976.

S. Yun, P. Segall, and H. Zebker. Constraints on magma chamber geometry at sierra negra volcano, galapagos islands, based on insar observations. *Journal of Volcanology and Geothermal Research*, 150:232–243, 2006.

J. Zak and S. R. Paterson. Characteristics of internal contacts in the tuolumne batholith, central sierra nevada, california (usa): Implications for episodic emplacement and physical processes in a continental arc magma chamber. *GSA Bulletin*, 117(9/10):1242–1255, 2005.

G. Zolezzi and G. Seminara. Downstream and upstream influence in river meandering. part 1. general theory and applications to overdeepening. *Journal of Applied Physics*, 438: 183–211, 2001.